Journal of Membrane Science 643 (2022) 120049

Contents lists available at ScienceDirect

Journal of Membrane Science

journal homepage: www.elsevier.com/locate/memsci

Using the spreading pressure to inter-relate the characteristics of unary, binary and ternary mixture permeation across microporous membranes

Rajamani Krishna [*], Jasper M. van Baten

Van 't Hoff Institute for Molecular Sciences, University of Amsterdam, Science Park 904, 1098 XH, Amsterdam, the Netherlands

A R T I C L E I N F O

Keywords:
Mixture adsorption
Permeation selectivity
Microporous membrane
Surface potential
Permeabilities

A B S T R A C T

The primary objective of this article is to investigate the possibility of inter-relating the characteristics of unary, binary, and ternary mixtures across microporous zeolite membranes. Towards this end, we performed Configurational-Bias Monte Carlo (CBMC) simulations of mixture adsorption equilibrium, and Molecular Dynamics (MD) simulations of guest diffusivities in unary (CO_2, CH_4, N_2, and H_2), binary (CO_2/CH_4, CO_2/N_2, CH_4/N_2, CO_2/H_2), and ternary ($CO_2/CH_4/N_2$, $CO_2/CH_4/H_2$, $CO_2/N_2/H_2$) mixtures in four zeolites: CHA, DDR, MFI, and FAU. The combined CBMC and MD data are used to obtain fundamental insights into the adsorption, diffusion, and permeation characteristics of the variety of guest/host combinations. Application of the Myers-Prausnitz theory shows that the adsorption selectivity for the *i-j* pair, $S_{ads,ij}$, in ternary mixtures has practically the same value as for the binary *i-j* mixture, provided the comparison is made as the same surface potential Φ, a convenient and practical proxy for the spreading pressure π, that is calculable on the basis of the data on the unary isotherms of the constituent guests. For the mixtures investigated, departures from thermodynamic idealities do not cause deviations from the uniqueness of the $S_{ads,ij}$ vs Φ dependence because the ratios of the activity coefficients γ_i/γ_j also appear to uniquely depend on Φ.

The surface potential Φ is also the thermodynamically correct metric to describe the loading dependence of diffusivities. Compared at the same Φ, the diffusion selectivity for the *i-j* pair, $S_{diff,ij}$, in ternary mixtures has practically the same value as for the binary *i-j* mixture. Consequently, the permeation selectivity, $S_{perm,ij} = S_{ads,ij} \times S_{diff,ij}$ is also uniquely dependent on Φ. When compared at the same Φ, the component permeabilities, Π_i for CO_2, CH_4, and N_2 are found to be independent of the partners in the binary and ternary mixtures investigated and have practically the same as the values for the corresponding unary permeabilities.

1. Introduction

Membrane technologies find applications for separation a variety of gaseous mixtures, such as CO_2/CH_4, CO_2/N_2, CO_2/H_2, and CH_4/N_2 [1–6]. The perm-selective membrane layers often consist of crystalline microporous materials such as zeolites (alumino-silicates) [7–18] metal-organic frameworks (MOFs) [19], or zeolitic imidazolate frameworks (ZIFs) [20–22].

For any given application, the separation performance of a microporous membrane is characterized by two metrics: permeability and permeation selectivity. The permeability of component *i* is defined as

$$\Pi_i = \frac{N_i}{\Delta f_i/\delta} \tag{1}$$

where N_i is the permeation flux and $\Delta f_i = f_i - f_{i\delta}$ is the difference in the partial fugacities between the upstream (f_i) and downstream $(f_{i\delta})$ faces of the membrane layer of thickness δ. For the *i-j* pair in *n*-component mixtures, the membrane permeation selectivity, $S_{perm,ij}$, is defined as the ratio of the component permeabilities

$$S_{perm,ij} = \frac{N_i/\Delta f_i}{N_j/\Delta f_j} = \frac{\Pi_i}{\Pi_j} \tag{2}$$

In previous works [23,24], we had established the benefits of using the *spreading* pressure, π, defined by the Gibbs adsorption equation [25], to characterize the component permeabilities. These studies showed that the component permeabilities Π_i for *binary* mixture permeation are relatable to the corresponding *unary* permeabilities, provided the comparisons are made at the same values of π. The primary objective of the

---

[*] Corresponding author.
E-mail address: r.krishna@contact.uva.nl (R. Krishna).

https://doi.org/10.1016/j.memsci.2021.120049
Received 11 June 2021; Received in revised form 2 November 2021; Accepted 5 November 2021

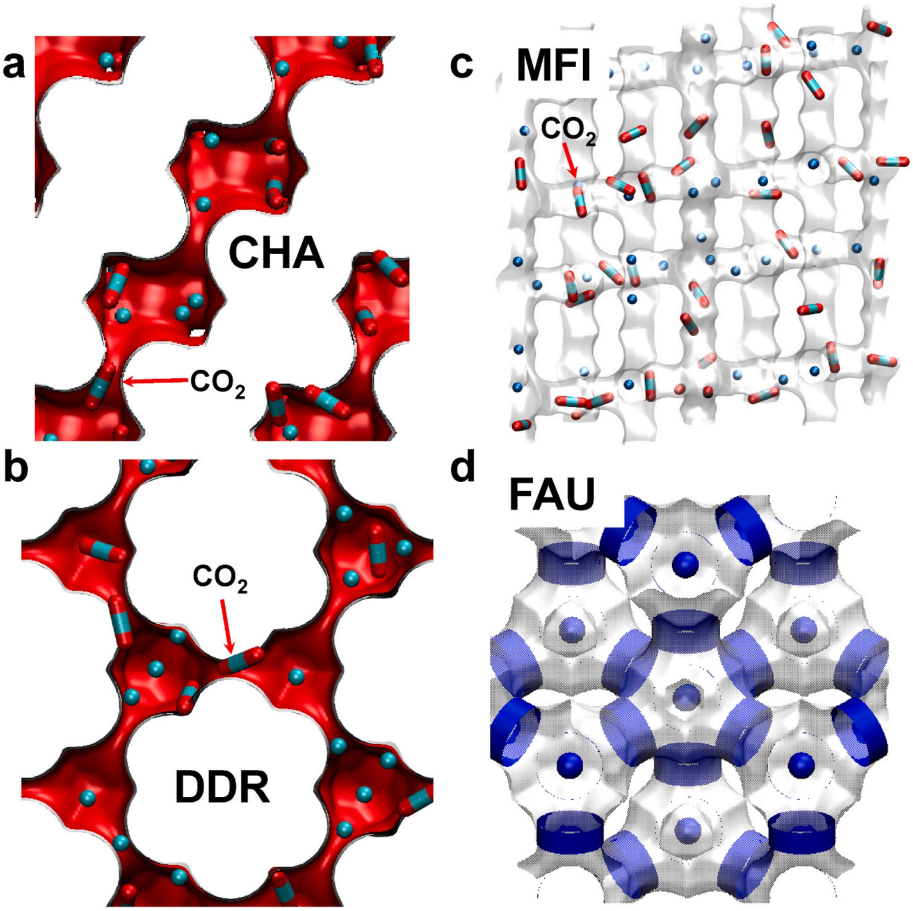

Fig. 1. Pore landscapes of (a) CHA, (b) DDR, (c) MFI, and (d) FAU zeolite.

present communication is to extend the previous analyses to include *ternary* mixtures. Using a fundamental thermodynamic analysis of adsorption and diffusion of mixtures of guest molecules in microporous materials, we aim to show that the permeation characteristics of n-component mixtures, with $n = 1$, 2 or 3, are relatable to one another provided the comparisons at the same value of π. The secondary objective is to demonstrate that the conclusions drawn in this work are not significantly altered by departures from thermodynamic idealities in mixture adsorption.

To meet the objective set for this article, we undertake molecular simulations of both mixture adsorption and intra-crystalline diffusion in CHA, DDR, MFI, and FAU zeolites, each in the all-silica form (i.e. Si/Al $\rightarrow\infty$). The pore landscapes of these four materials, commonly used as perm-selective membranes, are shown in Fig. 1. CHA zeolite consists of cages of volume 316 Å^3, separated by 8-ring windows of 3.8 Å × 4.2 Å size. DDR zeolite has cages of 278 Å^3 volume, separated by 8-ring windows of 3.65 Å × 4.37 Å size. MFI zeolite consists of a set of intersecting straight channels, and zig-zag (or sinusoidal) channels of 5.5 Å size. FAU zeolite has cages of 786 Å^3 volume, separated by 7.4 Å 12-ring windows. FAU is commonly used in cation-exchanged form called NaX or 13X; per unit cell of NaX zeolite we have 106 Si, 86 Al, 86 Na^+ with Si/Al = 1.23.

We undertake Configurational-Bias Monte Carlo (CBMC) simulations for adsorption of light gaseous unary guests (CO_2, CH_4, N_2, H_2), binary (CO_2/CH_4, CO_2/N_2, CH_4/N_2, CO_2/H_2) mixtures, ternary ($CO_2/CH_4/N_2$, $CO_2/CH_4/H_2$, $CO_2/N_2/H_2$), and quaternary ($CO_2/CH_4/N_2/H_2$) mixtures. Molecular Dynamics (MD) simulations are also undertaken to determine the self-diffusivities, $D_{i,self}$, of each guest species in corresponding unary, binary and ternary mixtures. For MFI and FAU, additional simulations on adsorption and diffusion of $CH_4/C_2H_6/C_3H_8$ mixtures, along with the constituent binary mixtures were also investigated. To specifically investigate the influence of thermodynamic non-idealities adsorption simulations for NaX zeolite were conducted for $CO_2/CH_4/N_2$, and $CO_2/CH_4/C_3H_8$ mixtures. The CBMC and MD simulation methodologies are detailed in the Supplementary Material accompanying this publication.

2. Thermodynamics of mixture adsorption

The Gibbs adsorption equation [25] relates π to the molar chemical potential, μ_i, and the component molar loading, q_i, in the adsorbed phase as follows

$$A d\pi = \sum_{i=1}^{n} q_i d\mu_i \tag{3}$$

where A represents the surface area per kg of framework. At phase equilibrium, equating the component chemical potentials, μ_i, in adsorbed phase and in the bulk gas phase mixture in the upstream membrane compartment, we write

$$d\mu_i = RTd\ln f_i \tag{4}$$

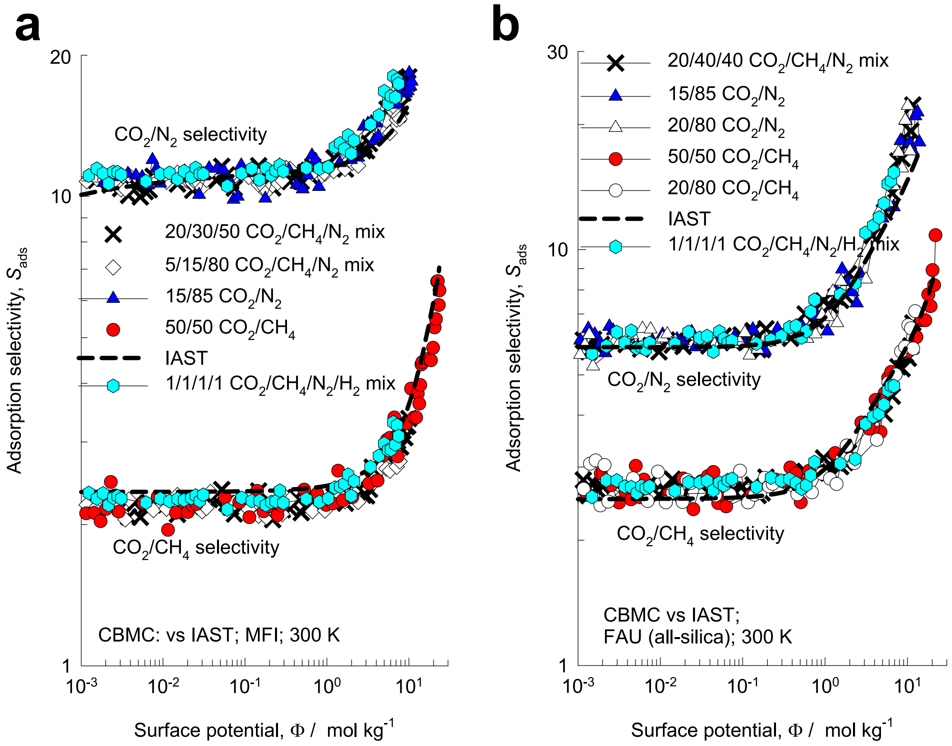

Fig. 2. (a, b) CBMC simulations of CO$_2$/CH$_4$, and CO$_2$/N$_2$ adsorption selectivities, S_{ads}, in (a) MFI, (b) FAU zeolites at 300 K, plotted as function of the surface potential, Φ. The pair selectivities are determined from CBMC data for binary, ternary, and quaternary mixtures. The dashed lines are IAST estimates of $S_{ads,ij}$. All calculation details and input data are provided in the Supplementary Material accompanying this publication.

Using the analogy with vapor/liquid equilibrium, Myers and Prausnitz [26] write the following expression relating the partial fugacities in the bulk gas mixture

$$f_i \; = \; P_i^0 \gamma_i x_i; \quad i = 1,2,...n \tag{5}$$

to the mole fractions, x_i, in the adsorbed phase mixture

$$x_i = \frac{q_i}{q_1 + q_2 + ... q_n}; \quad i = 1,2,...n \tag{6}$$

In eq (5), P_i^0 is the pressure for sorption of every component i, which yields the same spreading pressure, π for each of the pure components, as that for the n-component mixture:

$$\frac{\pi A}{RT} = \int_0^{P_1^0} \frac{q_1^0(f)}{f} df = \int_0^{P_2^0} \frac{q_2^0(f)}{f} df = \int_0^{P_3^0} \frac{q_3^0(f)}{f} df \tag{7}$$

In eq (7), $q_i^0(f)$ is the *pure* component adsorption isotherm. Since the surface area A is not directly accessible from experimental data, the surface potential $\pi A/RT \equiv \Phi$, with the units mol kg^{-1}, serves as a convenient and practical proxy for the spreading pressure π [23,24,27,28]. From eq (7), it is evident that the value of Φ depends on partial fugacities f_i of each of the guests, along with the unary isotherms; the isotherms reflect the specific guest/host interactions. In view of eq (5), we may express the adsorption selectivity for the *i-j* pair in *n*-component mixtures as follows

$$S_{ads,ij} = \frac{q_i/q_j}{f_i/f_j} = \frac{x_i/f_i}{x_j/f_j} = \frac{P_j^0 \gamma_j}{P_i^0 \gamma_i} \tag{8}$$

In the *Ideal* Adsorbed Solution Theory (IAST), we further assume that the activity coefficients of each of the components in the mixture are equal to unity, leading the following simplification

$$\gamma_i = \gamma_j = 1; \quad S_{ads,ij} = \frac{P_j^0}{P_i^0}; \quad i,j = 1,2...n \tag{9}$$

The applicability of eq (9) mandates: (i) all of the adsorption sites within the microporous material are equally accessible to each of the guest molecules, implying a homogeneous distribution of guest adsorbates within the pore landscape, (ii) there are no preferential locations of any guest species in the pore landscape, and (iii) there is no molecular clustering as a result of say hydrogen bonding between guest molecules as is the case for water/alcohol mixtures [29–32].

Applying the restriction specified by eq (7), it follows that $S_{ads,ij}$ is uniquely determined by the surface potential Φ. It is important to note that eq (9) is valid irrespective of the total number of components in the mixture. The presence of component 3 in the ternary mixture influences the adsorption selectivity $S_{ads,12} = P_2^0/P_1^0$ for the 1–2 pair, *only* via the values of the sorption pressures P_i^0 which must satisfy eq (7) to yield the same value of surface potential Φ for each of the individual components in the mixture. A further point that requires to be underscored is that the calculation of the surface potential Φ does *not* mandate that $\gamma_i = 1$.

In Fig. 2a and b, the CO$_2$/CH$_4$, and CO$_2$/N$_2$ adsorption selectivities in MFI and FAU zeolites determined from CBMC simulations data for binary mixtures are compared with the values determined for CO$_2$/CH$_4$/N$_2$ and CO$_2$/CH$_4$/N$_2$/H$_2$ mixtures. The CBMC data for each binary pair on S_{ads} displays a unique dependence on the surface potential Φ, as anticipated from the application of eq (7), and (9). Also, the CBMC data

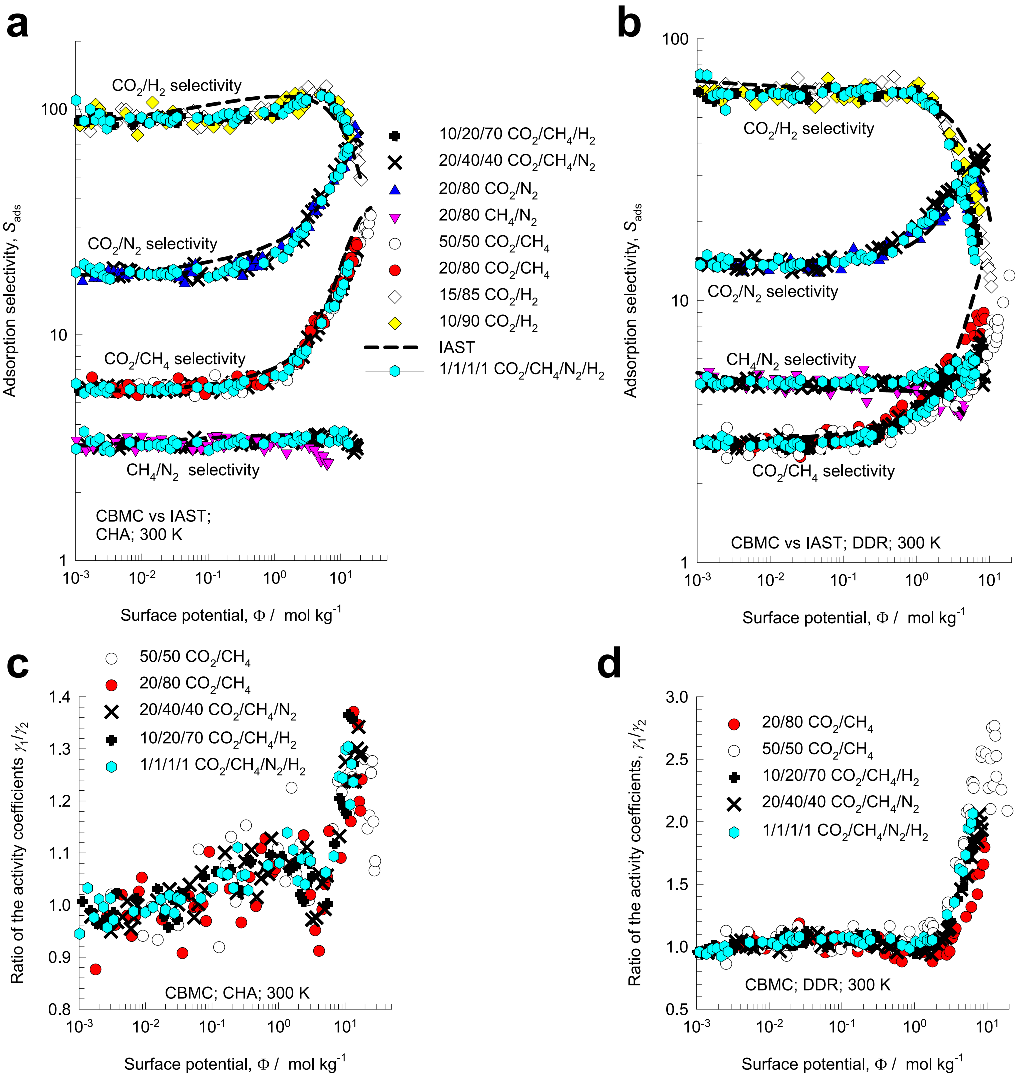

Fig. 3. (a, b) CBMC simulations of CO_2/CH_4, CO_2/H_2, CO_2/N_2, and CH_4/N_2 adsorption selectivities, S_{ads}, in (a) CHA, and (b) DDR zeolites at 300 K, plotted as function of the surface potential, Φ. The pair selectivities are determined from CBMC data for binary, ternary, and quaternary mixtures. The dashed lines are IAST estimates of S_{ads}. (c, d) CBMC simulations of the ratio of activity coefficients of ratio of activity coefficients of CO_2, and CH_4, γ_1/γ_2, in (c) CHA, and (d) DDR zeolites, as function of the surface potential Φ. All calculation details and input data are provided in the Supplementary Material accompanying this publication.

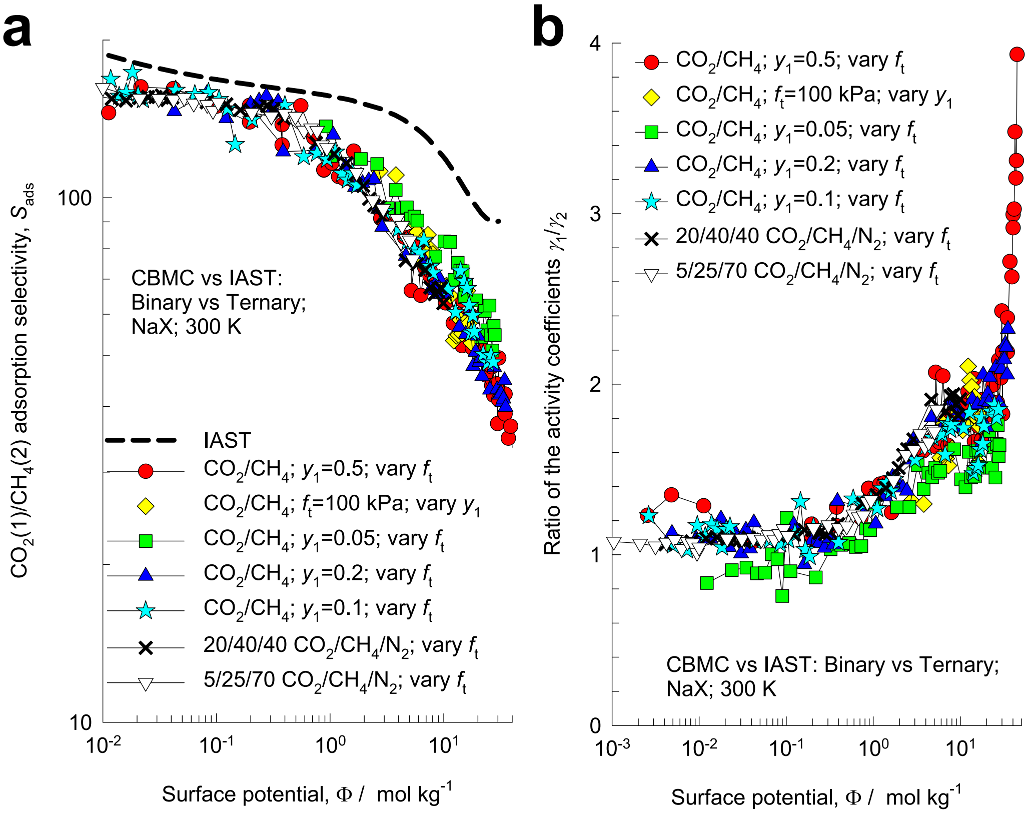

Fig. 4. (a) CBMC simulations of the CO_2/CH_4 adsorption selectivity, S_{ads}, for binary and ternary mixture adsorption in NaX zeolite at 300 K. The adsorption selectivities are plotted as function of the surface potential Φ. The dashed lines are the IAST estimates of S_{ads} (b) CBMC simulations of the ratio of activity coefficients of CO_2, and CH_4 plotted as function of the surface potential Φ. All calculation details and input data are provided in the Supplementary Material accompanying this publication.

are in excellent agreement with the IAST estimates, determined from dual-Langmuir-Freundlich fits of the unary isotherms; see details in the Supplementary Material.

Fig. 3a and b plots the selectivities for CO_2/CH_4, CO_2/N_2, CO_2/H_2, and CH_4/N_2 pairs in CHA, and DDR zeolites determined from CBMC data for adsorption of binary, ternary and quaternary mixtures of a variety of compositions. Each of the individual pair selectivities displays a unique dependence on Φ, irrespective of the number of components in the mixture. The IAST calculations (indicated by dashed lines in Fig. 3a and b) shows small deviations from the CBMC simulated data due to non-idealities caused by preferential perching of CO_2 at the window regions of CHA and DDR; detailed explanations are provided in our earlier works [29–32]. For further elucidation of the influence of thermodynamic non-idealities, the ratio of the activity coefficient of $CO_2(1)$ to that of $CH_4(2)$, γ_1/γ_2, is plotted in Fig. 3c and d as a function of Φ. The procedure for determination of the activity coefficients from CBMC simulation data is detailed in Chapter 4 of the Supplementary Material. We note that γ_1/γ_2 for both binary and ternary mixtures are uniquely related to Φ. For this reason, the $CO_2(1)/CH_4(2)$ adsorption selectivity shows a unique dependence on Φ, despite the small deviations of IAST estimates of adsorption selectivities from CBMC data.

The inescapable conclusion to be drawn is that for the adsorption of light gaseous molecules (CO_2, CH_4, N_2, H_2) in the four host materials (CHA, DDR, MFI, FAU) considered in this article, the uniqueness of the S_{ads} vs Φ relationship is not affected by non-idealities in mixture adsorption. Further detailed confirmation for other mixture/host combination are provided for CHA (see Figs. S26–S29), DDR (see Figs. S41–S45), MFI (see Figs. S66–S68), and all-silica FAU (see Fig. S81).

For adsorption of CO_2/CH_4 mixtures in cation-exchanged NaX zeolite, the thermodynamic non-idealities are much stronger due to the congregation of CO_2 molecules around the Na^+ cations [29–33]; this causes an inhomogeneous distribution of adsorbates in the pore space, violating the IAST mandate of homogeneous distribution [31,33]. Fig. 4a shows CBMC simulations of the CO_2/CH_4 adsorption selectivity, S_{ads}, for binary and ternary mixture adsorption in NaX zeolite. Despite the large deviations from the IAST estimates (shown by the dashed line), the S_{ads} vs Φ relationship is practically the same for both binary and ternary mixtures. Fig. 4b confirms that the ratio of the activity coefficient of $CO_2(1)$ to that of $CH_4(2)$, γ_1/γ_2, is uniquely dependent on surface potential Φ. Other examples demonstrating that the ratios of activity coefficients are uniquely determined by Φ are presented in Figs. S92–S113 of the Supplementary Material.

3. Mixture diffusion and permeation

As derived in detail in Chapter 3 of the Supplementary Material, the fractional pore occupancy, θ, is related to the surface potential by

$$\theta = 1 - \exp\left(-\frac{\Phi}{q_{sat,mix}}\right) \qquad (10)$$

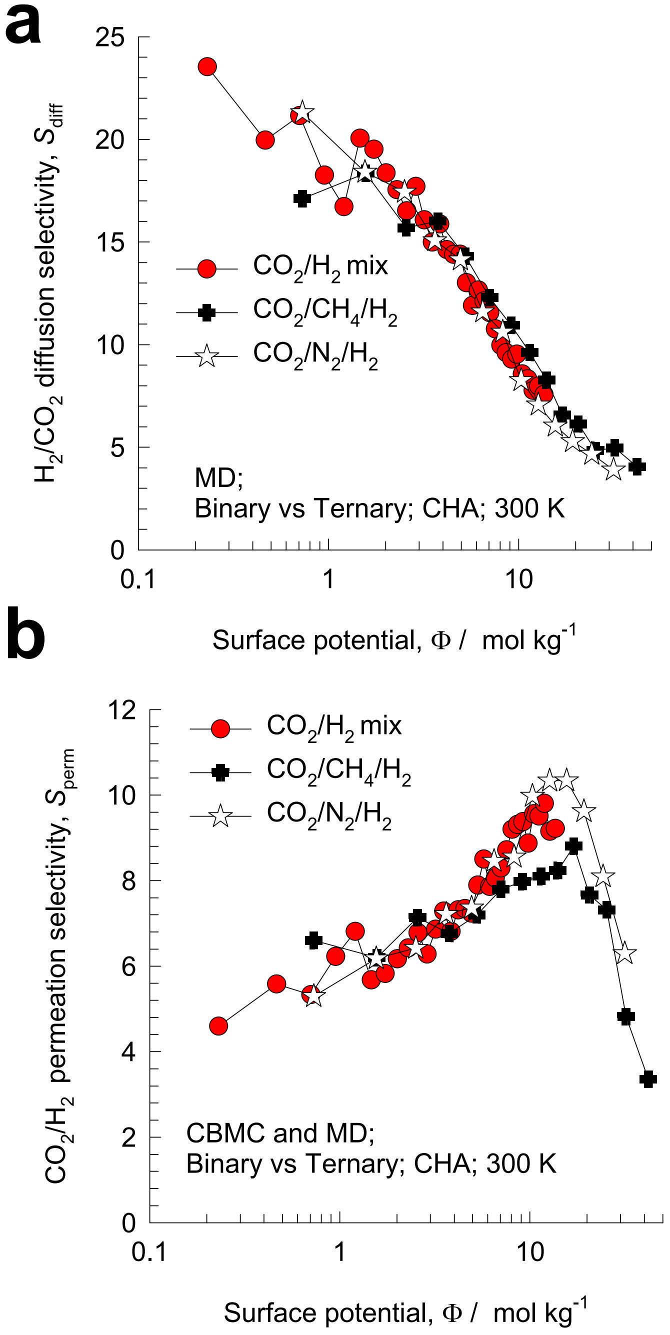

Fig. 5. (a) MD simulations of the H_2/CO_2 diffusion selectivities, S_{diff}, determined from both binary (CO_2/H_2) and ternary ($CO_2/N_2/H_2$, and $CO_2/CH_4/H_2$) mixtures in CHA zeolite at 300 K, plotted as function of the surface potential Φ. (b) Plot of the CO_2/H_2 permeation selectivity S_{perm} as function of the surface potential Φ. All calculation details and input data are provided in the Supplementary Material accompanying this publication.

where $q_{sat,mix}$ is the saturation capacity for mixture adsorption. Eq (10) implies that Φ may also be interpreted as a proxy for the pore occupancy. Consequently, Φ is also the thermodynamically appropriate parameter to describe the loading dependence of diffusivities in microporous materials [23,24,34]. In all of the simulation data presented in this work, the values of the surface potential Φ range from about 10^{-3} to 40 mol kg^{-1}; values of $\Phi \approx 40$ mol kg^{-1} correspond to pore saturation conditions, $\theta \approx 1$; see the θ vs Φ calculations for CHA, DDR, MFI, and FAU presented in Fig. S4 of the Supplementary Material.

Fig. 5a plots the data for H_2/CO_2 diffusion selectivities defined by

$$S_{diff,ij} = \frac{D_{i,self}}{D_{j,self}} \tag{11}$$

that were determined from MD simulations for both binary (CO_2/H_2) and ternary ($CO_2/N_2/H_2$, and $CO_2/CH_4/H_2$) mixtures in CHA zeolite at 300 K, plotted as function of the surface potential Φ. The S_{diff} vs Φ relation is unique for the three MD data sets.

If the partial fugacities of the components at the downstream face are negligibly small in comparison with those at the upstream face, $\Delta f_i \approx f_i$, the component permeabilities may be estimated from

$$\Pi_i = \frac{\rho D_{i,self} q_i}{f_i} \tag{12}$$

In earlier work [35] we had used the Maxwell-Stefan diffusion formulation to establish the validity of the use of the component self-diffusivities in determining the $S_{diff,ij}$, and Π_i in eq (11), and (12); further details are provided in Chapter 6 of the Supplementary Material.

Combining eqs ((2), (8), (11) and (12) we conclude that the permeation selectivity is a product of the adsorption and diffusion selectivities

$$S_{perm,ij} = S_{ads,ij} \times S_{diff,ij} \tag{13}$$

Since we have already established that both $S_{ads,ij}$ and $S_{diff,ij}$ are uniquely determined by Φ for both binary and ternary mixtures, we should expect $S_{perm,ij}$ to exhibit the analogous unique dependence on the surface potential Φ. The CO_2/H_2 permeation selectivity calculations for CHA zeolite in Fig. 5b confirm this expectation. Precisely analogous results for $S_{diff,ij}$ vs Φ, and $S_{perm,ij}$ vs Φ dependences are obtained for CO_2/CH_4, CO_2/N_2, CH_4/N_2, and CO_2/H_2 pairs in the various hosts; see Figures S30-S36, S46-S49, S69-S76, and S82-S88.

Fig. 6 and Fig. 7 present data on the permeabilities, Π_i, for CO_2, CH_4, N_2 and H_2 in CHA, and DDR zeolites, respectively, determined using eq (12) by combining CBMC and MD simulation data on mixture adsorption and diffusion data. Noteworthily, the Π_i for any component in binary and ternary mixtures in both CHA and DDR has practically the same values as the unary permeabilities when compared at the same values of surface potential Φ; the unary permeability of H_2 is slightly higher than in mixtures. Analogous results for component permeabilities in MFI and FAU zeolites are presented in Figs. S78 and S90 of the of the Supplementary Material.

As validation of the CBMC/MD data in Figs. 6 and 8 presents a re-analysis of the experimental data of Li et al. [7–9] for permeances of (a) CO_2, (b) CH_4, (c) N_2 and (d) H_2, determined for unary, binary and ternary mixture permeation across SAPO-34 membrane at 295 K. Compared at the same Φ, the component permeances of each of the four guests is the same in binary and ternary mixtures. These data also suggest that the permeation selectivities in mixtures can be estimated to a reasonably fair accuracy on the basis of unary permeances, determined at the same surface potential Φ.

Confirmation of the data in Fig. 7 for DDR is available for binary CO_2/CH_4, and CH_4/N_2 mixtures only; see the re-analysis of the published experimental data of Van den Bergh et al. [12,18] and Himeno et al. [17] presented in Figs. S52–S55 of the Supplementary Material.

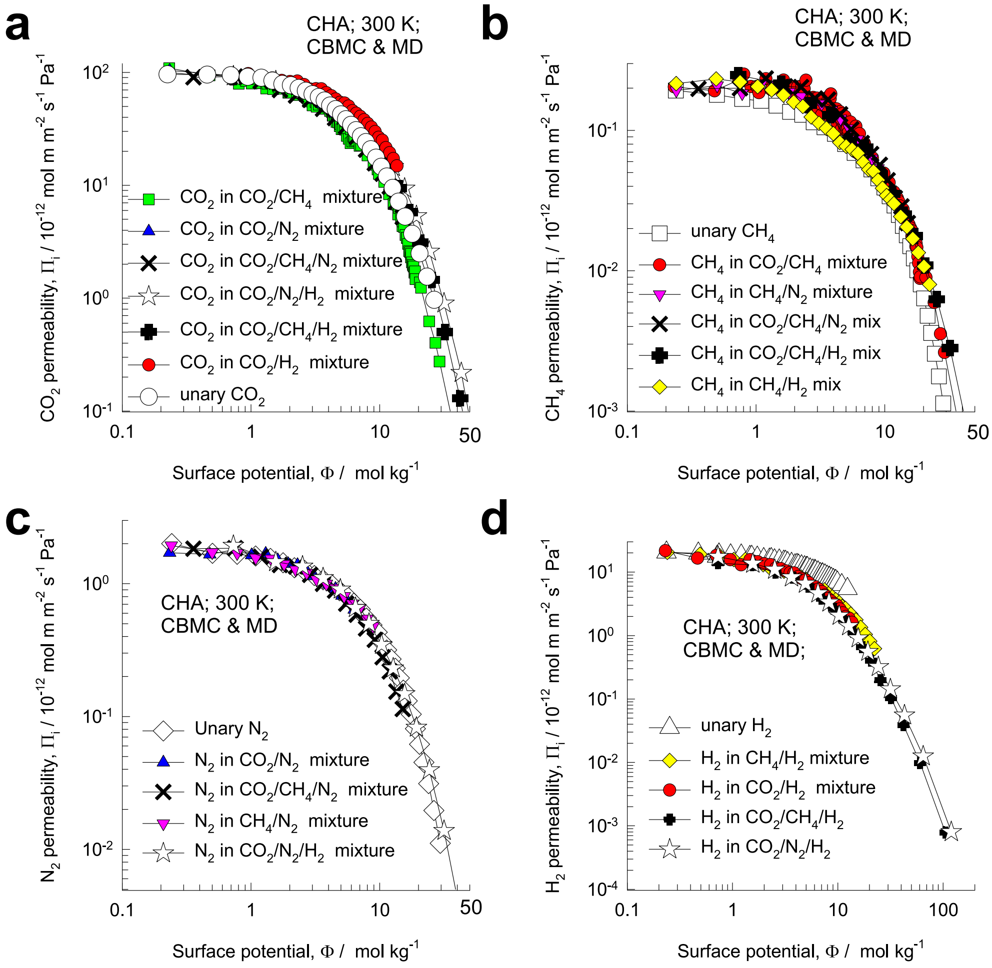

Fig. 6. CBMC/MD simulations of the permeabilities, Π_i, of (a) CO_2, (b) CH_4, (c) N_2 and (d) H_2 in different equimolar binary ($q_1 = q_2$) (CO_2/CH_4, CO_2/N_2, CO_2/H_2, CH_4/N_2, CH_4/H_2) and equimolar ($q_1 = q_2 = q_3$) ternary ($CO_2/CH_4/N_2$, $CO_2/CH_4/H_2$, $CO_2/N_2/H_2$) mixtures in CHA zeolite at 300 K, plotted as a function of the surface potential Φ. Also plotted are the corresponding values of the unary permeabilities.

4. Conclusions

The adsorption and diffusion characteristics of binary (CO_2/CH_4, CO_2/N_2, CH_4/N_2, CO_2/H_2), and ternary ($CO_2/CH_4/N_2$, $CO_2/CH_4/H_2$, $CO_2/N_2/H_2$) mixtures in four all-silica zeolites: CHA, DDR, MFI, and FAU were investigated using CBMC and MD simulations. The following major conclusions emerge.

(1) The adsorption selectivity $S_{ads,ij}$ of the *i-j* pair is uniquely determined by the surface potential, Φ, irrespective of mixture composition and total fugacity, f_t. The presence of additional species does not influence $S_{ads,ij}$, provided the comparison is made at the same Φ.
(2) For the mixtures investigated, ratios of the activity coefficients γ_i/γ_j also appear to uniquely depend on Φ. Consequently, departures from thermodynamic idealities do not cause significant deviations from the uniqueness of the $S_{ads,ij}$ vs Φ dependence.
(3) The surface potential Φ also represents the thermodynamically correct metric to describe the loading dependence of diffusivities. Compared at the same Φ, the diffusion selectivity, $S_{diff,ij}$, in ternary mixtures has practically the same value as for the corresponding binary *i-j* mixture.
(4) When compared at the same Φ, the component permeabilities, Π_i, for CO_2, CH_4, and N_2 in binary and ternary mixtures investigated are found to be largely independent of the partners and have practically the same as the values for the corresponding unary permeabilities.

CRediT authorship contribution statement

Rajamani Krishna: Conceptualization, Data curation, Investigation, Validation, Methodology, Writing. Jasper van Baten: Molecular simulations, including code development.

Declaration of competing interest

The authors declare that they have no known competing financial interests or personal relationships that could have appeared to influence the work reported in this paper.

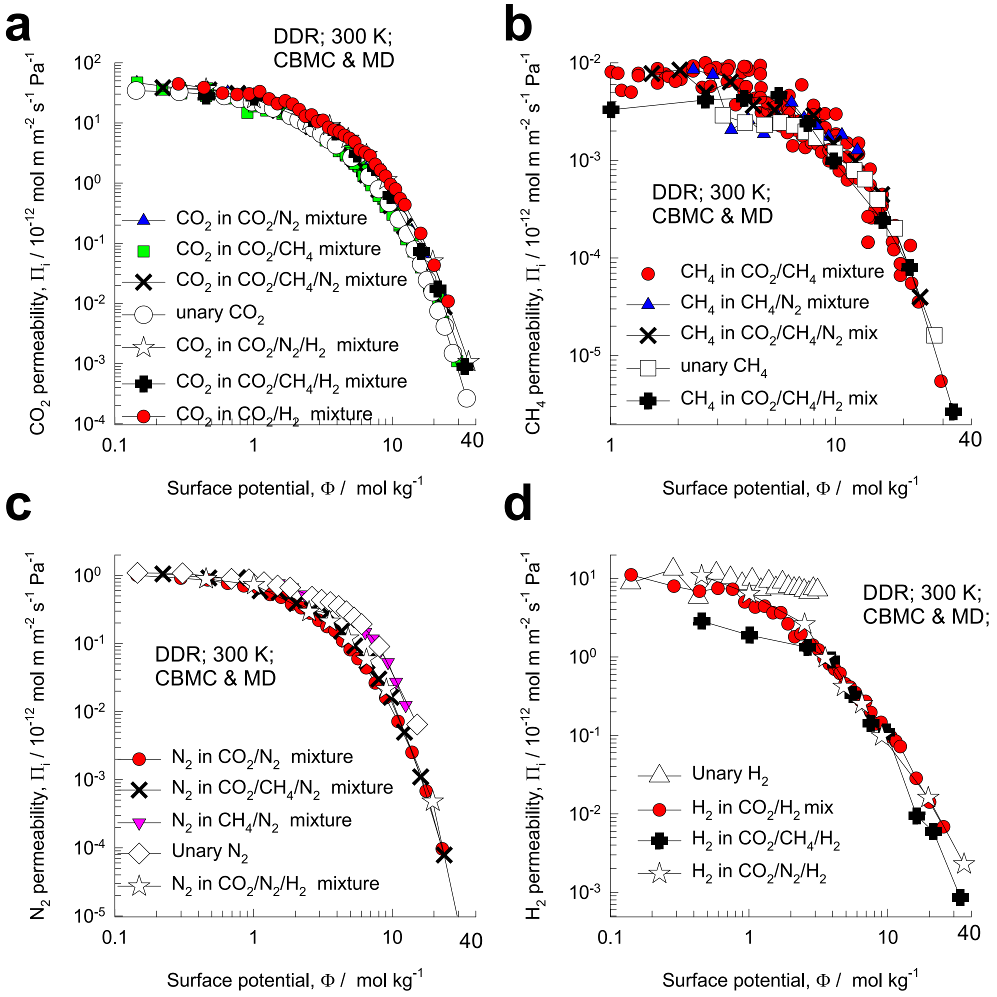

Fig. 7. CBMC/MD simulations of the permeabilities, Π_i, of (a) CO_2, (b) CH_4, (c) N_2 and (d) H_2 in different equimolar binary ($q_1 = q_2$) (CO_2/CH_4, CO_2/N_2, CO_2/H_2, CH_4/N_2) and equimolar ($q_1 = q_2 = q_3$) ternary ($CO_2/CH_4/N_2$, $CO_2/CH_4/H_2$, $CO_2/N_2/H_2$) mixtures in DDR zeolite at 300 K, plotted as a function of the surface potential Φ. Also plotted are the corresponding values of the unary permeabilities.

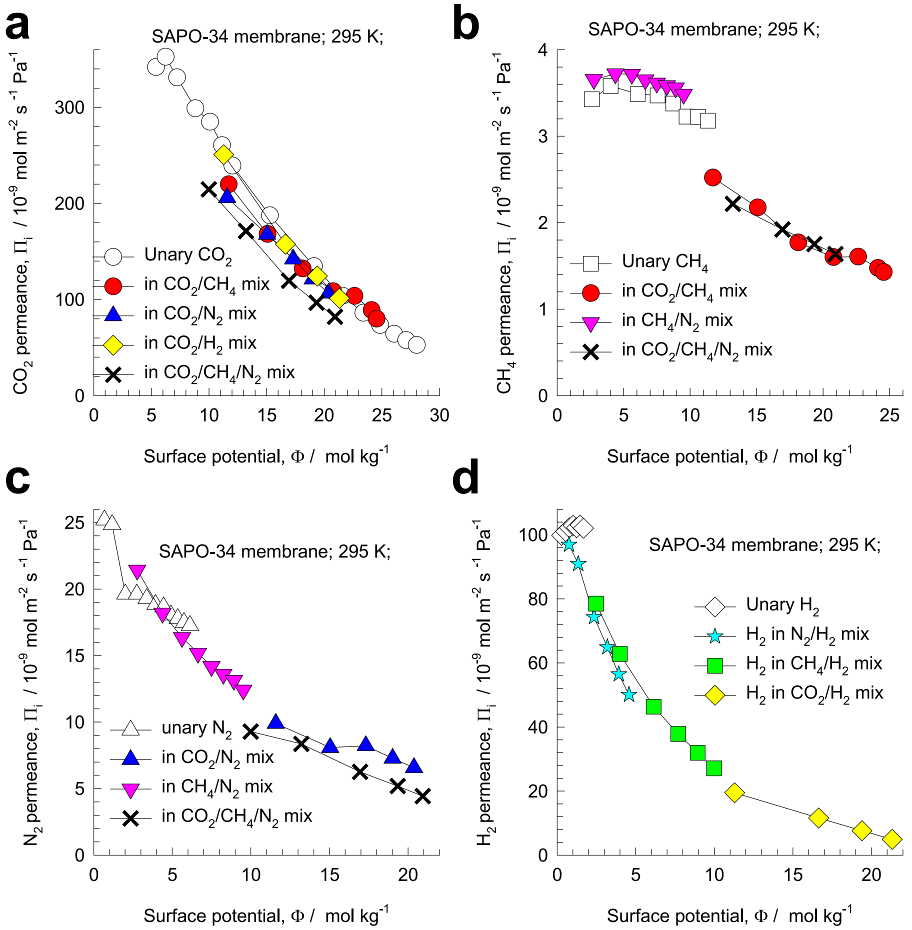

Fig. 8. Re-analysis of the experimental data of Li et al. [7–9] for permeances of (a) CO$_2$, (b) CH$_4$, (c) N$_2$ and (d) H$_2$, determined for equimolar binary and ternary mixture permeation across SAPO-34 membrane at 295 K, compared with unary permeance, when plotted as function of the surface potential Φ at the upstream face of the membrane. All calculation details and input data are provided in the Supplementary Material accompanying this publication.

Nomenclature

Latin alphabet

A	surface area per kg of framework, m^2 kg^{-1}
$D_{i,self}$	self-diffusivity of species *i*, m^2 s^{-1}
f_i	partial fugacity of species *i*, Pa
f_t	total fugacity of bulk gas mixture, Pa
N_i	permeation flux of species *i* with respect to membrane, mol m^{-2} s^{-1}
p_i	partial pressure of species *i*, Pa
p_t	total pressure, Pa
P_i^0	sorption pressure, Pa
q_i	component molar loading of species *i*, mol kg^{-1}
$q_{i,sat}$	molar loading of species *i* at saturation, mol kg^{-1}
q_t	total molar loading in mixture, mol kg^{-1}
R	gas constant, 8.314 J mol^{-1} K^{-1}
S_{ads}	adsorption selectivity, dimensionless
S_{diff}	diffusion selectivity, dimensionless
S_{perm}	permeation selectivity, dimensionless
T	absolute temperature, K
x_i	mole fraction of species *i* in adsorbed phase, dimensionless

Greek alphabet

δ	thickness of membrane, m
γ_i	activity coefficient of component *i* in adsorbed phase, dimensionless
μ_i	molar chemical potential of component *i*, J mol^{-1}
π	spreading pressure, N m^{-1}
θ	fractional occupancy, dimensionless
Π_i	membrane permeability of species *i*, mol m m^{-2} s^{-1} Pa^{-1}
ρ	crystal framework density, kg m^{-3}
Φ	surface potential, mol kg^{-1}

Subscripts

0	referring to upstream side of membrane
i	referring to component *i*
t	referring to total mixture
sat	referring to saturation conditions
δ	referring to downstream side of membrane

Appendix A. Supplementary data

Supplementary data to this article can be found online at https://doi.org/10.1016/j.memsci.2021.120049.

References

[1] R.W. Baker, Membrane Technology and Applications, third ed., John Wiley, New York, 2012.

[2] J.A. Wesselingh, R. Krishna, Mass Transfer in Multicomponent Mixtures, VSSD, Delft, 2000.

[3] J. Caro, Are MOF membranes better in gas separation than those made of zeolites? Curr. Opin. Chem. Eng. 1 (2011) 77–83.

[4] N. Rangnekar, N. Mittal, B. Elyassi, J. Caro, M. Tsapatsis, Zeolite membranes –A review and comparison with MOFs, Chem. Soc. Rev. 44 (2015) 7128–7154.

[5] M. Pera-Titus, Porous inorganic membranes for CO2 capture: present and prospects, Chem. Rev. 114 (2014) 1413–1492.

[6] R. Krishna, Using the maxwell-stefan formulation for highlighting the influence of interspecies (1-2) friction on binary mixture permeation across microporous and polymeric membranes, J. Membr. Sci. 540 (2017) 261–276, https://doi.org/10.1016/j.memsci.2017.06.062.

[7] R. Krishna, S. Li, J.M. van Baten, J.L. Falconer, R.D. Noble, Investigation of slowing-down and speeding-up effects in binary mixture permeation across SAPO-34 and MFI membranes, Separ. Purif. Technol. 60 (2008) 230–236.

[8] S. Li, J.L. Falconer, R.D. Noble, R. Krishna, Modeling permeation of CO_2/CH_4, CO_2/N_2, and N_2/CH_4 mixtures across SAPO-34 membrane with the Maxwell-Stefan equations, Ind. Eng. Chem. Res. 46 (2007) 3904–3911.

[9] S. Li, J.L. Falconer, R.D. Noble, R. Krishna, Interpreting unary, binary and ternary mixture permeation across a SAPO-34 membrane with loading-dependent Maxwell-Stefan diffusivities, J. Phys. Chem. C 111 (2007) 5075–5082.

[10] X. Feng, Z. Zong, S. Elsaidi, J.B. Jasinski, R. Krishna, P.K. Thallapally, M. A. Carreon, Kr/Xe separation over a chabazite zeolite membrane, J. Am. Chem. Soc. 138 (2016) 9791–9794.

[11] L. Sandström, E. Sjöberg, J. Hedlund, Very high flux MFI membrane for CO_2 separation, J. Membr. Sci. 380 (2011) 232–240.

[12] J. van den Bergh, W. Zhu, J. Gascon, J.A. Moulijn, F. Kapteijn, Separation and permeation characteristics of a DD3R zeolite membrane, J. Membr. Sci. 316 (2008) 35–45.

[13] J.M. van de Graaf, F. Kapteijn, J.A. Moulijn, Modeling permeation of binary mixtures through zeolite membranes, A.I.Ch.E.J. 45 (1999) 497–511.

[14] P.F. Zito, A. Brunetti, A. Caravella, E. Drioli, G. Barbieri, Mutual influence in permeation of CO_2-containing mixtures through a SAPO-34 membrane, J. Membr. Sci. 595 (2020) 117534, https://doi.org/10.1016/j.memsci.2019.117534.

[15] L. Yu, M.S. Nobandegani, J. Hedlund, Industrially relevant CHA membranes for CO_2/CH_4 separation, J. Membr. Sci. XX (2021) XXX, https://doi.org/10.1016/j.memsci.2021.119888.

[16] Y. Hasegawa, K. Nishida, S. Oguro, Y. Fujimura, K. Yajima, M. Niino, M. Isomura, T. Tomita, Gas separation process for CO_2 removal from natural gas with DDR-type zeolite membrane, Energy Procedia 114 (2017) 32–36.

[17] S. Himeno, T. Tomita, K. Suzuki, K. Nakayama, S. Yoshida, Synthesis and permeation properties of a DDR-type zeolite membrane for separation of CO_2/CH_4 gaseous mixtures, Ind. Eng. Chem. Res. 46 (2007) 6989–6997.

[18] J. van den Bergh, W. Zhu, J.C. Groen, F. Kapteijn, J.A. Moulijn, K. Yajima, K. Nakayama, T. Tomita, S. Yoshida, Natural gas purification with a DDR zeolite membrane; permeation modelling with maxwell-stefan equations, Stud. Surf. Sci. Catal. 170 (2007) 1021–1027.

[19] Q. Qian, P.A. Asinger, M.J. Lee, G. Han, K.M. Rodriguez, S. Lin, F.M. Benedetti, A. X. Wu, W.S. Chi, Z.P. Smith, MOF-based membranes for gas separations, Chem. Rev. 120 (2020) 8161–8266, https://doi.org/10.1021/acs.chemrev.0c00119.

[20] H. Bux, C. Chmelik, R. Krishna, J. Caro, Ethene/ethane separation by the MOF membrane ZIF-8: molecular correlation of permeation, adsorption, diffusion, J. Membr. Sci. 369 (2011) 284–289.

[21] H. Bux, C. Chmelik, J.M. Van Baten, R. Krishna, J. Caro, Novel MOF-membrane for molecular sieving predicted by IR-diffusion studies and molecular modeling, Adv. Mater. 22 (2010) 4741–4743, https://doi.org/10.1002/adma.201002066.

[22] C. Chmelik, J.M. van Baten, R. Krishna, Hindering effects in diffusion of CO_2/CH_4 mixtures in ZIF-8 crystals, J. Membr. Sci. 397–398 (2012) 87–91, https://doi.org/10.1016/j.memsci.2012.01.013.

[23] R. Krishna, Thermodynamic insights into the characteristics of unary and mixture permeances in microporous membranes, ACS Omega 4 (2019) 9512–9521, https://doi.org/10.1021/acsomega.9b00907.

[24] R. Krishna, J.M. Van Baten, Using molecular simulations to unravel the benefits of characterizing mixture permeation in microporous membranes in terms of the spreading pressure, ACS Omega 5 (2020) 32769–32780, https://doi.org/10.1021/acsomega.0c05269.

[25] D.M. Ruthven, Principles of Adsorption and Adsorption Processes, John Wiley, New York, 1984.

[26] A.L. Myers, J.M. Prausnitz, Thermodynamics of mixed gas adsorption, A.I.Ch.E.J. 11 (1965) 121–130.

[27] O. Talu, A.L. Myers, Rigorous thermodynamic treatment of gas-adsorption, A.I.Ch.E.J. 34 (1988) 1887–1893.

[28] F.R. Siperstein, A.L. Myers, Mixed-gas adsorption, A.I.Ch.E.J. 47 (2001) 1141–1159.

[29] R. Krishna, J.M. van Baten, Segregation effects in adsorption of CO_2 containing mixtures and their consequences for separation selectivities in cage-type zeolites, Separ. Purif. Technol. 61 (2008) 414–423, https://doi.org/10.1016/j.seppur.2007.12.003.

[30] R. Krishna, J.M. Van Baten, Investigating the non-idealities in adsorption of CO_2-bearing mixtures in cation-exchanged zeolites, Separ. Purif. Technol. 206 (2018) 208–217, https://doi.org/10.1016/j.seppur.2018.06.009.

[31] R. Krishna, J.M. Van Baten, How reliable is the ideal adsorbed solution theory for estimation of mixture separation selectivities in microporous crystalline adsorbents? ACS Omega 6 (2021) 15499–15513, https://doi.org/10.1021/acsomega.1c02136.

[32] R. Krishna, J.M. van Baten, R. Baur, Highlighting the origins and consequences of thermodynamic nonidealities in mixture separations using zeolites and metal-organic frameworks, Microporous Mesoporous Mater. 267 (2018) 274–292, https://doi.org/10.1016/j.micromeso.2018.03.013.

[33] R. Krishna, J.M. Van Baten, Using molecular simulations for elucidation of thermodynamic non-idealities in adsorption of CO_2-containing mixtures in NaX zeolite, ACS Omega 5 (2020) 20535–20542, https://doi.org/10.1021/acsomega.0c02730.

[34] R. Krishna, Occupancy dependency of Maxwell−Stefan diffusivities in ordered crystalline microporous materials, ACS Omega 3 (2018) 15743–15753, https://doi.org/10.1021/acsomega.8b02465.

[35] R. Krishna, J.M. van Baten, In silico screening of zeolite membranes for CO_2 capture, J. Membr. Sci. 360 (2010) 323–333.

Supplementary Material

Using the Spreading Pressure to Inter-Relate the Characteristics of Unary, Binary and Ternary Mixture Permeation across Microporous Membranes

Rajamani Krishna* and Jasper M. van Baten

Van ‘t Hoff Institute for Molecular Sciences
University of Amsterdam
Science Park 904
1098 XH Amsterdam, The Netherlands
email: r.krishna@contact.uva.nl

Table of Contents

1 Preamble

The Supplementary Material accompanying our article *Using the Spreading Pressure to Inter-Relate the Characteristics of Unary, Binary and Ternary Mixture Permeation across Microporous Membranes* provides: (a) CBMC and MD simulation methodologies, (b) Details of IAST calculations, (c) Maxwell-Stefan formulation for mixture diffusion, (d) CBMC data on unary isotherms and isotherm fits, (e) CBMC and MD data on adsorption, diffusion, and permeation of variety of binary and ternary mixtures.

2 Configurational-Bias Monte Carlo Simulation Methodology

The simulation methodologies and the force field information used are the same as detailed in the Supplementary Materials accompanying our earlier publications.[1-7] A short summary is provided hereunder.

2.1 Zeolites (all silica)

CH_4 molecules are described with a united atom model, in which each molecule is treated as a single interaction center.[8] The interaction between adsorbed molecules is described with Lennard-Jones terms; see Figure S1. The Lennard-Jones parameters for CH_4-zeolite interactions are taken from Dubbeldam et al.[9]. The force field for H_2 corresponds to that given by Kumar et al.[10] In implementing this force field, quantum effects for H_2 have been ignored because the work of Kumar et al.[10] has shown that quantum effects are of negligible importance for temperatures above 200 K; all our simulations were performed at 300 K. The Lennard-Jones parameters for CO_2-zeolite and N_2-zeolite are essentially those of Makrodimitris et al.[11]; see also García-Pérez et al.[12]. For simulations with linear alkanes with two or more C atoms, the beads in the chain are connected by harmonic bonding potentials. A harmonic cosine bending potential models the bond bending between three neighboring beads, a Ryckaert-Bellemans potential controls the torsion angle. The beads in a chain separated by more than three bonds interact with each other through a Lennard-Jones potential; see schematic in Figure S1. The force fields of Dubbeldam et al.[9] was used for the variety of potentials. The Lennard-Jones potentials are shifted and cut at 12 Å.

The zeolite frameworks were considered to be rigid in all the simulation results reported in the article.

2.2 MOFs

The metal organic framework structures were considered to be rigid in the simulations. For the atoms in the host metal organic framework, the generic UFF[13] and DREIDING[14] force fields were used. The Lorentz-Berthelot mixing rules were applied for calculating σ and ε/k_B for guest-host interactions.

The structural information on MgMOF-74 (= Mg_2(dobdc) = Mg\(dobdc) with dobdc = (dobdc^{4-} = 1,4-dioxido-2,5-benzenedicarboxylate)) was obtained from a variety of references.[15-20] The simulations for MgMOF-74 were carried out with the force field information provided by Yazaydin et al.[20]

The structural information for Co(BDP) with (BDP^{2-} = 1,4-benzenedipyrazolate) is from Choi et al. [21] and Salles et al. [22].

2.3 Force fields and CBMC simulation methodology for water/alcohol mixtures

For simulations of adsorption of guest molecules water, methanol, and ethanol, the force field implementation follows earlier publications.[23-28] Water is modeled using the Tip5pEw potential.[29] The alcohols are described with the TraPPE force field.[30] Intramolecular potentials are included to describe the flexibility of alcohols, while the water molecules are kept rigid. The bond lengths are fixed for all molecules. Bond bending potentials are considered for methanol and ethanol, and a torsion potential is used for ethanol.[30] The force field parameters are summarized in Table S1.

All simulations are performed in the grand canonical ensemble; the chemical potentials of each component in the bulk fluid phase equal that of the corresponding guest adsorbate within the microporous framework. In our simulations, the partial fugacities in the bulk fluid mixture as specified; this fixes the values of the chemical potentials.

Following Kiselev and co-workers,[31] the zeolite is modeled as a rigid crystal. The interactions of the guest (pseudo) atoms with the host zeolite atoms aredominated by the dispersive interactions with the oxygen atoms, these interactions are described with a Lennard-Jones potential; see Table S2.

The Lorentz-Berthelot mixing rules were applied for calculating the Lennard-Jones parameters describing guest-host interactions

$$\begin{aligned}\sigma_{guest-host} &= \frac{\left(\sigma_{guest}+\sigma_{host}\right)}{2} \\ \frac{\varepsilon_{guest-host}}{k_B} &= \sqrt{\frac{\varepsilon_{guest}}{k_B}\times\frac{\varepsilon_{host}}{k_B}}\end{aligned} \tag{S1}$$

The Lennard-Jones potentials are shifted and cut at 12 Å. Periodic boundary conditions were employed. The Configurational-Bias Monte Carlo (CBMC) simulation technique used is identical to that used by Kuhn et al.,[26] and is described in detail by Frenkel and Smit.[32]

2.4 Cation-exchanged zeolites

The followingcation-exchanged structures were investigated

NaX (106 Si, 86 Al, 86 Na^+, Si/Al=1.23)

The presence of cations reduces the accessible pore volume. The location of the cations are pictured in Figure S3.

The force field information for the simulations with cations are taken from García-Sanchez et al.[33] In the MC simulations, the cations were allowed to move within the framework and both Lennard-Jones and Coulombic interactions are taken into consideration.

In the CBMC simulations both Lennard-Jones and Coulombic interactions are taken into consideration; see schematic sketch in Figure S2.

2.5 CBMC code

All simulations reported in this work were carried out using an in-house BIGMAC code, originally developed by T.J.H. Vlugt. This code was modified to handle rigid molecular structures and charges. The calculation of the accessible pore volume using the Widom insertion of He probe atoms is implemented within the BIGMAC code.

All CBMC simulations reported in this work were conducted at a temperature $T = 300$ K.

2.6 CBMC simulation campaigns

CBMC simulation campaigns for adsorption of different binary mixtures (CO_2/CH_4, CO_2/N_2, CO_2/H_2, CH_4/N_2, CH_4/C_2H_6, CH_4/C_3H_8) were undertaken in all-silica zeolites (CHA, DDR, FAU, MFI) at a temperature $T = 300$ K. In the campaigns, the bulk fluid phase composition held constant at $\frac{f_1}{f_1 + f_2} \equiv y_1$, and the bulk fluid phase fugacity $f_t = f_1 + f_2$ was varied over a wide range from the Henry regime of adsorption, $f_t \to 0; \quad \Phi \to 0$, to pore saturation conditions, typically $\Phi \equiv \frac{\pi A}{RT} > 10$.

Additionally, CBMC simulation campaigns for adsorption of ternary mixtures ($CO_2/CH_4/N_2$, $CO_2/CH_4/H_2$, $CO_2/N_2/H_2$, $CH_4/C_2H_6/C_3H_8$, water/methanol/ethanol) were undertaken in all-silica zeolites (CHA, DDR, FAU, MFI) at a temperature $T = 300$ K. In the campaigns, the bulk fluid phase composition held constant at $\frac{f_1}{f_1 + f_2 + f_3} \equiv y_1; \frac{f_2}{f_1 + f_2 + f_3} \equiv y_2$, and the bulk fluid phase fugacity $f_t = f_1 + f_2 + f_3$ was varied over a wide range from the Henry regime of adsorption, $f_t \to 0; \quad \Phi \to 0$, to pore saturation conditions, typically $\Phi \equiv \frac{\pi A}{RT} > 10$.

2.7 List of Tables for Configurational-Bias Monte Carlo Simulation Methodology

Table S1. Lennard-Jones parameters for guest pseudo-atoms. as provided in Table 1 of Kuhn et al.[26] The water model has two off-center charges that are labeled M in the Table. The name “alcohol” refers to both methanol and ethanol molecules.

Molecule	(pseudo-) atom	σ / Å	ε/k_B / K	charge
water	O	3.097	89.516	0
water	H	0	0	0.241
water	M	0	0	-0.241
methanol	CH3	3.75	98	0.265
ethanol	CH3	3.75	98	0
ethanol	CH2	3.95	46	0.265
alcohol	O	3.02	93	-0.7
alcohol	H	0	0	0.435

Table S2. Lennard-Jones parameters for host atoms in all-silica zeolites.

(pseudo-) atom	σ / Å	ε/k_B / K	charge
Si			2.05
O	3	93.53	-1.025

2.8 List of Figures for Configurational-Bias Monte Carlo Simulation Methodology

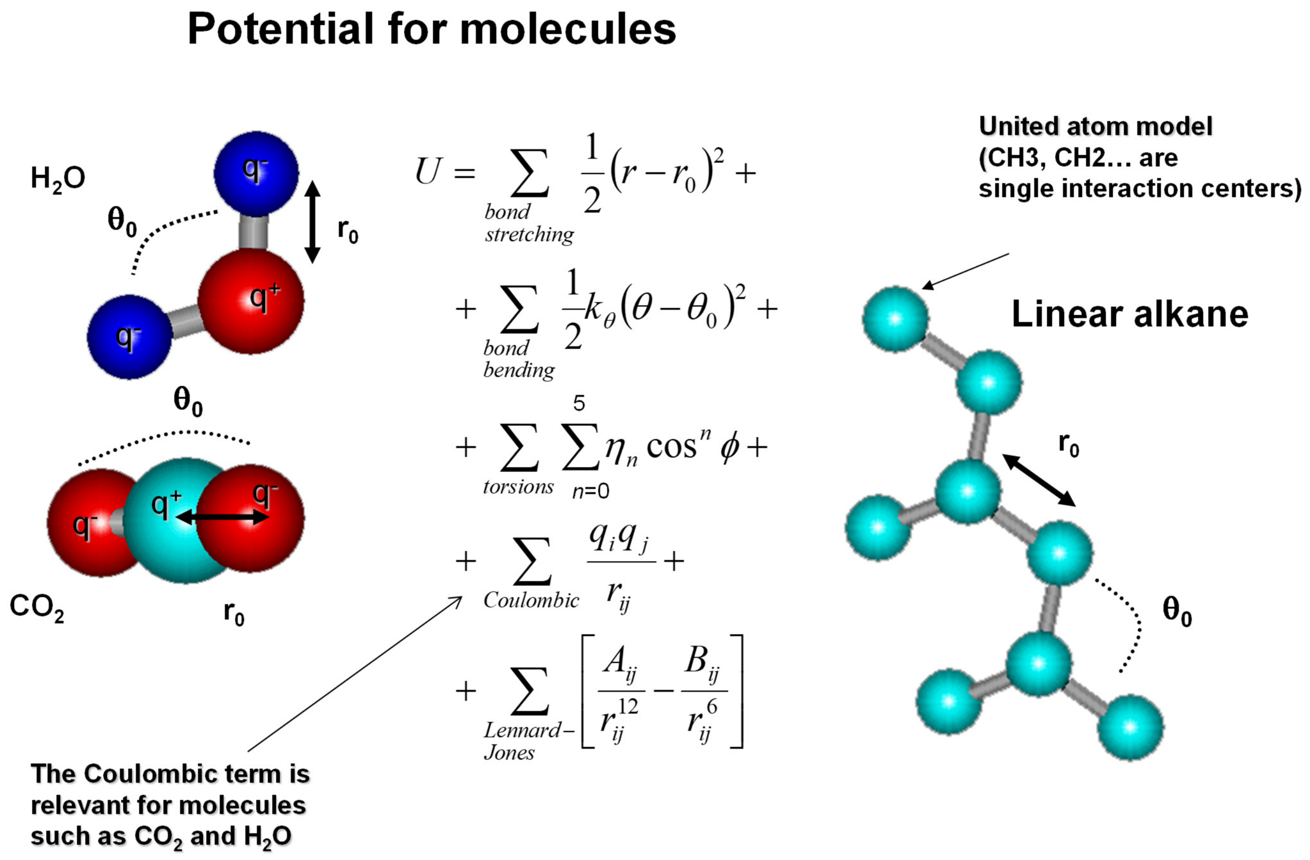

Potential for molecules

$$U = \sum_{\substack{bond\\stretching}} \frac{1}{2}(r-r_0)^2 + \sum_{\substack{bond\\bending}} \frac{1}{2}k_\theta(\theta-\theta_0)^2 + \sum_{torsions}\sum_{n=0}^{5}\eta_n\cos^n\phi + \sum_{Coulombic}\frac{q_iq_j}{r_{ij}} + \sum_{\substack{Lennard-\\Jones}}\left[\frac{A_{ij}}{r_{ij}^{12}} - \frac{B_{ij}}{r_{ij}^{6}}\right]$$

United atom model
(CH3, CH2… are
single interaction centers)

The Coulombic term is
relevant for molecules
such as CO_2 and H_2O

Figure S1. Potential for molecules.

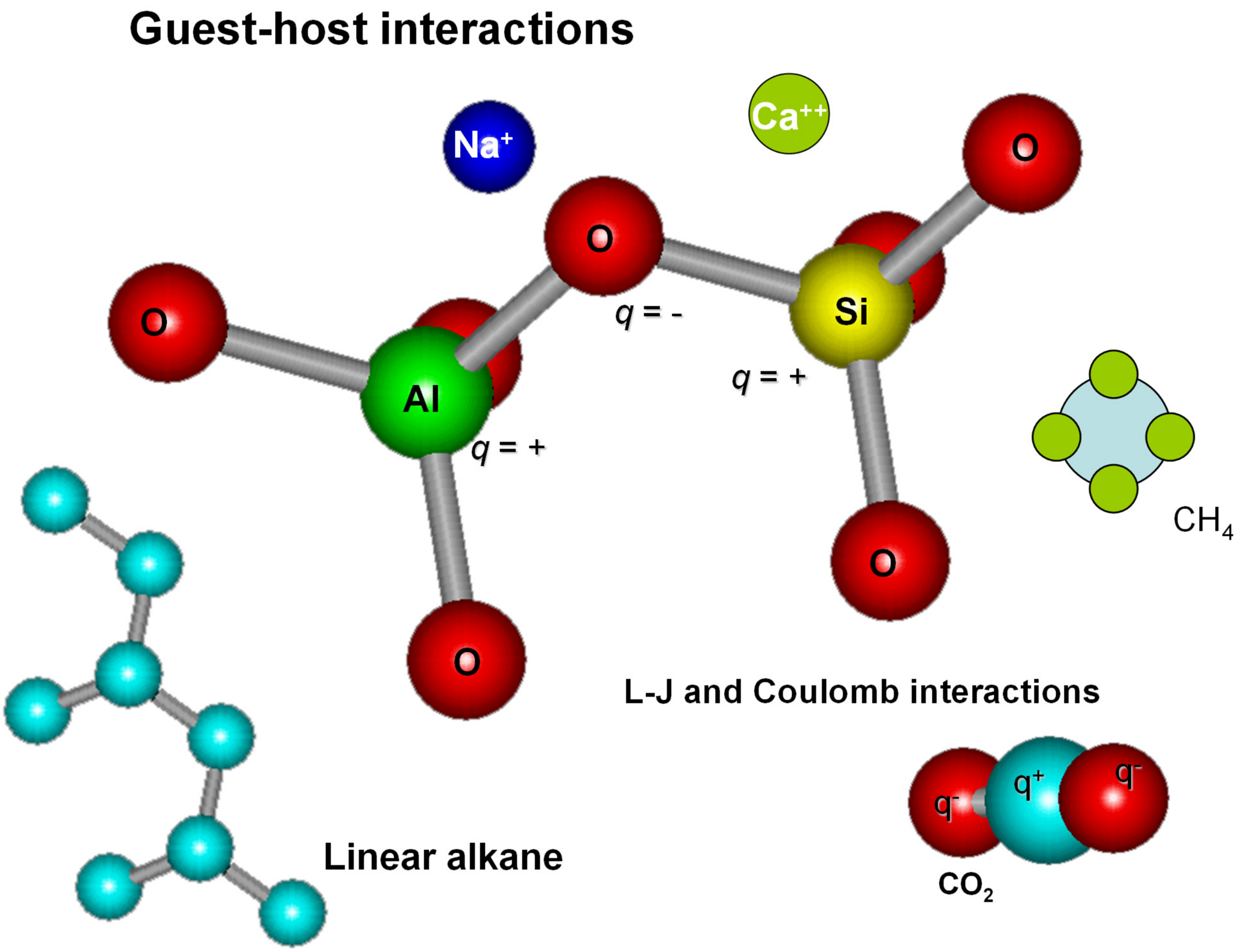

Figure S2. Guest-host interactions.

NaX (106 Si, 86 Al, 86 Na+, Si/Al=1.23)

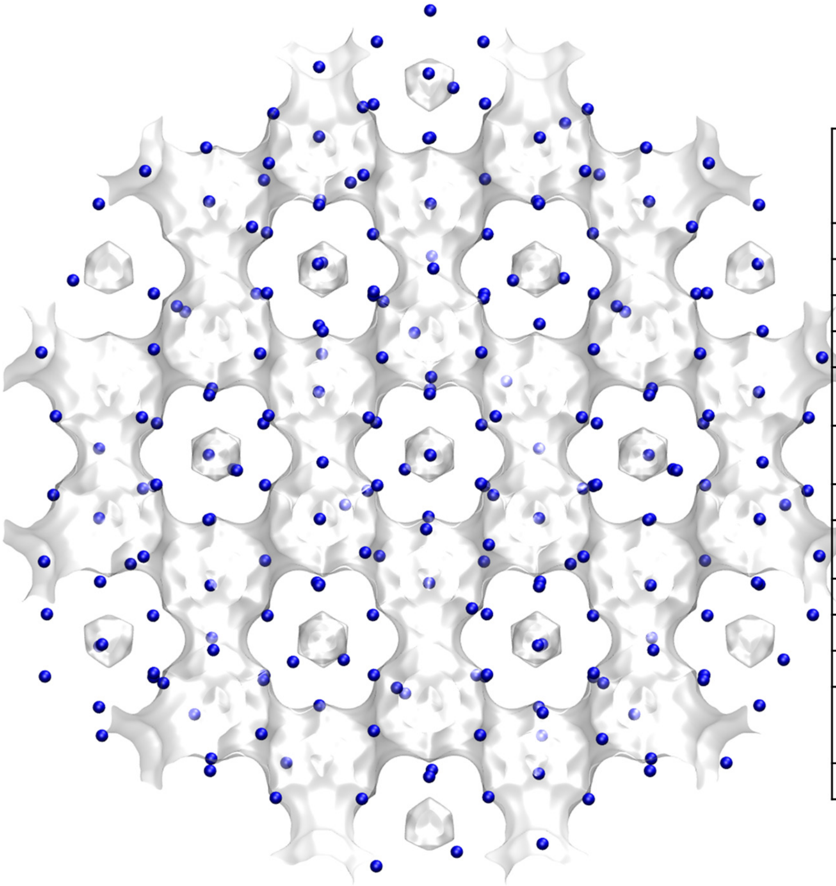

	FAU 86 Na/uc
a /Å	25.028
b /Å	25.028
c /Å	25.028
Cell volume / Å^3	15677.56
conversion factor for [molec/uc] to [mol per kg Framework]	0.0745
conversion factor for [molec/uc] to [kmol/m^3]	0.2658
ρ [kg/m3] (with cations)	1421.277
MW unit cell [g/mol(framework+cations)]	13418.42
ϕ, fractional pore volume	0.399
open space / Å^3/uc	6248.0
Pore volume / cm^3/g	0.280
Surface area /m^2/g	
DeLaunay diameter /Å	7.37

Figure S3. Location of cations for NaX zeolite (106 Si, 86 Al, 86 Na$^+$, Si/Al=1.23)

3 Thermodynamics of Mixture Adsorption in Micro-porous Materials

Within microporous crystalline materials, the guest molecules exist in the adsorbed phase, and the thermodynamics of mixture adsorption has an important bearing on the diffusion characteristics of guest molecules. For that reason, we provide below a brief summary of the Ideal Adsorbed Solution Theory (IAST) theory of Myers and Prausnitz.[34]

3.1 Brief outline of theory

The Gibbs adsorption equation[35] in differential form is

$$A d\pi = \sum_{i=1}^{n} q_i d\mu_i \tag{S2}$$

The quantity A is the surface area per kg of framework, with units of m^2 per kg of the framework of the crystalline material; q_i is the molar loading of component i in the adsorbed phase with units moles per kg of framework; μ_i is the molar chemical potential of component i. The spreading pressure π has the same units as surface tension, i.e. N m^{-1}.

The chemical potential of any component in the adsorbed phase, μ_i, equals that in the bulk fluid phase. If the partial fugacities in the bulk fluid phase are f_i, we have

$$d\mu_i = RTd\ln f_i \tag{S3}$$

where R is the gas constant (= 8.314 J mol^{-1} K^{-1}).

Briefly, the basic equation of Ideal Adsorbed Solution Theory (IAST) theory of Myers and Prausnitz[34] is the analogue of Raoult's law for vapor-liquid equilibrium, i.e.

$$f_i = P_i^0 x_i; \quad i = 1,2,...n \tag{S4}$$

where x_i is the mole fraction in the adsorbed phase

$$x_i = \frac{q_i}{q_1 + q_2 + ...q_n} \tag{S5}$$

and P_i^0 is the pressure for sorption of every component *i*, which yields the same spreading pressure, π for each of the pure components, as that for the mixture:

$$\frac{\pi A}{RT} = \int_0^{P_1^0} \frac{q_1^0(f)}{f} df = \int_0^{P_2^0} \frac{q_2^0(f)}{f} df = \int_0^{P_3^0} \frac{q_3^0(f)}{f} df = ... \tag{S6}$$

where $q_i^0(f)$ is the *pure* component adsorption isotherm. The units of $\Phi \equiv \frac{\pi A}{RT}$, also called the surface potential, [27, 36-39] are mol kg^{-1}.

The unary isotherm may be described by say the 1-site Langmuir isotherm

$$q^0(f) = q_{sat} \frac{bf}{1+bf}; \quad \theta = \frac{bf}{1+bf} \tag{S7}$$

where we define the fractional *occupancy* of the adsorbate molecules, $\theta = q^0(f)/q_{sat}$. The superscript 0 is used to emphasize that $q^0(f)$ relates the *pure component* loading to the bulk fluid fugacity. For all of the guest/host combinations considered in this article, the unary isotherms need to be described by the dual-Langmuir-Freundlich model

$$q^0(f) = q_{A,sat} \frac{b_A f^{\nu A}}{1+b_A f^{\nu A}} + q_{B,sat} \frac{b_B f^{\nu B}}{1+b_B f^{\nu B}} \tag{S8}$$

Each of the integrals in eq (S6) can be evaluated analytically. For the dual-site Langmuir-Freundlich isotherm, for example, the integration yields for component *i*,

$$\begin{aligned} \Phi \equiv \frac{\pi A}{RT} &= \int_{f=0}^{P_i^0} \frac{q_i^0(f)}{f} df = \frac{q_{A,sat}}{\nu_A} \ln\left(1 + b_A \left(P_i^0\right)^{\nu_A}\right) + \frac{q_{B,sat}}{\nu_B} \ln\left(1 + b_B \left(P_i^0\right)^{\nu_B}\right); \\ \Phi \equiv \frac{\pi A}{RT} &= \int_{f=0}^{P_i^0} \frac{q_i^0(f)}{f} df = \frac{q_{A,sat}}{\nu_A} \ln\left(1 + b_A \left(\frac{f_i}{x_i}\right)^{\nu_A}\right) + \frac{q_{B,sat}}{\nu_B} \ln\left(1 + b_B \left(\frac{f_i}{x_i}\right)^{\nu_B}\right) \end{aligned} \tag{S9}$$

The right hand side of eq (S9) is a function of P_i^0. For multicomponent mixture adsorption, each of the equalities on the right hand side of Eq (S6) must be satisfied. These constraints may be solved using a suitable equation solver, to yield the set of values of P_1^0, P_2^0, P_3^0,.. P_n^0, each of which satisfy eq (S6). The corresponding values of the integrals using these as upper limits of integration must yield the same value of Φ for each component; this ensures that the obtained solution is the correct one.

The adsorbed phase mole fractions x_i are then determined from

$$x_i = \frac{f_i}{P_i^0}; \quad i = 1, 2, ...n \tag{S10}$$

The applicability of eqs (S4) and (S10) mandates that all of the adsorption sites within the microporous material are equally accessible to each of the guest molecules, implying a homogeneous distribution of guest adsorbates within the pore landscape, with no preferential locations of any guest species. The circumstances in which this mandate is not fulfilled are highlighted in recent works.[38-40]

A key assumption of the IAST is that the adsorption enthalpies and surface areas of the adsorbed molecules do not change upon mixing. If the total mixture loading is q_t, the area covered by the adsorbed mixture is $\frac{A}{q_t}$ with units of m^2 (mol mixture)$^{-1}$. Therefore, the assumption of no surface area change due to mixture adsorption translates as $\frac{A}{q_t} = \frac{Ax_1}{q_1^0\left(P_1^0\right)} + \frac{Ax_2}{q_2^0\left(P_2^0\right)} + \cdots \frac{Ax_n}{q_n^0\left(P_n^0\right)}$; the total mixture loading is q_t is calculated from

$$q_t = q_1 + q_2 ... + q_n = \frac{1}{\frac{x_1}{q_1^0(P_1^0)} + \frac{x_2}{q_2^0(P_2^0)} + ... + \frac{x_n}{q_n^0(P_n^0)}} \tag{S11}$$

in which $q_1^0(P_1^0)$, $q_2^0(P_2^0)$,... $q_n^0(P_n^0)$ are determined from the unary isotherm fits, using the sorption pressures for each component P_1^0, P_2^0, P_3^0,.. P_n^0 that are available from the solutions to equations Eqs (S6), and (S9).

The occurrence of molecular clustering and hydrogen bonding should be expected to applicability of eq (S11) because the surface area occupied by a molecular cluster is different from that of each of the un-clustered guest molecules in the adsorbed phase.

The entire set of eqs (S4) to (S11) need to be solved numerically to obtain the loadings, q_i of the individual components in the mixture.

For the interpretation and analysis of the MD simulations for binary mixture diffusion in microporous host materials, the IAST calculation procedure has to be performed differently because in the MD simulations, the molar loadings q_1, and q_2 in the mixture are specified, and the partial fugacities in the bulk fluid mixture are not known *a priori*. Also in this case, the equalities in eq (S9) must be satisfied in conjunction with eq (S11). The entire set of eqs (S4) to (S11) need to be solved numerically to obtain the partial fugacities, f_i of the individual components in the mixture, that yield the same loadings as chosen in the MD simulations. In all of the calculations presented in this article, the set of equations were solved using an Excel macro that was developed for this specific purpose.

3.2 Selectivity for mixture adsorption

For *n*-component mixture adsorption, the selectivity of guest constituent *i* with respect to another guest constituent *j*, in that mixture, $S_{ads,ij}$, is defined by

$$S_{ads,ij} = \frac{q_i/q_j}{f_i/f_j} = \frac{x_i/f_i}{x_j/f_j} \tag{S12}$$

where q_i, q_j are the molar loadings of the constituents *i* and *j*, in the adsorbed phase in equilibrium with a bulk fluid phase mixture with partial fugacities f_i, f_j, and mole fractions $y_i = f_i/f_t$; $f_t = \left(\sum_{k=1}^{n} f_k\right)$. In view of eqs (S10), and (S11), we may re-write eq (S12) as the ratio of the sorption pressures

$$S_{ads,ij} = \frac{P_j^0}{P_i^0} \tag{S13}$$

Applying the restriction specified by eq (S6), it follows that $S_{ads,ij}$ is uniquely determined by the surface potential Φ. It is important to note that eq (S13) is valid irrespective of the total number of components in the mixture. Put another way, the presence of component 3 in the ternary mixture has no influence of the adsorption selectivity $S_{ads,12}=\frac{P_2^0}{P_1^0}$ for the 1-2 pair, except insofar as the presence of component 3 alters the value of the surface potential Φ for the 1-2-3 mixture. Therefore, for an ideal adsorbed phase mixture, the presence of additional guest constituents, say species 3, 4, 5, etc. do not influence the selectivity of the 1-2 pair.

3.3 IAST model: 1-site Langmuir isotherms

The IAST procedure will be applied for binary mixture adsorption in which the unary isotherms are described by the 1-site Langmuir model in which the saturation capacities of components 1 and 2 are identical to each other, i.e. $q_{1,sat}=q_{2,sat}=q_{sat}$:

$$q_i^0\left(f\right)=q_{sat}\frac{b_i f}{1+b_i f} \tag{S14}$$

where

For unary adsorption, the surface potential for a 1-site Langmuir isotherm can be calculated analytically

$$\Phi\equiv\frac{\pi A}{RT}=q_{sat}\ln\left(1+bP^0\right) \tag{S15}$$

The objective is to determine the molar loadings, q_1, and q_2, in the adsorbed phase.

Performing the integration of eq (S6) results in an expression relating the sorption pressures P_i^0 of the two species

$$\begin{aligned}&\Phi\equiv\frac{\pi A}{RT}=q_{sat}\ln\left(1+b_1P_1^0\right)=q_{sat}\ln\left(1+b_2P_2^0\right)\\&b_1P_1^0=b_2P_2^0=\exp\left(\frac{\pi A}{q_{sat}RT}\right)-1\end{aligned} \tag{S16}$$

The adsorbed phase mole fractions of component 1, and component 2 are given by eq (S10)

$$x_1=\frac{f_1}{P_1^0};\quad x_2=1-x_1=\frac{f_2}{P_2^0} \tag{S17}$$

Combining eqs (S16), and (S17):

$$\exp\left(\frac{\pi A}{q_{sat}RT}\right)-1=b_1\frac{f_1}{x_1}=b_2\frac{f_2}{1-x_1} \tag{S18}$$

The adsorbed phase mole fractions can be determined

$$\frac{x_1}{x_2}=\frac{q_1}{q_2}=\frac{b_1f_1}{b_2f_2};\quad x_1=\frac{q_1}{q_t}=\frac{b_1f_1}{b_1f_1+b_2f_2};\quad x_2=\frac{q_2}{q_t}=\frac{b_2f_2}{b_1f_1+b_2f_2} \tag{S19}$$

Once x_1, and $x_2=1-x_1$ are determined, the sorption pressures can be calculated:

$$P_1^0=\frac{f_1}{x_1};\quad P_2^0=\frac{f_2}{x_2}=\frac{f_2}{1-x_1} \tag{S20}$$

From eqs (S16), and (S20) we get

$$\begin{aligned}&b_iP_1^0=\frac{b_1f_1}{x_1}=b_2P_2^0=\frac{b_2f_2}{x_2}=b_1f_1+b_2f_2\\&1+b_iP_1^0=1+b_2P_2^0=1+b_1f_1+b_2f_2\end{aligned} \tag{S21}$$

Combining eqs (S16), and (S21) we obtain the following explicit expression for the surface potential

$$\Phi=q_{sat}\ln\left(1+b_1f_1+b_2f_2\right) \tag{S22}$$

The total amount adsorbed, $q_t=q_1+q_2$ can be calculated from Eq (S11)

$$q_t=q_1+q_2=q_{sat}\frac{b_1P_1^0}{1+b_1P_1^0}=q_{sat}\frac{b_2P_2^0}{1+b_2P_2^0}=q_{sat}\frac{b_1f_1+b_2f_2}{1+b_1f_1+b_2f_2} \tag{S23}$$

Combining eqs (S19), and (S23) we obtain the following explicit expressions for the component loadings, and fractional occupancies

$$\theta_1=\frac{q_1}{q_{sat}}=\frac{b_1f_1}{1+b_1f_1+b_2f_2};\quad \theta_2=\frac{q_2}{q_{sat}}=\frac{b_2f_2}{1+b_1f_1+b_2f_2} \tag{S24}$$

Eq (S24) is commonly referred to as the mixed-gas Langmuir model.

From eqs (S16), (S23), and (S24) we derive the following expression for the total occupancy of the mixture

$$\theta=\theta_1+\theta_2=\frac{q_t}{q_{sat}}=1-\exp\left(-\frac{\Phi}{q_{sat}}\right)=\frac{b_1f_1+b_2f_2}{1+b_1f_1+b_2f_2} \tag{S25}$$

For *unary* adsorption of component *i*, say, $f_i = P_i^0$, the occupancy of component 1 is

$$\theta_i = 1 - \exp\left(-\frac{\Phi}{q_{i,sat}}\right) = \frac{b_i f_i}{1 + b_i f_i}; \quad \text{unary adsorption of species i} \tag{S26}$$

From eqs (S25), and (S26) we may also conclude the *occupancy* may be considered to be the appropriate *proxy* for the spreading pressure. The conclusion that we draw from the foregoing analysis is that the equalities of spreading pressures for unary adsorption of component 1, unary adsorption of component 2, and binary 1-2 mixture adsorption also implies the corresponding equalities of the corresponding *occupancies* for unary adsorption of component 1, unary adsorption of component 2, and binary 1-2 mixture adsorption.

For *n*-component mixtures, eq (S22) may be generalized to

$$\Phi = q_{sat} \ln\left(1 + \sum_{i=1}^{n} b_i f_i\right) \tag{S27}$$

3.4 Generalized expression for fractional occupancy

From knowledge of the surface potential, Φ, the fractional occupancy for *n*-component mixture adsorption is then calculated using

$$\theta = 1 - \exp\left(-\frac{\pi A}{q_{sat,mix} RT}\right) = 1 - \exp\left(-\frac{\Phi}{q_{sat,mix}}\right) \tag{S28}$$

For an *n*-component mixture, the saturation capacity $q_{sat,mix}$ is calculated from the saturation capacities of the constituent guests

$$q_{sat,mix} = \frac{1}{\dfrac{x_1}{q_{1,sat}} + \dfrac{x_2}{q_{2,sat}} + \dots \dfrac{x_n}{q_{n,sat}}}; \quad q_{i,sat} = q_{i,A,sat} + q_{i,B,sat}; \quad i = 1, 2 \dots n \tag{S29}$$

where

$$x_i = \frac{q_i}{q_1 + q_2 + \dots q_n}; \quad i = 1, 2, \dots n \tag{S30}$$

are the mole fractions in the adsorbed mixture. For binary mixtures, eq (S28) simplifies to yield

$$q_{sat,mix} = \frac{1}{\frac{x_1}{q_{1,sat}} + \frac{x_2}{q_{2,sat}}}.$$

The fundamental justification of Eq (S29) is provided by invoking eq (S11).

Eq (S28) is the appropriate generalization of Eq (S25), derived in the following section for the mixed-gas Langmuir model. It is also to be noted that eq (15) of our earlier publication[41] has a typographical error in the calculation of $q_{sat,mix}$; the correct form is given by eq (S29).

For binary $CO_2(1)/CH_4(2)$ mixture adsorption in CHA, DDR, MFI, and all-silica FAU zeolite at 300 K, the pore occupancies for each host, calculated using eq (S28) are plotted as function of the corresponding surface potential Φ. We note that for all four hosts, the pore occupancy $\theta \rightarrow 1$ as $\Phi >> 30$ mol kg^{-1}.

3.5 List of Figures for Thermodynamics of Mixture Adsorption in Micro-porous Materials

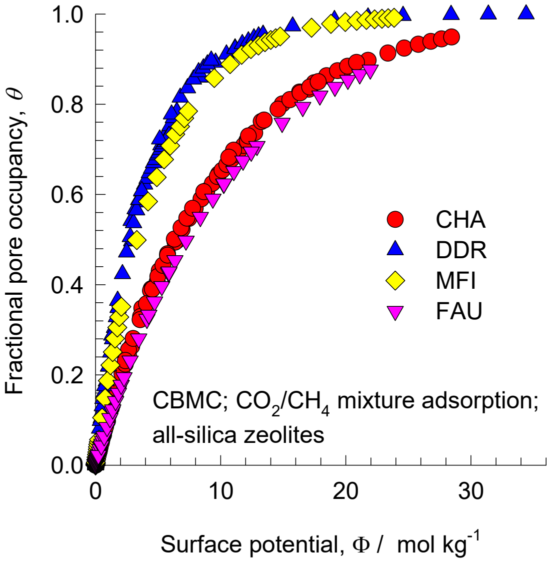

Figure S4. CBMC simulations of binary $CO_2(1)/CH_4(2)$ mixture adsorption in CHA, DDR, MFI, and all-silica FAU zeolite at 300 K. The pore occupancies for each host, calculated using eq (S28) are plotted as function of the corresponding surface potential Φ.

4 The Real Adsorbed Solution Theory (RAST)

To account for non-ideality effects in mixture adsorption, we introduce activity coefficients γ_i into Eq (S4) [34]

$$f_i = P_i^0 x_i \gamma_i \tag{S31}$$

The implementation of the activity coefficients is termed as the Real Adsorbed Solution Theory (RAST). From CBMC simulations of binary and ternary mixture adsorption in various microporous adsorbents, we can determine activity coefficients γ_i of the individual components in the various mixtures using

$$\gamma_i = \frac{f_i}{P_i^0 x_i} \tag{S32}$$

With the introduction of activity coefficients, the expression for the adsorption selectivity for binary mixtures is

$$S_{ads} = \frac{q_1/q_2}{y_1/y_2} = \frac{q_1/y_1}{q_2/y_2} = \frac{x_1/f_1}{x_2/f_2} = \frac{P_2^0 \gamma_2}{P_1^0 \gamma_1} \tag{S33}$$

We shall demonstrate later that the ratio of the activity coefficients for the *i-j* pair in binary mixtures shows the same dependence on surface potential Φ as for the same *i-j* pair in *n*-component mixtures. Consequently, the $S_{ads,ij}$ has nearly the same value for binary mixtures as for *n*-component mixtures, provided the comparison is made on the basis of the surface potential Φ. This is a useful, and practical result that we exploit in this article.

Following the approaches of Myers, Talu, Sieperstein, and Erto[36, 37, 42, 43] we model the excess Gibbs free energy for binary mixture adsorption as follows

$$\frac{G^{excess}}{RT} = x_1 \ln(\gamma_1) + x_2 \ln(\gamma_2) \tag{S34}$$

For calculation of the total mixture loading $q_t = q_1 + q_2$ we need to replace eq (S11) by

$$\frac{1}{q_t} = \frac{x_1}{q_1^0(P_1^0)} + \frac{x_2}{q_2^0(P_2^0)} + \left(\frac{1}{q_t}\right)^{excess} \tag{S35}$$

The excess reciprocal loading for the mixture can be related to the partial derivative of the Gibbs free energy with respect to the surface potential at constant composition

$$\left(\frac{1}{q_t}\right)^{excess} = \left.\frac{\partial\left(\frac{G^{excess}}{RT}\right)}{\partial\Phi}\right|_{T,x} \tag{S36}$$

4.1 Determination of activity coefficients from CBMC mixture adsorption data

For each CBMC mixture simulation campaigns for binary or ternary mixtures, activity coefficients of guest components can be determined from the use of eq (S32). The procedure is explained below using the example of ternary mixture.

Firstly, the mole fractions of the adsorbed phase, $x_1 = \frac{q_{1,CBMC}}{q_{t,CBMC}}; x_2 = \frac{q_{2,CBMC}}{q_{t,CBMC}}; x_3 = \frac{q_{3,CBMC}}{q_{t,CBMC}}$ are determined. $q_{t,CBMC} = q_{1,CBMC} + q_{2,CBMC} + q_{3,CBMC}$

The sorption pressures P_1^0, P_2^0, P_3^0, each of which satisfying eq (S6), can be determined from using the unary isotherm fits for each of the components in the ternary mixture.

The activity coefficients of the guest components $\gamma_{1,CBMC}; \gamma_{2,CBMC}; \gamma_{3,CBMC}$ are determined from eq (S32):

$$\gamma_{1,CBMC} = \frac{f_1}{P_1^0 x_{1,CBMC}}; \gamma_{2,CBMC} = \frac{f_2}{P_2^0 x_{2,CBMC}}; \gamma_{3,CBMC} = \frac{f_3}{P_3^0 x_{3,CBMC}} \tag{S37}$$

The activity coefficients of the two components $\gamma_{1,CBMC}; \gamma_{2,CBMC}; \gamma_{3,CBMC}$, determined using eq (S37) are subject to a degree of scatter that is inherent in the CBMC mixture simulation data.

5 Molecular Dynamics (MD) Simulation Methodology

Diffusion is simulated using Newton's equations of motion until the system properties, on average, no longer change in time. The Verlet algorithm is used for time integration. A time step of 1 fs was used in all simulations. For each simulation, *initializing* CBMC moves are used to place the molecules in the domain, minimizing the energy. Next, follows an *equilibration* stage. These are essentially the same as the production cycles, only the statistics are not yet taken into account. This removes any initial large disturbances in the system that do not affect statistics on molecular displacements. After a fixed number of initialization and equilibrium steps, the MD simulation *production* cycles start. For every cycle, the statistics for determining the mean square displacements (MSDs) are updated. The MSDs are determined for time intervals ranging from 2 fs to 1 ns. In order to do this, an order-*N* algorithm, as detailed in Chapter 4 of Frenkel and Smit[32] is implemented. The Nosé-Hoover thermostat is applied to all the diffusing particles. In the MD simulations the cations were allowed to move within the framework and both Lennard-Jones and Coulombic interactions are taken into consideration; see schematic sketch in Figure S2.

For all the MD simulation results presented in this article, the DLPOLY code[44] was used along with the force field implementation as described in the previous section. DL_POLY is a molecular dynamics simulation package written by W. Smith, T.R. Forester and I.T. Todorov and has been obtained from CCLRCs Daresbury Laboratory via the website.[44]

The MD simulations were carried out for a variety of loadings within the various structures. All simulations were carried out on the LISA clusters of PCs equipped with Intel Xeon processors running at 3.4 GHz on the Linux operating system.[45] Each MD simulation, for a specified loading, was run for a time duration that is sufficiently long to obtain reliable statistics for determination of the diffusivities. In several cases the campaigns were replicated and the results averaged.

The self-diffusivities $D_{i,self}$ are computed from MD simulations by analyzing the mean square displacement of each species *i* for each coordinate direction

$$D_{i,self} = \frac{1}{2n_i} \lim_{\Delta t \to \infty} \frac{1}{\Delta t} \left\langle \left(\sum_{l=1}^{n_i} \left(\mathbf{r}_{l,i}(t+\Delta t) - \mathbf{r}_{l,i}(t) \right)^2 \right) \right\rangle \tag{S38}$$

In this expression n_i represents the number of molecules of species *i*, and $\mathbf{r}_{l,i}(t)$ is the position of molecule *l* of species *i* at any time *t*.

For three-dimensional pore networks (e.g. MFI, FAU, CHA) the arithmetic average of the diffusivities in the three coordinate directions were used in further analysis and reported. For DDR the reported diffusivities are the averages in *x*- and *y*- directions.

MD simulations were performed to determine the self-diffusivities $D_{i,self}$ in a variety of equimolar $(q_1 = q_2)$ binary and ternary $(q_1 = q_2 = q_3)$ mixtures. In a few cases, the MD simulations were performed for mixtures in which the total loading $q_t = q_1 + q_2$ was held constant and the mole fraction of the adsorbed phase mixture, $x_1 = \frac{q_1}{q_1 + q_2}$ was varied from 0 to 1. All MD simulations reported in this work were conducted at a temperature $T = 300$ K.

For the interpretation and analysis of the MD simulations for mixture diffusion in microporous host materials, the IAST calculation procedure needs to be performed differently because in the MD simulations, the molar loadings q_i in the mixture are specified, and the partial fugacities in the bulk fluid mixture are not known *a priori*. Also, in this case, the equalities in eq (S6) must be satisfied in conjunction with eq (S9). The entire set of eqs (S4) to (S11) need to be solved numerically to obtain the partial fugacities, f_i of the individual components in the mixture, that yield the same loadings as chosen in the MD simulations. The IAST calculations also determine the surface potential Φ. In all of the calculations presented in this article, the set of equations were solved using an Excel macro that was developed for this specific purpose.

6 Diffusion in Microporous Crystalline Materials

6.1 The Babbitt equation for unary diffusion in micropores

For describing the *unary* transport of bound moisture in wood, Babbitt[46, 47] suggested the use of the gradient of the spreading pressure $d\pi/dz$ as the thermodynamically correct driving force. The units of $d\pi/dz$ are N m^{-2}, and this represents the force acting per m^2 of material surface. The number of moles of adsorbate, species *i*, per m^2 of surface is $\frac{q_i}{A}$. Therefore, the force per mole of adsorbate is $-\left(\frac{d\pi}{dz}\right)\Big/\left(\frac{q_i}{A}\right)=-\frac{d\mu_i}{dz}$. This force is balanced by friction between the mobile adsorbates and the surface of the material

$$-\left(\frac{d\pi}{dz}\right)\Big/\left(\frac{q_i}{A}\right)=-\frac{d\mu_i}{dz}=\frac{RT}{Đ_i}u_i \tag{S39}$$

where u_i is the velocity of motion of the adsorbate with respect to the framework material. The quantity $\frac{RT}{Đ_i}$ in the right member of equation is interpreted as the "drag coefficient". The unary diffusivity $Đ_i$, with the units m^2 s^{-1}, is to be interpreted as an inverse drag coefficient between the adsorbate and the surface. If we define N_i as the number of moles of species *i* transported per m^2 of crystalline material per second

$$N_i \equiv \rho q_i u_i \tag{S40}$$

where ρ is the framework density of the microporous crystalline material with units of kg m^{-3}, we obtain the flux relation

$$-\rho\frac{A}{RT}\frac{d\pi}{dz}=\frac{N_i}{Đ_i} \tag{S41}$$

If the unary adsorption isotherm is described by the 1-site Langmuir isotherm, equation (S14), the spreading pressure, or its proxy, the adsorption potential can be calculated using equation (S15). A much more convenient proxy for the spreading pressure is the fractional occupancy, determined by equation

(S26) for a 1-site Langmuir isotherm. More generally, if the unary adsorption isotherm is described by the dual-Langmuir-Freundlich isotherm, equation (S8), the fractional occupancy can be determined as follows

$$\begin{gathered}\frac{\pi A}{RT}=\frac{q_{A,sat}}{\nu_A}\ln\left(1+b_A\left(f_i\right)^{\nu_A}\right)+\frac{q_{B,sat}}{\nu_B}\ln\left(1+b_B\left(f_i\right)^{\nu_B}\right);\quad q_{i,sat}=q_{A,sat}+q_{B,sat}\\ \theta_i=1-\exp\left(-\frac{\pi A}{q_{i,sat}RT}\right);\quad \text{unary adsorption of species i}\end{gathered}\tag{S42}$$

Combining equations (S39), and (S41) we obtain

$$-\rho\frac{q_i}{RT}\frac{d\mu_i}{dz}=\frac{N_i}{Đ_i}\tag{S43}$$

The Babbitt equation (S43) is a limiting case of the more general Maxwell-Stefan (M-S) formulation[7, 48, 49] for *n*-component diffusion, developed in the next section.

6.2 The Maxwell-Stefan (M-S) description of diffusion

Within micro-porous crystalline materials, such as zeolites, metal-organic frameworks (MOFs), and zeolitic imidazolate frameworks (ZIFs), the guest molecules exist in the adsorbed phase. The Maxwell-Stefan (M-S) equations for *n*-component diffusion in porous materials is applied in the following manner[6, 7, 50-55]

$$-\rho\frac{q_i}{RT}\frac{\partial\mu_i}{\partial r}=\sum_{\substack{j=1\\ j\neq i}}^{n}\frac{x_jN_i-x_iN_j}{Đ_{ij}}+\frac{N_i}{Đ_i};\qquad i=1,2,..n\tag{S44}$$

where ρ is the framework density with units of kg m^{-3}, q_i is the molar loading of adsorbate, and the adsorbed phase mole fractions are $x_i=q_i/q_t$ where q_t is the *total* mixture loading $q_t=\sum_{i=1}^{n}q_i$. The fluxes N_i in equations (S44) are defined in terms of the moles transported per m^2 of the *total surface of crystalline material*.

An important, persuasive, argument for the use of the M-S formulation for mixture diffusion is that the M-S diffusivity $Đ_i$ in mixtures can be estimated using information on the loading dependence of the corresponding unary diffusivity values, provided the comparison is made at the same value of the adsorption potential, calculated from IAST using eq (S6), or its proxy the occupancy, θ, calculated using eqs (S28), (S29), (S30). Essentially this implies that the M-S diffusivity $Đ_i$ can be estimated from experimental data on *unary* diffusion in the porous material.

The *exchange coefficients* $Đ_{ij}$, defined by the first right member of eq (S44), are introduced to quantify the coupling between species diffusion. At the molecular level, the $Đ_{ij}$ reflect how the facility for transport of species *i correlates* with that of species *j*.

The Maxwell-Stefan diffusion formulation is consistent with the theory of irreversible thermodynamics. The Onsager Reciprocal Relations imply that the M-S pair diffusivities are symmetric

$$Đ_{ij}=Đ_{ji} \tag{S45}$$

6.3 Thermodynamic correction factors

At thermodynamic equilibrium, the chemical potential of component *i* in the bulk fluid mixture equals the chemical potential of that component in the adsorbed phase. For the bulk fluid phase mixture we have

$$\frac{1}{RT}\frac{\partial \mu_i}{\partial r}=\frac{\partial \ln f_i}{\partial r}=\frac{1}{f_i}\frac{\partial f_i}{\partial r}; \qquad i=1,2,..n \tag{S46}$$

The chemical potential gradients $\partial \mu_i/\partial r$ can be related to the gradients of the molar loadings, q_i, by defining thermodynamic correction factors Γ_{ij}

$$\frac{q_i}{RT}\frac{\partial \mu_i}{\partial r}=\sum_{j=1}^{n}\Gamma_{ij}\frac{\partial q_j}{\partial r}; \quad \Gamma_{ij}=\frac{q_i}{f_i}\frac{\partial f_i}{\partial q_j}; \qquad i,j=1,....n \tag{S47}$$

The thermodynamic correction factors Γ_{ij} can be calculated by differentiation of the model describing mixture adsorption equilibrium. Generally speaking, the Ideal Adsorbed Solution Theory (IAST) of Myers and Prausnitz[34] is the preferred method for estimation of mixture adsorption equilibrium. In the special case in which the unary isotherms are described for every component with the 1-site Langmuir model with equal saturation capacities, the mixed-gas Langmuir model

$$\frac{q_i}{q_{sat}} = \theta_i = \frac{b_i f_i}{1 + \sum_{i=1}^{n} b_i f_i}; \quad i = 1, 2, \ldots n \tag{S48}$$

Is derivable from the IAST. Analytic differentiation of eq (S48) yields

$$\Gamma_{ij} = \delta_{ij} + \left(\frac{\theta_i}{\theta_V} \right); \qquad i, j = 1, 2 \ldots n \tag{S49}$$

where the fractional vacancy θ_V is defined as

$$\theta_V = 1 - \theta_t = 1 - \sum_{i=1}^{n} \theta_i \tag{S50}$$

The elements of the matrix of thermodynamic factors Γ_{ij} can be calculated explicitly from information on the component loadings q_i in the adsorbed phase; this is the persuasive advantage of the use of the mixed-gas Langmuir model. By contrast, the IAST does not allow the calculation of Γ_{ij} explicitly from knowledge on the component loadings q_i in the adsorbed phase; a numerical procedure is required.

6.4 M-S formulation for binary mixture diffusion

For binary mixture diffusion inside microporous crystalline materials the Maxwell-Stefan equations (S44) are written

$$\begin{aligned} -\rho \frac{q_1}{RT} \frac{\partial \mu_1}{\partial r} &= \frac{x_2 N_1 - x_1 N_2}{Đ_{12}} + \frac{N_1}{Đ_1} \\ -\rho \frac{q_2}{RT} \frac{\partial \mu_2}{\partial r} &= \frac{x_1 N_2 - x_2 N_1}{Đ_{12}} + \frac{N_2}{Đ_2} \end{aligned} \tag{S51}$$

The first members on the right hand side of eq (S51) are required to quantify slowing-down effects that characterize binary mixture diffusion.[6, 7, 56] There is no experimental technique for direct determination of the exchange coefficients $Đ_{12}$, that quantify molecule-molecule interactions; the $Đ_{12}$ are accessible from MD simulations.

In two-dimensional matrix notation, eq (S47) take the form

$$-\begin{pmatrix} \frac{q_1}{RT}\frac{\partial \mu_1}{\partial r} \\ \frac{q_2}{RT}\frac{\partial \mu_2}{\partial r} \end{pmatrix} = [\Gamma]\begin{pmatrix} \frac{\partial q_1}{\partial r} \\ \frac{\partial q_2}{\partial r} \end{pmatrix} \tag{S52}$$

For the mixed-gas Langmuir model, eq (S48), we can derive simple analytic expressions for the four elements of the matrix of thermodynamic factors:[57]

$$\begin{bmatrix} \Gamma_{11} & \Gamma_{12} \\ \Gamma_{21} & \Gamma_{22} \end{bmatrix} = \frac{1}{1-\theta_1-\theta_2}\begin{bmatrix} 1-\theta_2 & \theta_1 \\ \theta_2 & 1-\theta_1 \end{bmatrix} \tag{S53}$$

where the fractional occupancies, θ_i, are defined by eq (S48).

Let us define the square matrix $[B]$

$$[B] = \begin{bmatrix} \frac{1}{Đ_1}+\frac{x_2}{Đ_{12}} & -\frac{x_1}{Đ_{12}} \\ -\frac{x_2}{Đ_{12}} & \frac{1}{Đ_2}+\frac{x_1}{Đ_{12}} \end{bmatrix}; \quad [B]^{-1} = \frac{1}{1+\frac{x_1 Đ_2}{Đ_{12}}+\frac{x_2 Đ_1}{Đ_{12}}}\begin{bmatrix} Đ_1\left(1+\frac{x_1 Đ_2}{Đ_{12}}\right) & \frac{x_1 Đ_1 Đ_2}{Đ_{12}} \\ \frac{x_2 Đ_1 Đ_2}{Đ_{12}} & Đ_2\left(1+\frac{x_2 Đ_1}{Đ_{12}}\right) \end{bmatrix} \tag{S54}$$

In proceeding further, it is convenient to define a 2×2 dimensional square matrix $[\Lambda]$:

$$[\Lambda] = \begin{bmatrix} \frac{1}{Đ_1}+\frac{x_2}{Đ_{12}} & -\frac{x_1}{Đ_{12}} \\ -\frac{x_2}{Đ_{12}} & \frac{1}{Đ_2}+\frac{x_1}{Đ_{12}} \end{bmatrix}^{-1} = \frac{1}{1+\frac{x_1 Đ_2}{Đ_{12}}+\frac{x_2 Đ_1}{Đ_{12}}}\begin{bmatrix} Đ_1\left(1+\frac{x_1 Đ_2}{Đ_{12}}\right) & \frac{x_1 Đ_1 Đ_2}{Đ_{12}} \\ \frac{x_2 Đ_1 Đ_2}{Đ_{12}} & Đ_2\left(1+\frac{x_2 Đ_1}{Đ_{12}}\right) \end{bmatrix} \tag{S55}$$

The elements of the Maxwell-Stefan matrix Λ_{ij} are accessible from MD simulations [3, 6, 41, 52, 55, 58] by monitoring the individual molecular displacements

$$\Lambda_{ij} = \frac{1}{2}\lim_{\Delta t\to\infty}\frac{1}{n_j}\frac{1}{\Delta t}\left\langle \left(\sum_{l=1}^{n_i}\left(\mathbf{r}_{l,i}(t+\Delta t)-\mathbf{r}_{l,i}(t)\right)\right)\bullet\left(\sum_{k=1}^{n_j}\left(\mathbf{r}_{k,j}(t+\Delta t)-\mathbf{r}_{k,j}(t)\right)\right)\right\rangle \tag{S56}$$

In this expression n_i and n_j represent the number of molecules of species i and j respectively, and $\mathbf{r}_{l,i}(t)$ is the position of molecule l of species i at any time t. In this context we note a typographical error in equation (S56) as printed in earlier publications[4, 59, 60] wherein the denominator in the right member had n_i instead of n_j. The simulation results presented in these publications are, however, correct as the proper formula given in equation (S56) was used.

Compliance with the Onsager Reciprocal Relations demands

$$n_j \Lambda_{ij} = n_i \Lambda_{ji}; \quad i,j = 1,2,....n \tag{S57}$$

Eq (S51) can be re-cast into 2-dimensional matrix notation

$$(N) = -\rho[\Lambda][\Gamma]\frac{\partial(q)}{\partial r};$$
$$\begin{pmatrix} N_1 \\ N_2 \end{pmatrix} = -\frac{\rho}{1+\frac{x_1 Đ_2}{Đ_{12}}+\frac{x_2 Đ_1}{Đ_{12}}}\begin{bmatrix} Đ_1\left(1+\frac{x_1 Đ_2}{Đ_{12}}\right) & \frac{x_1 Đ_1 Đ_2}{Đ_{12}} \\ \frac{x_2 Đ_1 Đ_2}{Đ_{12}} & Đ_2\left(1+\frac{x_2 Đ_1}{Đ_{12}}\right) \end{bmatrix}\begin{bmatrix} \Gamma_{11} & \Gamma_{12} \\ \Gamma_{21} & \Gamma_{22} \end{bmatrix}\begin{pmatrix} \frac{\partial q_1}{\partial r} \\ \frac{\partial q_2}{\partial r} \end{pmatrix} \tag{S58}$$

The elements of $[B]$ can be obtained by inverting the matrix $[\Lambda]$:

$$\begin{bmatrix} B_{11} & B_{12} \\ B_{21} & B_{22} \end{bmatrix} = \begin{bmatrix} \frac{1}{Đ_1}+\frac{x_2}{Đ_{12}} & -\frac{x_1}{Đ_{12}} \\ -\frac{x_2}{Đ_{12}} & \frac{1}{Đ_2}+\frac{x_1}{Đ_{12}} \end{bmatrix} = [\Lambda]^{-1} \tag{S59}$$

The three M-S diffusivities can be backed-out from the four elements $\begin{bmatrix} B_{11} & B_{12} \\ B_{21} & B_{22} \end{bmatrix}$ using

$$Đ_{12} = -\frac{x_1}{B_{12}} = -\frac{x_2}{B_{21}}; \quad Đ_1 = \frac{1}{B_{11}+B_{21}}; \quad Đ_2 = \frac{1}{B_{22}+B_{12}} \tag{S60}$$

As illustration, Figure S5 presents MD simulated values of $\Lambda_{11}, \Lambda_{12} = \Lambda_{21}, \Lambda_{22}$ for equimolar (q_1=q_2) binary CO_2(1)/N_2(2), CH_4(1)/N_2(2), CH_4(1)/H_2(2), Ne(1)/Ar(2), CO_2(1)/CH_4(2), and CO_2(1)/H_2(2) mixtures in MFI zeolite at 300 K plotted as a function of the total mixture loading $q_t = q_1 + q_2$. From these data, the values of the Maxwell-Stefan diffusivities, $Đ_1, Đ_2$, backed-out using eq (S60) for the six binary mixtures are shown in Figure S6. The M-S diffusivities are loading-dependent, and the values reduce as saturation conditions are approached. Except at vanishingly small loadings, we note that in all cases the Maxwell-Stefan diffusivities, $Đ_1, Đ_2$ do not have precisely same values as the corresponding values of the unary diffusivities.

Figure S7 present MD simulated values of $\Lambda_{11},\Lambda_{12},\Lambda_{21},\Lambda_{22}$ for Ne(1)/Ar(2), CO_2(1)/CH_4(2), and CO_2(1)/H_2(2) mixtures in MFI zeolite at 300 K, in which the total loading $\Theta_t = \Theta_1 + \Theta_2$ is held constant. The data are plotted as function of the mole fraction of component 1 in the mixture, $x_1 = \frac{\Theta_1}{\Theta_t}$. Even though the total mixture loading is held constant, we note the elements $\Lambda_{11},\Lambda_{12},\Lambda_{21},\Lambda_{22}$ are strongly dependent on the composition of the mixture.

In Figure S8, the MD simulated values of the backed-out M-S diffusivities, $Đ_1,Đ_2$ for binary CO_2(1)/N_2(2), CH_4(1)/N_2(2), CH_4(1)/H_2(2), Ne(1)/Ar(2), CO_2(1)/CH_4(2), and CO_2(1)/H_2(2) mixtures in MFI zeolite at 300 K are plotted as a function of the occupancy θ, calculated using eq (S28). The fractional occupancy is a proxy for the surface potential, Φ. For Ne(1)/Ar(2), CO_2(1)/CH_4(2), and CO_2(1)/H_2(2) mixtures, we have plotted both sets of MD data from Figure S5 and Figure S7. We note that the constituent M-S diffusivities, $Đ_1,Đ_2$ have practically the same values as the corresponding unary diffusivities, when compared at the same occupancy irrespective of the total mixture loading and the mixture composition; further evidence is provided in our earlier publications.[41, 58]

Figure S9a,b,c,d present MD simulated values of the M-S diffusivities, $Đ_1,Đ_2$, self-diffusivities, $D_{1,self}, D_{2,self}$, and $\Lambda_{11},\Lambda_{12},\Lambda_{21},\Lambda_{22}$ for binary Ne(1)/Ar(2) mixtures in FAU zeolite at 300 K. Also plotted in Figure S9a are the diffusivities in the constituent unaries, as function of the molar loadings. Two different MD campaigns were conducted: (i) equimolar $q_1 = q_2$ mixtures, and (ii) mixtures for which $\Theta_t = \Theta_1 + \Theta_2$ = 100 uc^{-1}. We note that the $\Lambda_{11},\Lambda_{12},\Lambda_{21},\Lambda_{22}$, along with the M-S diffusivities, $Đ_1,Đ_2$ are strongly dependent on the total mixture loadings. Also, at constant mixture loading $\Theta_t = \Theta_1 + \Theta_2$ = 100 uc^{-1}, the diffusivities are strongly dependent on the mole fraction of component 1 in the mixture, $x_1 = \frac{\Theta_1}{\Theta_t}$. In Figure S9e the M-S diffusivities, $Đ_1,Đ_2$ are plotted as function of the pore occupancy θ, calculated using eq (S28). The fractional occupancy is a proxy for the surface potential, Φ. We note that the constituent M-S diffusivities, $Đ_1,Đ_2$ have practically the same values as the corresponding unary diffusivities, when compared at the same occupancy irrespective of the total mixture loading and the mixture composition; further evidence is provided in our earlier publications.[41, 58] From Figure S9f we note the component self-diffusivities $D_{1,self},D_{2,self}$ for binary Ne(1)/Ar(2) mixtures in all-silica FAU zeolite have practically the same values as the corresponding unary diffusivities, when compared at the same occupancy θ.

Precisely analogous results are realized for binary Ne(1)/Ar(2) mixtures in MFI zeolite, CuBTC, and IRMOF-1; see Figure S10, Figure S11, and Figure S12. The data show that component M-S diffusivities, $Đ_1,Đ_2$ and self-diffusivities $D_{1,self},D_{2,self}$ in binary mixtures have practically the same values as the corresponding unary diffusivities, when compared at the same occupancy, θ, irrespective of the total mixture loading and the mixture composition.

The above findings regarding the unique θ-dependence of component M-S diffusivities, $Đ_1,Đ_2$ and self-diffusivities $D_{1,self},D_{2,self}$ in binary mixtures and in the constituent unaries are confirmed for other guest/host combinations. As illustration, we present data for

CH_4(1)/C_2H_6(2) mixtures in all-silica ISV zeolite, see Figure S13.

CH_4(1)/C_3H_8(2) mixtures in all-silica BEA zeolite, see Figure S14.

CH_4(1)/nC_4H_{10}(2) mixtures in IRMOF-1, see Figure S15.

CH_4(1)/C_2H_6(2) mixtures in NaY (144 Si, 48 Al, 48 Na^+, Si/Al=3) zeolite, see Figure S16.

CH_4(1)/C_3H_8(2) mixtures in NaY (144 Si, 48 Al, 48 Na^+, Si/Al=3) zeolite, see Figure S17.

CH_4(1)/C_2H_6(2) mixtures in NaX (106 Si, 86 Al, 86 Na^+, Si/Al=1.23) zeolite, see Figure S18.

CH_4(1)/C_3H_8(2) mixtures in NaX (106 Si, 86 Al, 86 Na^+, Si/Al=1.23) zeolite, see Figure S19.

For CO_2(1)/H_2(2) mixture diffusion, the in IRMOF-1 and MFI zeolite, the correlation effects are very strong and the self-diffusivities in mixtures are lowered below the values of the unary diffusivities for hydrogen:

$CO_2(1)/H_2(2)$ mixtures in IRMOF-1, see Figure S20

$CO_2(1)/H_2(2)$ mixtures in MFI zeolite, see Figure S21

We return to this point regarding $CO_2(1)/H_2(2)$ mixture diffusion later in this document.

In this article, we exploit the uniqueness of the dependence of component self-diffusivities as functions of the occupancy θ, that serves as a proxy for the surface potential, Φ. Though microporous crystalline materials are the main focus of this article, it is worth mentioning that the uniqueness of the $D_{i,self} - \theta$, and $D_{i,self} - \Phi$ dependences in mixtures with the corresponding unary diffusivities also holds for mesoporous BTP-COF, that has one-dimensional hexagonal channels of 34 Å size;[61] see Figure S22.

6.5 Analytic expressions for self-diffusivities

Applying eqs (S51) to a binary mixture of two components that are identical; one is tagged and the other is untagged, we derive the following expressions for the self-diffusivities[7]

$$\frac{1}{D_{1,self}} = \frac{1}{Đ_1} + \frac{x_1}{Đ_{11}} + \frac{x_2}{Đ_{12}}; \quad \frac{1}{D_{2,self}} = \frac{1}{Đ_2} + \frac{x_2}{Đ_{22}} + \frac{x_1}{Đ_{12}} \tag{S61}$$

6.6 Correlation effects for M-S diffusivities

Of the four all-silica zeolites investigated in this work, correlation effects are of importance in MFI and FAU. For values of $Đ_1/Đ_{12} \to 0$, and $Đ_2/Đ_{12} \to 0$, the contribution of the first right member of M-S Eq (S51) can be ignored and correlations can be considered to be of negligible importance; we derive

$$\frac{Đ_1}{Đ_{12}} \to 0; \quad \frac{Đ_2}{Đ_{12}} \to 0; \quad \begin{bmatrix} \Lambda_{11} & \Lambda_{12} \\ \Lambda_{21} & \Lambda_{22} \end{bmatrix} \to \begin{bmatrix} Đ_1 & 0 \\ 0 & Đ_2 \end{bmatrix}$$
$$\begin{pmatrix} N_1 \\ N_2 \end{pmatrix} = -\rho \begin{bmatrix} Đ_1 & 0 \\ 0 & Đ_2 \end{bmatrix} \begin{bmatrix} \Gamma_{11} & \Gamma_{12} \\ \Gamma_{21} & \Gamma_{22} \end{bmatrix} \begin{pmatrix} \dfrac{\partial q_1}{\partial r} \\ \dfrac{\partial q_2}{\partial r} \end{pmatrix} \tag{S62}$$

Eq (S62) is valid, as a first approximation, for diffusion in cage-type zeolites with 8-ring windows (CHA, DDR, LTA, ERI) and ZIF-8.[3-5, 52, 62-65] When correlation effects are negligible, the diffusional coupling effects are solely traceable to mixture adsorption thermodynamics, embodied in the matrix $\left[\Gamma\right]$. When correlations are negligible, we obtain the self-diffusivities can be identified with the Maxwell-Stefan diffusivities.

$$Đ_1/Đ_{12} \to 0; \quad Đ_2/Đ_{12} \to 0; \quad D_{1,self} = Đ_1; \quad D_{2,self} = Đ_2 \tag{S63}$$

6.7 Membrane permeation selectivities

For any given application, the separation performance of a microporous membrane is characterized by two metrics: permeability and permeation selectivity. The permeability of component *i* is defined as

$$\Pi_i = \frac{N_i}{\Delta f_i/\delta} \tag{S64}$$

where N_i is the permeation flux and $\Delta f_i = f_i - f_{i\delta}$ is the difference in the partial fugacities between the upstream $\left(f_i\right)$ and downstream $\left(f_{i\delta}\right)$ faces of the membrane layer of thickness δ. If the gas mixtures may be considered to be thermodynamically ideal, the partial fugacities may be replaced by the corresponding partial pressures p_i. Often, the component permeances, defined by $N_i/\Delta f_i \equiv \Pi_i/\delta$, are more easily accessible from experiments because of uncertainties in the precise values of the membrane thickness, δ.

If the downstream compartments of the membrane are evacuated we may approximate the concentration differences as follows

$$\frac{\Delta q_1}{\delta} \approx \frac{q_1}{\delta}; \quad \frac{\Delta q_2}{\delta} \approx \frac{q_2}{\delta} \tag{S65}$$

where q_i are the molar loadings in equilibrium with the partial fugacities q_i in the upstream face of the membrane.

Let us further assume that the M-S diffusivities vary with the fractional occupancies according to

$$Đ_i = Đ_i(0)\left(1-\theta\right) \tag{S66}$$

where $Đ_i(0)$ are the zero-loading diffusivities. For multicomponent Langmuir isotherm, the M-S equations for binary mixtures can be integrated analytically to obtain [66]

$$\begin{aligned} N_1 &= \rho\Lambda_{11}\frac{q_1}{\delta} + \rho\Lambda_{12}\frac{q_2}{\delta} \\ N_2 &= \rho\Lambda_{21}\frac{q_1}{\delta} + \rho\Lambda_{22}\frac{q_2}{\delta} \end{aligned} \tag{S67}$$

where the elements of the matrix $[\Lambda]$ are evaluated at the upstream loadings. It is convenient to define the effective diffusivities, $D_{i,\mathrm{eff}}$,

$$\begin{aligned} D_{1,eff} &= \Lambda_{11} + \Lambda_{12}\frac{q_2}{q_1} \\ D_{2,eff} &= \Lambda_{22} + \Lambda_{21}\frac{q_1}{q_2} \end{aligned} \tag{S68}$$

From eqs (S65), (S66), (S67), (S68) we derive the following explicit expressions

$$\begin{aligned} D_{1,eff} &= \Lambda_{11} + \Lambda_{12}\frac{q_2}{q_1} = \frac{Đ_1\left(1+\frac{x_1Đ_2}{Đ_{12}}\right)}{1+\frac{x_1Đ_2}{Đ_{12}}+\frac{x_2Đ_1}{Đ_{12}}} + \frac{Đ_1\frac{x_1Đ_2}{Đ_{12}}}{1+\frac{x_1Đ_2}{Đ_{12}}+\frac{x_2Đ_1}{Đ_{12}}}\frac{q_2}{q_1} = \frac{Đ_1\left(1+\frac{Đ_2}{Đ_{12}}\right)}{1+\frac{x_1Đ_2}{Đ_{12}}+\frac{x_2Đ_1}{Đ_{12}}} \\ D_{2,eff} &= \Lambda_{22} + \Lambda_{21}\frac{q_1}{q_2} = \frac{Đ_2\left(1+\frac{x_2Đ_1}{Đ_{12}}\right)}{1+\frac{x_1Đ_2}{Đ_{12}}+\frac{x_2Đ_1}{Đ_{12}}} + \frac{Đ_2\frac{x_2Đ_1}{Đ_{12}}}{1+\frac{x_1Đ_2}{Đ_{12}}+\frac{x_2Đ_1}{Đ_{12}}}\frac{q_1}{q_2} = \frac{Đ_2\left(1+\frac{Đ_1}{Đ_{12}}\right)}{1+\frac{x_1Đ_2}{Đ_{12}}+\frac{x_2Đ_1}{Đ_{12}}} \end{aligned} \tag{S69}$$

For separation of a binary mixture, the permeation selectivity is

$$S_{perm} = \frac{N_1/f_1}{N_2/f_2} \tag{S70}$$

In view of eqs (S67), (S68), and (S69) the permeation selectivity can be expressed as

$$S_{perm} = \frac{N_1/f_1}{N_2/f_2} = \frac{D_{1,eff}}{D_{2,eff}}\frac{q_1/f_1}{q_2/f_2} \tag{S71}$$

For separation of a binary mixture, the diffusion selectivity can be defined as follows

$$S_{diff} = \frac{D_{1,eff}}{D_{2,eff}} \tag{S72}$$

From eqs (S69) and (S72) we get

$$\frac{D_{1,eff}}{D_{2,eff}}=\frac{\left(\frac{1}{Đ_2}+\frac{1}{Đ_{12}}\right)}{\left(\frac{1}{Đ_1}+\frac{1}{Đ_{12}}\right)}=\frac{Đ_1}{Đ_2}\frac{\left(1+\frac{Đ_2}{Đ_{12}}\right)}{\left(1+\frac{Đ_1}{Đ_{12}}\right)} \tag{S73}$$

We now show that S_{diff} can be approximated by the ratio of self-diffusivities. From eqs (S61) the ratio of self-diffusivities can be written as follows

$$\frac{D_{1,self}}{D_{2,self}}=\frac{\frac{1}{Đ_2}+\frac{x_2}{Đ_{22}}+\frac{x_1}{Đ_{12}}}{\frac{1}{Đ_1}+\frac{x_1}{Đ_{11}}+\frac{x_2}{Đ_{12}}}=\frac{Đ_1}{Đ_2}\frac{1+\frac{x_2Đ_2}{Đ_{22}}+\frac{x_1Đ_2}{Đ_{12}}}{1+\frac{x_1Đ_1}{Đ_{11}}+\frac{x_2Đ_1}{Đ_{12}}} \tag{S74}$$

In view of the Vignes interpolation formula [6]

$$Đ_{12}=\left(Đ_{11}\right)^{x_1}\left(Đ_{22}\right)^{x_2} \tag{S75}$$

we conclude that the ratio of the self-diffusivities is a good approximation for the diffusion selectivities

$$\frac{D_{1,self}}{D_{2,self}}\approx\frac{Đ_1}{Đ_2}\frac{1+\frac{Đ_2}{Đ_{12}}}{1+\frac{Đ_1}{Đ_{12}}}=\frac{D_{1,eff}}{D_{2,eff}}=S_{diff} \tag{S76}$$

As conformation of the accuracy of eq (S76), Figure S23 presents MD simulation data for (a) CO_2/CH_4, (b) H_2/CO_2, (c) C_2H_6/CH_4, and (d) C_3H_8/CH_4 diffusion selectivities, S_{diff}, for mixtures determined from equimolar binary $\left(q_1=q_2\right)$ mixtures in MFI zeolite at 300 K, plotted as function of the surface potential Φ. The diffusion selectivities calculated from $\frac{D_{1,self}}{D_{2,self}}$ agree reasonably well with those calculated from $\frac{D_{1,eff}}{D_{2,eff}}$. For all the MD simulation data reported in this article for CHA, DDR, MFI and FAU, we use calculations based on the ratio of self-diffusivities: $\frac{D_{1,self}}{D_{2,self}}=S_{diff}$.

In view of eq **Error! Reference source not found.**, the adsorption selectivity for the binary 1-2 mixture is

$$S_{ads} = \frac{q_1/q_2}{f_1/f_2} = \frac{x_1/f_1}{x_2/f_2} = \frac{P_2^0\gamma_2}{P_1^0\gamma_1} \tag{S77}$$

Therefore, the permeation selectivity is the product of the adsorption selectivity and the diffusion selectivity

$$S_{perm} = S_{ads} \times S_{diff} \tag{S78}$$

6.8 List of Figures for Diffusion in Microporous Crystalline Materials

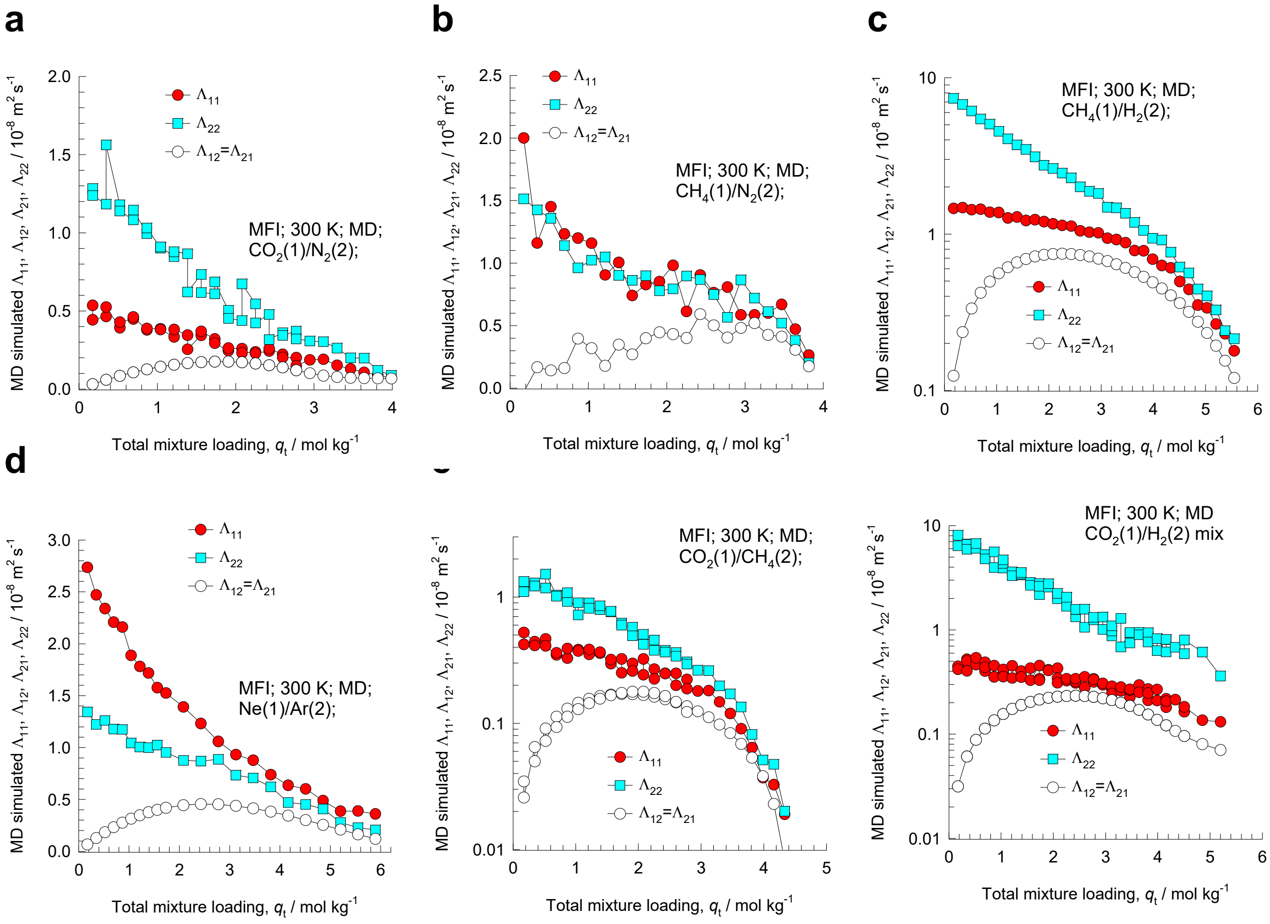

Figure S5. MD simulated values of $\Lambda_{11},\Lambda_{12}=\Lambda_{21},\Lambda_{22}$ for equimolar $q_1=q_2$ binary CO$_2$(1)/N$_2$(2), CH$_4$(1)/N$_2$(2), CH$_4$(1)/H$_2$(2), Ne(1)/Ar(2), CO$_2$(1)/CH$_4$(2), and CO$_2$(1)/H$_2$(2) mixtures in MFI zeolite at 300 K plotted as a function of the total mixture loading $q_t=q_1+q_2$.

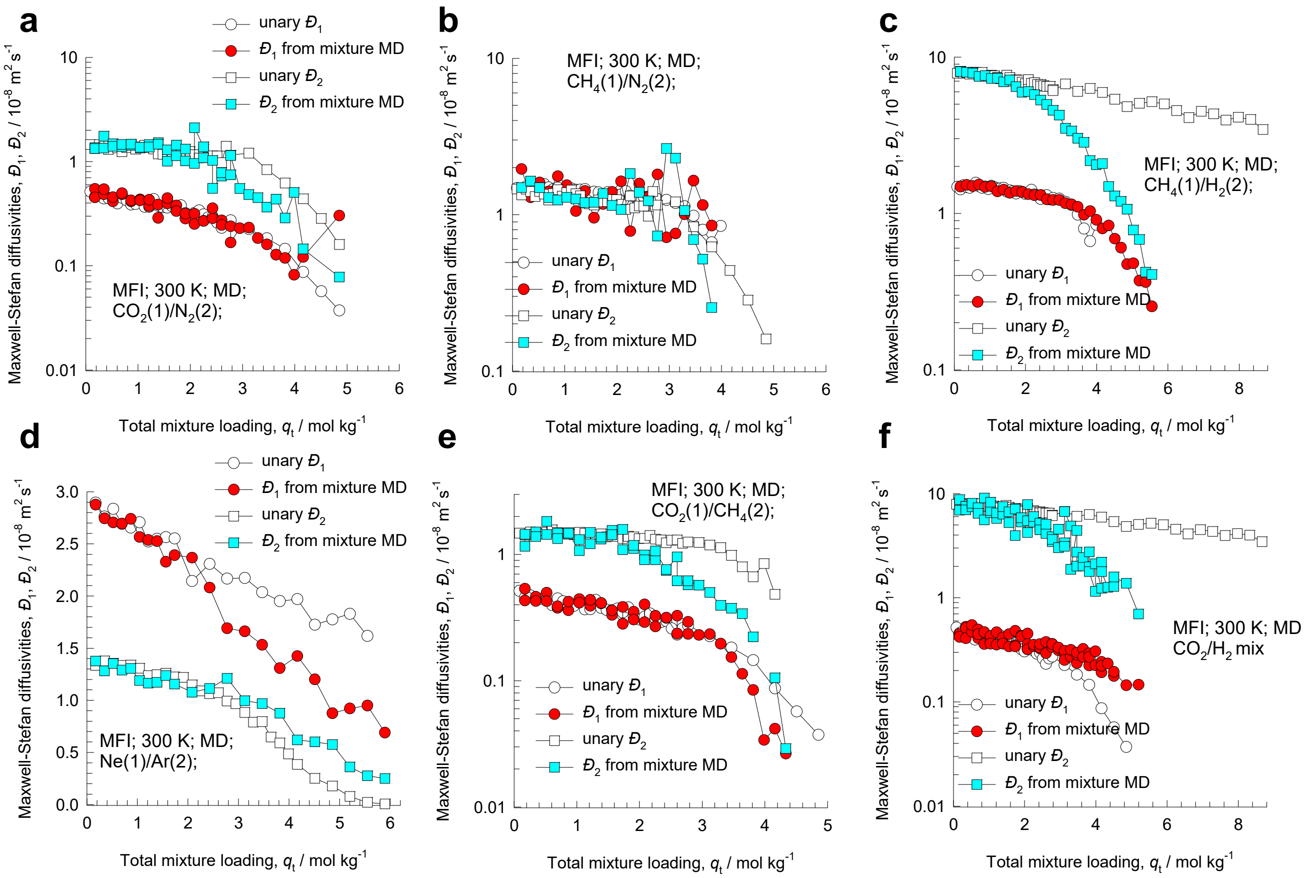

Figure S6. MD simulated values of the backed-out M-S diffusivities, $Đ_1, Đ_2$ for equimolar $q_1 = q_2$ binary CO2(1)/N2(2), CH4(1)/N2(2), CH4(1)/H2(2), Ne(1)/Ar(2), CO2(1)/CH4(2), and CO2(1)/H2(2) mixtures in MFI plotted as a function of the total mixture loading $q_t = q_1 + q_2$.

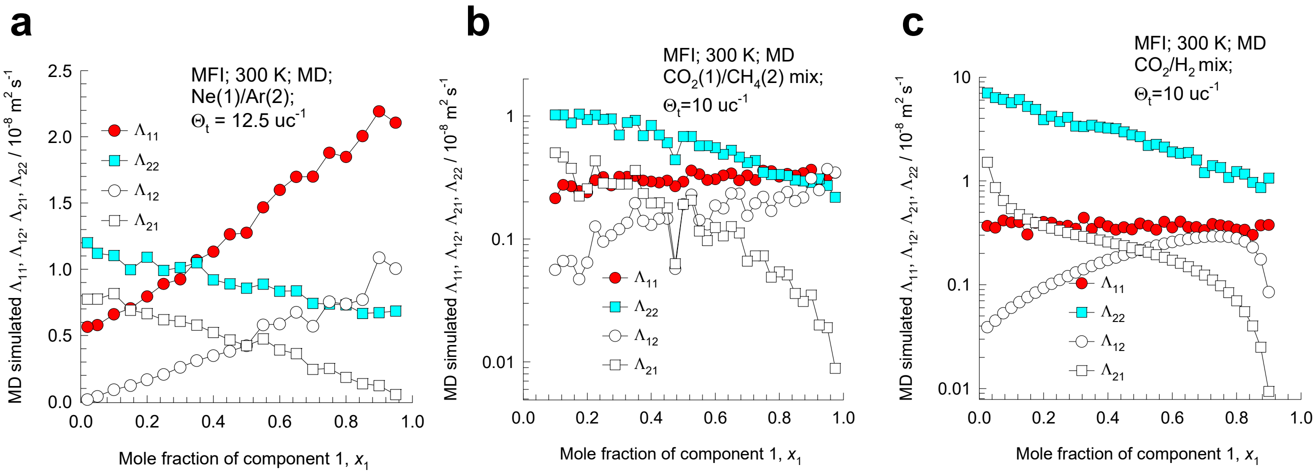

Figure S7. MD simulated values of $\Lambda_{11},\Lambda_{12},\Lambda_{21},\Lambda_{22}$ for Ne(1)/Ar(2), CO_2(1)/CH_4(2), and CO_2(1)/H_2(2) mixtures in MFI zeolite at 300 K, in which the total loading $\Theta_t = \Theta_1 + \Theta_2$ is held constant. The data are plotted as function of the mole fraction of component 1 in the mixture, $x_1 = \frac{\Theta_1}{\Theta_t}$.

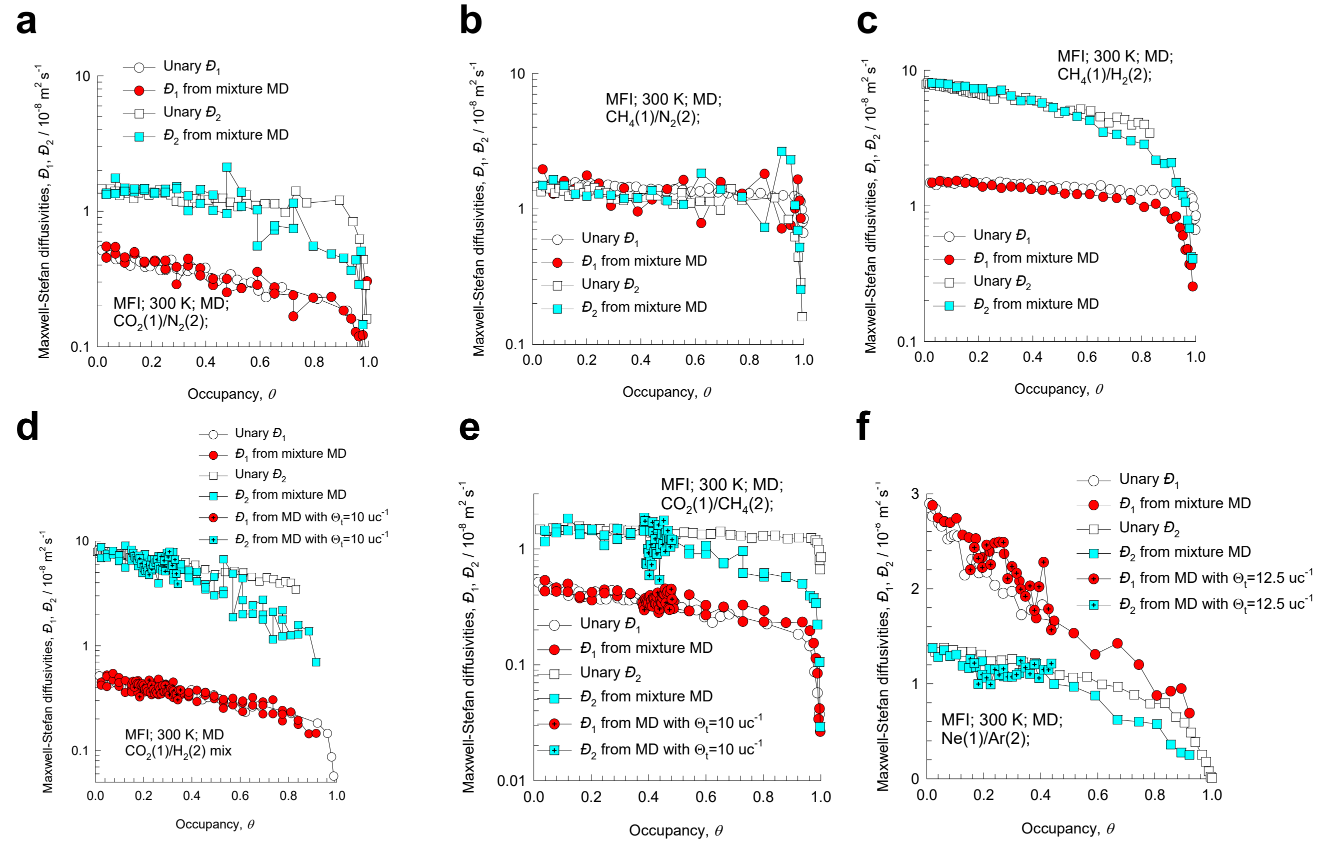

Figure S8. MD simulated values of the backed-out M-S diffusivities, $Đ_1, Đ_2$ for binary $CO_2(1)/N_2(2)$, $CH_4(1)/N_2(2)$, $CH_4(1)/H_2(2)$, Ne(1)/Ar(2), $CO_2(1)/CH_4(2)$, and $CO_2(1)/H_2(2)$ mixtures in MFI zeolite at 300 K plotted as a function of the occupancy θ.

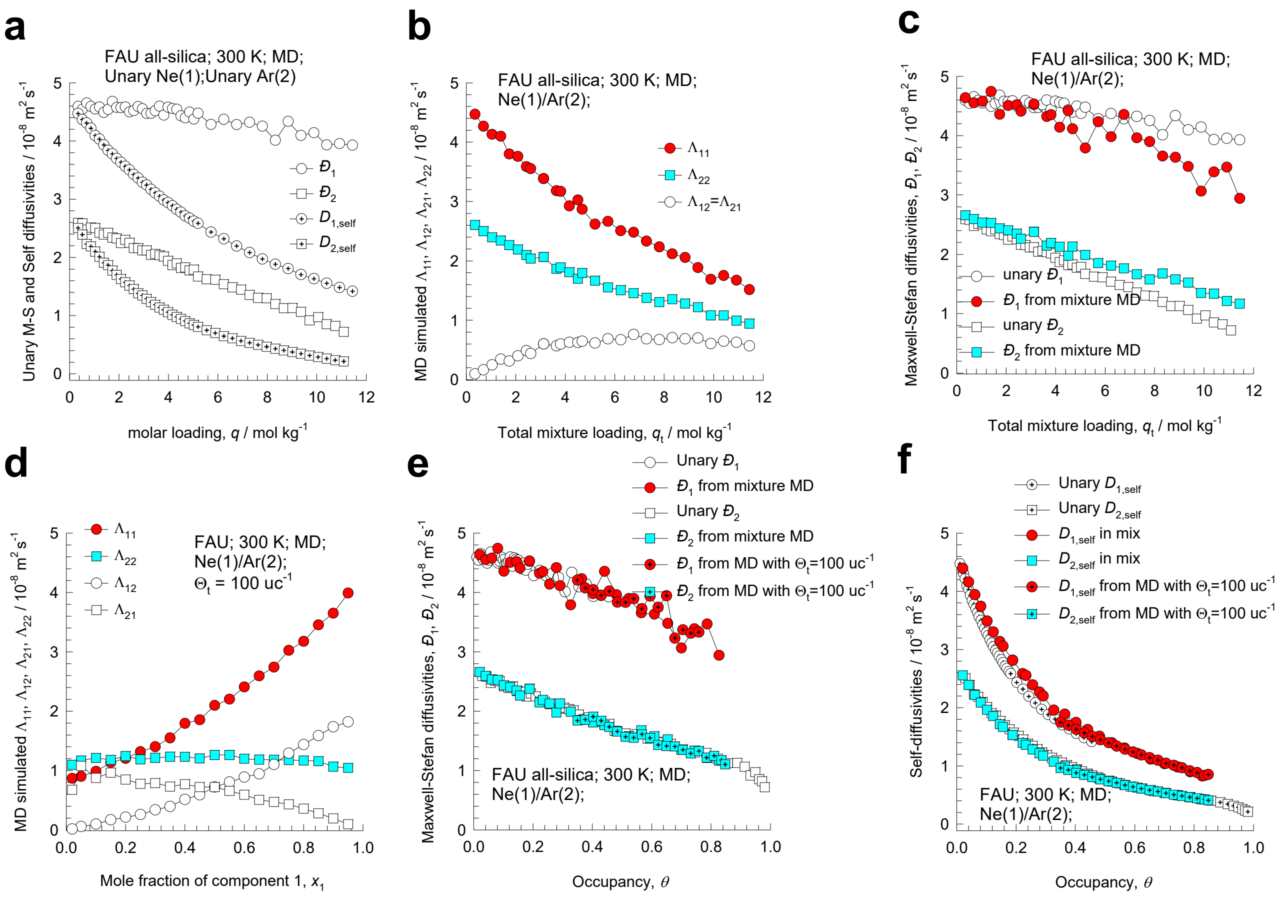

Figure S9. MD simulated values of the M-S diffusivities, $Đ_1, Đ_2$, self-diffusivities, $D_{1,self}, D_{2,self}$, and $\Lambda_{11}, \Lambda_{12}, \Lambda_{21}, \Lambda_{22}$ for binary Ne(1)/Ar(2) mixtures in FAU zeolite at 300 K. Two different MD campaigns were conducted: (i) equimolar $q_1 = q_2$ mixtures, and (ii) mixtures for which $\Theta_t = \Theta_1 + \Theta_2$ = 100 uc^{-1}. In (e, f) the M-S diffusivities, $Đ_1, Đ_2$, and self-diffusivities, $D_{1,self}, D_{2,self}$, are plotted as a function of the occupancy θ.

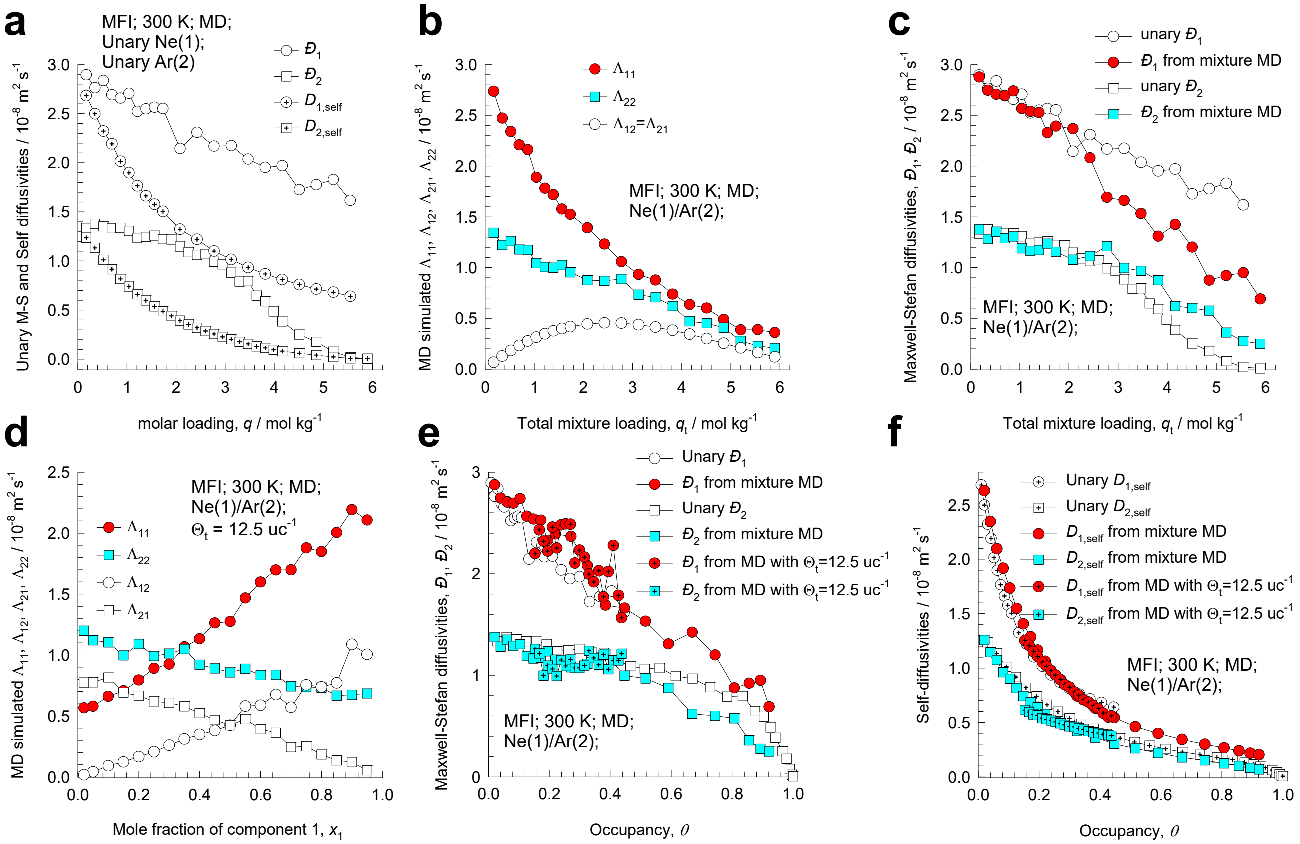

Figure S10. MD simulated values of the M-S diffusivities, $Đ_1, Đ_2$, self-diffusivities, $D_{1,self}, D_{2,self}$, and $\Lambda_{11}, \Lambda_{12}, \Lambda_{21}, \Lambda_{22}$ for binary Ne(1)/Ar(2) mixtures in MFI zeolite at 300 K. Two different MD campaigns were conducted: (i) equimolar $q_1 = q_2$ mixtures, and (ii) mixtures for which $\Theta_t = \Theta_1 + \Theta_2$ = 12.5 uc^{-1}. In (e, f) the M-S diffusivities, $Đ_1, Đ_2$, and self-diffusivities, $D_{1,self}, D_{2,self}$, are plotted as a function of the occupancy θ.

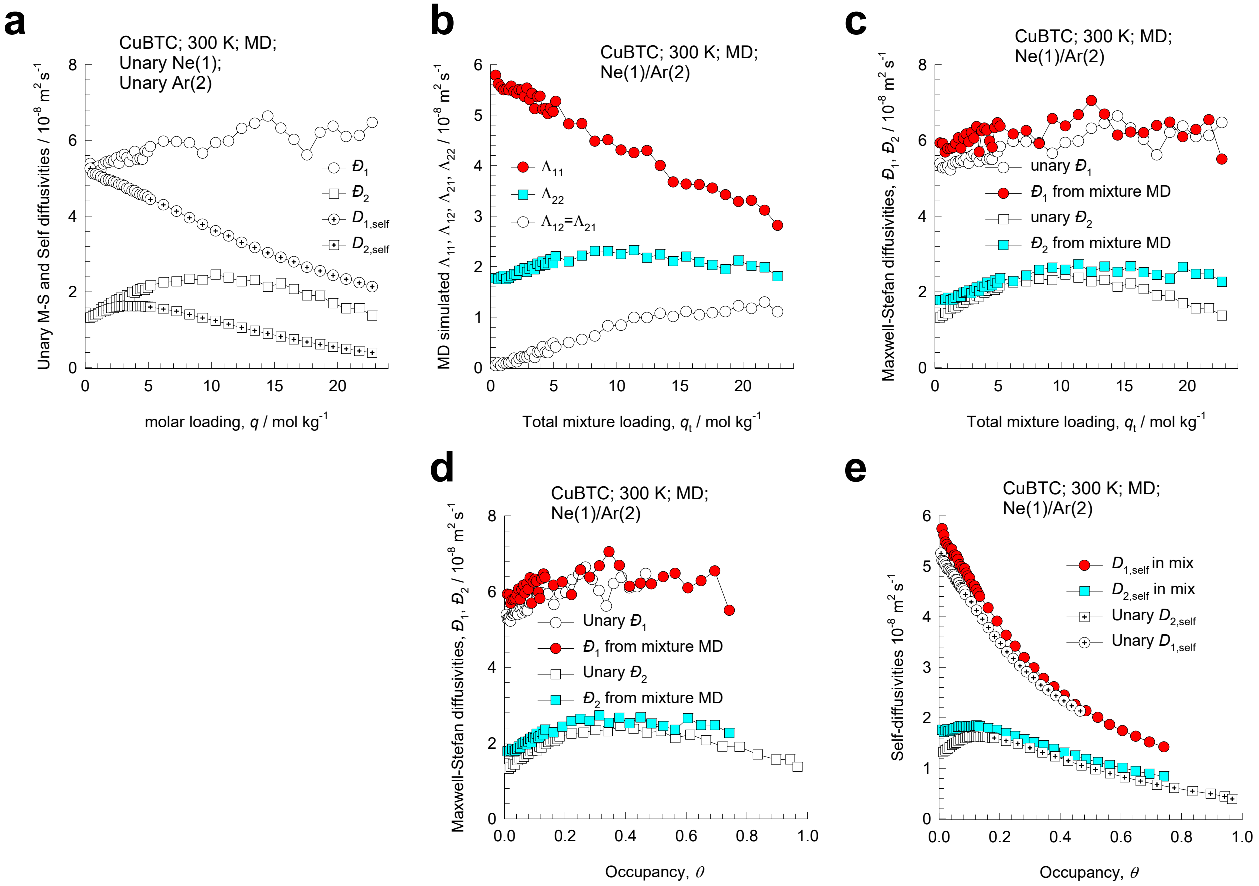

Figure S11. MD simulated values of the M-S diffusivities, $Đ_1, Đ_2$, self-diffusivities, $D_{1,self}, D_{2,self}$, and $\Lambda_{11}, \Lambda_{12} = \Lambda_{21}, \Lambda_{22}$ for equimolar binary $q_1 = q_2$ Ne(1)/Ar(2) mixtures in CuBTC at 300 K. In (d, e) the M-S diffusivities, $Đ_1, Đ_2$, and self-diffusivities, $D_{1,self}, D_{2,self}$, are plotted as a function of the occupancy θ.

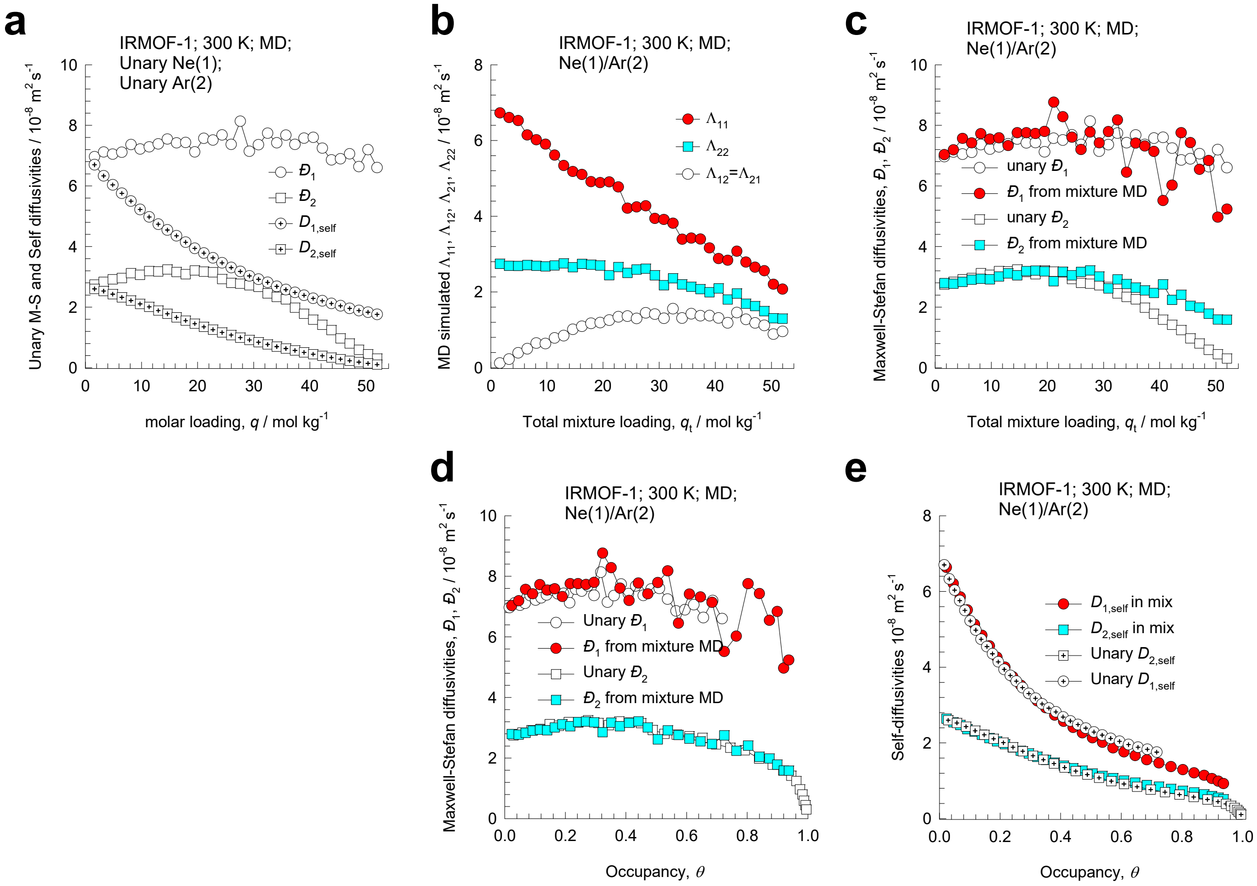

Figure S12. MD simulated values of the M-S diffusivities, $Đ_1, Đ_2$, self-diffusivities, $D_{1,self}, D_{2,self}$, and $\Lambda_{11}, \Lambda_{12} = \Lambda_{21}, \Lambda_{22}$ for equimolar binary $q_1 = q_2$ Ne(1)/Ar(2) mixtures in IRMOF-1 at 300 K. In (d, e) the M-S diffusivities, $Đ_1, Đ_2$, and self-diffusivities, $D_{1,self}, D_{2,self}$, are plotted as a function of the occupancy θ.

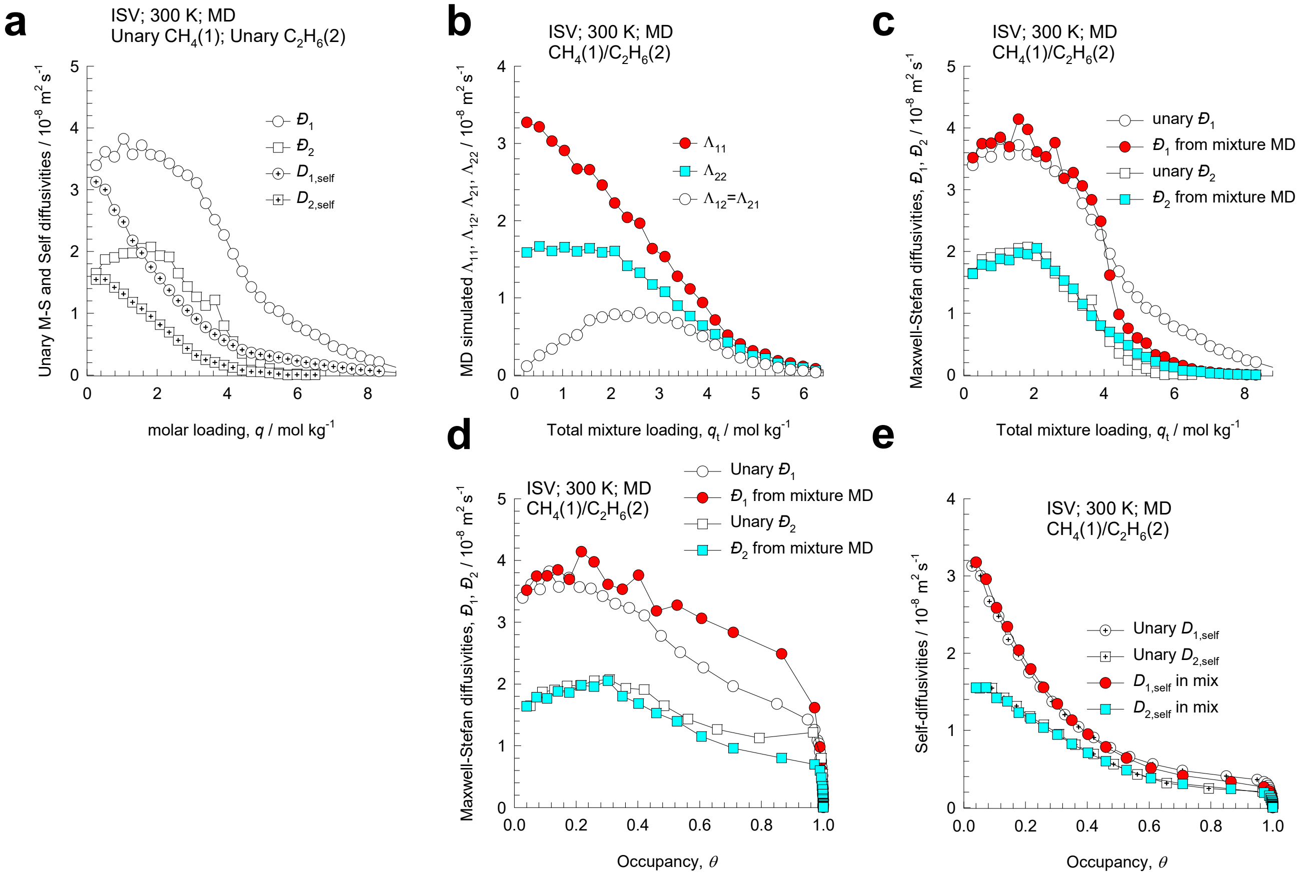

Figure S13. MD simulated values of the M-S diffusivities, $Đ_1,Đ_2$, self-diffusivities, $D_{1,self},D_{2,self}$, and $\Lambda_{11},\Lambda_{12}=\Lambda_{21},\Lambda_{22}$ for equimolar binary $q_1=q_2$ CH4(1)/C2H6(2) mixtures in ISV zeolite at 300 K. In (d, e) the M-S diffusivities, $Đ_1,Đ_2$, and self-diffusivities, $D_{1,self},D_{2,self}$, are plotted as a function of the occupancy θ.

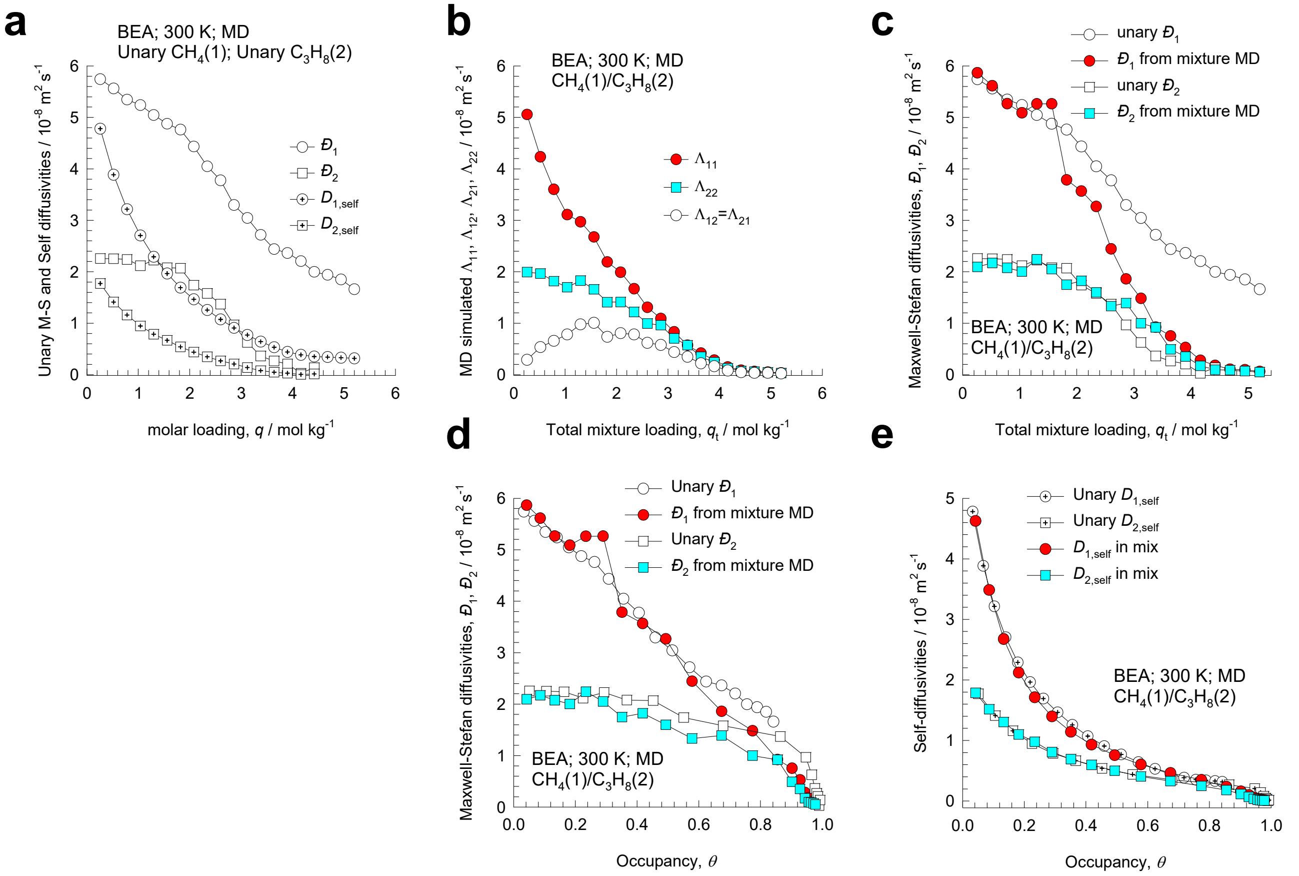

Figure S14. MD simulated values of the M-S diffusivities, $Đ_1, Đ_2$, self-diffusivities, $D_{1,self}, D_{2,self}$, and $\Lambda_{11}, \Lambda_{12} = \Lambda_{21}, \Lambda_{22}$ for equimolar binary $q_1 = q_2$ CH4(1)/C3H8(2) mixtures in BEA zeolite at 300 K. In (d, e) the M-S diffusivities, $Đ_1, Đ_2$, and self-diffusivities, $D_{1,self}, D_{2,self}$, are plotted as a function of the occupancy θ.

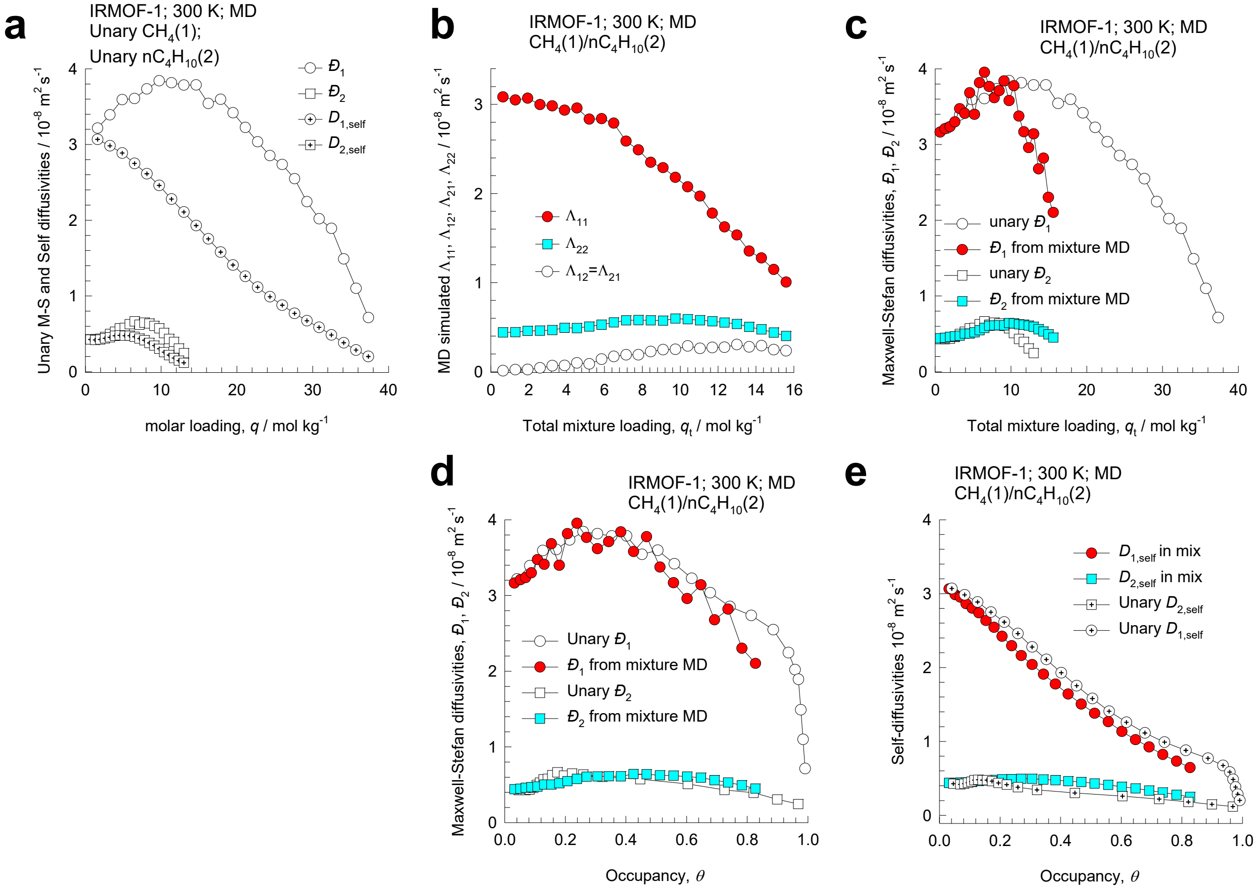

Figure S15. MD simulated values of the M-S diffusivities, $Ð_1,Ð_2$, self-diffusivities, $D_{1,self},D_{2,self}$, and $\Lambda_{11},\Lambda_{12}=\Lambda_{21},\Lambda_{22}$ for equimolar binary $q_1=q_2$ CH4(1)/nC4H10(2) mixtures in IRMOF-1 at 300 K. In (d, e) the M-S diffusivities, $Ð_1,Ð_2$, and self-diffusivities, $D_{1,self},D_{2,self}$, are plotted as a function of the occupancy θ.

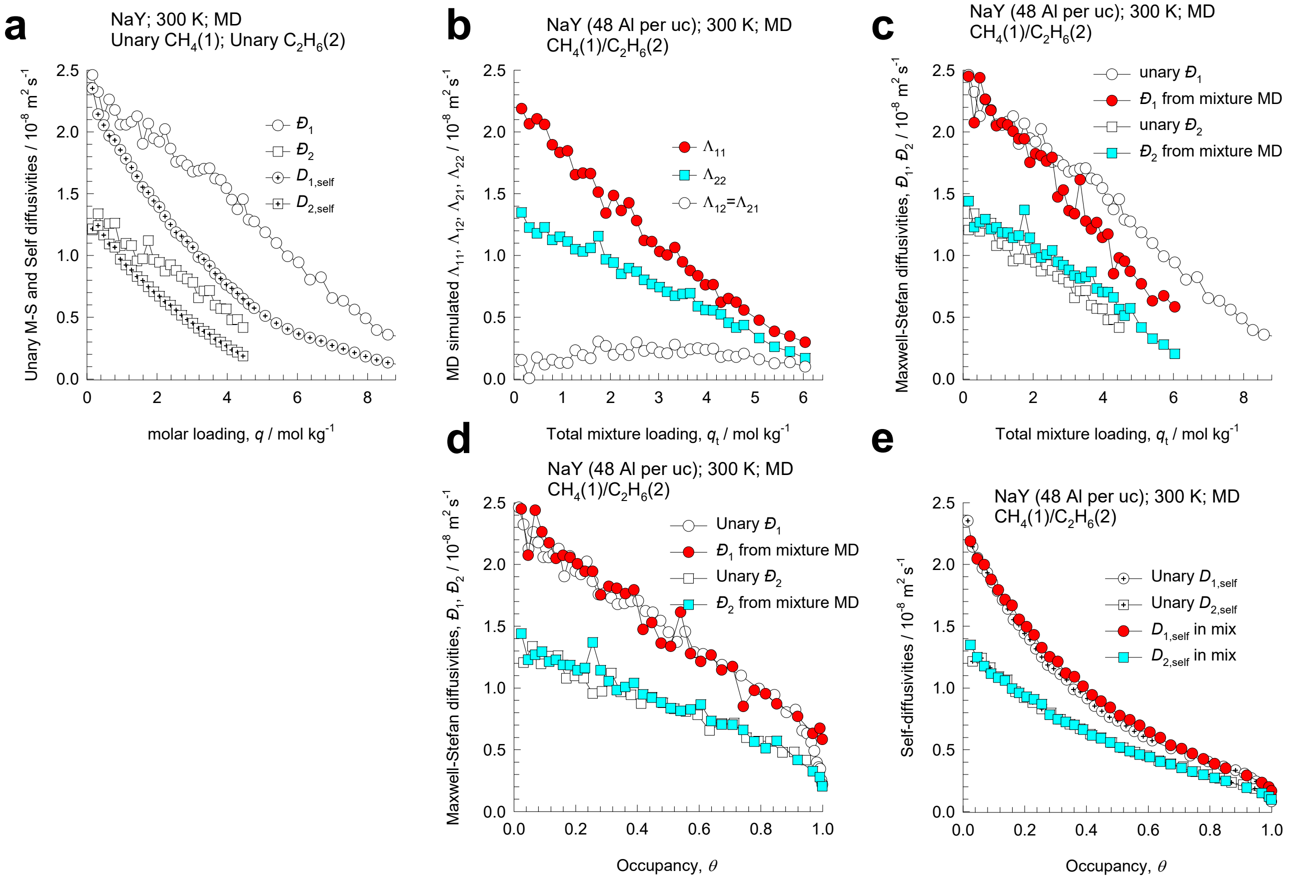

Figure S16. MD simulated values of the M-S diffusivities, $Đ_1, Đ_2$, self-diffusivities, $D_{1,self}, D_{2,self}$, and $\Lambda_{11}, \Lambda_{12} = \Lambda_{21}, \Lambda_{22}$ for equimolar binary $q_1 = q_2$ CH$_4$(1)/C$_2$H$_6$(2) mixtures in NaY zeolite at 300 K. In (d, e) the M-S diffusivities, $Đ_1, Đ_2$, and self-diffusivities, $D_{1,self}, D_{2,self}$, are plotted as a function of the occupancy θ.

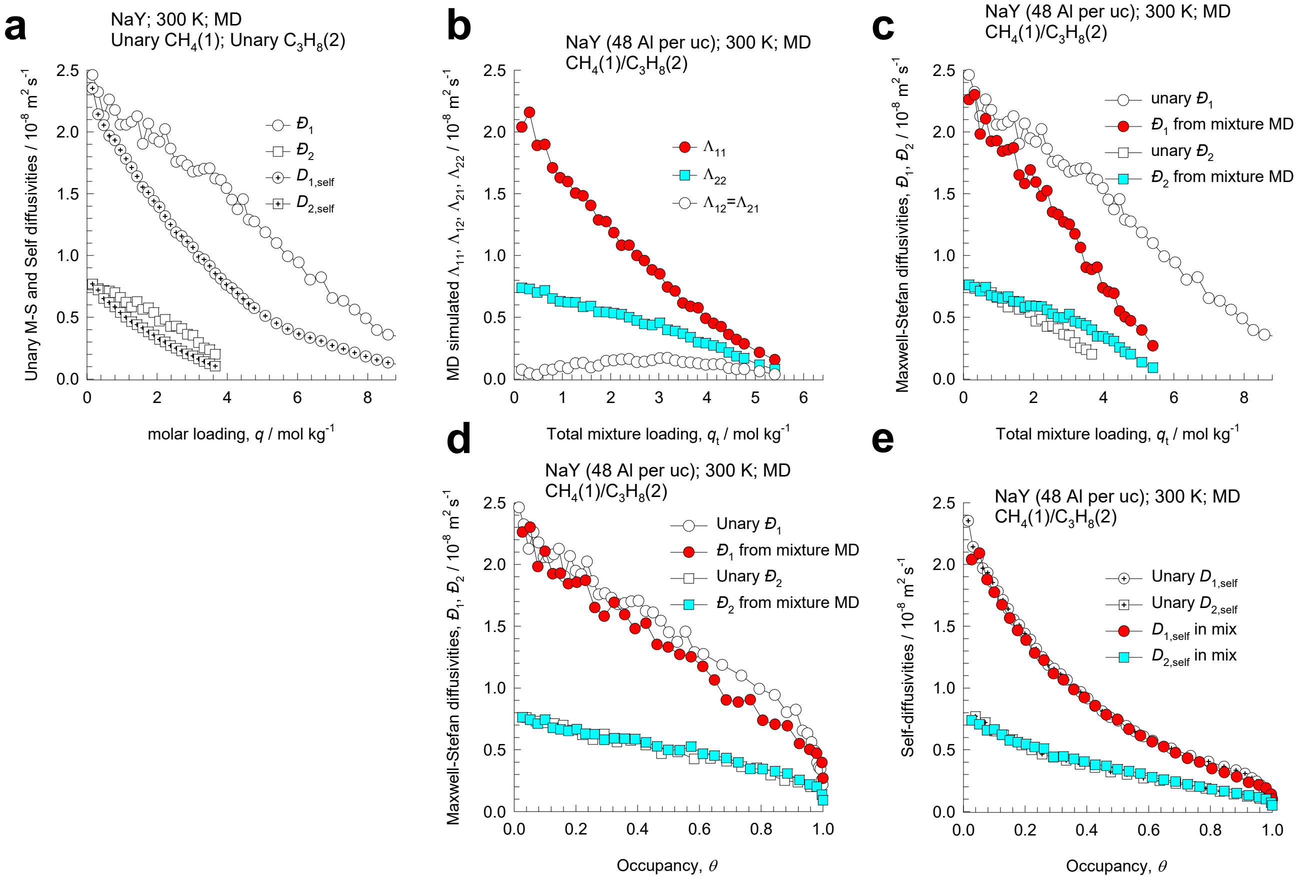

Figure S17. MD simulated values of the M-S diffusivities, $Đ_1,Đ_2$, self-diffusivities, $D_{1,self},D_{2,self}$, and $\Lambda_{11},\Lambda_{12}=\Lambda_{21},\Lambda_{22}$ for equimolar binary $q_1 = q_2$ $CH_4(1)/C_3H_8(2)$ mixtures in NaY zeolite at 300 K. In (d, e) the M-S diffusivities, $Đ_1,Đ_2$, and self-diffusivities, $D_{1,self},D_{2,self}$, are plotted as a function of the occupancy θ.

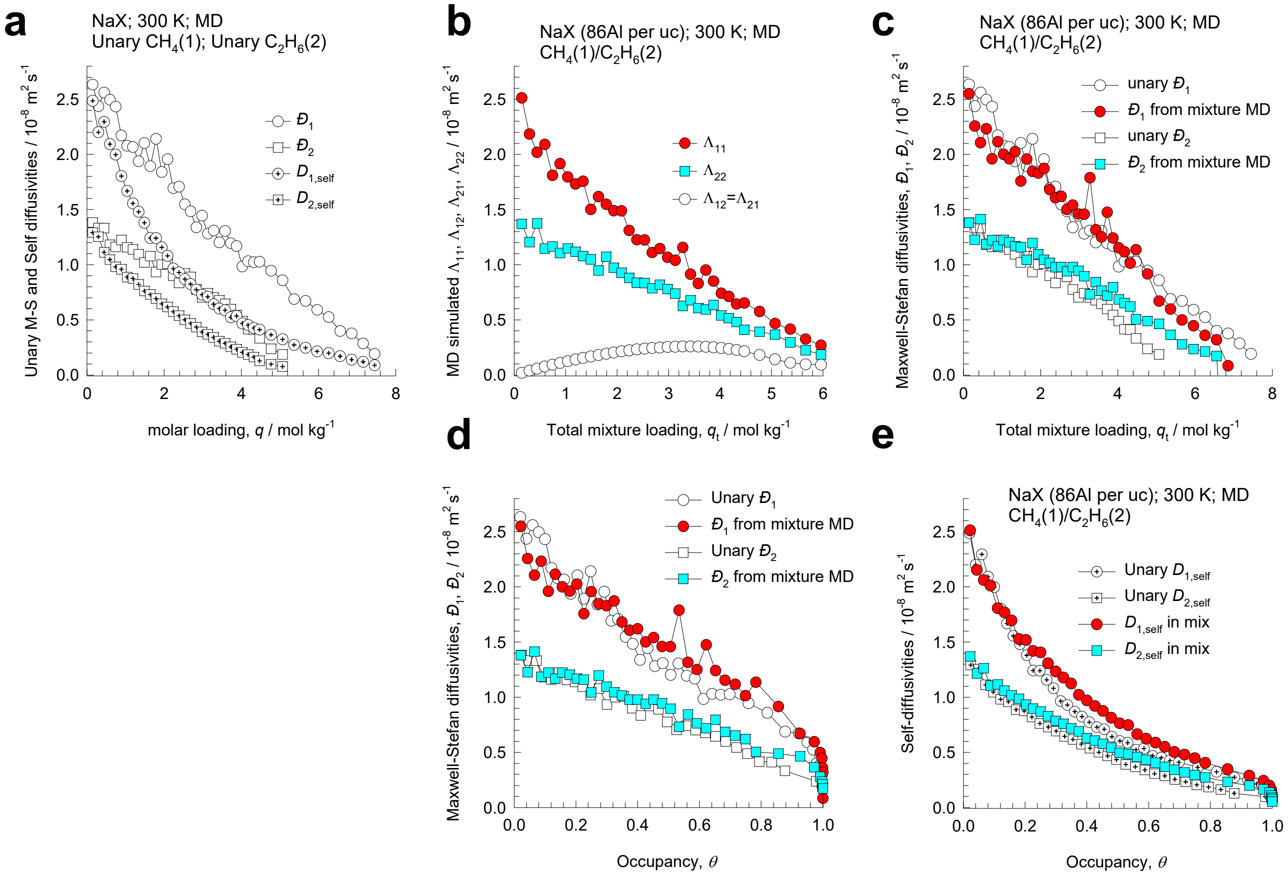

Figure S18. MD simulated values of the M-S diffusivities, $Đ_1, Đ_2$, self-diffusivities, $D_{1,self}, D_{2,self}$, and $\Lambda_{11}, \Lambda_{12} = \Lambda_{21}, \Lambda_{22}$ for equimolar binary $q_1 = q_2$ CH4(1)/C2H6(2) mixtures in NaX zeolite at 300 K. In (d, e) the M-S diffusivities, $Đ_1, Đ_2$, and self-diffusivities, $D_{1,self}, D_{2,self}$, are plotted as a function of the occupancy θ.

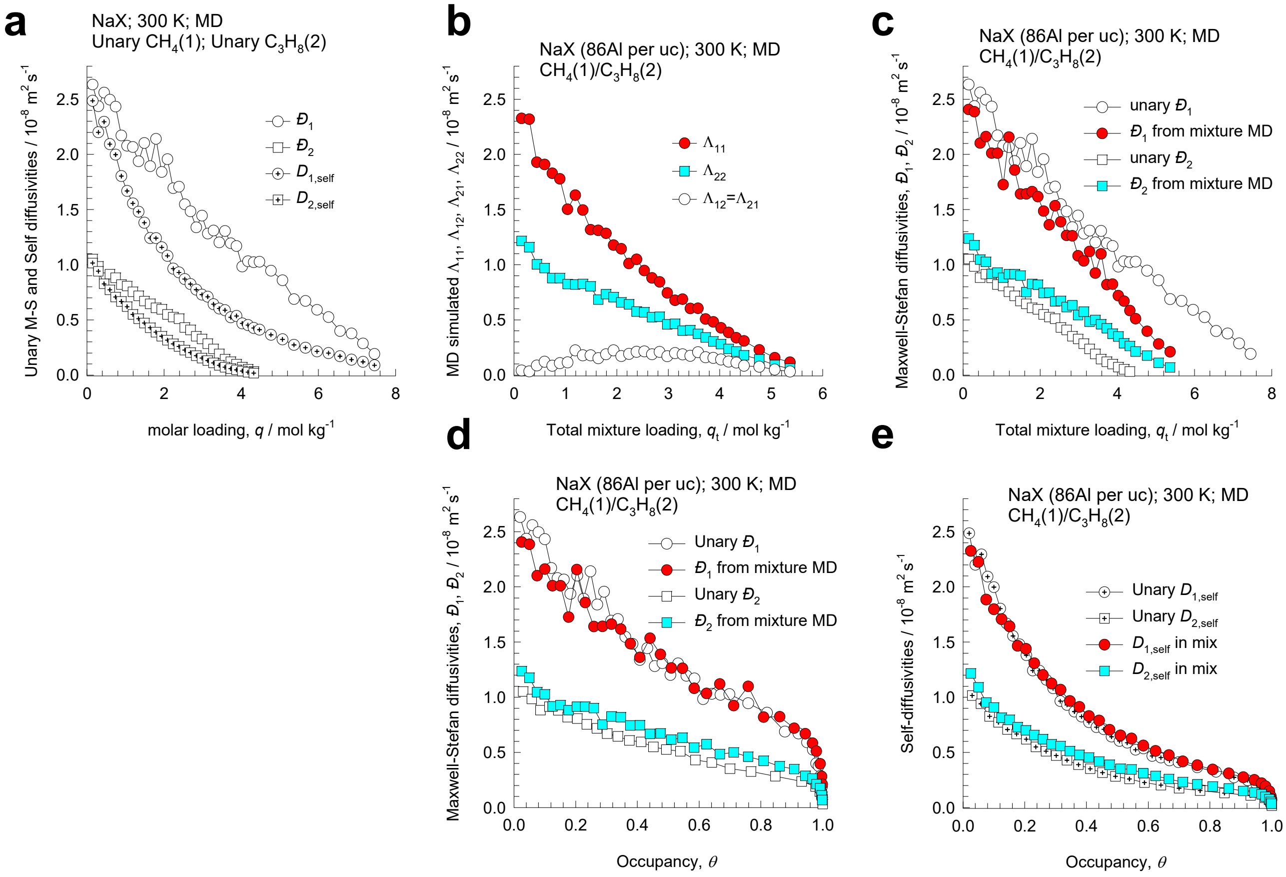

Figure S19. MD simulated values of the M-S diffusivities, $Đ_1,Đ_2$, self-diffusivities, $D_{1,self},D_{2,self}$, and $\Lambda_{11},\Lambda_{12}=\Lambda_{21},\Lambda_{22}$ for equimolar binary $q_1=q_2$ CH4(1)/C3H8(2) mixtures in NaX zeolite at 300 K. In (d, e) the M-S diffusivities, $Đ_1,Đ_2$, and self-diffusivities, $D_{1,self},D_{2,self}$, are plotted as a function of the occupancy θ.

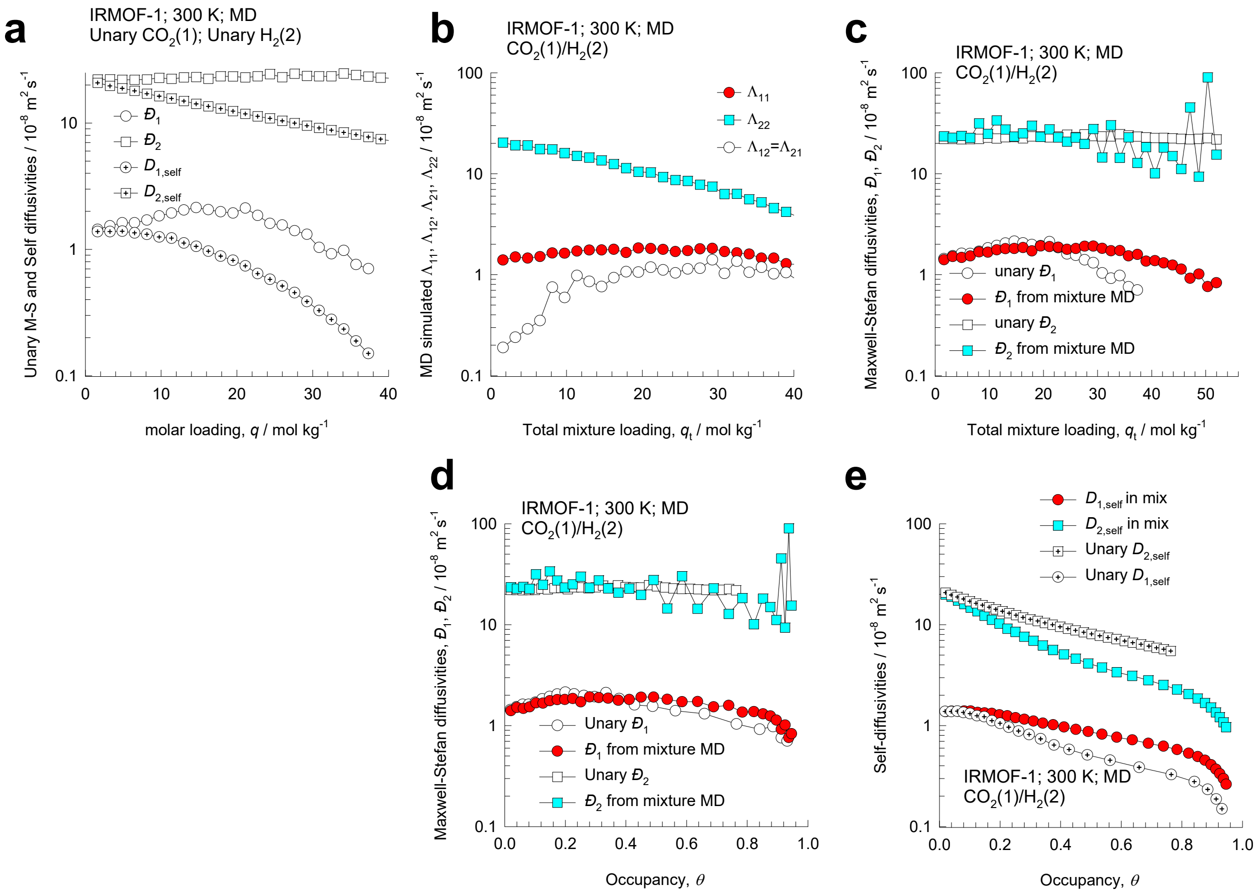

Figure S20. MD simulated values of the M-S diffusivities, $Đ_1, Đ_2$, self-diffusivities, $D_{1,self}, D_{2,self}$, and $\Lambda_{11}, \Lambda_{12} = \Lambda_{21}, \Lambda_{22}$ for equimolar binary $q_1 = q_2$ CO2(1)/H2(2) mixtures in IRMOF-1 at 300 K. In (d, e) the M-S diffusivities, $Đ_1, Đ_2$, and self-diffusivities, $D_{1,self}, D_{2,self}$, are plotted as a function of the occupancy θ.

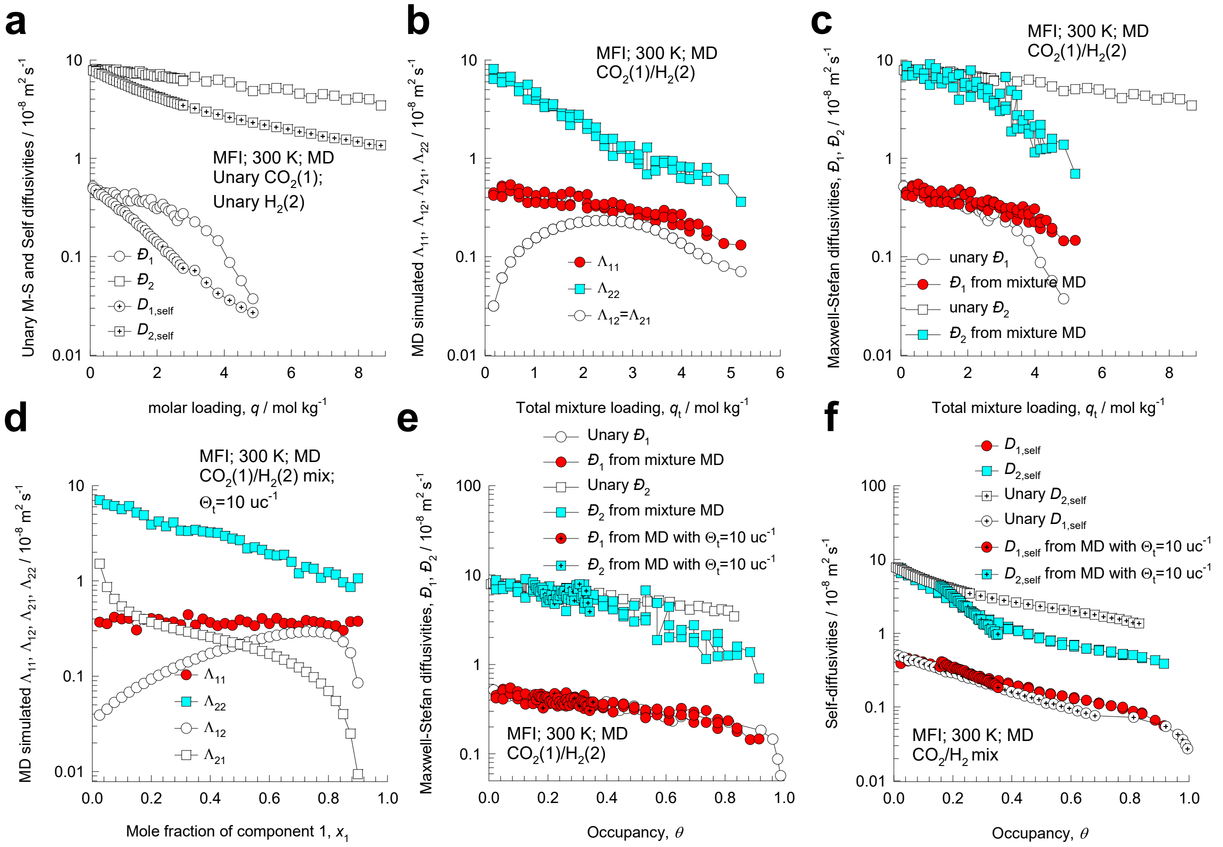

Figure S21. MD simulated values of the M-S diffusivities, $Đ_1,Đ_2$, self-diffusivities, $D_{1,self},D_{2,self}$, and $\Lambda_{11},\Lambda_{12},\Lambda_{21},\Lambda_{22}$ for binary $CO_2(1)/H_2(2)$ mixtures in MFI zeolite at 300 K. Two different MD campaigns were conducted: (i) equimolar $q_1 = q_2$ mixtures, and (ii) mixtures for which $\Theta_t = \Theta_1 + \Theta_2 = 10$ uc^{-1}. In (e, f) the M-S diffusivities, $Đ_1,Đ_2$, and self-diffusivities, $D_{1,self},D_{2,self}$, are plotted as a function of the occupancy θ.

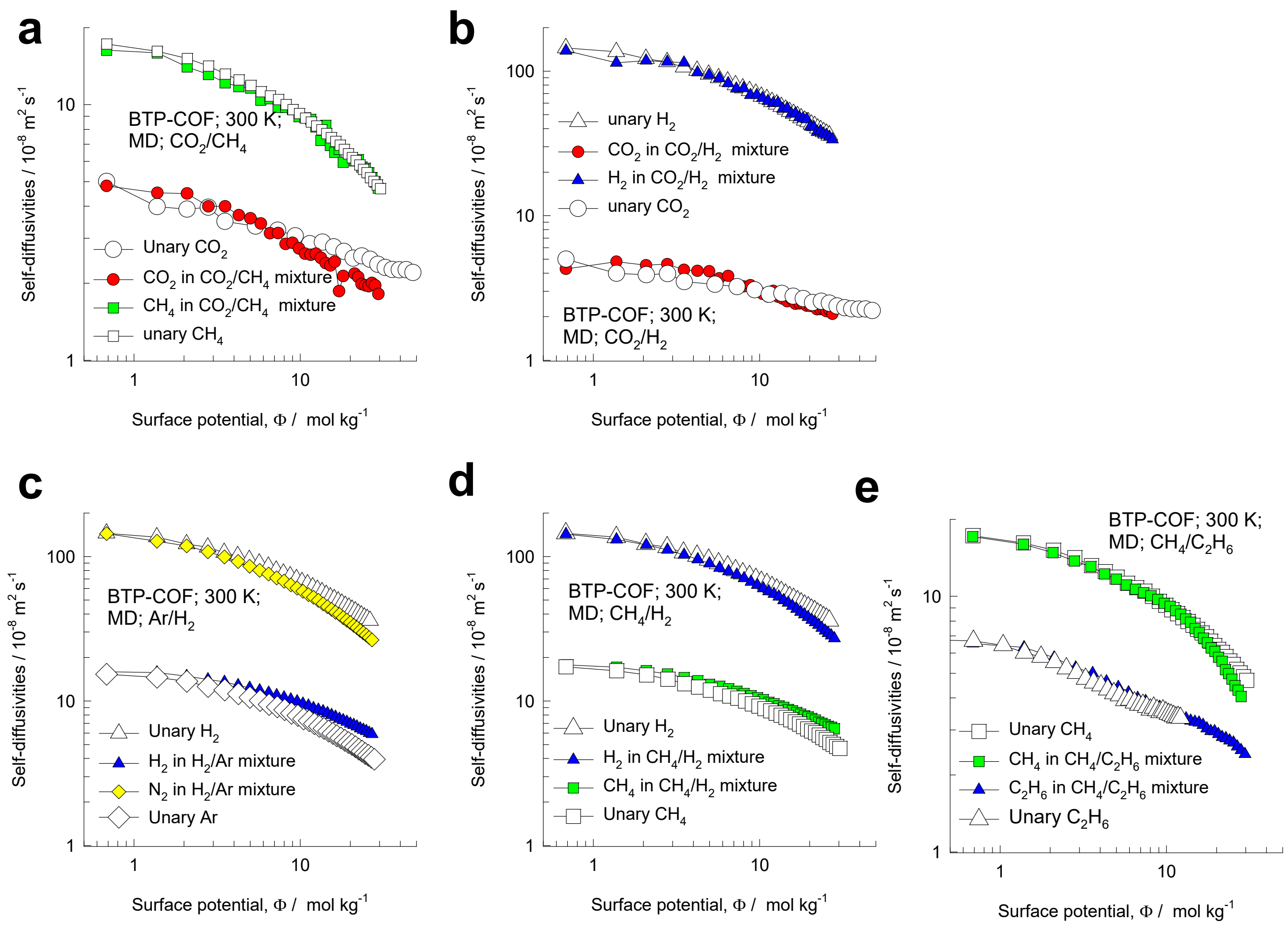

Figure S22. MD simulations of the self-diffusivities, $D_{i,self}$, of components in equimolar ($q_1=q_2$) binary (a) CO_2/CH_4, (b) CO_2/H_2, (c) Ar/H_2, (d) CH_4/H_2, and (e) CH_4/C_2H_6 mixtures in BTP-COF at 300 K, plotted as a function of the surface potential, Φ. Also plotted are the corresponding values of the unary self-diffusivities.

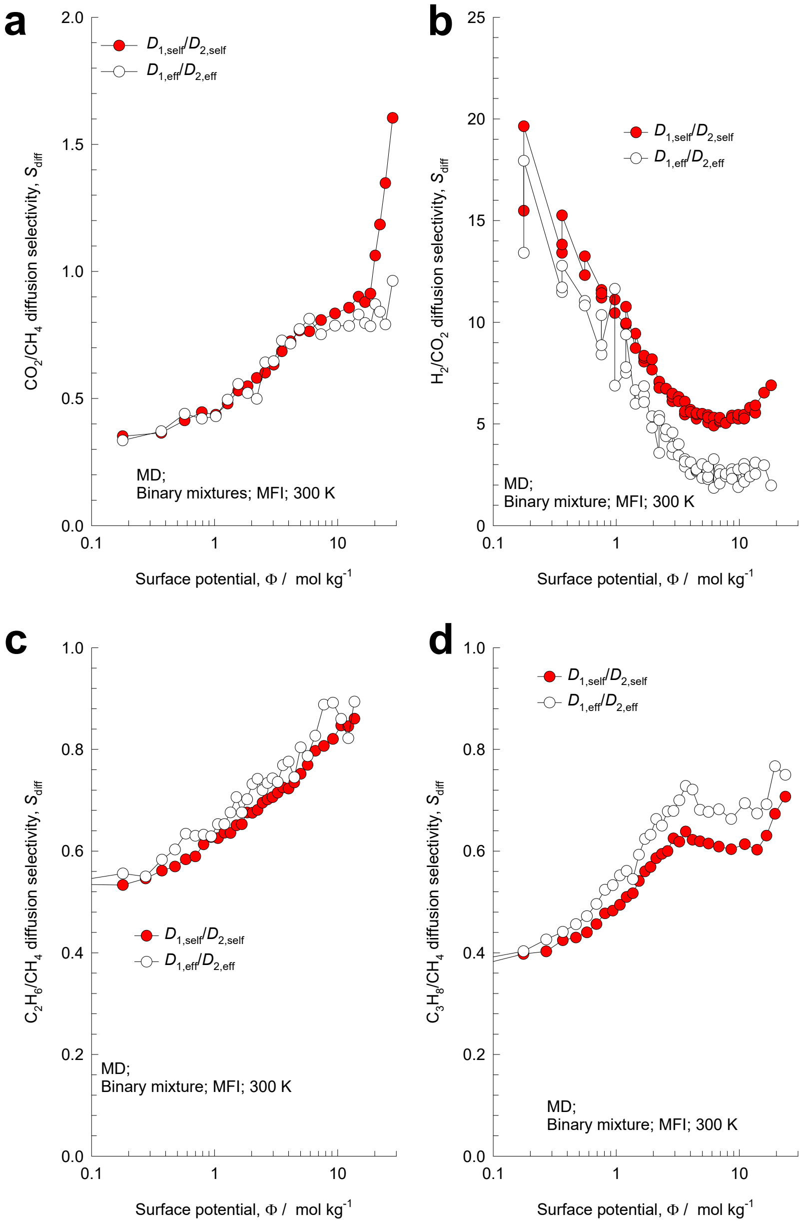

Figure S23. MD simulations of (a) CO_2/CH_4, (b) H_2/CO_2, (c) C_2H_6/CH_4, and (d) C_3H_8/CH_4 diffusion selectivities, S_{diff}, for mixtures determined from equimolar binary $\left(q_1 = q_2\right)$ mixtures in MFI zeolite at 300 K, plotted as function of the surface potential Φ.

7 Adsorption, Diffusion, Permeation in CHA zeolite

CHA zeolite consists of cages of volume 316 Å^3, separated by 3.8 Å × 4.2 Å 8-ring windows; the pore landscape and structural details are provided in Figure S24, and Figure S25. SAPO-34 has the same structural topology of CHA zeolite.

CBMC simulations of the unary isotherms of CO_2, CH_4, N_2 and H_2 were fitted with the dual-site Langmuir-Freundlich model, eq (S8); the fit parameters for each guest molecule (with sites A, and B) are tabulated for each guest in Table S3.

7.1 Dependence of adsorption selectivitities on Φ

Figure S26a shows CBMC simulation data[63] of the adsorption selectivity, S_{ads}, for CO_2(1)/CH_4(2) mixtures in CHA zeolite at 300 K, determined from three different campaigns:

(i) the bulk gas phase mole fractions are maintained at $y_1 = y_2 = 0.5$, and the total mixture fugacity $f_t = f_1 + f_2$ is varied upto f_t = 10 MPa at which pore saturation conditions are approached,

(ii) the bulk gas phase mole fractions are maintained at $y_1 = 0.20$, and the total mixture fugacity $f_t = f_1 + f_2$ is varied up to f_t = 10 MPa at which pore saturation conditions are approached,

(iii) the total bulk gas mixture fugacity is held constant, $f_t = f_1 + f_2 = 10^6$ Pa, and the mole fraction of the bulk gas mixture of CO_2(1), y_1, is varied from 0 to 1.

For all three CBMC data sets, the CBMC simulated values of the adsorption selectivity, S_{ads}, follows a near-unique dependence on the surface potential Φ, as anticipated by the IAST development; see Figure S26a. A further important point to note is that for the adsorption selectivity as defined in eq (S13) for component 1 with respect to component 2, also holds for the same guest components in the presence of other guest species, 3, 4, 5, ..etc. Eq (S6) implies that if the comparisons are made at the same surface potential Φ, the value of S_{ads} for component 1 with respect to component 2, remains the same irrespective of the presence of additional guest components in the same host.

To confirm this anticipation, CBMC simulations were also performed for (a) 20/40/40 $CO_2/CH_4/N_2$, (b) 10/20/70 $CO_2/CH_4/H_2$, and (c) quaternary 1/1/1/1 $CO_2/CH_4/N_2/H_2$ mixtures in CHA zeolite at 300 K, in which the bulk gas phase mole fractions are maintained constant and the total mixture fugacity $f_t = f_1 + f_2 + f_3$ is varied up to $f_t = 10$ MPa. The values of the CO_2/CH_4 adsorption selectivity in the two ternary mixtures are also plotted (indicated by crosses, and plusses) in Figure S26a. The ternary and quaternary CBMC data sets follow the same unique dependence on Φ. Put another way, the presence of component 3 and/or component 4 in the ternary and quaternary mixtures have no influence of the adsorption selectivity for the 1-2 pair.

Figure S27a plots data obtained from CBMC simulations of the CO_2/N_2 adsorption selectivities in binary (15/85 CO_2/N_2, and 20/80 CO_2/N_2), ternary (20/40/40 $CO_2/CH_4/N_2$), and quaternary 1/1/1/1 $CO_2/CH_4/N_2/H_2$ mixtures in CHA zeolite at 300 K. The CO_2/N_2 adsorption selectivities for binary, ternary and quaternary mixtures display unique dependence on Φ.

The IAST calculations of the adsorption selectivity (indicated by dashed lines in Figure S26a and Figure S27a) show some deviations from the CBMC simulated data due to non-idealities caused by preferential perching of CO_2 at the window regions; detailed explanations are provided in our earlier works.[28, 40, 63, 67] With the introduction of activity coefficients, the expression for the adsorption selectivity for the $CO_2(1)/CH_4(2)$ and $CO_2(1)/N_2(2)$ pairs in binary, ternary, and quaternary mixtures is

$$S_{ads,12} = \frac{q_1/q_2}{f_1/f_2} = \frac{x_1/f_1}{x_2/f_2} = \frac{P_2^0\gamma_2}{P_1^0\gamma_1} \tag{S79}$$

Using the CBMC data for binary and ternary mixture adsorption, the activity coefficients of $CO_2(1)/CH_4(2)$ and $CO_2(1)/N_2(2)$ pairs were determined for both binary and ternary mixtures. Figure S26b, and Figure S27b plot the ratio of the activity coefficient of component (1) to that of component (2), $\frac{\gamma_1}{\gamma_2}$, as a function of Φ. We note that $\frac{\gamma_1}{\gamma_2}$ for binary, ternary, and quaternary mixtures are of comparable magnitudes when plotted as a function of Φ. For this reason, the CO_2(1)/CH_4(2) and CO_2(1)/N_2(2) pairs adsorption selectivity shows a unique dependence on Φ, despite the small deviations of IAST estimates from CBMC data.

Figure S28a plots data obtained from CBMC simulations of the CO_2/H_2 adsorption selectivities in binary (15/85 CO_2/H_2, and 10/90 CO_2/H_2), ternary (10/20/70 CO_2/CH_4/H_2), and quaternary 1/1/1/1 CO_2/CH_4/N_2/H_2 mixtures in CHA zeolite at 300 K. The CO_2/H_2 adsorption selectivities for binary, ternary and quaternary mixtures display unique dependence on Φ.

Figure S28b plots data obtained from CBMC simulations of the CH_4/H_2 adsorption selectivities in binary (50/50 CH_4/H_2, and 20/80 CH_4/H_2), ternary (10/20/70 CO_2/CH_4/H_2), and quaternary 1/1/1/1 CO_2/CH_4/N_2/H_2 mixtures in CHA zeolite at 300 K. The CH_4/H_2 adsorption selectivities for binary, ternary and quaternary mixtures display unique dependence on Φ.

Figure S29 plots data obtained from CBMC simulations of the CH_4/N_2 adsorption selectivities in binary (20/80 CH_4/N_2), ternary (20/40/40 CO_2/CH_4/N_2), and quaternary 1/1/1/1 CO_2/CH_4/N_2/H_2 mixtures in CHA zeolite at 300 K. The CH_4/N_2 adsorption selectivities for binary, ternary and quaternary mixtures display unique dependence on Φ.

7.2 Diffusion and permeation selectivities of binary pairs

MD simulations were performed to determine the self-diffusivities $D_{i,self}$ in equimolar binary $\left(q_1 = q_2\right)$ CO_2/CH_4, CO_2/N_2 and CH_4/N_2 mixtures and equimolar ternary $\left(q_1 = q_2 = q_3\right)$ CO_2/CH_4/N_2 mixtures. In a few cases, the MD simulations were performed for mixtures in which the total loading $q_t = q_1 + q_2$ was held constant and the mole fraction of the adsorbed phase mixture, $x_1 = \frac{q_1}{q_1 + q_2}$ was varied from 0 to 1. All MD simulations reported in this work were conducted at a temperature T = 300 K.

Let us consider MD simulation data on self-diffusivities $D_{i,self}$ for binary CO_2/CH_4 mixtures in CHA zeolite at 300 K. For this mixture, four different MD simulation campaigns were conducted as follows:

(i) equimolar ($q_1 = q_2; \quad x_1 = 1 - x_2 = 0.5$) mixtures with varying total load, $q_t = q_1 + q_2$; indicated by green squares

(ii) mixtures at constant load $q_t = 5.78$ mol kg^{-1} ($\Theta_t =$ 25 molecules uc^{-1}) and varying mole fraction of CO2 in the adsorbed phase, $x_1 = q_1/q_t$; indicate by red circles,

(iii) mixtures at constant load $q_t = 2.89$ mol kg^{-1} ($\Theta_t =$ 12.5 molecules uc^{-1}) and varying mole fraction of CO2 in the adsorbed phase, $x_1 = q_1/q_t$; indicated by inverted pink triangles, and

(iv) mixtures in which the CH4 load $q_2 = 0.693$ mol kg^{-1} ($\Theta_2 =$ 3 molecules uc^{-1}) and loadings of CO2, q_1 are varied; indicated by blue triangles.

In Figure S30a the $S_{diff} = \frac{D_{1,self}}{D_{2,self}}$ data for campaign (i) are plotted as function of $q_t = q_1 + q_2$. The diffusion selectivities decrease strongly with increasing total loading. In Figure S30b the $S_{diff} = \frac{D_{1,self}}{D_{2,self}}$ data for campaigns (ii), (iii), and (iv) are plotted as function of the mole fraction of CO2 in the adsorbed phase, $x_1 = q_1/q_t$. The diffusion selectivities are also influenced by the mixture composition.

All four MD campaigns for $S_{diff} = \frac{D_{1,self}}{D_{2,self}}$ are plotted in Figure S30c as function of the total mixture loading $q_t = q_1 + q_2$; we note that the diffusion selectivity is not a unique function of $q_t = q_1 + q_2$.

The four sets of MD data on diffusion selectivities are plotted in Figure S30d as function of the surface potential, Φ, indicating that Φ uniquely determines the diffusion selectivity.

Additionally, we also performed MD simulations to determine the self-diffusivites $D_{i,self}$ for equimolar $\left(q_1 = q_2 = q_3\right)$ ternary CO2/CH4/N2, and CO2/CH4/H2 mixtures in CHA zeolite at 300 K. The CO2/CH4 diffusion selectivities, S_{diff}, determined for the binary pair in the *ternary* mixtures follow the same unique dependence on Φ, as for the four different binary mixture campaigns (indicated by red circles) discussed in the foregoing paragraphs; see Figure S31a.

We should expect the permeation selectivity $S_{perm} = \frac{D_{1,self} q_1 / f_1}{D_{2,self} q_2 / f_2} = S_{ads} \times S_{diff}$ to be also uniquely dependent on Φ. The plot of S_{perm} vs Φ for the binary and ternary mixture campaigns also show unique dependence on Φ; see Figure S31b.

The unique dependence of adsorption, diffusion, and permeation selectivities on Φ also holds for CO_2/N_2, CO_2/H_2, CH_4/N_2 and CH_4/H_2 mixtures. This is confirmed by the combined CBMC/MD data on (a) diffusion selectivities, S_{diff}, and (b) permeation selectivities, S_{perm}, in different equimolar binary $\left(q_1 = q_2\right)$ binary (CO_2/CH_4, CO_2/N_2, CO_2/H_2, CH_4/N_2, CH_4/H_2) and equimolar $\left(q_1 = q_2 = q_3\right)$ ternary ($CO_2/CH_4/N_2$, $CO_2/CH_4/H_2$, $CO_2/N_2/H_2$) mixtures in CHA zeolite at 300 K that are presented in Figure S32 Figure S33, Figure S34, and Figure S35.

Figure S36a,b summarize the data on the CO_2/CH_4, $CO_2//H_2$, $CO_2//N_2$, and N_2/CH_4 permeation selectivities S_{perm} as function of the surface potential Φ, determined from binary and ternary campaigns.

7.3 MD data on component self-diffusivities

Figure S37 presents MD simulations of the self-diffusivities, $D_{i,self}$, of (a) CO_2, (b) CH_4, (c) N_2 and (d) H_2 in different equimolar $\left(q_1 = q_2\right)$ binary (CO_2/CH_4, CO_2/N_2, CO_2/H_2, CH_4/N_2, CH_4/H_2) and equimolar $\left(q_1 = q_2 = q_3\right)$ ternary ($CO_2/CH_4/N_2$, $CO_2/CH_4/H_2$, $CO_2/N_2/H_2$) mixtures in CHA zeolite at 300 K, plotted as function of the surface potential Φ. The data demonstrate that the component self-diffusivities in binary and ternary mixtures are nearly the same, independent of the partner(s) in the mixtures. Except for H_2, the self-diffusivities in the binary and ternary mixtures are also nearly the same as the unary self-diffusivities. The unary self-diffusivity for H_2, appears to be slightly larger in value for those in mixtures.

7.4 Membrane permeabilities of individual components

For use of the materials in membrane constructs, the permeability of the membrane, Π_i, is defined by

$$\Pi_i = \frac{N_i}{\Delta f_i / \delta} \tag{S80}$$

where N_i is the permeation flux, δ is the thickness of the crystalline layer on the membrane, and $\Delta f_i = f_{i0} - f_{i\delta}$ is the difference in the partial fugacities in the bulk fluid mixtures in the upstream (z = 0) and downstream (z = δ) compartments. If the downstream conditions are such that the loadings are negligibly small, the permeability can be determined from MD simulations by using the following expression[2]

$$\Pi_i = \frac{\rho D_{i,self} q_i}{f_i} \tag{S81}$$

where ρ is the crystal framework density. In SI units, the permeability has the units mol m m^{-2} s^{-1} Pa^{-1}. The more commonly used engineering unit for permeability is the Barrer expressed in cm^3 (STP) cm cm^{-2} s^{-1} (cm Hg)$^{-1}$. To convert to the commonly used engineering units of Barrers we divide the value in mol m m^{-2} s^{-1} Pa^{-1} by 3.348×10^{-16}.

Often in experimental investigations of membrane permeation, the precise thickness of the membrane is not easily determinable and, therefore, the experimental data are presented in terms of the permeances calculated from

$$\frac{N_i}{\Delta f_i} \equiv \frac{\Pi_i}{\delta} \tag{S82}$$

In SI units, the permeance has the units mol m^{-2} s^{-1} Pa^{-1}.

In the MD simulations, the component molar loadings q_i in the binary and ternary mixture are specified, and the partial fugacities in the bulk fluid mixture are not known *a priori*. Also, in this case, the equalities in eq (S9) must be satisfied in conjunction with eq (S11). The entire set of eqs (S4) to (S11) need to be solved numerically to obtain the partial fugacities, f_i of the individual components in the mixture, that yield the same loadings as chosen in the MD simulations. The unary isotherm fits required in the IAST calculations are based on the CBMC simulations of the unary isotherms. The IAST calculations also determine the surface potential Φ. In all of the calculations presented in this article, the set of equations were solved using an Excel macro that was developed for this specific purpose. Combination of the MD data on the self-diffusivities in the mixture, along with IAST calculations of the partial fugacities in the bulk fluid phase mixture, in equilibrium with the adsorbed phase mixture, allows the calculation of the component permeabilities Π_i by use of eq (S81).

Figure S38 presents data on the permeabilities, Π_i, of (a) CO_2, (b) CH_4, (c) N_2 and (d) H_2 in different equimolar binary $\left(q_1 = q_2\right)$ (CO_2/CH_4, CO_2/N_2, CO_2/H_2, CH_4/N_2, CH_4/H_2) and equimolar $\left(q_1 = q_2 = q_3\right)$ ternary ($CO_2/CH_4/N_2$, $CO_2/CH_4/H_2$, $CO_2/N_2/H_2$) mixtures in CHA zeolite at 300 K, plotted as a function of the surface potential Φ. The data demonstrate that the component permeabilities in binary and ternary mixtures are nearly the same, independent of the partner(s) in the mixtures. Except for H_2, the permeabilities in the binary and ternary mixtures are also nearly the same as the unary permeabilities. The unary permeability for H_2, appears to be slightly larger in value for those in mixtures.

7.5 List of Tables for Adsorption, Diffusion, Permeation in CHA zeolite

Table S3. Dual-site Langmuir-Freundlich parameters for unary isotherms of CO_2, CH_4, N_2 and H_2 in CHA (all-silica) at 300 K.

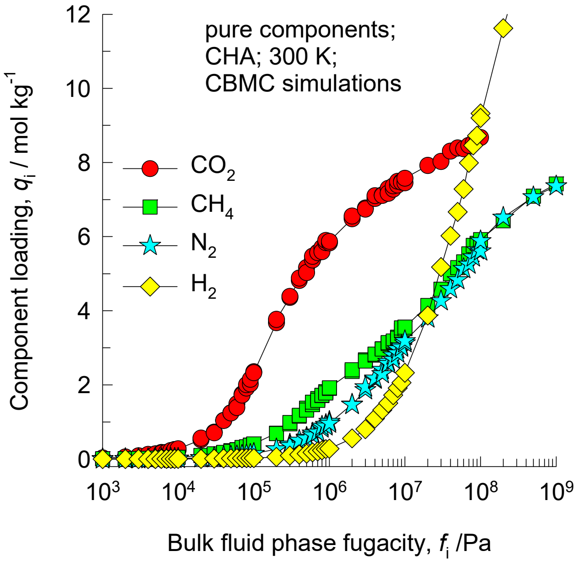

	Site A			Site B		
	$q_{A,sat}$ mol kg^{-1}	b_A $\mathrm{Pa}^{-\nu A}$	ν_A dimensionless	$q_{B,sat}$ mol kg^{-1}	b_B $\mathrm{Pa}^{-\nu B}$	ν_B dimensionless
CO_2	6.8	2.4464E-06	1.06	2.8	5.181E-06	0.7
CH_4	2.7	1.3131E-06	1.02	5.5	2.703E-07	0.84
N_2	5.1	1.019E-07	0.88	2.9	4.013E-07	1
H_2	14.563	2.58E-08	0.73	15.719	1.57E-08	1

7.6 List of Figures for Adsorption, Diffusion, Permeation in CHA zeolite

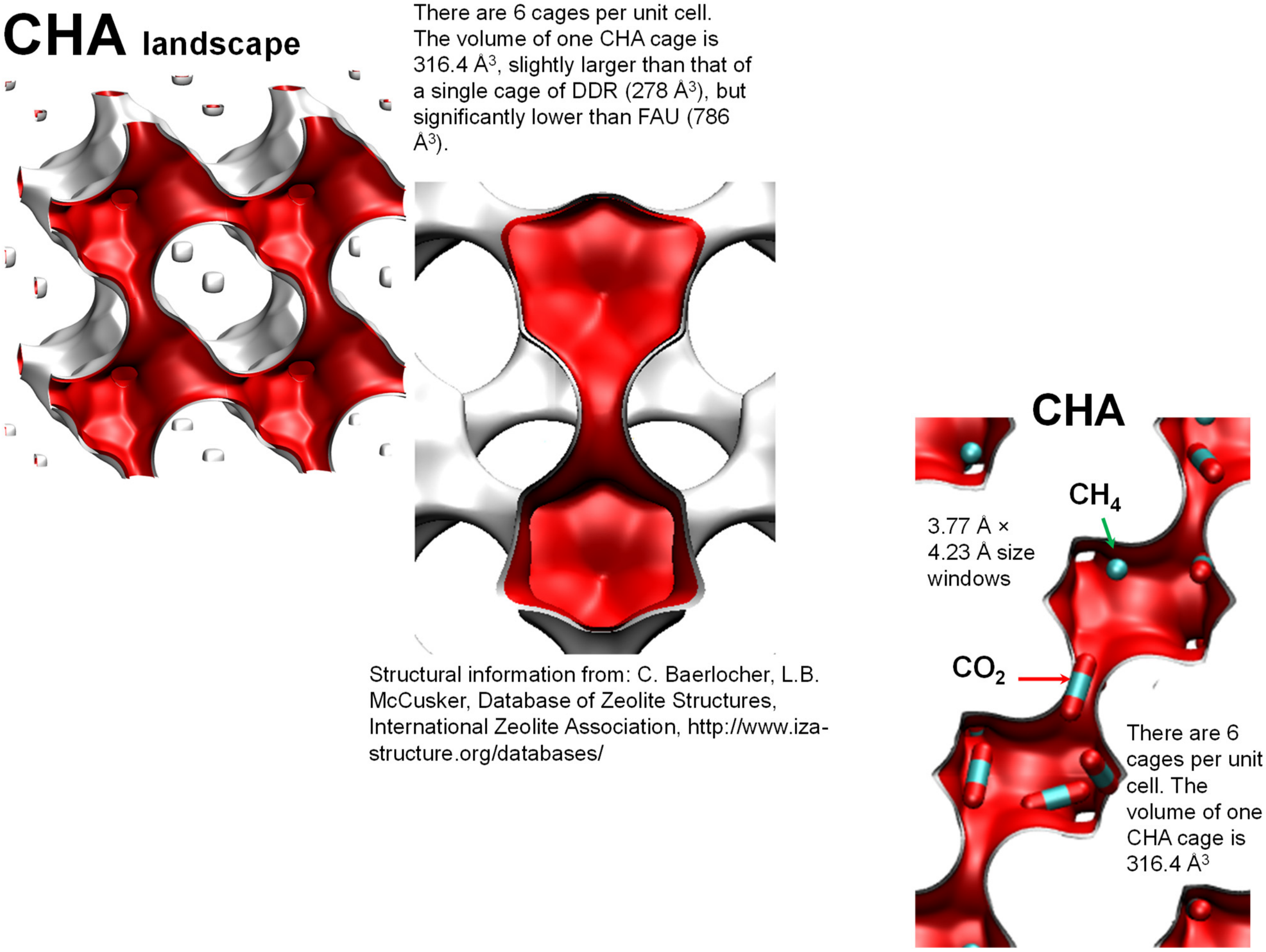

There are 6 cages per unit cell. The volume of one CHA cage is 316.4 Å^3, slightly larger than that of a single cage of DDR (278 Å^3), but significantly lower than FAU (786 Å^3).

Structural information from: C. Baerlocher, L.B. McCusker, Database of Zeolite Structures, International Zeolite Association, http://www.iza-structure.org/databases/

3.77 Å × 4.23 Å size windows

There are 6 cages per unit cell. The volume of one CHA cage is 316.4 Å^3

Figure S24. Pore landscape of all-silica CHA zeolite.

CHA window and pore dimensions

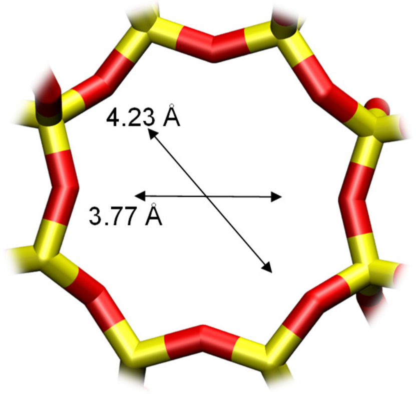

CHA

The window dimensions calculated using the van der Waals diameter of framework atoms = 2.7 Å are indicated above by the arrows.

	CHA
a /Å	15.075
b /Å	23.907
c /Å	13.803
Cell volume / Å^3	4974.574
conversion factor for [molec/uc] to [mol per kg Framework]	0.2312
conversion factor for [molec/uc] to [kmol/m^3]	0.8747
ρ [kg/m3]	1444.1
MW unit cell [g/mol(framework)]	4326.106
ϕ, fractional pore volume	0.382
open space / Å^3/uc	1898.4
Pore volume / cm^3/g	0.264
Surface area /m^2/g	758.0
DeLaunay diameter /Å	3.77

Figure S25. Structural details for CHA zeolite.

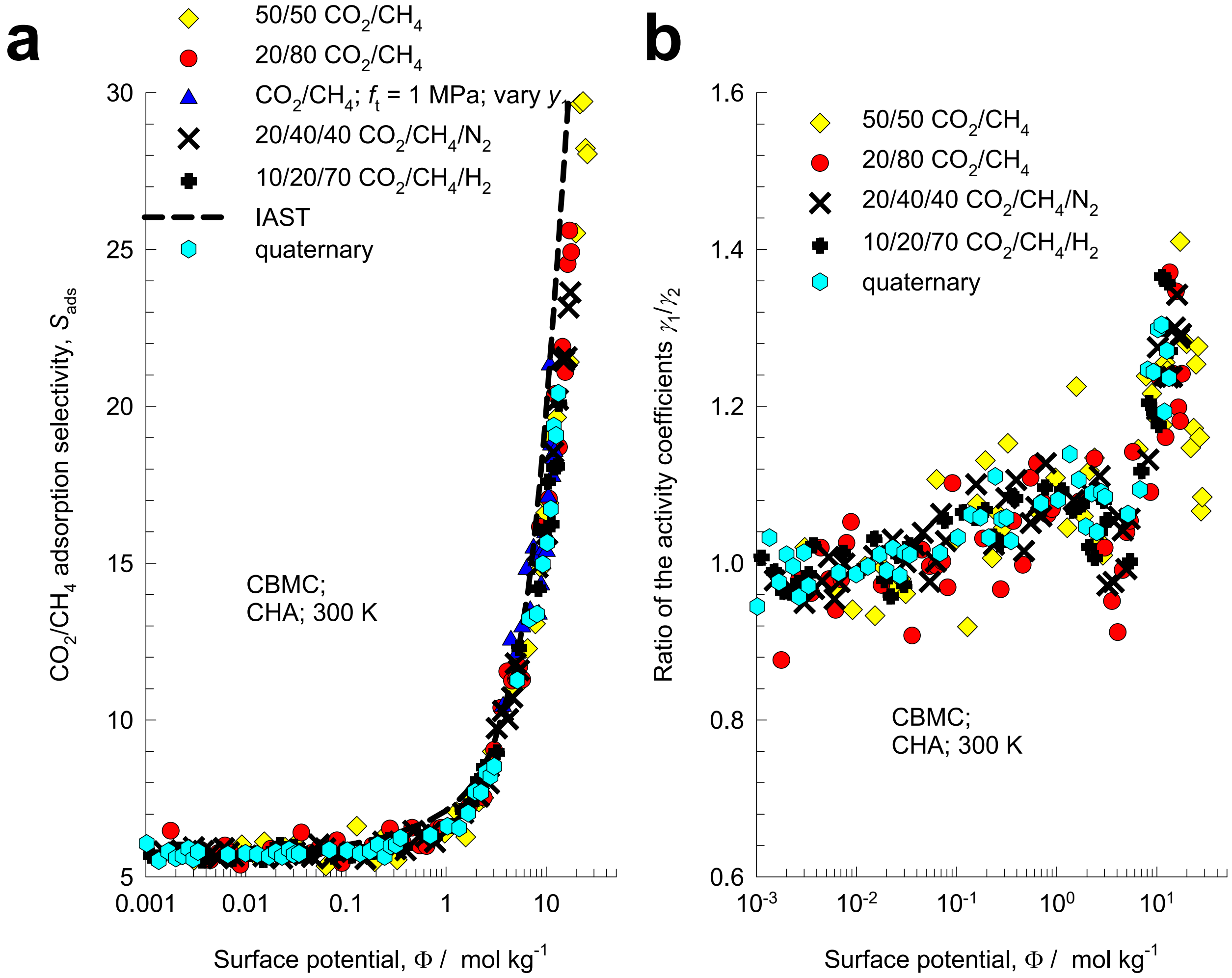

Figure S26. (a) CBMC simulations of CO_2(1)/CH_4(2) adsorption selectivities, S_{ads}, for binary, ternary, and quaternary mixture adsorption in CHA zeolite at 300 K. The selectivities are plotted as function of the surface potential Φ. The dashed lines are the IAST calculations; the unary isotherm fit parameters are provided in Table S3. (b) CBMC simulations of the ratio of activity coefficients of $\frac{\gamma_1}{\gamma_2}$ for binary CO_2(1)/CH_4(2) pair plotted as function of the surface potential Φ.

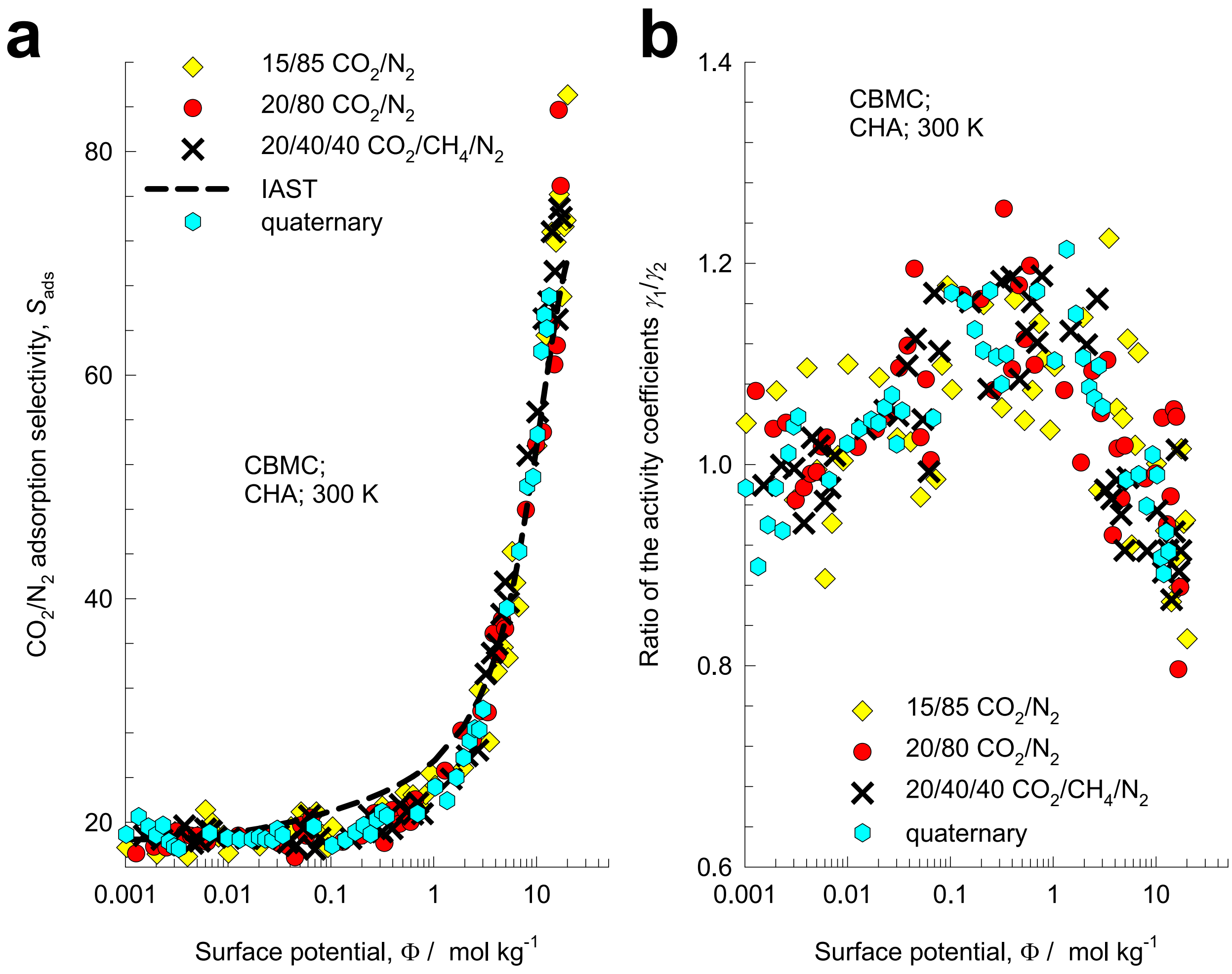

Figure S27. (a) CBMC simulations of CO2(1)/N2(2) adsorption selectivities, S_{ads}, for binary, ternary, and quaternary mixture adsorption in CHA zeolite. The selectivities are plotted as function of the surface potential Φ. The dashed lines are the IAST calculations; the unary isotherm fit parameters are provided in Table S3. (b) CBMC simulations of the ratio of activity coefficients of $\frac{\gamma_1}{\gamma_2}$ for CO2(1)/N2(2) pair plotted as function of the surface potential Φ.

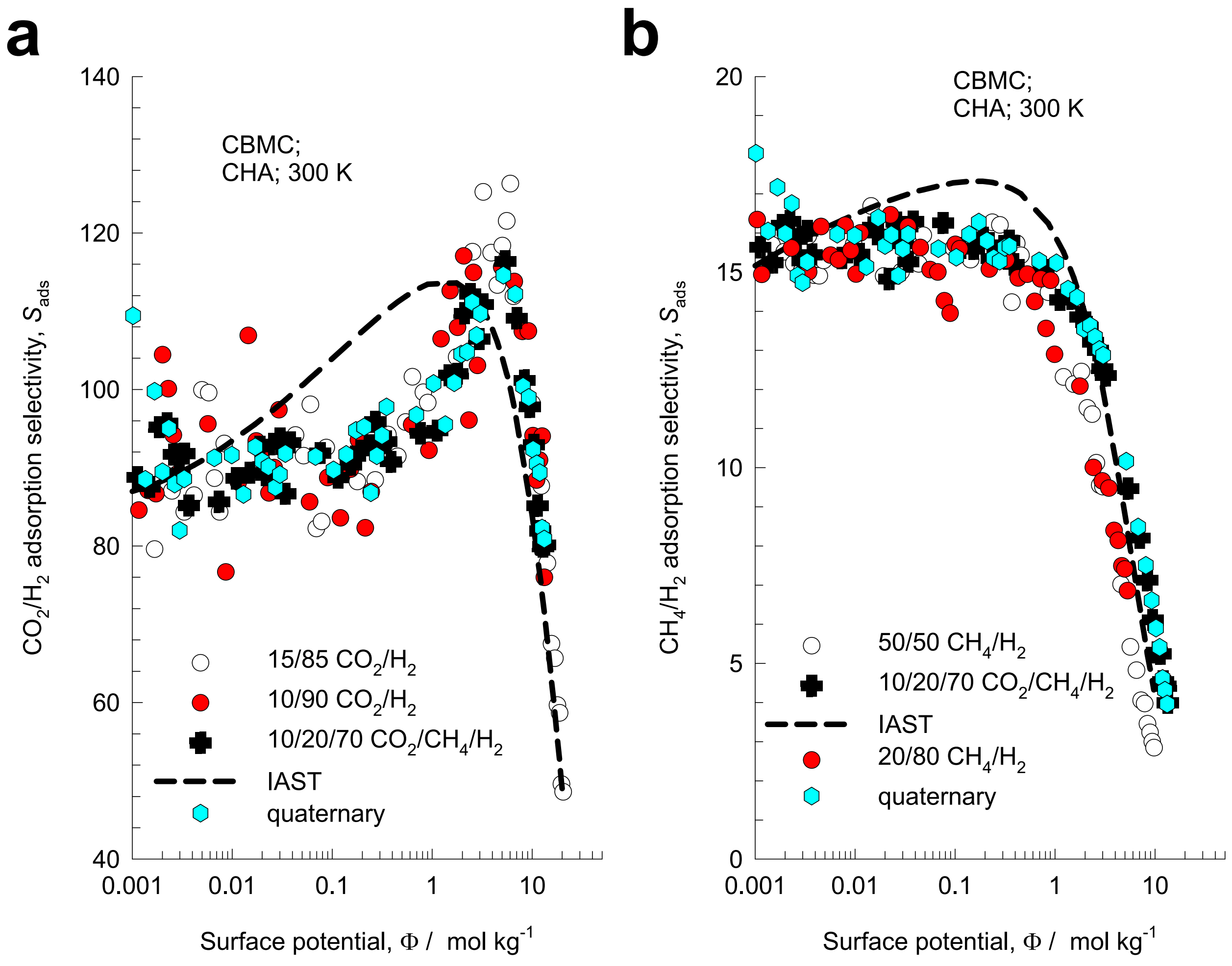

Figure S28. (a) CBMC simulations of the CO_2/H_2 adsorption selectivity, S_{ads}, for binary, ternary, and quaternary mixture adsorption CHA zeolite at 300 K. (b) CBMC simulations of the CH_4/H_2 adsorption selectivities for binary, ternary, and quaternary mixtures in CHA zeolite at 300 K. The selectivities are plotted as function of the surface potential Φ. The dashed lines are the IAST calculations; the unary isotherm fit parameters are provided in Table S3.

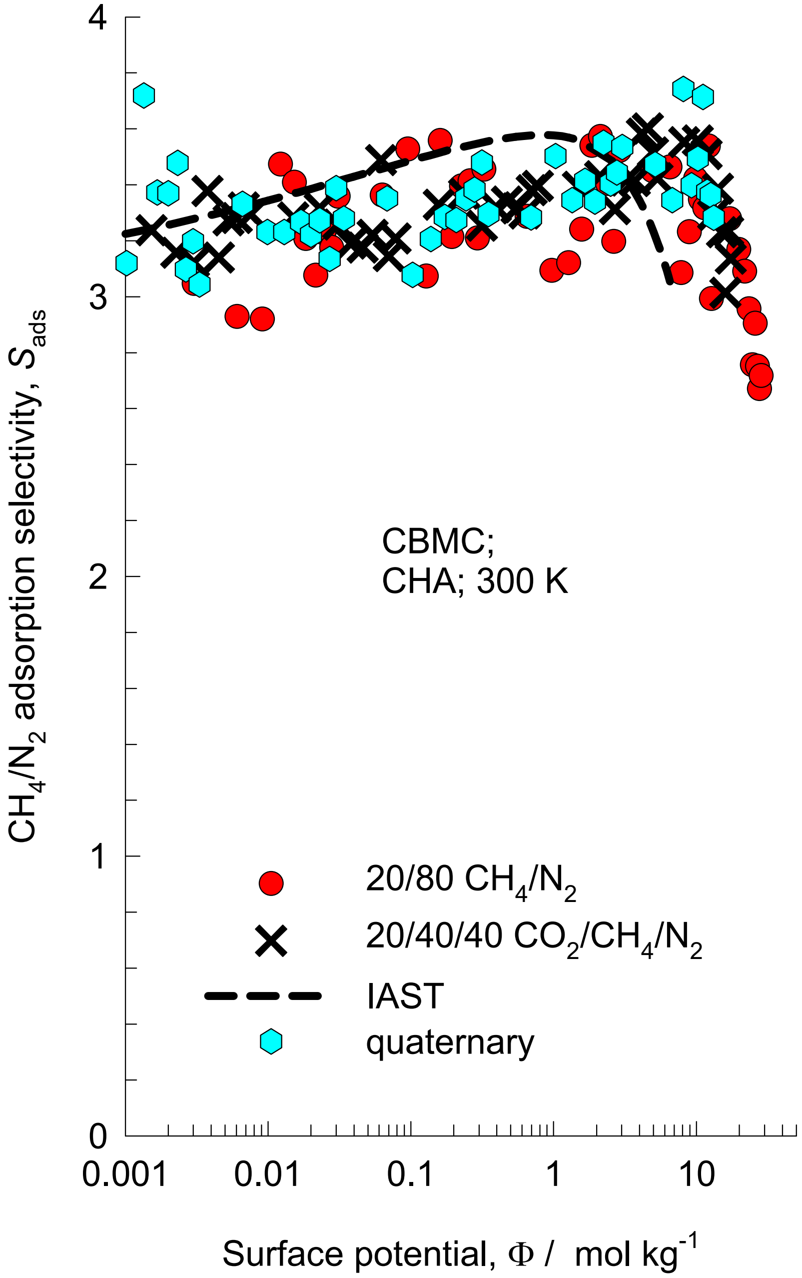

Figure S29. (a) CBMC simulations of the CH4/N2 adsorption selectivity, S_{ads}, for binary, ternary, and quaternary mixture adsorption CHA zeolite at 300 K. The dashed lines are the IAST calculations; the unary isotherm fit parameters are provided in Table S3.

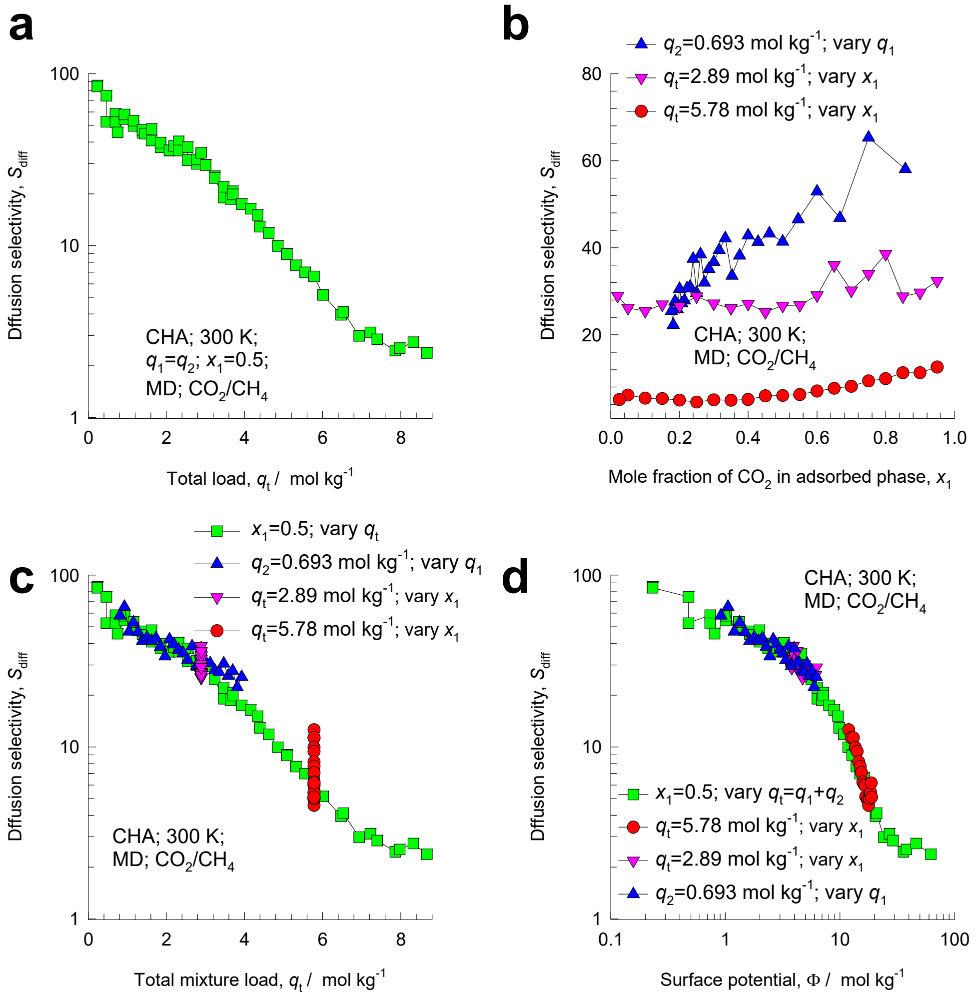

Figure S30. (a) MD simulations of the diffusion selectivities, S_{diff}, for equimolar $\left(q_1 = q_2; x_1 = 0.5\right)$ CO2/CH4 mixtures in CHA zeolite at 300 K, plotted vs total load, q_t. (b) MD simulations of the diffusion selectivities, S_{diff}, for CO2/CH4 mixtures from three different campaigns in CHA zeolite at 300 K, plotted as function the mole fraction of CO2 in the adsorbed phase, x_1, (c) All four MD campaigns plotted as function of the total load, q_t. (d) All four MD campaigns plotted as function of the surface potential Φ.

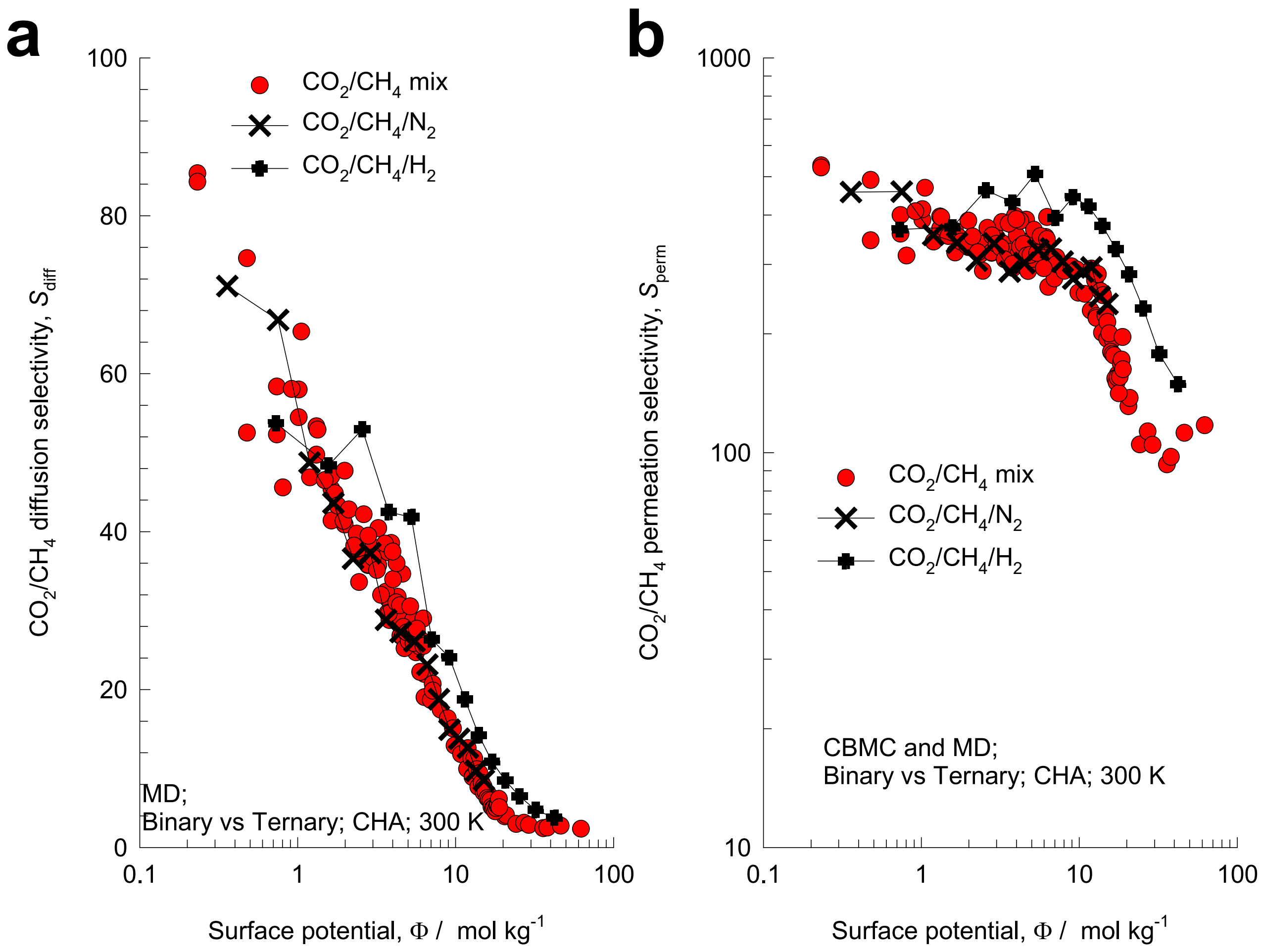

Figure S31. (a) MD simulations of the CO2/CH4 diffusion selectivities, S_{diff}, determined from both binary mixtures (four different MD campaigns) and equimolar $\left(q_1 = q_2 = q_3\right)$ ternary (CO2/CH4/N2, and CO2/CH4/H2) mixtures in CHA zeolite at 300 K, plotted as function of the surface potential Φ. (b) Plot of the CO2/CH4 permeation selectivity S_{perm} as function of the surface potential Φ, determined from binary and ternary (CO2/CH4/N2, and CO2/CH4/H2) MD campaigns.

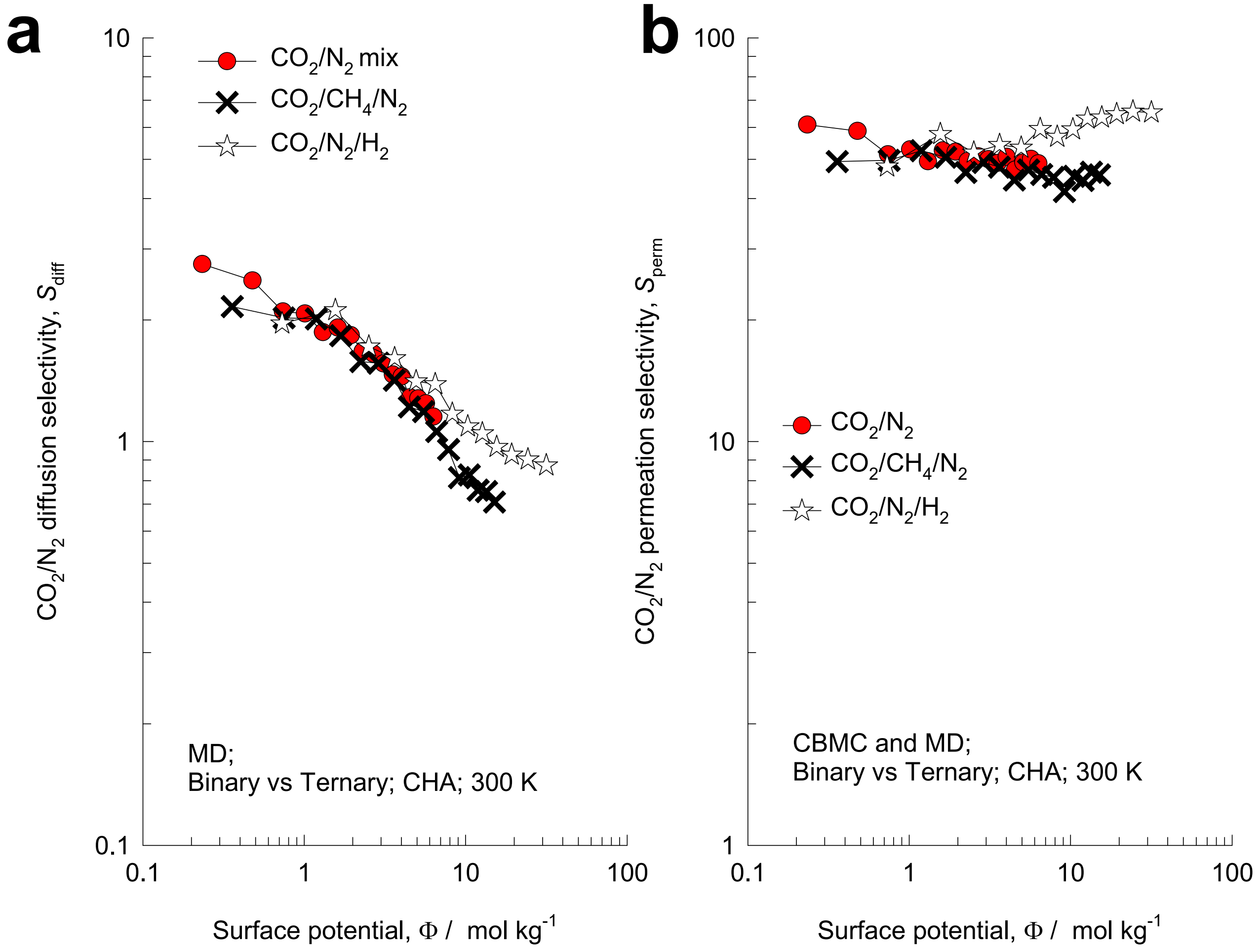

Figure S32. (a) MD simulations of the CO_2/N_2 diffusion selectivities, S_{diff}, determined from both equimolar binary $\left(q_1 = q_2\right)$ and equimolar $\left(q_1 = q_2 = q_3\right)$ ternary ($CO_2/CH_4/N_2$, and $CO_2/N_2/H_2$) mixtures in CHA zeolite at 300 K, plotted as function of the surface potential Φ. (b) Plot of the CO_2/N_2 permeation selectivity S_{perm} as function of the surface potential Φ, determined from binary and ternary ($CO_2/CH_4/N_2$, and $CO_2/N_2/H_2$) mixtures MD campaigns.

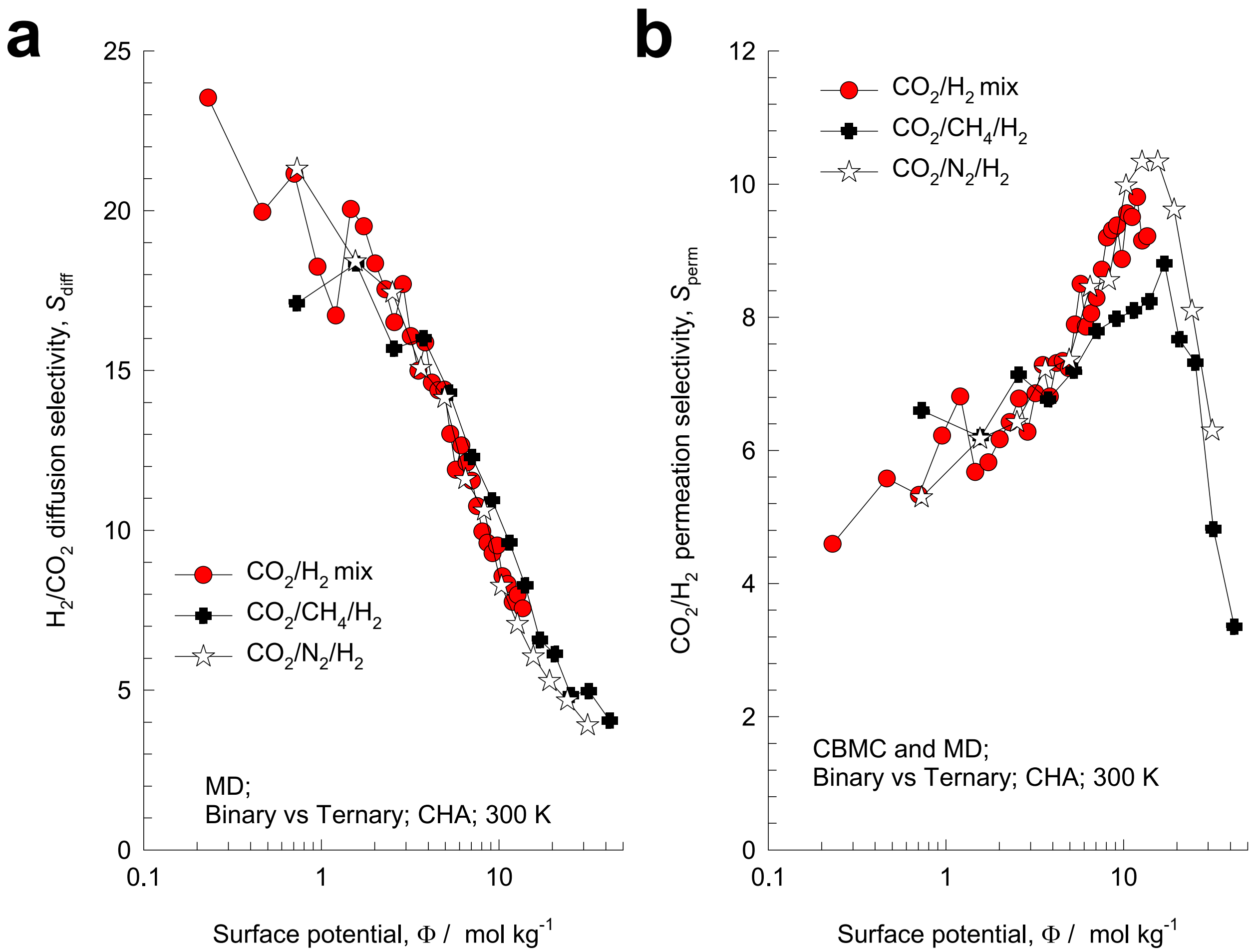

Figure S33. (a) MD simulations of the H_2/CO_2 diffusion selectivities, S_{diff}, determined from both equimolar binary $\left(q_1 = q_2\right)$ and equimolar $\left(q_1 = q_2 = q_3\right)$ ternary ($CO_2/N_2/H_2$, and $CO_2/CH_4/H_2$) mixtures in CHA zeolite at 300 K, plotted as function of the surface potential Φ. (b) Plot of the CO_2/H_2 permeation selectivity S_{perm} as function of the surface potential Φ, determined from binary and ternary ($CO_2/N_2/H_2$, and $CO_2/CH_4/H_2$) MD campaigns.

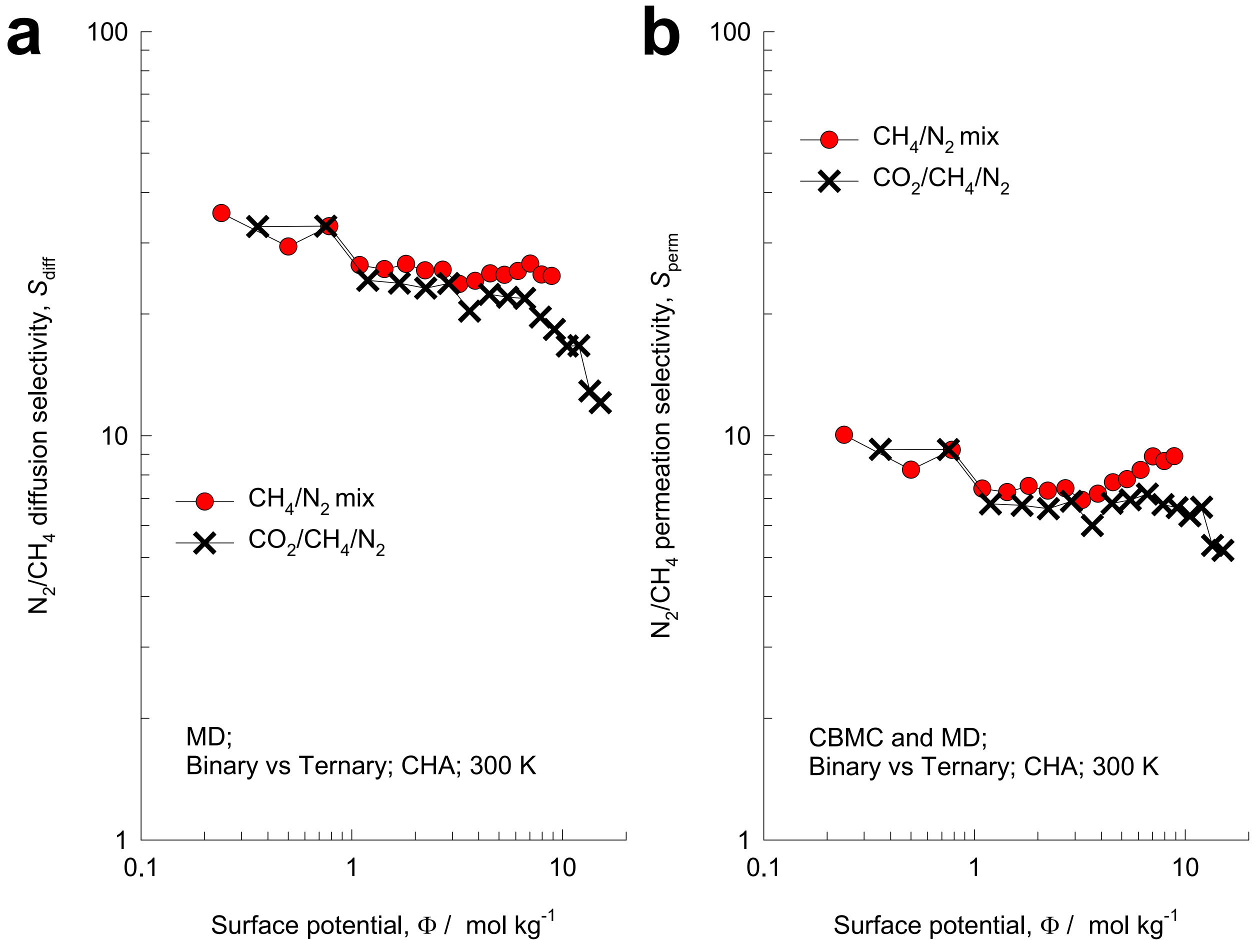

Figure S34. (a) MD simulations of the N_2/CH_4 diffusion selectivities, S_{diff}, determined from both equimolar binary $(q_1 = q_2)$ and equimolar $(q_1 = q_2 = q_3)$ ternary ($CO_2/CH_4/N_2$) mixtures in CHA zeolite at 300 K, plotted as function of the surface potential Φ. (b) Plot of the N_2/CH_4 permeation selectivity S_{perm} as function of the surface potential Φ, determined from binary and ternary ($CO_2/CH_4/N_2$) MD campaigns.

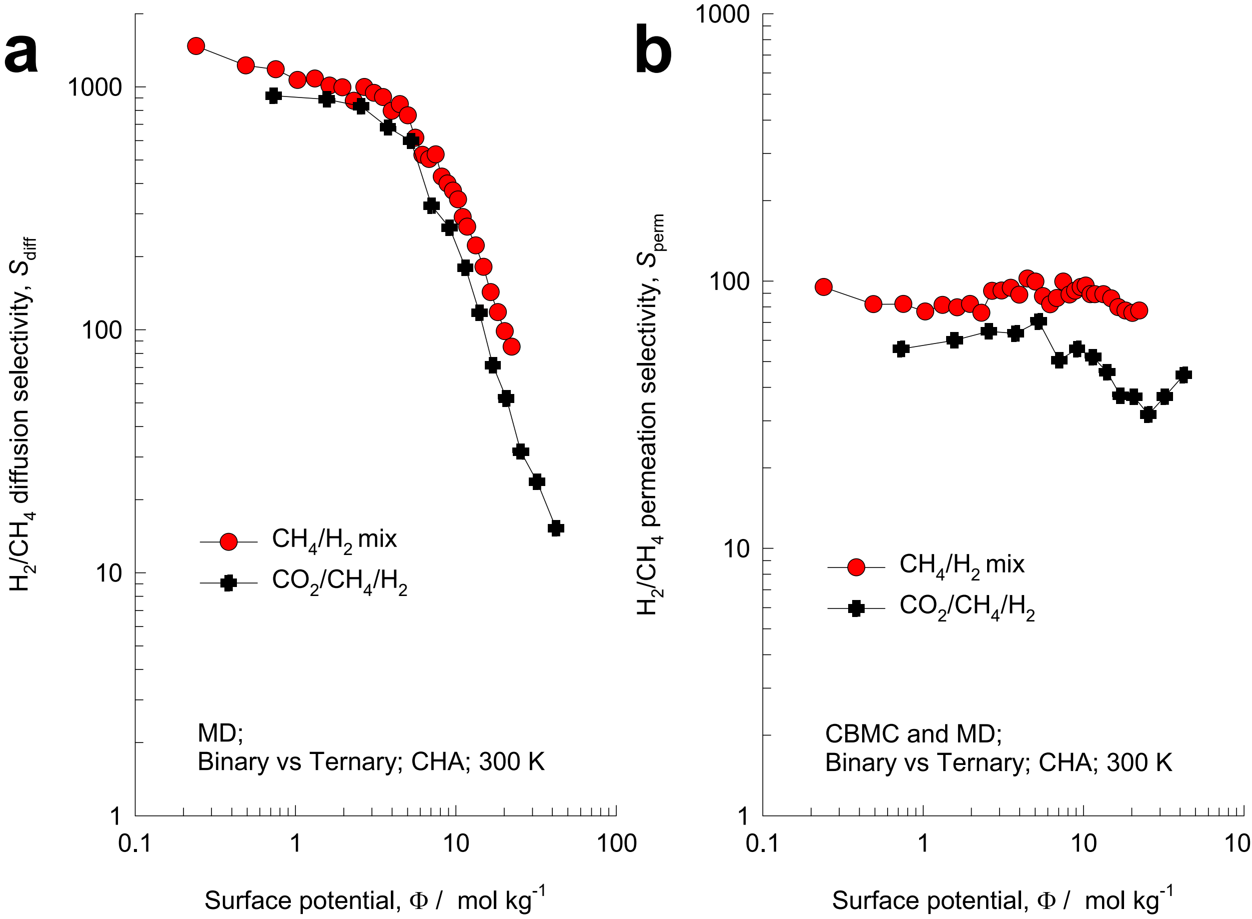

Figure S35. (a) MD simulations of the H_2/CH_4 diffusion selectivities, S_{diff}, determined from both equimolar binary $(q_1 = q_2)$ and equimolar $(q_1 = q_2 = q_3)$ ternary ($CO_2/CH_4/H_2$) mixtures in CHA zeolite at 300 K, plotted as function of the surface potential Φ. (b) Plot of the H_2/CH_4 permeation selectivity S_{perm} as function of the surface potential Φ, determined from binary and ternary ($CO_2/CH_4/H_2$) MD campaigns.

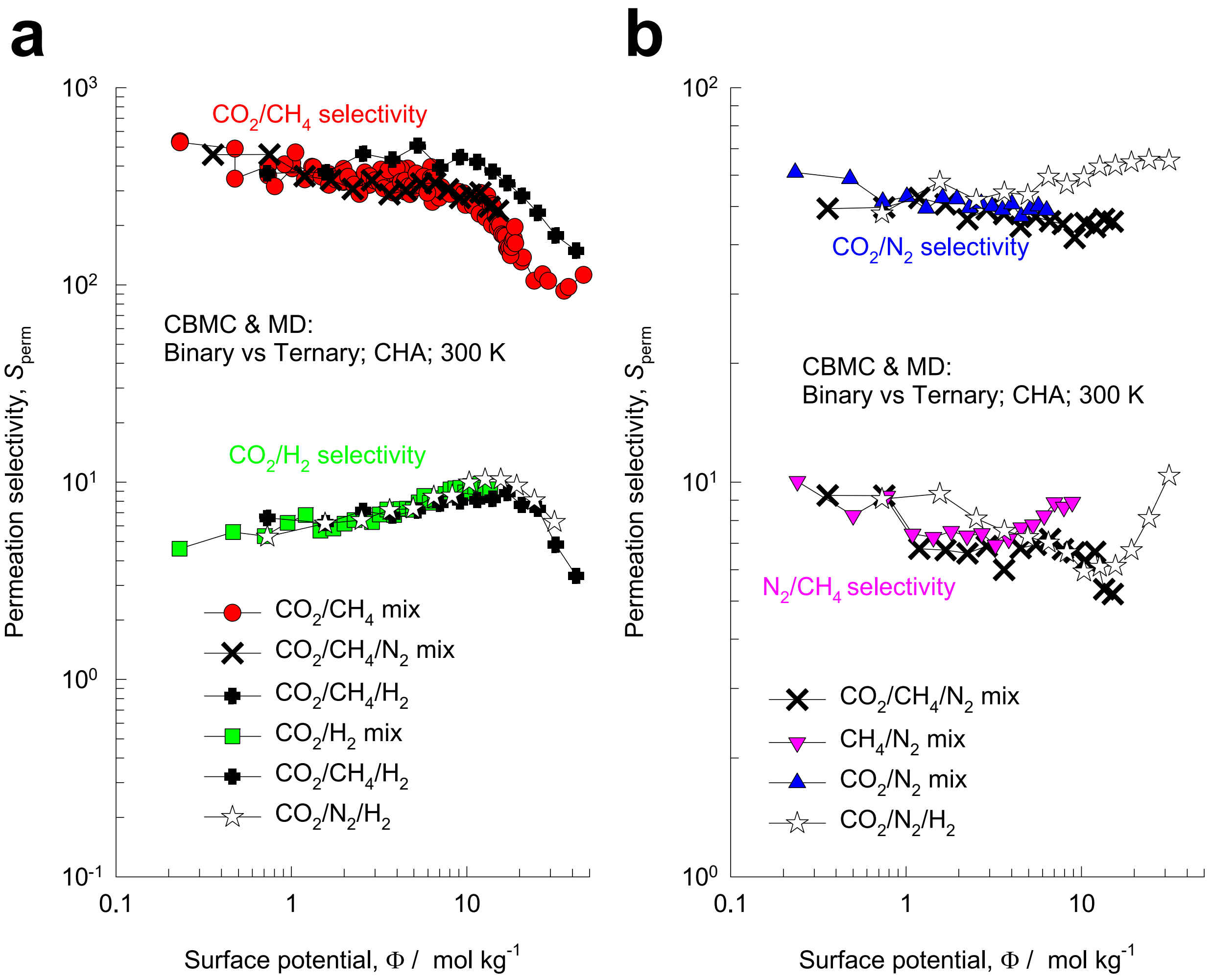

Figure S36. (a, b) Plots of the CO2/CH4, CO2//H2, CO2//N2, and N2/CH4 permeation selectivities S_{perm} as function of the surface potential Φ, determined from binary and ternary campaigns.

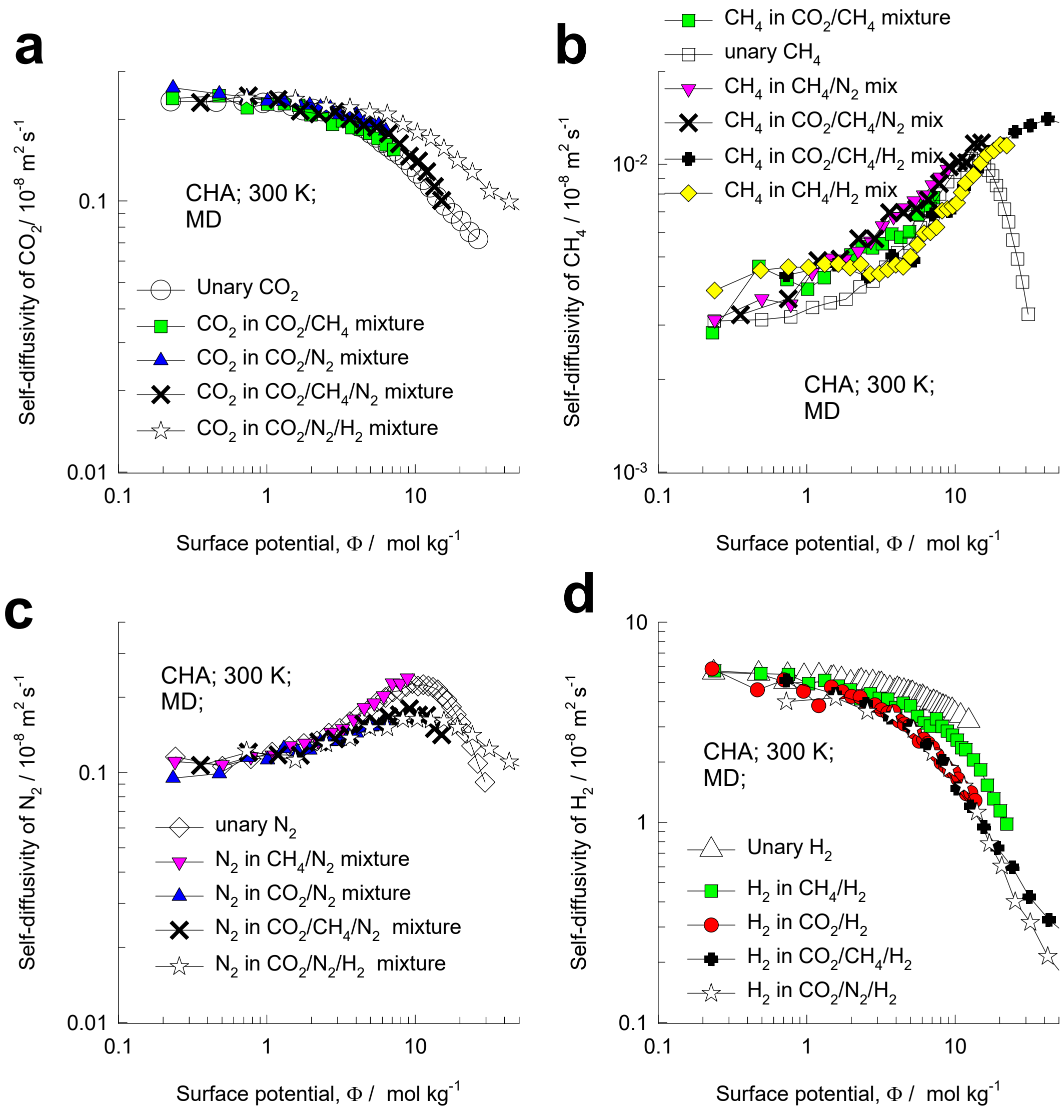

Figure S37. MD simulations of the self-diffusivities, $D_{i,self}$, of (a) CO_2, (b) CH_4, (c) N_2 and (d) H_2 in different equimolar binary $(q_1 = q_2)$ (CO_2/CH_4, CO_2/N_2, CO_2/H_2, CH_4/N_2, CH_4/H_2) and equimolar $(q_1 = q_2 = q_3)$ ternary ($CO_2/CH_4/N_2$, $CO_2/CH_4/H_2$, $CO_2/N_2/H_2$) mixtures in CHA zeolite at 300 K, plotted as function of the surface potential Φ. Also plotted are the corresponding values of the unary self-diffusivities.

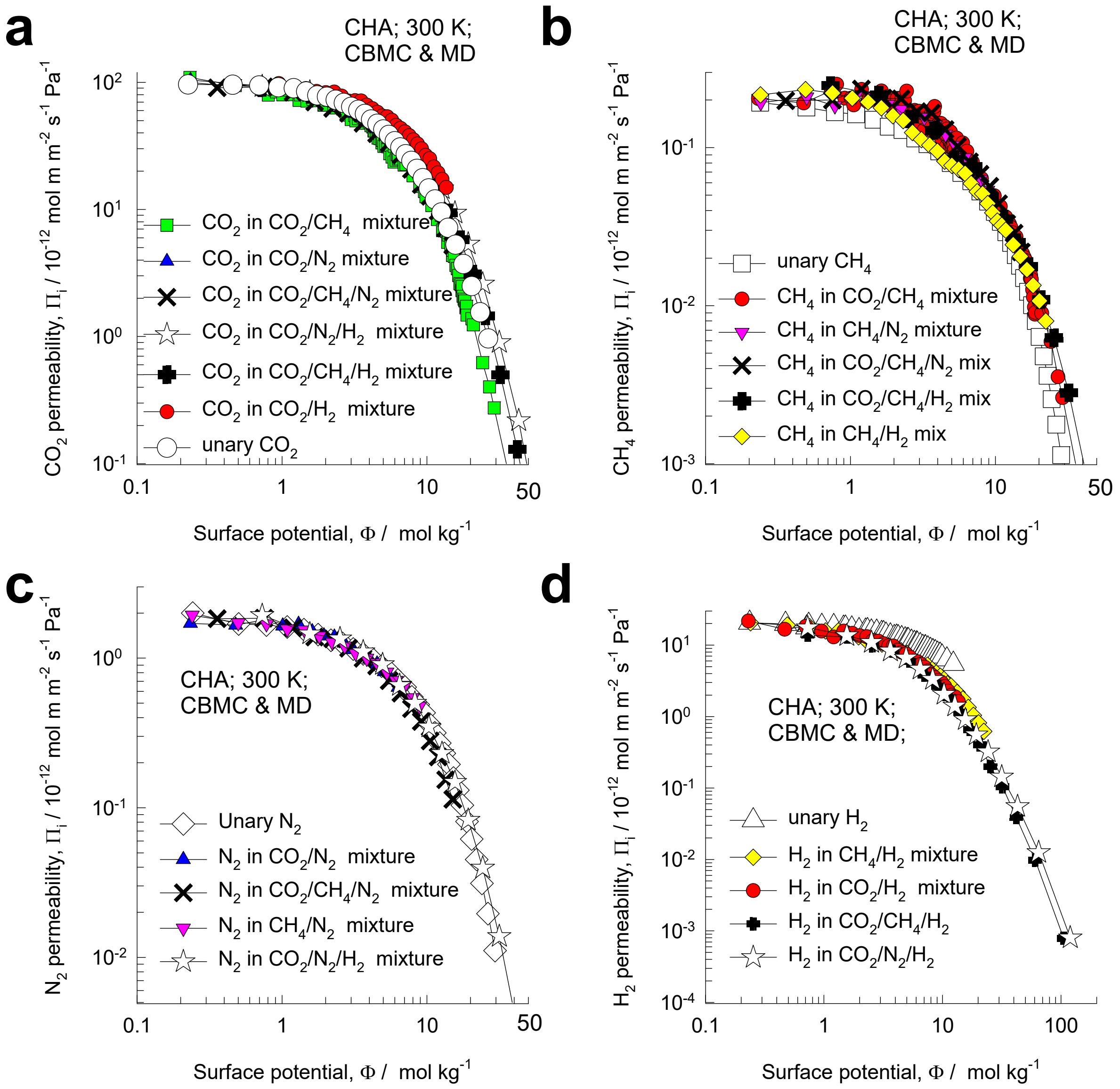

Figure S38. CBMC/MD simulations of the permeabilities, Π_i, of (a) CO_2, (b) CH_4, (c) N_2 and (d) H_2 in different equimolar binary $(q_1 = q_2)$ (CO_2/CH_4, CO_2/N_2, CO_2/H_2, CH_4/N_2, CH_4/H_2) and equimolar $(q_1 = q_2 = q_3)$ ternary ($CO_2/CH_4/N_2$, $CO_2/CH_4/H_2$, $CO_2/N_2/H_2$) mixtures in CHA zeolite at 300 K, plotted as a function of the surface potential Φ. Also plotted are the corresponding values of the unary permeabilities.

8 Adsorption, Diffusion, Permeation in DDR zeolite

DDR consists of cages of 277.8 Å^3 volume, separated by 3.65 Å × 4.37 Å 8-ring windows; the pore landscapes and structural details are provided in Figure S39, and Figure S40.

CBMC simulations of the unary isotherms of CO_2, CH_4, N_2 and H_2 were fitted with the dual-site Langmuir-Freundlich model, eq (S8); the fit parameters for each guest molecule (with sites A, and B) are tabulated for each guest molecule (with sites A, and B) are tabulated for each guest in Table S4.

8.1 Dependence of adsorption selectivity on Φ

CBMC simulation data of the adsorption selectivity, S_{ads}, for CO_2(1)/CH_4(2) mixtures in DDR zeolite at 300 K were determined from three different campaigns:

(i) the bulk gas phase mole fractions are maintained at $y_1 = y_2 = 0.5$, and the total bulk mixture fugacity $f_t = f_1 + f_2$ is varied up to $f_t = 10$ MPa at which pore saturation conditions are approached,

(ii) the bulk gas phase mole fractions are maintained at $y_1 = 0.20$, and the total mixture fugacity $f_t = f_1 + f_2$ is varied up to $f_t = 10$ MPa at which pore saturation conditions are approached,

(iii) the total bulk gas mixture fugacity is held constant, $f_t = f_1 + f_2 = 10^6$ Pa, and the mole fraction of the bulk gas mixture of CO_2(1), y_1, is varied from 0 to 1

The three sets of CBMC data for binary mixture adsorption are plotted in Figure S41 as function of the total bulk mixture fugacity $f_t = f_1 + f_2$. We note that the S_{ads} is not uniquely determined by $f_t = f_1 + f_2$ and is also a function of the bulk mixture composition y_1.

For all three CBMC data sets, the CBMC simulated values of the adsorption selectivity, S_{ads}, follows a near-unique dependence on the surface potential Φ, see Figure S42a.

CBMC simulations were also performed for 20/40/40 $CO_2/CH_4/N_2$, 10/20/70 $CO_2/CH_4/H_2$ and quaternary 1/1/1/1 $CO_2/CH_4/N_2/H_2$ mixtures in DDR zeolite at 300 K, in which the bulk gas phase mole fractions are maintained constant and the total mixture fugacity $f_t = f_1 + f_2 + f_3$ is varied up to $f_t = 10$ MPa. The values of the CO_2/CH_4 adsorption selectivity in ternary and quaternary mixtures are also plotted in Figure S42a. Put another way, the presence of component 3 and/or component 4 in the ternary and quaternary mixtures have no influence of the adsorption selectivity for the 1-2 pair.

The IAST calculations (indicated by dashed lines in Figure S42a) of the adsorption selectivity show some deviations from the CBMC simulated data due to non-idealities caused by preferential perching of CO_2 at the window regions; detailed explanations are provided in our earlier works.[28, 40, 63, 67] With the introduction of activity coefficients, the expression for the adsorption selectivity for the $CO_2(1)/CH_4(2)$ pair in binary, ternary and quaternary mixtures is

$$S_{ads,12} = \frac{q_1/q_2}{f_1/f_2} = \frac{x_1/f_1}{x_2/f_2} = \frac{P_2^0\gamma_2}{P_1^0\gamma_1} \qquad \text{(S83)}$$

Using the CBMC data for binary, ternary and quaternary mixture adsorption, the activity coefficients of $CO_2(1)$ and $CH_4(2)$ were determined for binary, ternary and quaternary mixtures. Figure S42b plots the ratio of the activity coefficient of $CO_2(1)$ to that of $CH_4(2)$, $\frac{\gamma_1}{\gamma_2}$, as a function of Φ. We note that $\frac{\gamma_1}{\gamma_2}$ for binary, ternary and quaternary mixtures are of comparable magnitudes when plotted as a function of Φ. For this reason, the CO_2/CH_4 adsorption selectivity shows a unique dependence on Φ, despite the deviations from IAST estimates.

Figure S43a shows CBMC simulation data of the adsorption selectivity, S_{ads}, for $CO_2(1)/N_2(2)$ mixtures in DDR zeolite at 300 K, determined from two different campaigns:

(i) the bulk gas phase mole fractions are maintained at $y_1 = 0.15$, and the total mixture fugacity $f_t = f_1 + f_2$ is varied up to $f_t = 10$ MPa at which pore saturation conditions are approached,

(ii) the bulk gas phase mole fractions are maintained at $y_1 = y_2 = 0.20$, and the total mixture fugacity $f_t = f_1 + f_2$ is varied up to $f_t = 10$ MPa at which pore saturation conditions are approached,

For both CBMC data sets, the CBMC simulated values of the adsorption selectivity, S_{ads}, follows a near-unique dependence on the surface potential Φ, see Figure S43a. CBMC simulations were also performed for 20/40/40 $CO_2/CH_4/N_2$ and quaternary 1/1/1/1 $CO_2/CH_4/N_2/H_2$ mixtures in DDR zeolite at 300 K, in which the bulk gas phase mole fractions are maintained constant and the total mixture fugacity $f_t = f_1 + f_2 + f_3$ is varied up to $f_t = 10$ MPa. The values of the CO_2/N_2 adsorption selectivity in the ternary mixture are also plotted in Figure S43a. The ternary and quaternary CBMC data follows the same unique dependence on Φ, as prescribed by eq (S13). Put another way, the presence of component 3, and/or component 4 in the ternary and quaternary mixture have no influence of the adsorption selectivity for the 1-2 pair.

The IAST calculations of the adsorption selectivity (indicated by dashed lines in Figure S43a) show some deviations from the CBMC simulated data due to non-idealities caused by preferential perching of CO_2 at the window regions; detailed explanations are provided in our earlier works.[28, 40, 63, 67] Figure S43b plots the ratio of the activity coefficient of CO_2(1) to that of N_2(2), $\frac{\gamma_1}{\gamma_2}$, as a function of Φ. We note that $\frac{\gamma_1}{\gamma_2}$ for binary, ternary and quaternary mixtures are of comparable magnitudes when plotted as a function of Φ. For this reason, the CO_2/N_2 adsorption selectivity shows a unique dependence on Φ, despite the deviations from IAST estimates.

Figure S44a plots data obtained from CBMC simulations of the CO_2/H_2 adsorption selectivities in binary (15/85 CO_2/H_2, and 10/90 CO_2/H_2), ternary (10/20/70 $CO_2/CH_4/H_2$), and quaternary 1/1/1/1 $CO_2/CH_4/N_2/H_2$ mixtures in DDR zeolite at 300 K. The CO_2/H_2 adsorption selectivities for binary, ternary, and quaternary mixtures display unique dependence on Φ.

Figure S44b plots data obtained from CBMC simulations of the CH_4/H_2 adsorption selectivities in binary (20/80 CH_4/H_2), ternary (10/20/70 $CO_2/CH_4/H_2$), and quaternary 1/1/1/1 $CO_2/CH_4/N_2/H_2$ mixtures in DDR zeolite at 300 K. The CH_4/H_2 adsorption selectivities for binary, ternary, and quaternary mixtures display unique dependence on Φ.

Figure S45 plots data obtained from CBMC simulations of the CH_4/N_2 adsorption selectivities in binary (20/80 CH_4/N_2) and ternary (20/40/40 $CO_2/CH_4/N_2$) mixtures in DDR zeolite at 300 K. The CH_4/N_2 adsorption selectivities for binary, ternary, and quaternary mixtures display unique dependence on Φ.

8.2 Diffusion and permeation selectivities of binary pairs

Let us consider MD simulation data on self-diffusivities $D_{i,self}$ for binary CO_2/CH_4 mixtures in DDR zeolite at 300 K. For this mixture, five different MD simulation campaigns were conducted as follows:

(i) equimolar ($q_1 = q_2; \quad x_1 = 1 - x_2 = 0.5$) mixtures with varying total load, $q_t = q_1 + q_2$

(ii) ($q_1 / q_2 = 2/1; \quad x_1 = 2/3$) mixtures with varying total load, $q_t = q_1 + q_2$

(iii) ($q_1 / q_2 = 3/1; \quad x_1 = 3/4$) mixtures with varying total load, $q_t = q_1 + q_2$

(iv) ($q_1 / q_2 = 5/1; \quad x_1 = 5/6$) mixtures with varying total load, $q_t = q_1 + q_2$

(v) mixtures in which the CH_4 load $\Theta_2 =$ 8 molecules uc^{-1} and loadings of CO_2 are varied

The five sets of data on diffusion selectivities are plotted in Figure S46a as function of the surface potential, Φ; the data indicates that Φ uniquely determines the diffusion selectivity. Additionally, we also performed MD simulations to determine the self-diffusivites $D_{i,self}$ for $\left(q_1 = q_2 = q_3\right)$ ternary $CO_2/CH_4/N_2$ and $CO_2/CH_4/H_2$ mixtures in DDR zeolite. The CO_2/CH_4 diffusion selectivities, S_{diff}, determined for the binary pair in the ternary mixture (indicated by crosses, and plusses) follows the same unique dependence on Φ, as for the five different binary mixture campaigns (indicated by red circles); see Figure S46a.

In view of the fact that IAST also shows that the adsorption selectivity S_{ads} is also uniquely dependent on Φ, we should expect the permeation selectivity $S_{perm} = \frac{D_{1,self} q_1 / f_1}{D_{2,self} q_2 / f_2} = S_{ads} \times S_{diff}$ to be also uniquely dependent on Φ. The plot of S_{perm} vs Φ for the binary and ternary mixture data sets also lie on a unique curve; see Figure S46b.

The unique dependence of adsorption, diffusion, and permeation selectivities on Φ also holds for CO_2/N_2, CO_2/H_2, and CH_4/N_2 mixtures. This is confirmed by the CBMC/MD data on (a) diffusion selectivities, S_{diff}, and (b) permeation selectivities, S_{perm}, of three constituent binary pairs that are presented in Figure S47, Figure S48, and Figure S49 determined from simulation data for binary and ternary mixtures in DDR zeolite at 300 K. Plotted as function of the surface potential Φ, each of the pair selectivities are the same in the binary and ternary mixtures. This is a useful and practical conclusion.

8.3 Component self-diffusivities and permeabilities

Figure S50 presents MD simulations of the self-diffusivities, $D_{i,self}$, of (a) CO_2, (b) CH_4, (c) N_2 and (d) H_2 in different equimolar $(q_1 = q_2)$ binary (CO_2/CH_4, CO_2/N_2, CO_2/H_2, CH_4/N_2) and equimolar $(q_1 = q_2 = q_3)$ ternary ($CO_2/CH_4/N_2$, $CO_2/CH_4/H_2$, $CO_2/N_2/H_2$) mixtures in DDR zeolite at 300 K, plotted as function of the surface potential Φ. The data demonstrate that the component self-diffusivities in binary and ternary mixtures are nearly the same, independent of the partner(s) in the mixtures. Except for H_2, the self-diffusivities in the binary and ternary mixtures are also nearly the same as the unary self-diffusivities. The unary self-diffusivity for H_2, appears to be slightly larger in value for those in mixtures.

Figure S51 presents data on the permeabilities, Π_i, of (a) CO_2, (b) CH_4, (c) N_2 and (d) H_2 in different equimolar $(q_1 = q_2)$ binary (CO_2/CH_4, CO_2/N_2, CO_2/H_2, CH_4/N_2) and equimolar $(q_1 = q_2 = q_3)$ ternary ($CO_2/CH_4/N_2$, $CO_2/CH_4/H_2$, $CO_2/N_2/H_2$) mixtures in DDR zeolite at 300 K, plotted as a function of the surface potential Φ. The data demonstrate that the component permeabilities in binary and ternary mixtures are nearly the same, independent of the partner(s) in the mixtures. Except for H_2, the permeabilities in the binary and ternary mixtures are also nearly the same as the unary peremabilities. The unary permeability for H_2, appears to be slightly larger in value for those in mixtures.

8.4 Analysis of experimental data

Experimental data of Van den Bergh et al.[68, 69] for component permeances for 50/50 CO_2/CH_4, and 50/50 N_2/CH_4 mixtures in DDR membrane at 303 K are compared to unary permeation data in Figure S52, and Figure S53. The permeance data are plotted as function of (a) upstream partial pressures, p_{i0}, and (b) surface potential Φ at the upstream face of the membrane.

Figure S54 presents a comparison of CH_4 component permeances for 50/50 CO_2/CH_4 and 50/50 N_2/CH_4 binary mixture permeation across DDR membrane at 303 K, compared to unary permeance. The data are plotted as function of the surface potential Φ at the upstream face of the membrane.

Figure S55 presents experimental data of Himeno et al.[70] for component permeances for 50/50 CO_2/CH_4 binary mixture permeation across DDR membrane at 298 K, compared to unary permeation data. The data are plotted as function of (a) upstream partial pressures, p_{i0}, and (b) surface potential Φ at the upstream face of the membrane.

When compared at the same surface potential, the component permeances are the same for mixtures as for unary systems.

8.5 List of Tables for Adsorption, Diffusion, Permeation in DDR zeolite

Table S4. Dual-site Langmuir-Freundlich parameters for guest molecules in DDR (all-silica) at 300 K.

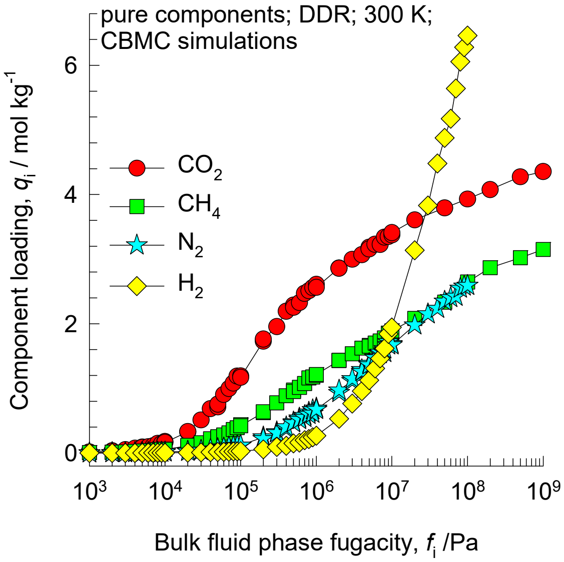

	Site A			Site B		
	$q_{A,sat}$ mol kg^{-1}	b_A $Pa^{-\nu A}$	ν_A dimensionless	$q_{B,sat}$ mol kg^{-1}	b_B $Pa^{-\nu B}$	ν_B dimensionless
CO_2	1.5	1.010E-06	0.79	3	6.076E-06	1
CH_4	1.4	4.035E-06	1	1.95	1.814E-06	0.75
N_2	1.25	9.8874E-07	1	1.55	5.549E-08	1
H_2	5	5.028E-08	1	12	2.442E-09	1

8.6 List of Figures for Adsorption, Diffusion, Permeation in DDR zeolite

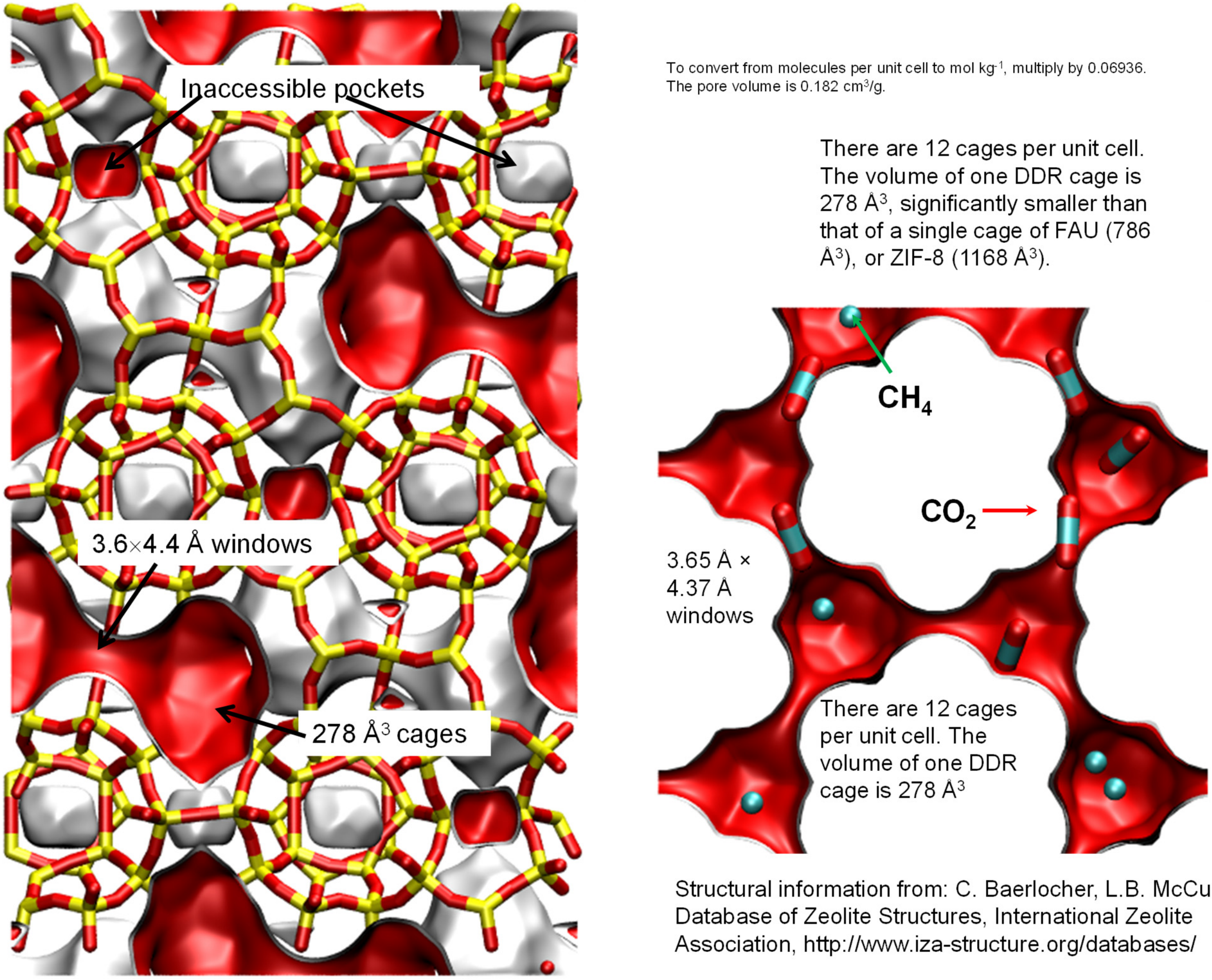

To convert from molecules per unit cell to mol kg^{-1}, multiply by 0.06936. The pore volume is 0.182 cm^3/g.

There are 12 cages per unit cell. The volume of one DDR cage is 278 Å^3, significantly smaller than that of a single cage of FAU (786 Å^3), or ZIF-8 (1168 Å^3).

There are 12 cages per unit cell. The volume of one DDR cage is 278 Å^3

Structural information from: C. Baerlocher, L.B. McCusker, Database of Zeolite Structures, International Zeolite Association, http://www.iza-structure.org/databases/

Figure S39. Pore landscape of all-silica DDR zeolite.

DDR window and pore dimensions

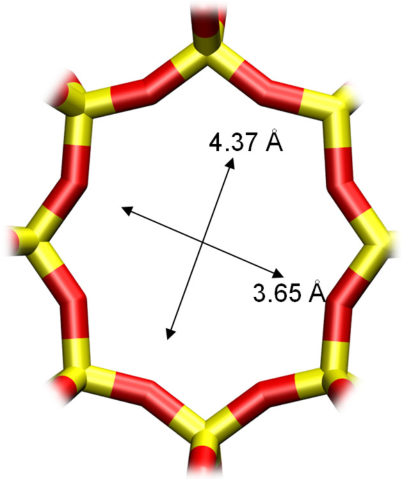

DDR

The window dimensions calculated using the van der Waals diameter of framework atoms = 2.7 Å are indicated above by the arrows.

	DDR
a /Å	24.006
b /Å	13.86
c /Å	40.892
Cell volume / Å^3	13605.72
conversion factor for [molec/uc] to [mol per kg Framework]	0.0693
conversion factor for [molec/uc] to [kmol/m^3]	0.4981
ρ [kg/m3]	1759.991
MW unit cell [g/mol(framework)]	14420.35
ϕ, fractional pore volume	0.245
open space / Å^3/uc	3333.5
Pore volume / cm^3/g	0.139
Surface area /m^2/g	350.0
DeLaunay diameter /Å	3.65

Figure S40. Structural details for DDR zeolite.

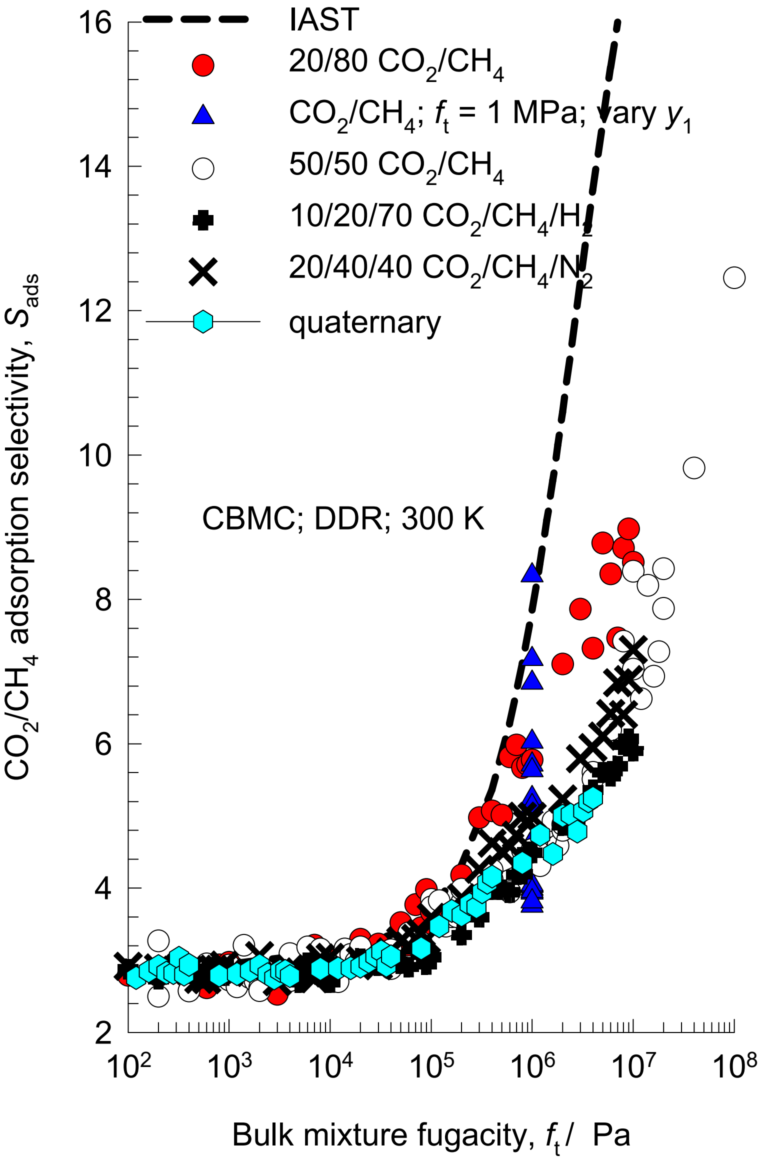

Figure S41. (a) CBMC simulations of the CO_2/CH_4 adsorption selectivity, S_{ads}, for binary, ternary, and quaternary mixture adsorption in DDR zeolite at 300 K. The adsorption selectivities are plotted as function of the total bulk mixture fugacity, f_t. The dashed lines are the IAST calculations; the unary isotherm fit parameters are provided in Table S4.

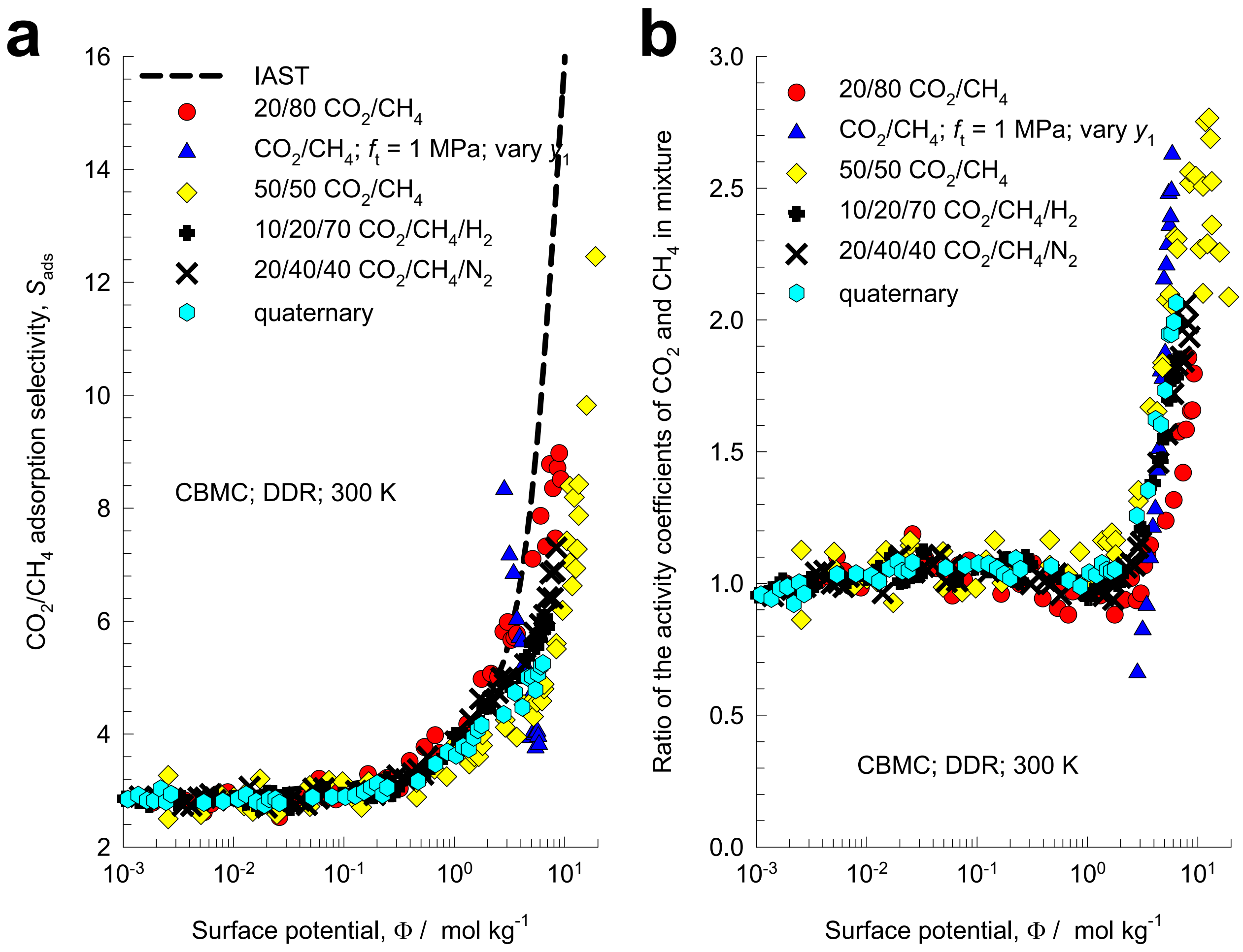

Figure S42. (a) CBMC simulations of the CO$_2$/CH$_4$ adsorption selectivity, S_{ads}, for binary, ternary, and quaternary mixture adsorption in DDR zeolite at 300 K The adsorption selectivities are plotted as function of the surface potential Φ. The dashed lines are the IAST calculations; the unary isotherm fit parameters are provided in Table S4. (b) CBMC simulations of the ratio of activity coefficients of CO$_2$, and CH$_4$ plotted as function of the surface potential Φ.

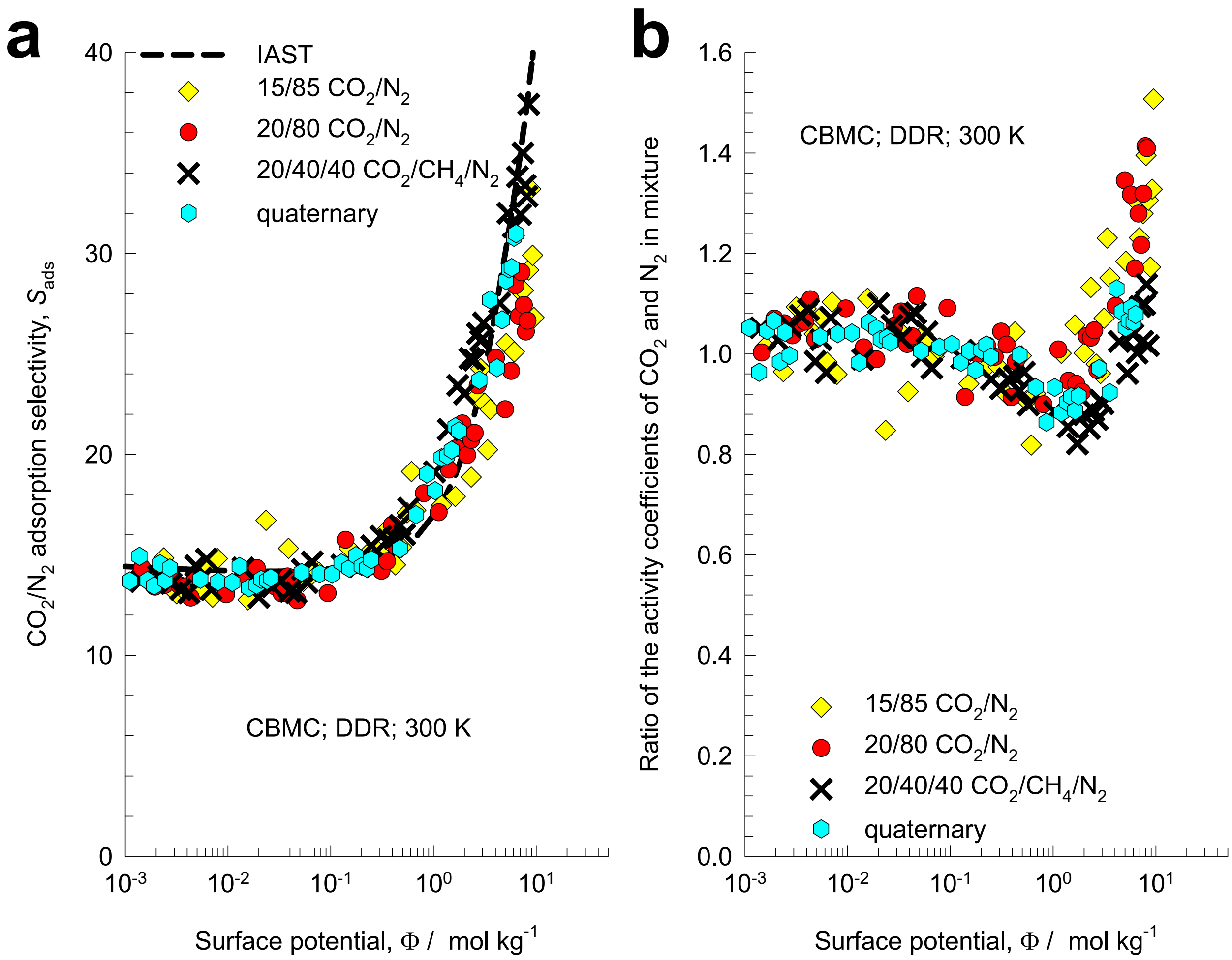

Figure S43. (a) CBMC simulations of the CO$_2$/N$_2$ adsorption selectivity, S_{ads}, for binary, ternary, and quaternary mixture adsorption in DDR zeolite at 300 K The adsorption selectivities are plotted as function of the surface potential Φ. The dashed lines are the IAST calculations; the unary isotherm fit parameters are provided in Table S4. (b) CBMC simulations of the ratio of activity coefficients of CO$_2$, and N$_2$ plotted as function of the surface potential Φ.

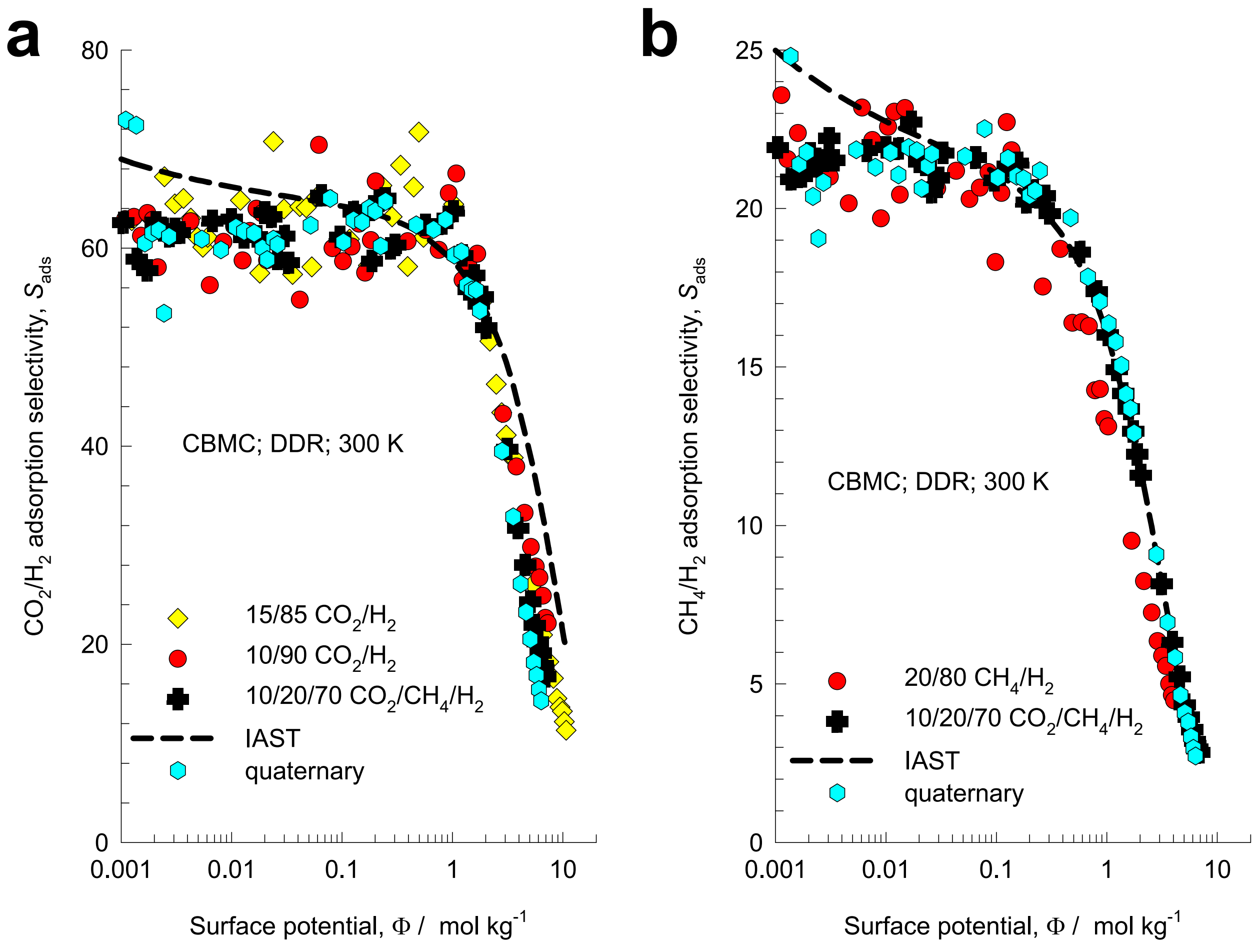

Figure S44. (a) CBMC simulations of the CO2/H2 adsorption selectivity, S_{ads}, for binary, ternary, and quaternary mixture adsorption in DDR zeolite at 300 K. (b) CBMC simulations of the CH4/H2 adsorpton selectivities for binary, ternary, and quaternary mixture adsorption in DDR zeolite at 300 K. The selectivities are plotted as function of the surface potential Φ. The dashed lines are the IAST calculations; the unary isotherm fit parameters are provided in Table S4.

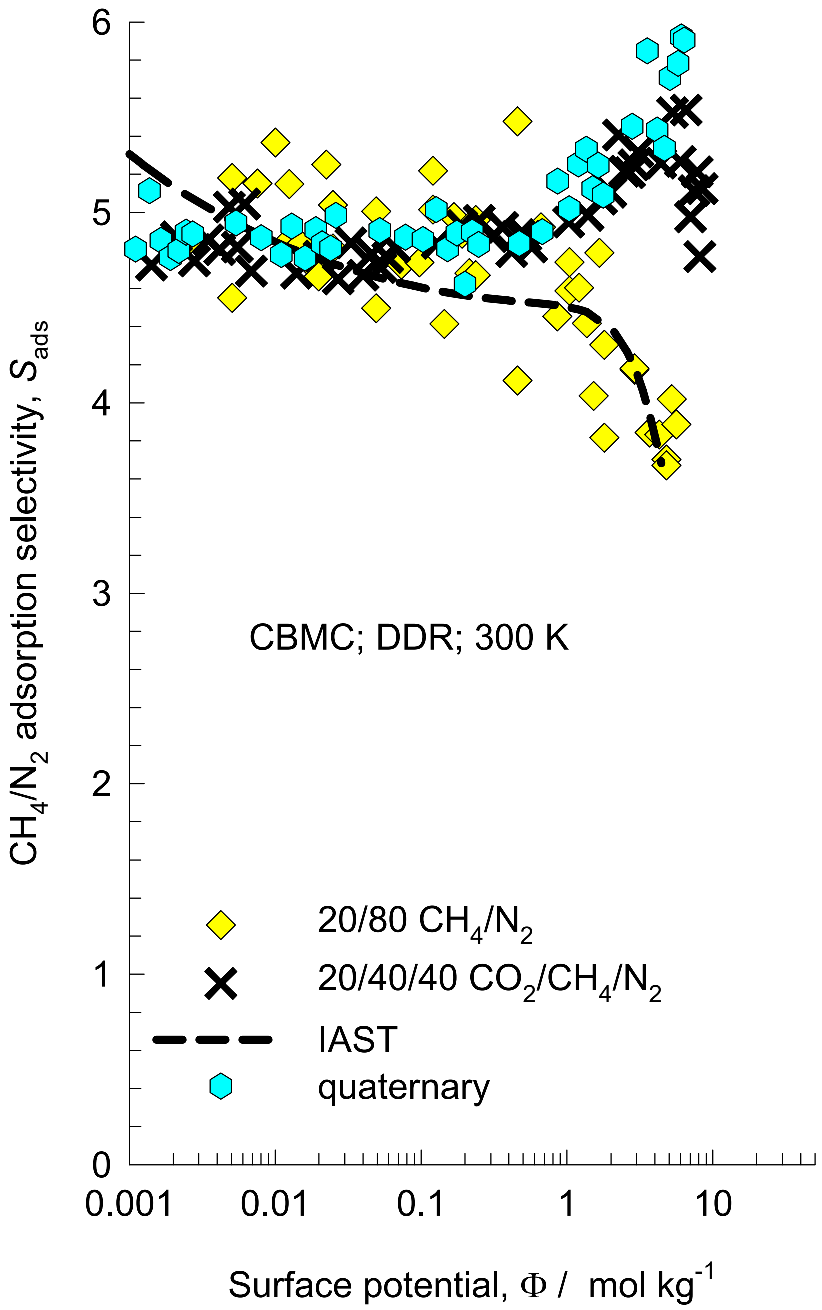

Figure S45. CBMC simulations of the CH4/N2 adsorption selectivity, S_{ads}, for binary, ternary, and quaternary mixture adsorption in DDR zeolite at 300 K. The selectivities are plotted as function of the surface potential Φ. The dashed lines are the IAST calculations; the unary isotherm fit parameters are provided in Table S4.

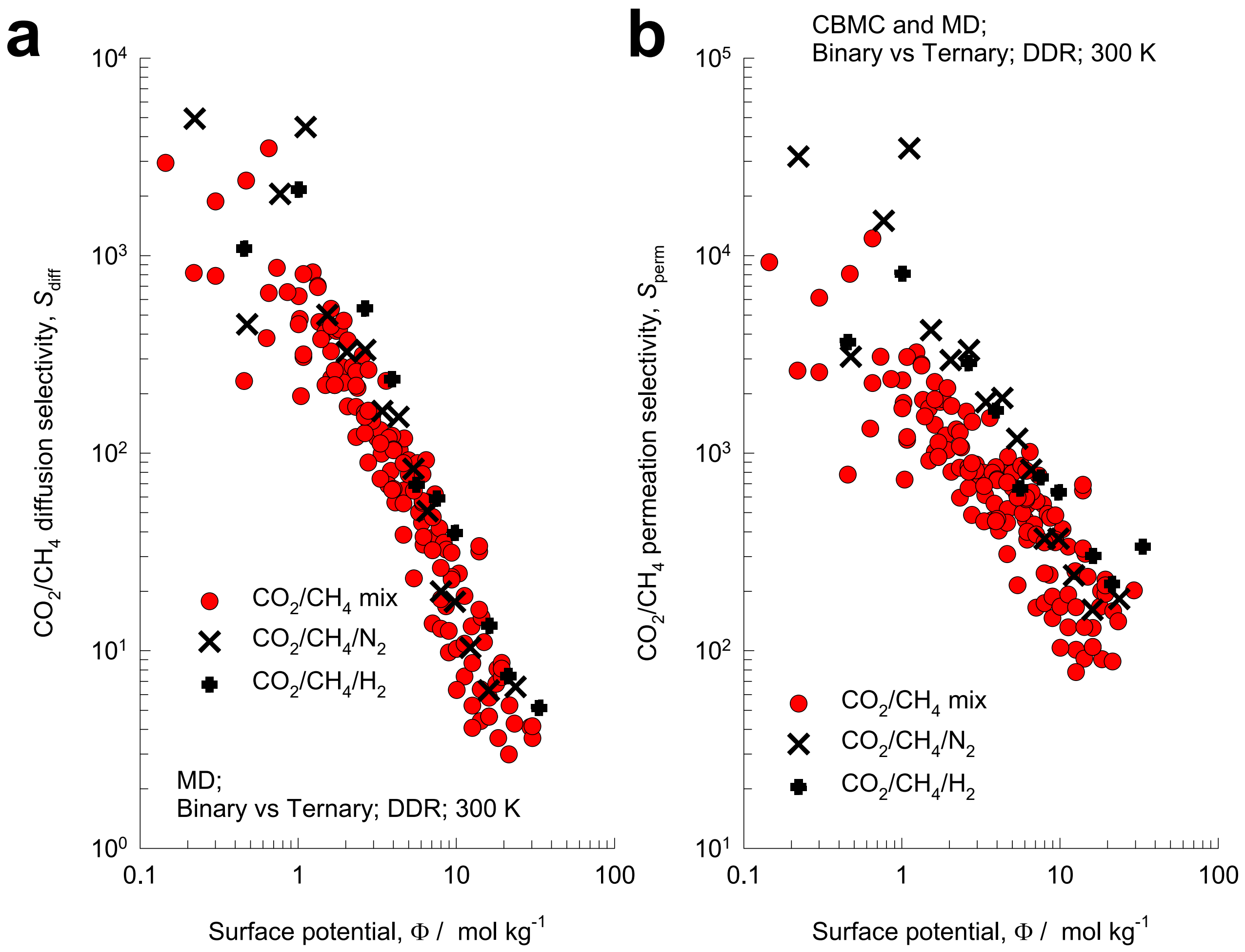

Figure S46. (a) MD simulations of the CO_2/CH_4 diffusion selectivities, S_{diff}, determined from both binary mixtures (five different MD campaigns) and equimolar $(q_1 = q_2 = q_3)$ ternary mixtures in DDR zeolite at 300 K, plotted as function of the surface potential Φ. (b) Plot of the CO_2/CH_4 permeation selectivity S_{perm} as function of the surface potential Φ, determined from binary and ternary MD campaigns.

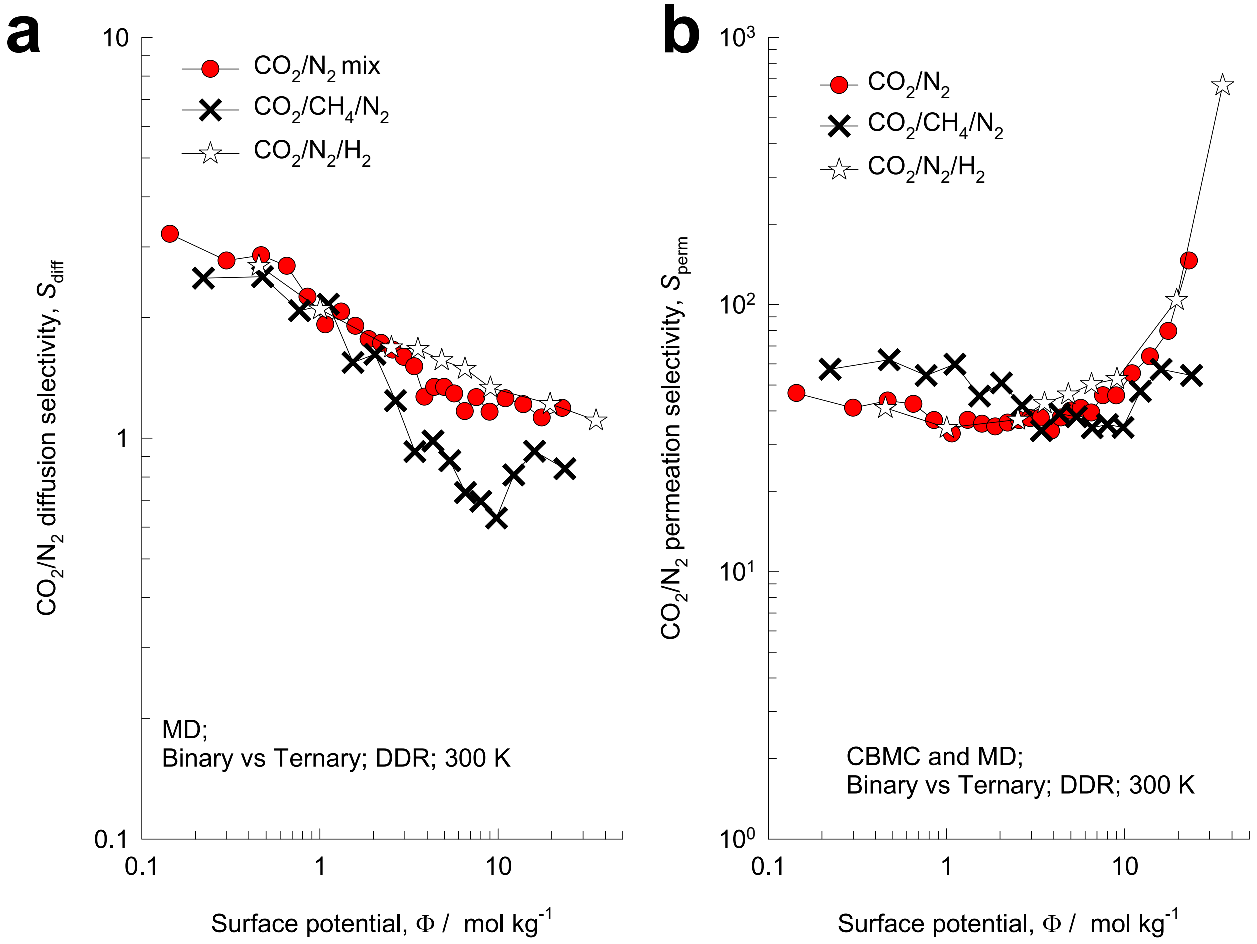

Figure S47. (a) MD simulations of the CO$_2$/N$_2$ diffusion selectivities, S_{diff}, determined from both equimolar $(q_1 = q_2)$ binary and equimolar $(q_1 = q_2 = q_3)$ ternary (CO$_2$/CH$_4$/N$_2$, and CO$_2$/N$_2$/H$_2$) mixtures in DDR zeolite at 300 K, plotted as function of the surface potential Φ. (b) Plot of the CO$_2$/N$_2$ permeation selectivity S_{perm} as function of the surface potential Φ, determined from binary and ternary (CO$_2$/CH$_4$/N$_2$, and CO$_2$/N$_2$/H$_2$) mixtures MD campaigns.

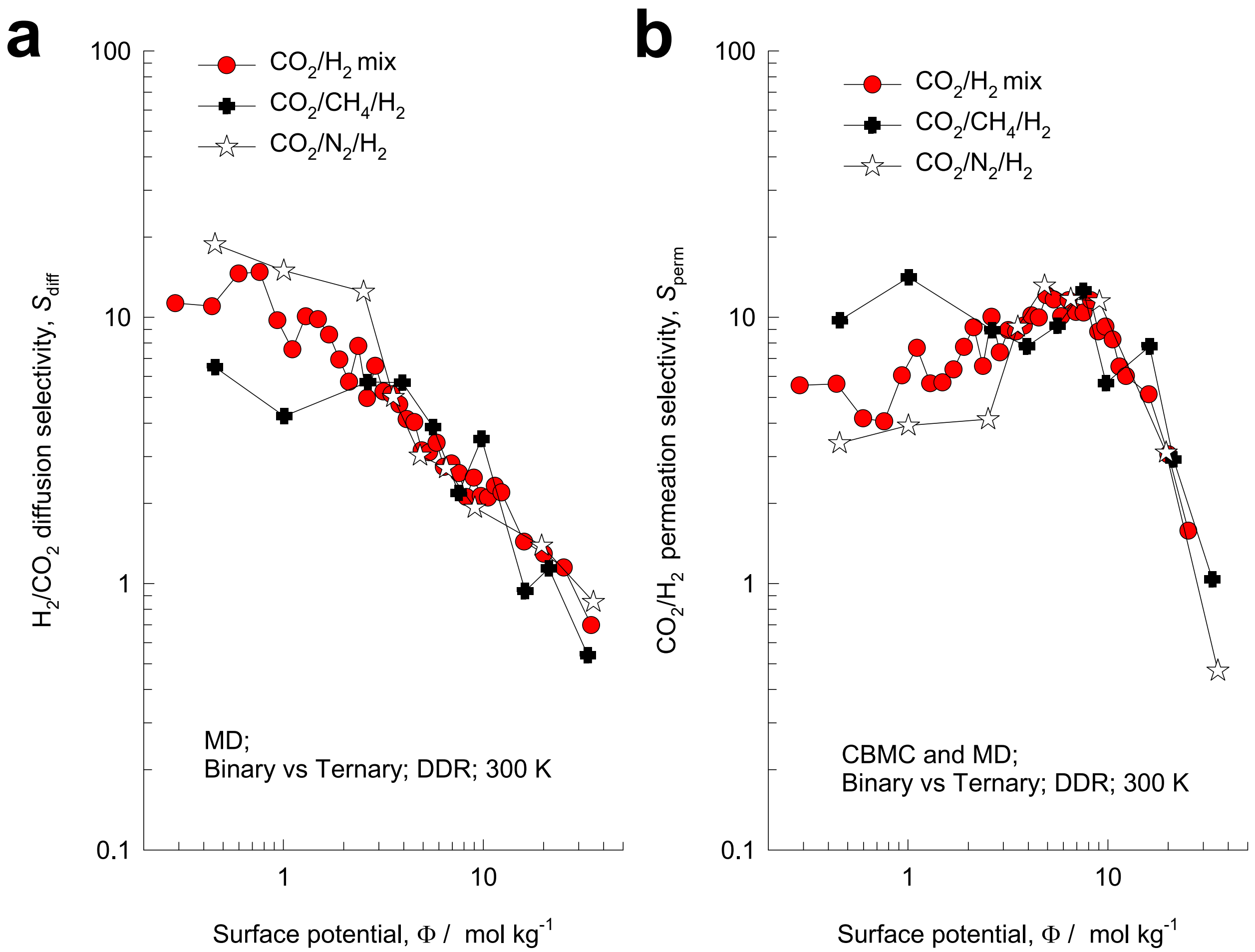

Figure S48. (a) MD simulations of the H_2/CO_2 diffusion selectivities, S_{diff}, determined from both equimolar $(q_1 = q_2)$ binary and equimolar $(q_1 = q_2 = q_3)$ ternary ($CO_2/N_2/H_2$, and $CO_2/CH_4/H_2$) mixtures in DDR zeolite at 300 K, plotted as function of the surface potential Φ. (b) Plot of the CO_2/H_2 permeation selectivity S_{perm} as function of the surface potential Φ, determined from binary and ternary ($CO_2/N_2/H_2$, and $CO_2/CH_4/H_2$) MD campaigns.

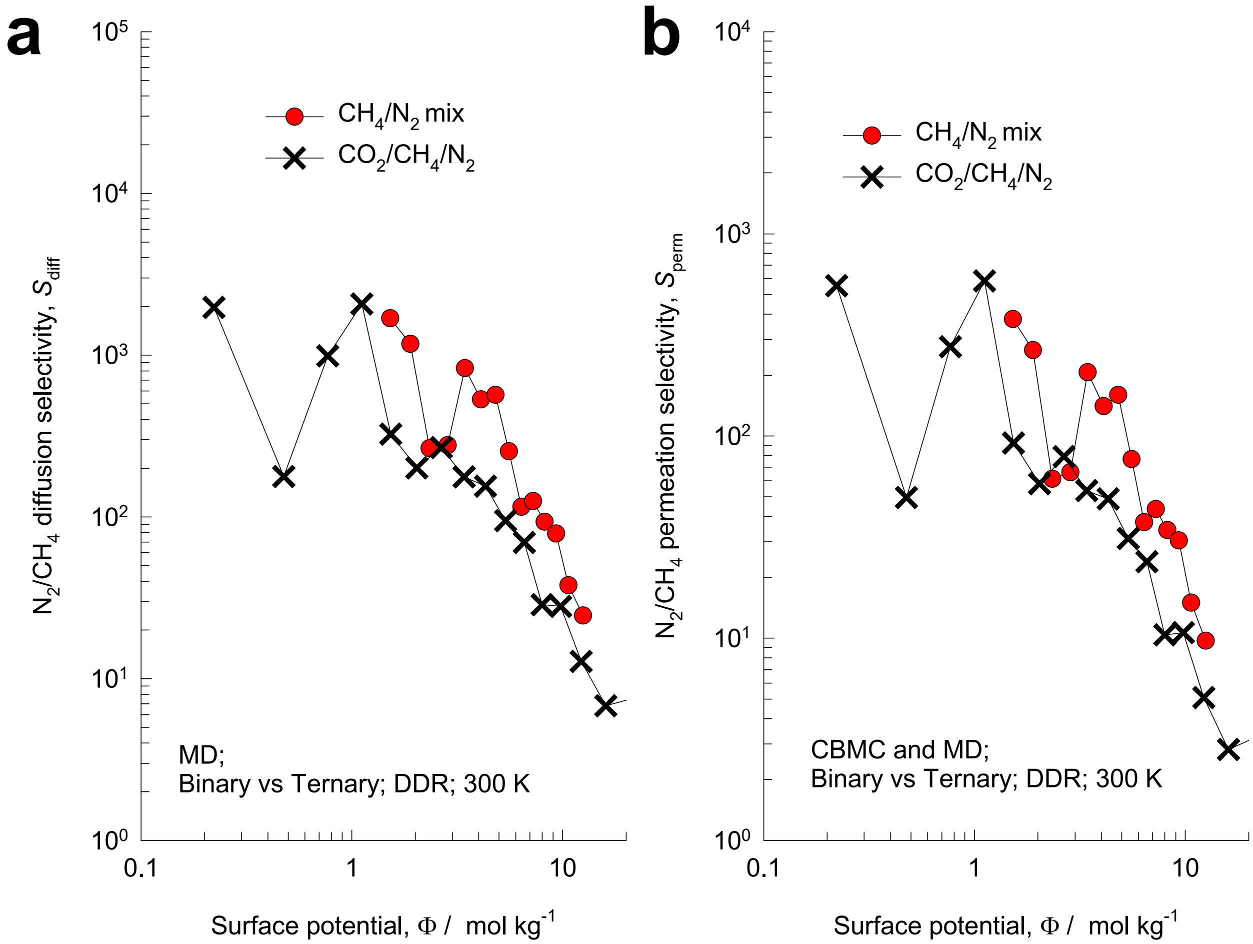

Figure S49. (a) MD simulations of the N_2/CH_4 diffusion selectivities, S_{diff}, determined from both equimolar $(q_1 = q_2)$ binary and equimolar $(q_1 = q_2 = q_3)$ ternary ($CO_2/CH_4/N_2$) mixtures in DDR zeolite at 300 K, plotted as function of the surface potential Φ. (b) Plot of the N_2/CH_4 permeation selectivity S_{perm} as function of the surface potential Φ, determined from binary and ternary MD campaigns.

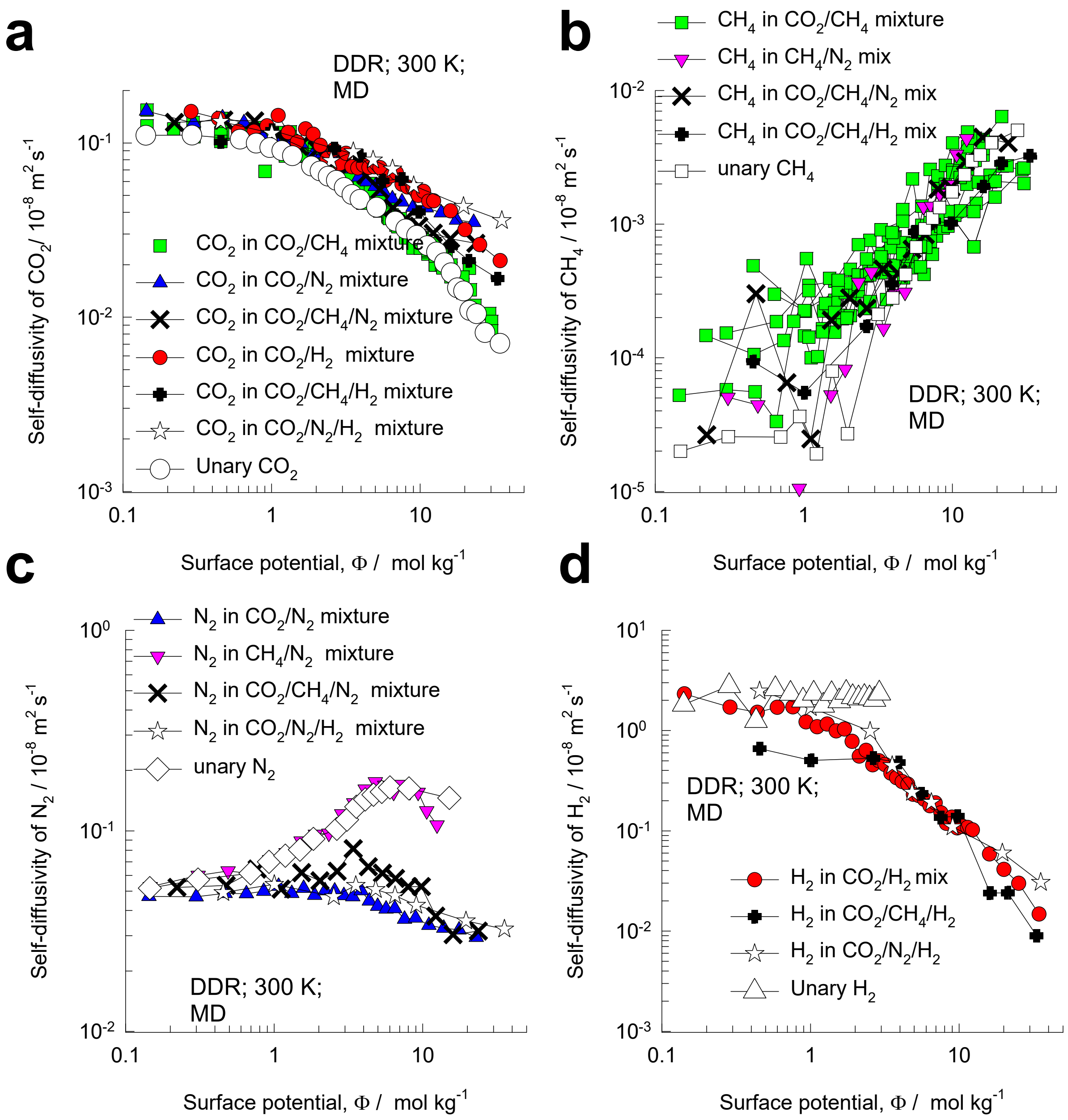

Figure S50. MD simulations of the self-diffusivities, $D_{i,self}$, of (a) CO_2, (b) CH_4, (c) N_2 and (d) H_2 in different equimolar $\left(q_1 = q_2\right)$ binary CO_2/CH_4, CO_2/N_2, CO_2/H_2, CH_4/N_2) and equimolar $\left(q_1 = q_2 = q_3\right)$ ternary ($CO_2/CH_4/N_2$, $CO_2/CH_4/H_2$, $CO_2/N_2/H_2$) mixtures in DDR zeolite at 300 K, plotted as function of the surface potential Φ. Also plotted are the corresponding values of the unary self-diffusivities.

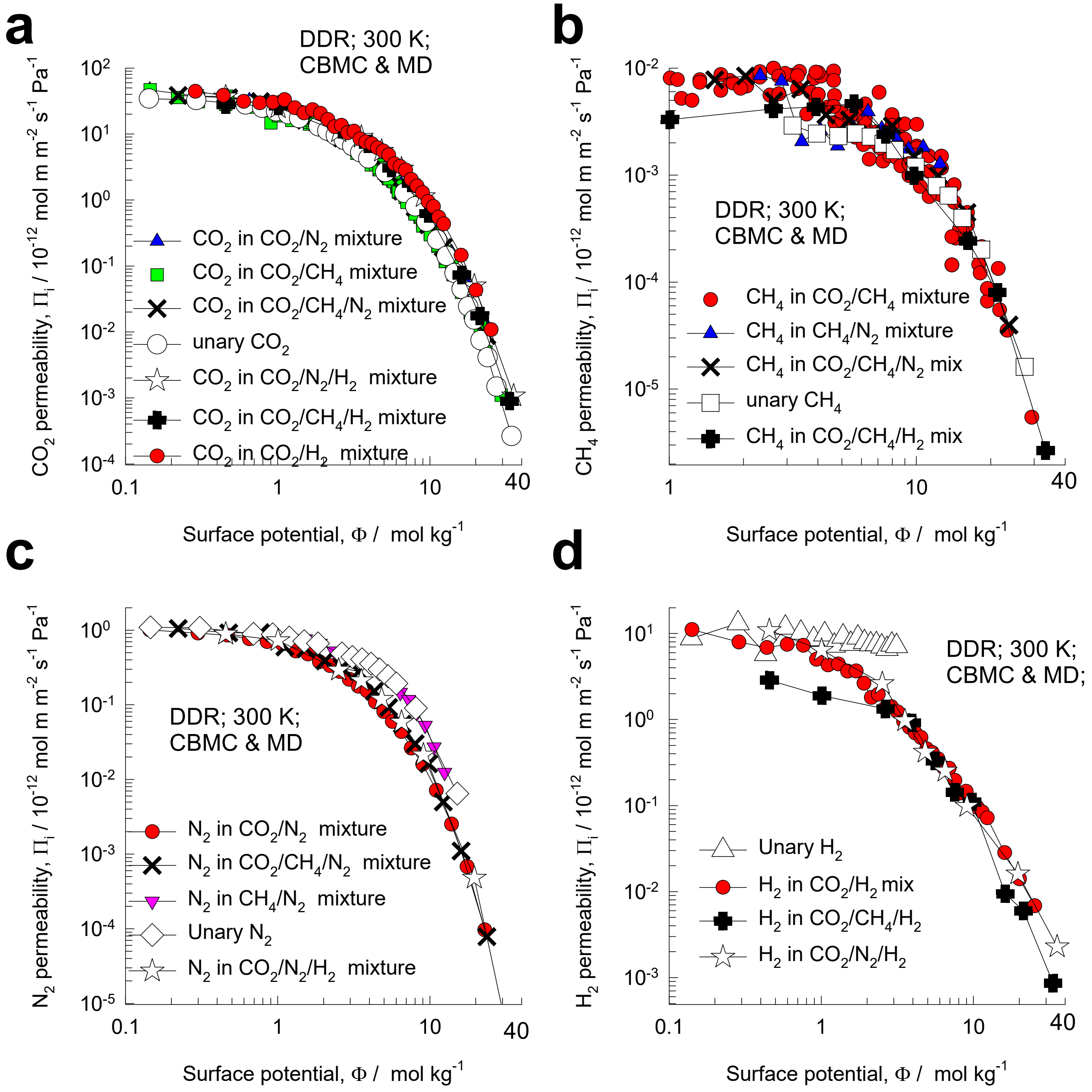

Figure S51. CBMC/MD simulations of the permeabilities, Π_i, of (a) CO_2, (b) CH_4, (c) N_2 and (d) H_2 in different equimolar $(q_1 = q_2)$ binary (CO_2/CH_4, CO_2/N_2, CO_2/H_2, CH_4/N_2, CH_4/H_2) and equimolar $(q_1 = q_2 = q_3)$ ternary ($CO_2/CH_4/N_2$, $CO_2/CH_4/H_2$, $CO_2/N_2/H_2$) mixtures in DDR zeolite at 300 K, plotted as a function of the surface potential Φ. Also plotted are the corresponding values of the unary permeabilities.

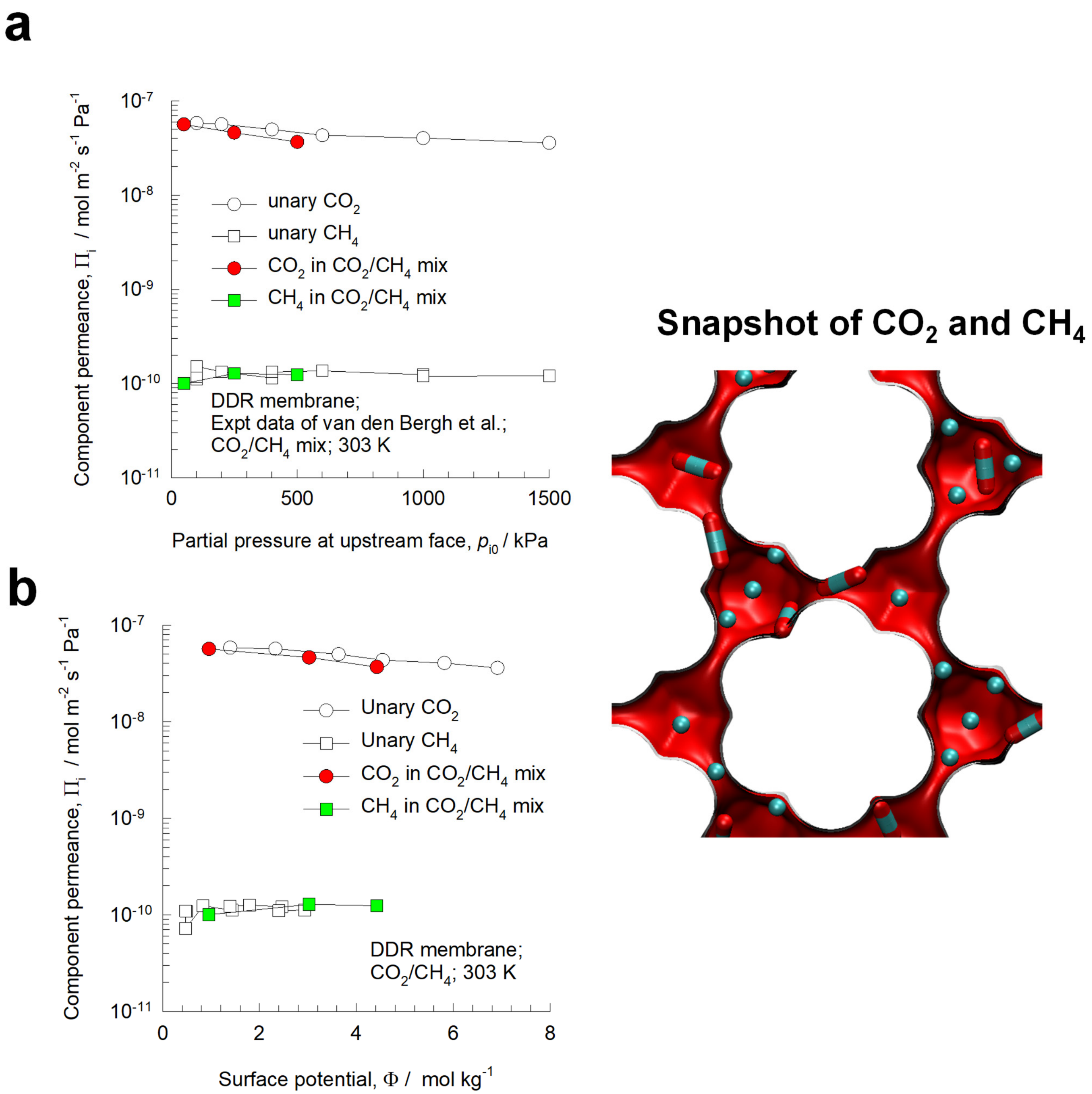

Figure S52. Experimental data of Van den Bergh et al.[68, 69] for component permeances for 50/50 CO_2/CH_4 binary mixture permeation across DDR membrane at 303 K, compared to unary permeation data. The data are plotted as function of (a) upstream partial pressures, p_{i0}, and (b) surface potential Φ at the upstream face of the membrane.

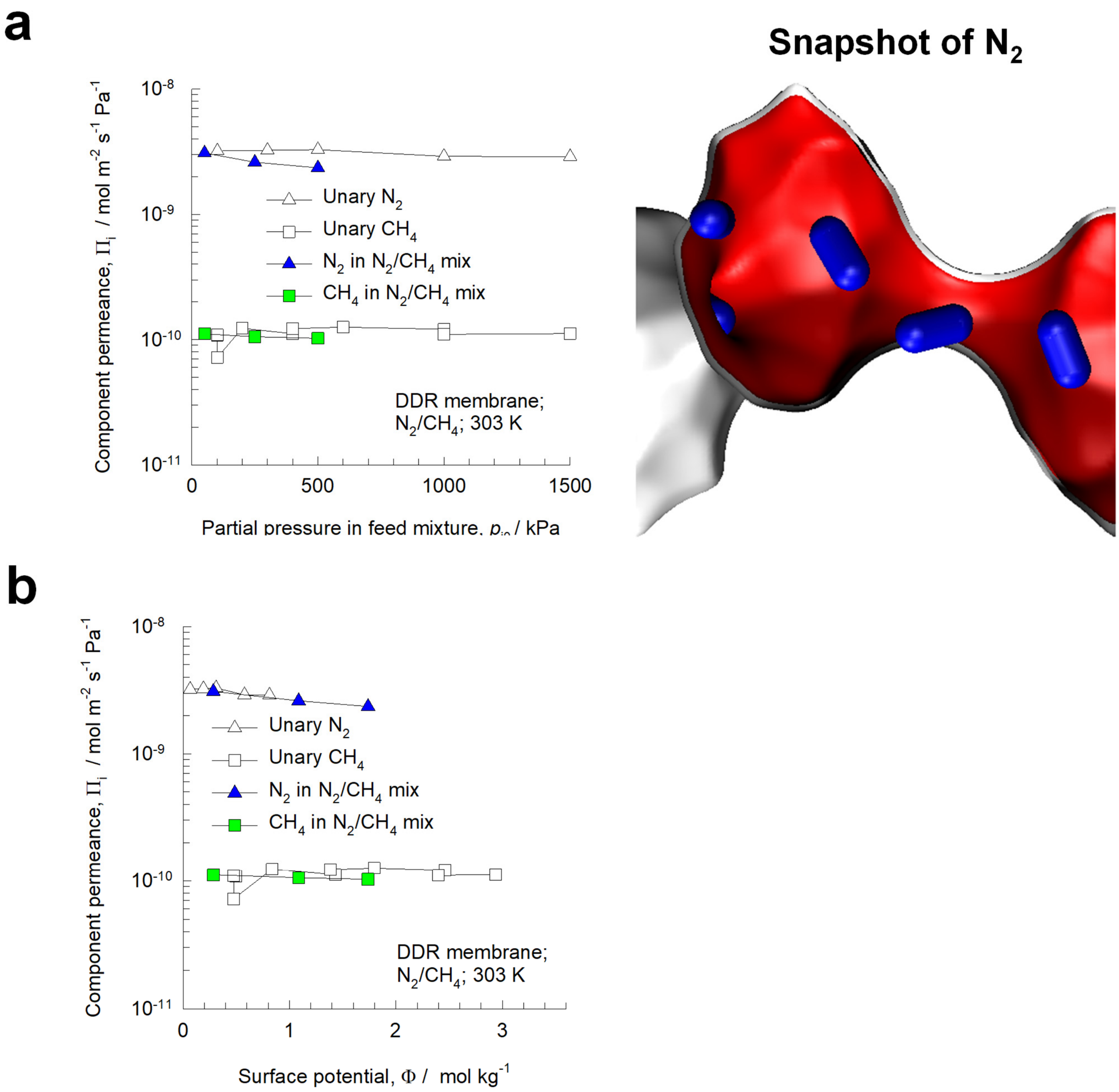

Figure S53. Experimental data of Van den Bergh et al.[68, 69] for component permeances for 50/50 N_2/CH_4 binary mixture permeation across DDR membrane at 303 K, compared to unary permeation data. The data are plotted as function of (a) upstream partial pressures, p_{i0}, and (b) surface potential Φ at the upstream face of the membrane.

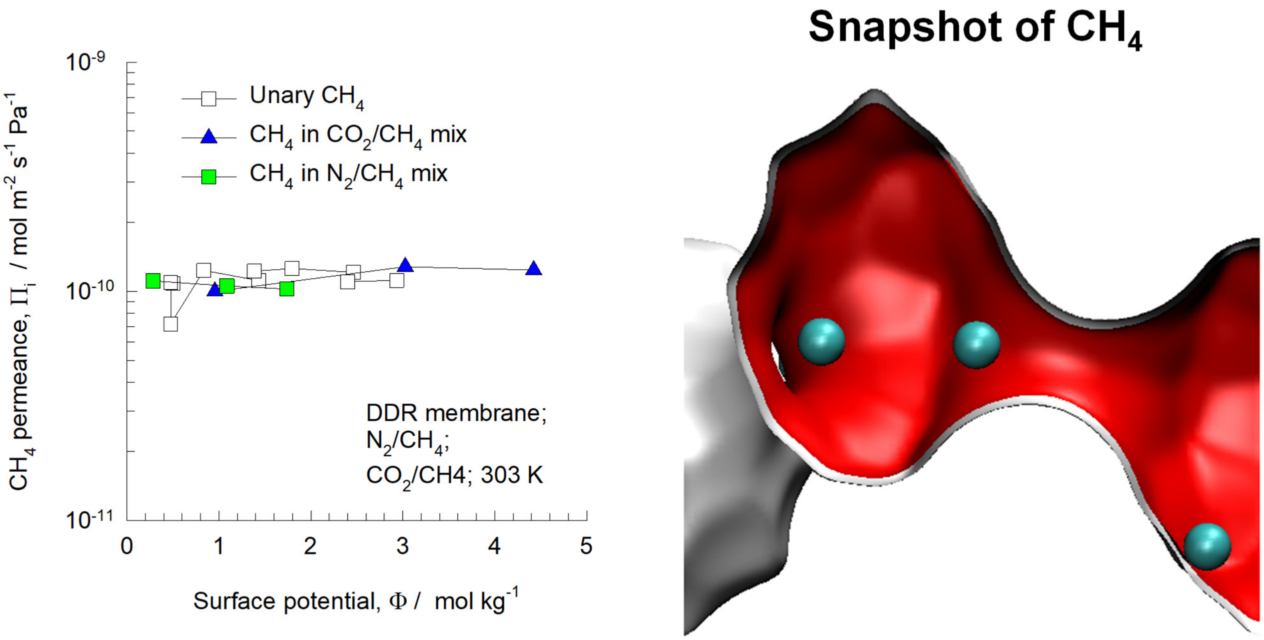

Figure S54. Comparison of CH_4 component permeances for 50/50 CO_2/CH_4 and 50/50 N_2/CH_4 binary mixture permeation across DDR membrane at 303 K, compared to unary permeance. The data are plotted as function of the surface potential Φ at the upstream face of the membrane.

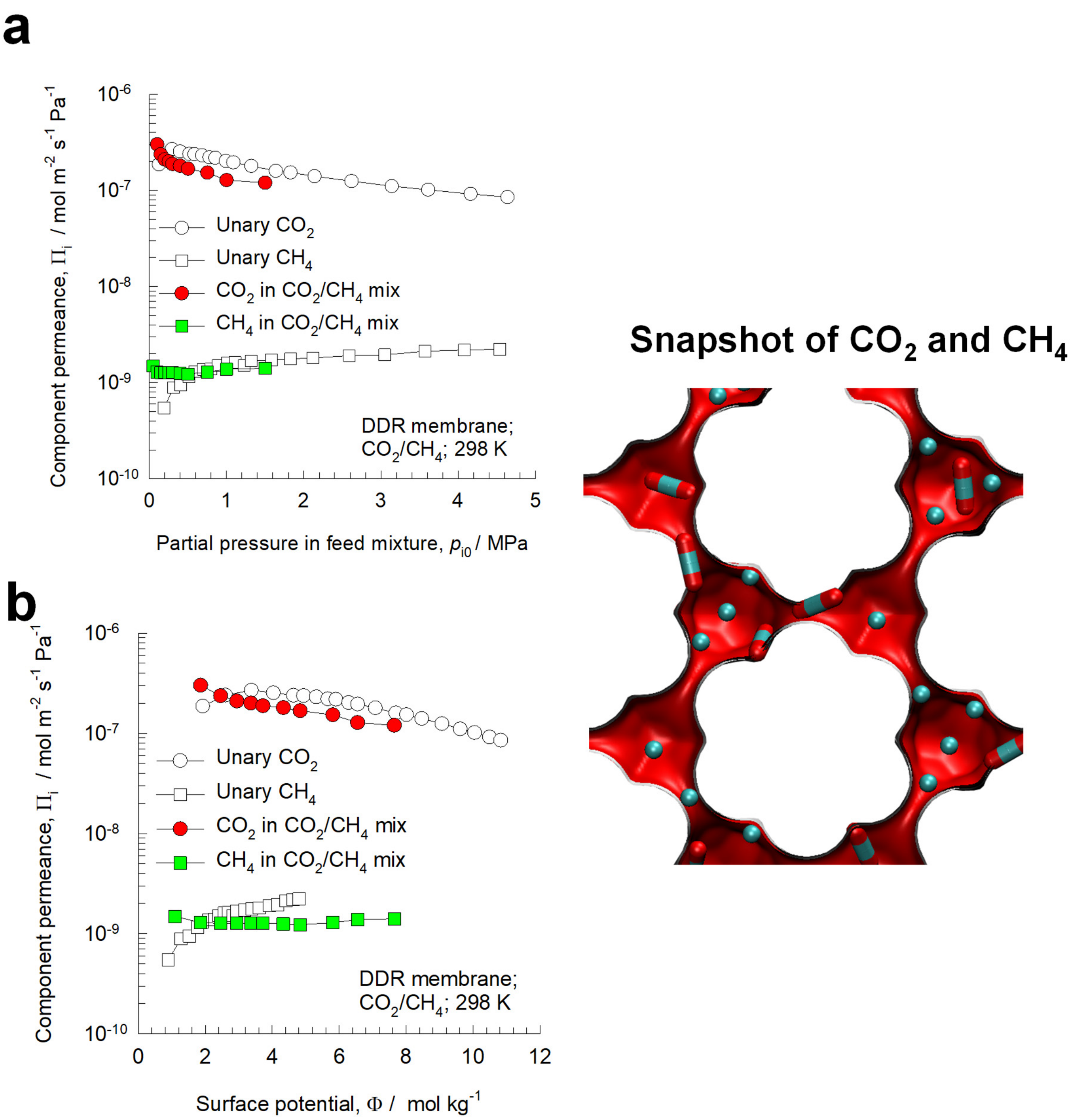

Figure S55. Experimental data of Himeno et al.,[70] scanned from Figures 6, 10, and 11 of their paper, for component permeances for 50/50 CO_2/CH_4 binary mixture permeation across DDR membrane at 298 K, compared to unary permeation data. The data are plotted as function of (a) upstream partial pressures, p_{i0}, and (b) surface potential Φ at the upstream face of the membrane.

9 SAPO-34 membrane permeation: experimental data analysis

SAPO-34 has the same structural topology as CHA zeolite, consisting of cages of volume 316 Å^3, separated by 3.8 Å × 4.2 Å 8-ring windows.

For adsorption in SAPO-34, the model based on statistical thermodynamics described in Chapter 3 of Ruthven[35] is particularly relevant and useful

$$q_i = \frac{q_{i,sat}}{\Omega_i} \frac{b_i f_i + \sum_{m=2}^{\Omega_i} \frac{(b_i f_i)^m}{(m-1)!} \left[\frac{1-\frac{m}{\Omega_i+1}}{1-\frac{1}{\Omega_i+1}} \right]^m}{1 + b_i f_i + \sum_{m=2}^{\Omega_i} \frac{(b_i f_i)^m}{(m)!} \left[\frac{1-\frac{m}{\Omega_i+1}}{1-\frac{1}{\Omega_i+1}} \right]^m} \tag{S84}$$

In Eq (S84) q_i represents the loading in mol kg^{-1}, $q_{i,sat}$ is the saturation loading in mol kg^{-1}, and Ω_i is maximum capacity expressed in molecules per cage. Based on the atomic composition of SAPO-34 used in our experiments of Li et al.,[71] $(Si_{0.061}Al_{0.483}P_{0.455})O_2$; we calculate $q_{i,sat} = 1.369\Omega_i$. The unary isotherms fit parameters are provided in Table S5. The mixture adsorption equilibrium was determined using the IAST.

The unary permeation data for CO_2, CH_4, N_2, and H_2 are summarized in Table S6, Table S7, Table S8, and Table S9.

The binary CO_2/CH_4 mixture permeation data are summarized in Table S10, Table S11; there are two separate campaigns wherein Table S10 provides data in which the feed composition is nearly constant. Table S11 provides the data for campaign in which the feed composition is varied.

The binary CO_2/N_2 mixture permeation data are summarized in Table S12.

The binary N_2/CH_4 mixture permeation data are summarized in Table S13.

SAPO-34 membrane permeation: experimental data analysis

The binary CO_2/H_2 mixture permeation data are summarized in Table S14, and Table S15; there are two separate campaigns wherein Table S14 provides data in which the feed composition is nearly constant. Table S15 provides the data for campaign in which the feed composition is varied.

The permeation data for $CO_2/CH_4/N_2$ mixtures are provided in Table S16.

Experimental data of Li et al.[71-73] for component permeances for CO_2/CH_4, CO_2/N_2, CH_4/N_2, CO_2/H_2 and CH_4/H_2 mixtures in SAPO-34 membrane at 295 K are compared to unary permeation data in Figure S56, Figure S57, Figure S58, and Figure S59, and Figure S60. The permeance data are plotted as function of (a) upstream partial pressures, p_{i0}, and (b) the surface potential Φ at the upstream face of the membrane.

Experimental data of Li et al.[71-73] for permeances of CO_2, CH_4, N_2, and H_2 determined for unary, binary, and ternary $CO_2/CH_4/N_2$ mixture permeation across SAPO-34 membrane at 295 K are summarized in Figure S61a,b,c,d data are plotted, as function of the upstream partial pressures, p_{i0}. Compared at the same component pressures at the upstream face, p_{i0}, the CO_2 permeance is hardly influenced by the presence or choice of the partner species in the mixtures. However, the values of CO_2 permeance in any mixture is lower than the values for unary CO_2 permeation. The situation is markedly different for the permeances of CH_4, N_2, and H_2. For these less-strongly-adsorbed guest molecules, the component permeances in a binary or ternary mixture depends on choice of the partner species. The component permeance of CH_4, N_2, and H_2 in mixtures are significantly lower than the corresponding unary permeances. On the basis of the data in Figure S61 we would conclude that the mixture permeation characteristics cannot be estimated on the basis of experimental data on unary permeances. Also, generally speaking, the permeation characteristics of *i-j* pairs in the ternary mixture are also not identifiable with the corresponding binary mixtures..[35]

In Figure S62, the same set of data on component permeances are plotted as function of the surface potential Φ at the upstream face of the membrane. These plots show that the component permeances in unaries, and binary mixtures are the same as in the ternary $CO_2/CH_4/N_2$ mixtures provided the comparison is made on the basis of the surface potential Φ. These results are precisely analogous to those obtained from CBMC/MD simulations and presented in Figure S38 for CHA zeolite.

SAPO-34 membrane permeation: experimental data analysis

Figure S63 compares the CO_2/CH_4, CO_2/N_2, and N_2/CH_4 permeation selectivities in binary and ternary mixtures for mixture permeation across SAPO-34 membrane at 295 K. Plotted as function of the surface potential Φ at the upstream face of the membrane, the permeation selectivities of the three pairs are of comparable magnitude in both binary mixtures and ternary mixtures. These data also suggest that the permeation selectivities in mixtures can be estimated to a reasonably fair accuracy on the basis of unary permeances, determined at the same surface potential Φ. These results are analogous to those obtained from CBMC/MD simulations and presented in Figure S36 for CHA zeolite.

9.1 List of Tables for SAPO-34 membrane permeation: experimental data analysis

Table S5. Pure component isotherm fit data for guest species in SAPO-34, as tabulated in Li et al.[71]

Molecule	b_i	Ω_i	$q_{i,sat}$
CO_2	7.67×10^{-5}	6	8.2
CH_4	5.87×10^{-6}	6	8.2
N_2	1.26×10^{-6}	6	8.2
H_2	2.84×10^{-7}	9	12.3

b_i is expressed in Pa^{-1}, Ω_i in molecules per cage, $q_{i,sat}$ in mol kg^{-1}.

Table S6. Unary CO_2 permeation data.

Upstream pressure, $f_{i,up}$	Downstream pressure, $f_{i,down}$	CO_2 flux, N_i
0.094	0.084	0.0033
0.118	0.084	0.0122
0.153	0.084	0.0228
0.222	0.084	0.0412
0.291	0.084	0.0589
0.360	0.084	0.0719
0.429	0.084	0.0825
0.773	0.084	0.1293
1.463	0.084	0.1857
2.152	0.084	0.2150
2.842	0.084	0.2377
3.531	0.084	0.2531
4.221	0.084	0.2657
4.910	0.084	0.2784
5.600	0.084	0.2903

$f_{i,up}$ and $f_{i,down}$ have the units MPa, N_i are expressed in mol m^{-2} s^{-1}

Table S7. Unary CH_4 permeation data.

Upstream pressure, $f_{i,up}$	Downstream pressure, $f_{i,down}$	CH_4 flux, N_i
0.43	0.084	0.0012
0.77	0.084	0.0025
1.46	0.084	0.0048
2.15	0.084	0.0072
2.84	0.084	0.0093
3.53	0.084	0.0111
4.22	0.084	0.0133
4.91	0.084	0.0154
5.60	0.084	0.0175
6.29	0.084	0.0197
7.08	0.084	0.0220

$f_{i,up}$ and $f_{i,down}$ have the units MPa, N_i are expressed in mol m^{-2} s^{-1}

Table S8. Unary N_2 permeation data.

Upstream pressure, $f_{i,up}$	Downstream pressure, $f_{i,down}$	N_2 flux, N_i
0.43	0.084	0.009
0.77	0.084	0.017
1.46	0.084	0.027
2.15	0.084	0.041
2.84	0.084	0.053
3.53	0.084	0.065
4.22	0.084	0.077
4.91	0.084	0.087
5.60	0.084	0.098
6.29	0.084	0.108
6.98	0.084	0.119

$f_{i,up}$ and $f_{i,down}$ have the units MPa, N_i are expressed in mol m^{-2} s^{-1}

Table S9. Unary H_2 permeation data.

Upstream pressure, $f_{i,up}$	Downstream pressure, $f_{i,down}$	H_2 flux, N_i
0.77	0.084	0.0688
1.46	0.084	0.1394
2.15	0.084	0.2114
2.84	0.084	0.2839
3.53	0.084	0.3524
4.22	0.084	0.4263
4.91	0.084	0.4926

$f_{i,up}$ and $f_{i,down}$ have the units MPa, N_i are expressed in mol m^{-2} s^{-1}

Table S10. CO_2/CH_4 permeation data.

Total upstream pressure f_{up}	CO_2 upstream partial pressure $f_{1,up}$	CH_4 upstream partial pressure $f_{2,up}$	CO_2 downstream partial pressure $f_{1,down}$	CH_4 downstream partial pressure $f_{2,down}$	CO_2 flux N_1	CH_4 flux N_2
0.77	0.37	0.40	0.083	0.0013	0.064	0.0010
1.46	0.69	0.77	0.083	0.0014	0.102	0.0017
2.50	1.14	1.35	0.083	0.0014	0.140	0.0024
3.88	1.72	2.14	0.082	0.0017	0.171	0.0035
5.26	2.27	2.95	0.082	0.0018	0.196	0.0044
6.70	2.82	3.83	0.082	0.0020	0.221	0.0055
7.19	3.00	4.13	0.082	0.0021	0.228	0.0059

$f_{i,up}$ and $f_{i,down}$ have the units MPa, N_i are expressed in mol m^{-2} s^{-1}

Table S11. Binary CO_2/CH_4 permeation data with varying compositions at constant upstream total pressure = 3.53 MPa.

Mole fraction of CO_2 in upstream compartment	CO_2 upstream partial pressure $f_{1,up}$	CH_4 upstream partial pressure $f_{2,up}$	CO_2 downstream partial pressure $f_{1,down}$	CH_4 downstream partial pressure $f_{2,down}$	CO_2 flux N_1	CH_4 flux N_2
0.35	1.24	2.29	0.082	0.0025	0.131	0.00400
0.45	1.59	1.93	0.082	0.0016	0.163	0.00309
0.59	2.09	1.44	0.083	0.0009	0.193	0.00198
0.83	2.92	0.60	0.084	0.0002	0.240	0.00065

$f_{i,up}$ and $f_{i,down}$ have the units MPa, N_i are expressed in mol m^{-2} s^{-1}

Table S12. Binary CO_2/N_2 permeation data.

Total upstream pressure f_{up}	CO_2 upstream partial pressure $f_{1,up}$	N_2 upstream partial pressure $f_{2,up}$	CO_2 downstream partial pressure $f_{1,down}$	N_2 downstream partial pressure $f_{2,down}$	CO_2 flux N_1	N_2 flux N_2
0.77	0.39	0.38	0.079	0.005	0.065	0.0037
1.46	0.72	0.74	0.080	0.004	0.108	0.0059
2.15	1.04	1.11	0.079	0.005	0.136	0.0091
2.83	1.35	1.48	0.079	0.005	0.154	0.0107
3.52	1.66	1.86	0.078	0.006	0.168	0.0122

$f_{i,up}$ and $f_{i,down}$ have the units MPa, N_i are expressed in mol m^{-2} s^{-1}

Table S13. Binary N_2/CH_4 permeation data.

Total upstream pressure f_{up}	N_2 upstream partial pressure $f_{1,up}$	CH_4 upstream partial pressure $f_{2,up}$	N_2 downstream partial pressure $f_{1,down}$	CH_4 downstream partial pressure $f_{2,down}$	N_2 flux N_1	CH_4 flux N_2
0.773	0.386	0.388	0.079	0.005	0.065	0.0037
1.463	0.728	0.735	0.080	0.004	0.108	0.0059
2.152	1.069	1.084	0.079	0.005	0.136	0.0091
2.842	1.409	1.433	0.079	0.005	0.154	0.0107
3.531	1.748	1.783	0.078	0.006	0.168	0.0122

$f_{i,up}$ and $f_{i,down}$ have the units MPa, N_i are expressed in mol m^{-2} s^{-1}

Table S14. CO_2/H_2 permeation data.

Total upstream pressure f_{up}	CO_2 upstream partial pressure $f_{1,up}$	H_2 upstream partial pressure $f_{2,up}$	CO_2 downstream partial pressure $f_{1,down}$	H_2 downstream partial pressure $f_{2,down}$	CO_2 flux N_1	H_2 flux N_2
0.773	0.369	0.404	0.076	0.0080	0.0734	0.0077
2.145	0.968	1.178	0.077	0.0074	0.1405	0.0136
3.509	1.517	1.992	0.077	0.0065	0.1792	0.0151
4.868	2.048	2.821	0.079	0.0055	0.1993	0.0139

$f_{i,up}$ and $f_{i,down}$ have the units MPa, N_i are expressed in mol m^{-2} s^{-1}

Table S15. CO_2/H_2 permeation data with varying feed compositions

Total upstream pressure f_{up}	CO_2 upstream partial pressure $f_{1,up}$	H_2 upstream partial pressure $f_{2,up}$	CO_2 downstream partial pressure $f_{1,down}$	H_2 downstream partial pressure $f_{2,down}$	CO_2 flux N_1	H_2 flux N_2
0.773	0.211	0.562	0.0569	0.0271	0.0356	0.0170
0.773	0.135	0.638	0.0433	0.0407	0.0271	0.0254
1.462	0.247	1.215	0.0546	0.0294	0.0546	0.0294
1.462	0.390	1.072	0.0622	0.0218	0.0621	0.0218
2.151	0.352	1.799	0.0602	0.0238	0.0766	0.0302
2.151	0.564	1.588	0.0643	0.0197	0.0817	0.0251
3.526	0.548	2.978	0.0643	0.0197	0.1081	0.0330
3.527	0.896	2.631	0.0665	0.0175	0.1118	0.0294
4.898	0.729	4.169	0.0658	0.0182	0.1322	0.0366
4.901	1.209	3.692	0.0686	0.0154	0.1380	0.0309

$f_{i,up}$ and $f_{i,down}$ have the units MPa, N_i are expressed in mol m^{-2} s^{-1}

Table S16. Ternary CO_2 /CH_4/N_2 permeation data.

CO_2 $f_{1,up}$	CH_4 $f_{2,up}$	N_2 $f_{3,up}$	CO_2 $f_{1,down}$	CH_4 $f_{2,down}$	N_2 $f_{3,down}$	CO_2 flux N_1	CH_4 flux N_2	N_2 flux N_3
0.26	0.26	0.25	0.0784	0.0011	0.0045	0.039	0.0006	0.0023
0.49	0.50	0.47	0.0784	0.0012	0.0044	0.070	0.0011	0.0039
0.94	0.98	0.93	0.0782	0.0014	0.0044	0.103	0.0019	0.0058
1.38	1.45	1.38	0.0780	0.0016	0.0044	0.126	0.0025	0.0072
1.78	1.88	1.80	0.0778	0.0017	0.0044	0.139	0.0031	0.0079

$f_{i,up}$ and $f_{i,down}$ have the units MPa, N_i are expressed in mol m^{-2} s^{-1}

9.2 List of Figures for SAPO-34 membrane permeation: experimental data analysis

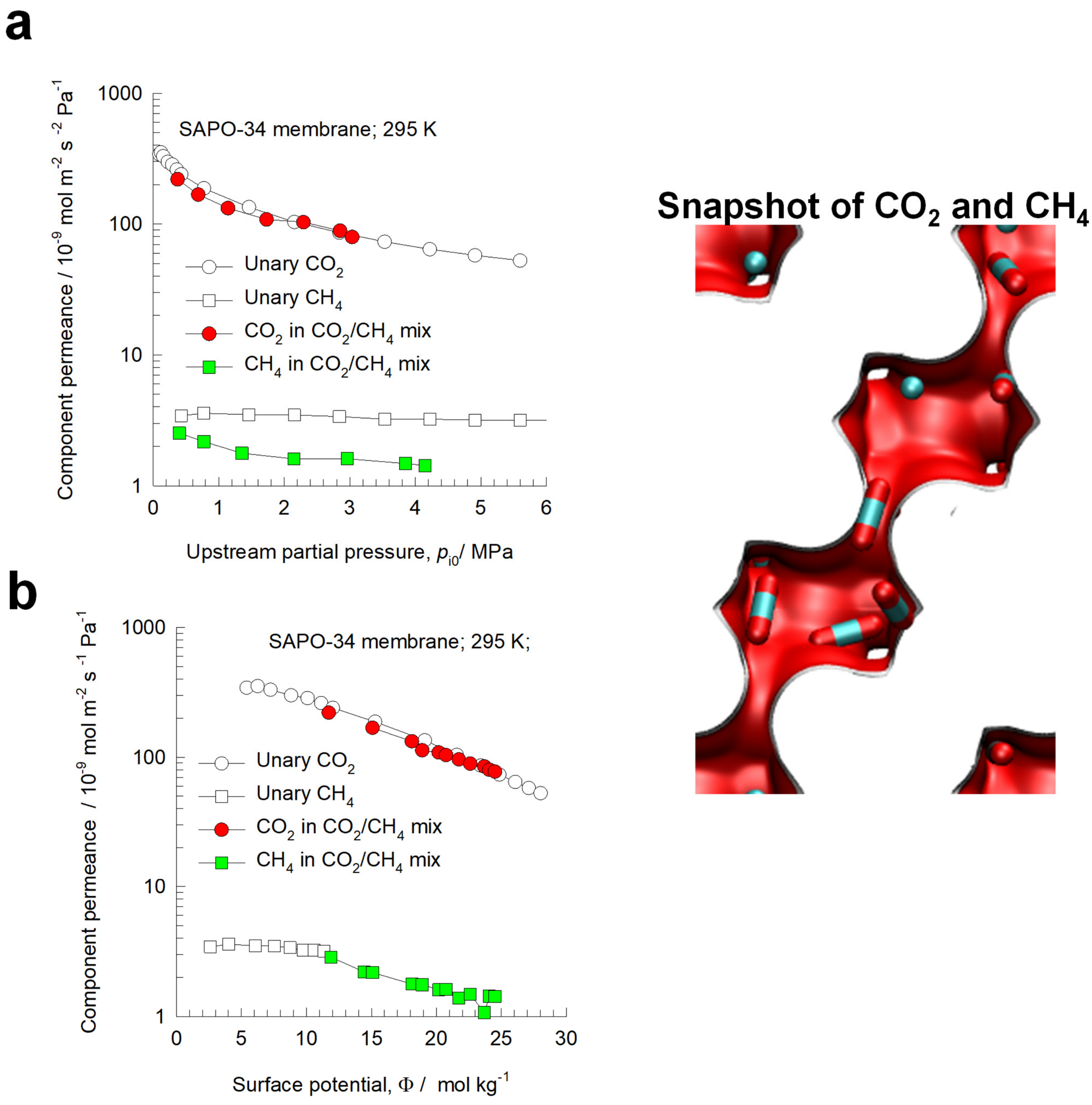

Figure S56. Experimental data of Li et al.[71-73] for component permeances for CO_2/CH_4 mixtures in SAPO-34 membrane at 295 K, compared to unary permeation data. The data are plotted as function of (a) upstream partial pressures, p_{i0},, and (b) surface potential Φ at the upstream face of the membrane.

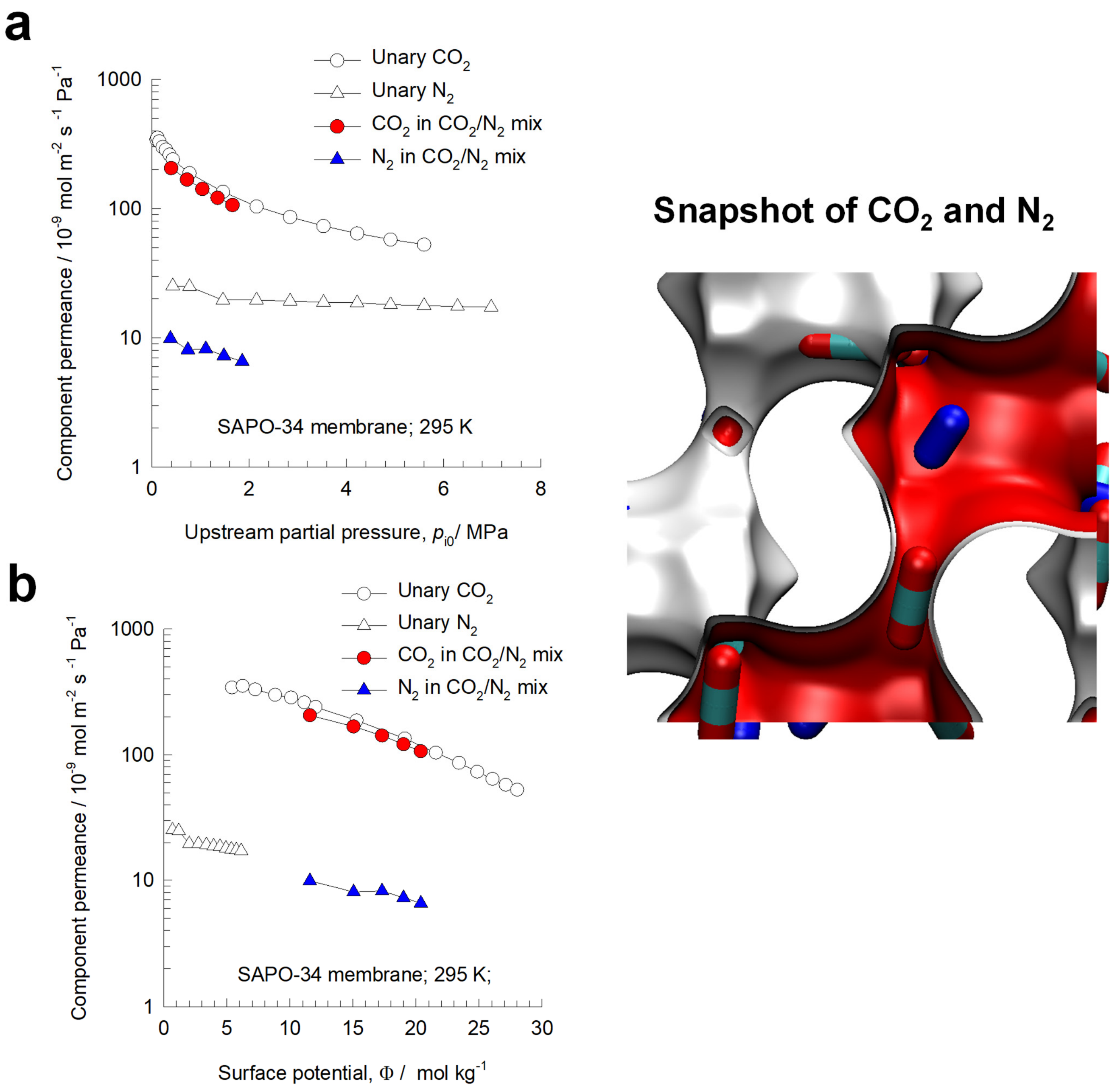

Figure S57. Experimental data of Li et al.[71-73] for component permeances for CO_2/N_2 mixtures in SAPO-34 membrane at 295 K, compared to unary permeation data. The data are plotted as function of (a) upstream partial pressures, p_{i0}, and (b) surface potential Φ at the upstream face of the membrane.

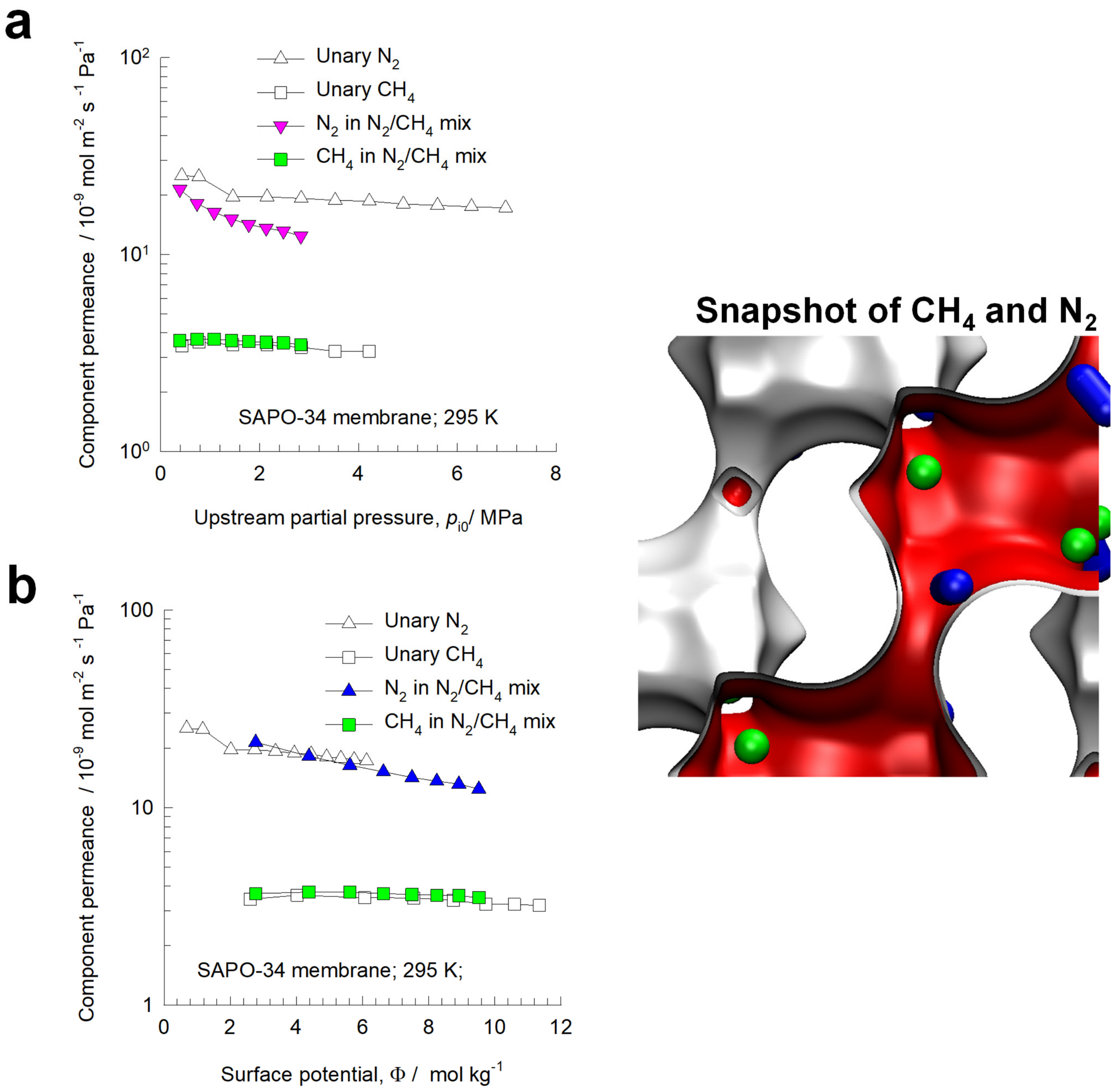

Figure S58. Experimental data of Li et al.[71-73] for component permeances for CH_4/N_2 mixtures in SAPO-34 membrane at 295 K, compared to unary permeation data. The data are plotted as function of (a) upstream partial pressures, p_{i0}, and (b) surface potential Φ at the upstream face of the membrane.

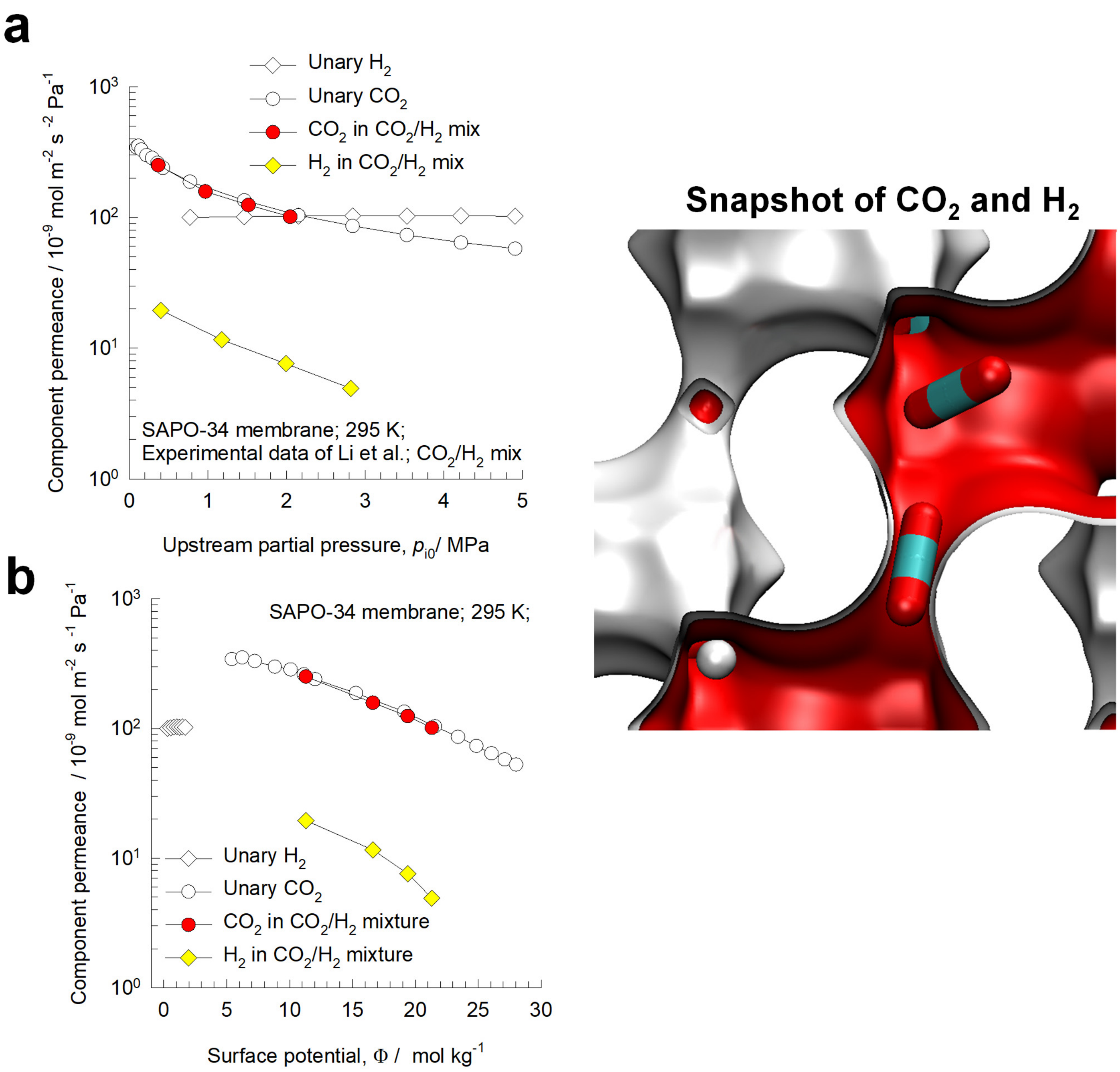

Figure S59. Experimental data of Li et al.[71-73] for component permeances for CO_2/H_2 mixtures in SAPO-34 membrane at 295 K, compared to unary permeation data. The data are plotted as function of (a) upstream partial pressures, p_{i0},, and (b) surface potential Φ at the upstream face of the membrane.

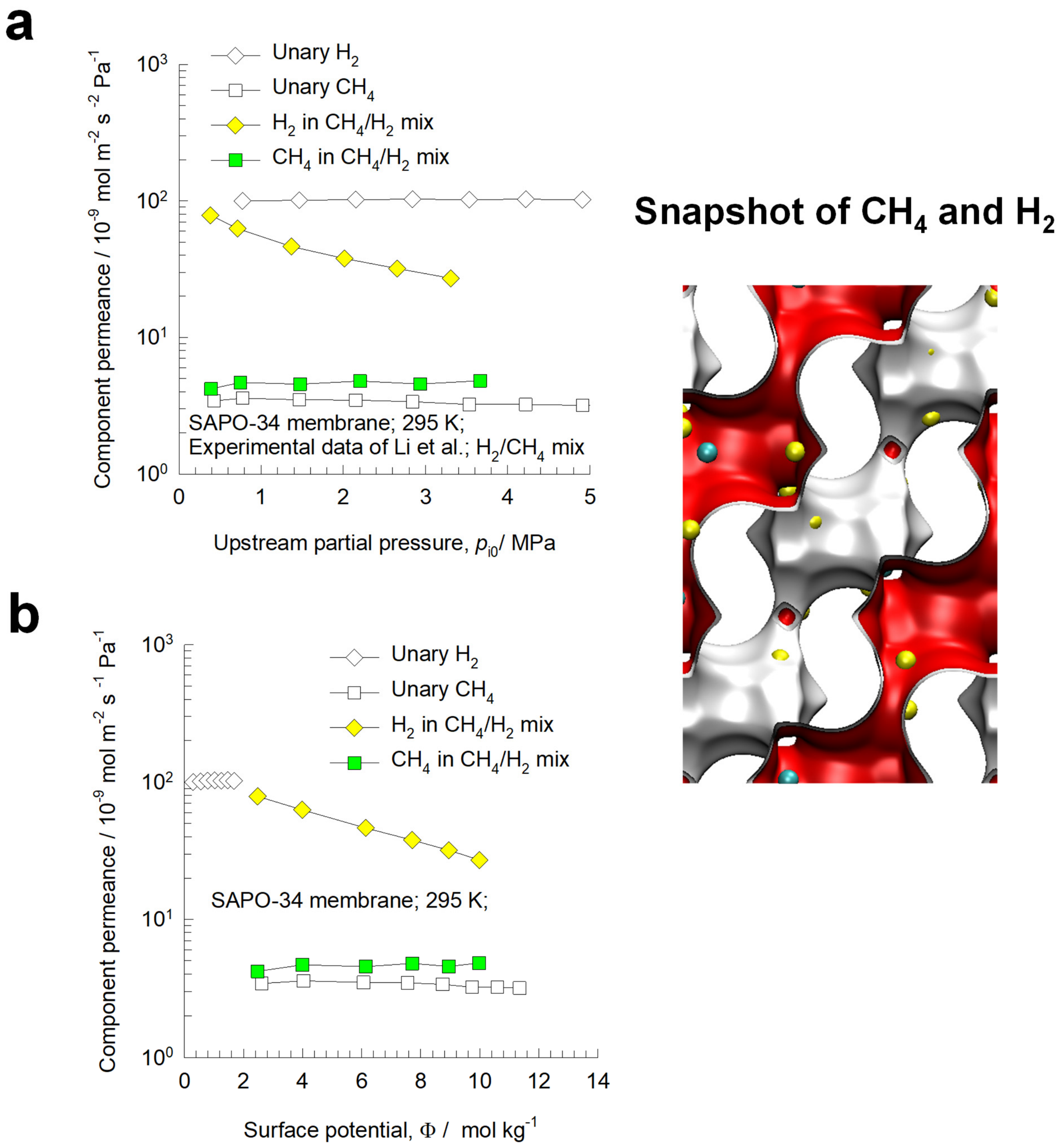

Figure S60. Experimental data of Li et al.[71-73] for component permeances for CH_4/H_2 mixtures in SAPO-34 membrane at 295 K, compared to unary permeation data. The data are plotted as function of (a) upstream partial pressures, p_{i0}, and (b) surface potential Φ at the upstream face of the membrane.

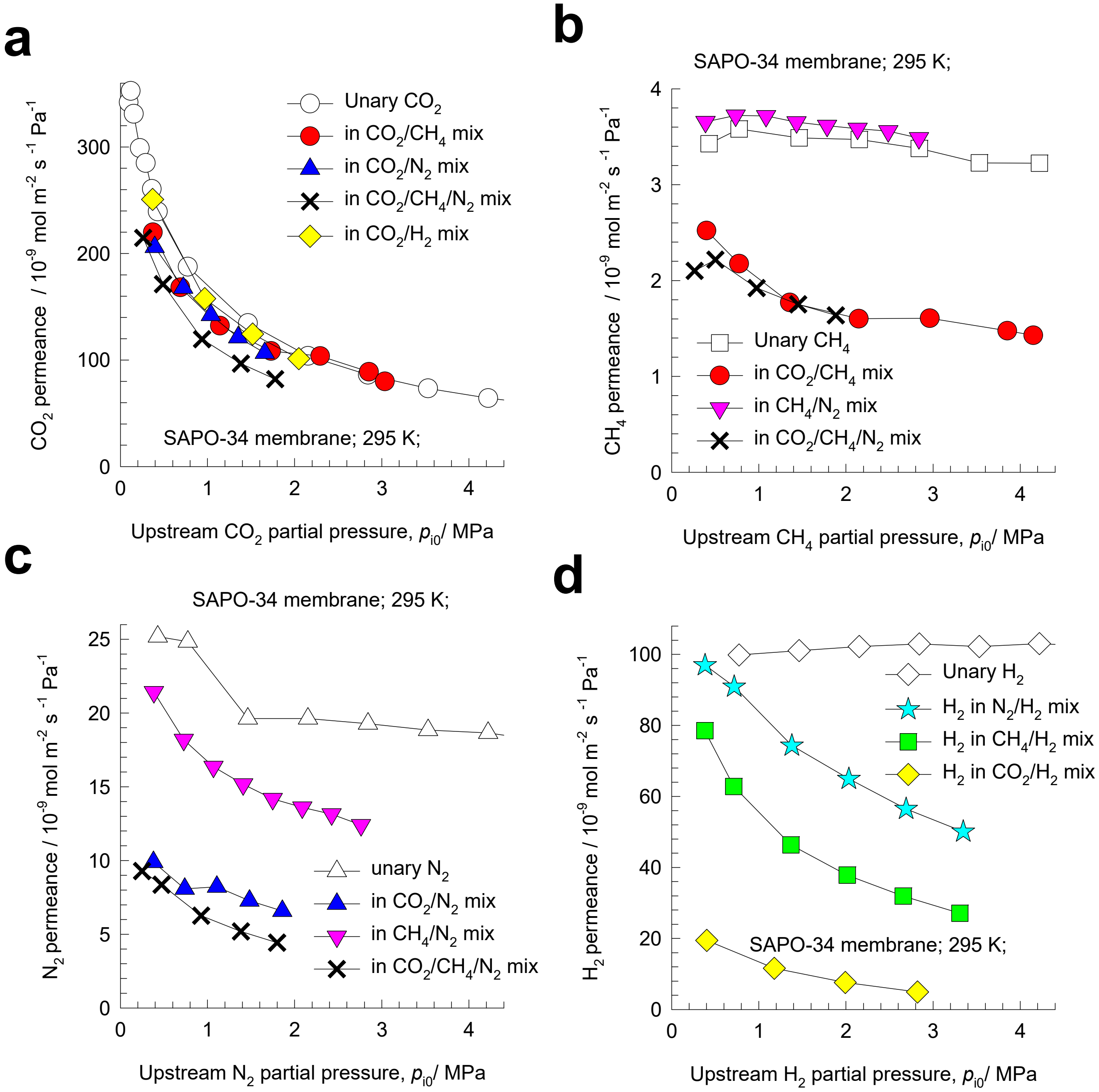

Figure S61. Summary of the experimental data of Li et al.[71-73] for permeances of CO_2, CH_4, N_2 and H_2, determined for equimolar binary (filled symbols) and ternary (crosses) mixture permeation across SAPO-34 membrane at 295 K, compared with unary permeance, plotted as function of the upstream partial pressures, p_{i0}.

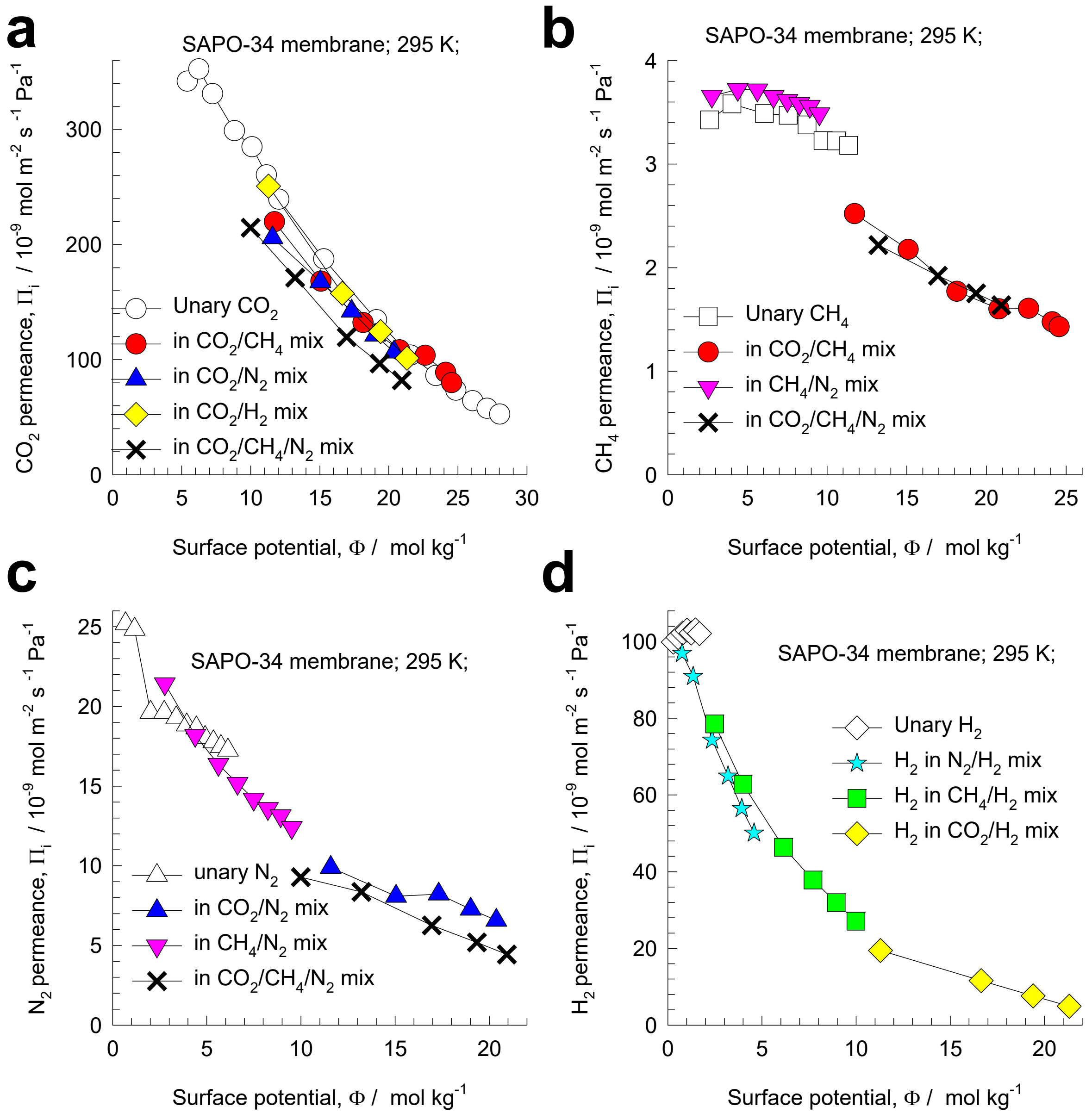

Figure S62. (a, b, c, d) Re-analysis of the experimental data of Li et al.[71-73] for permeances of (a) CO_2, (b) CH_4, (c) N_2 and (d) H_2, determined for equimolar binary (filled symbols) and ternary (crosses) mixture permeation across SAPO-34 membrane at 295 K, compared with unary permeance, when plotted as function of the surface potential Φ at the upstream face of the membrane.

.

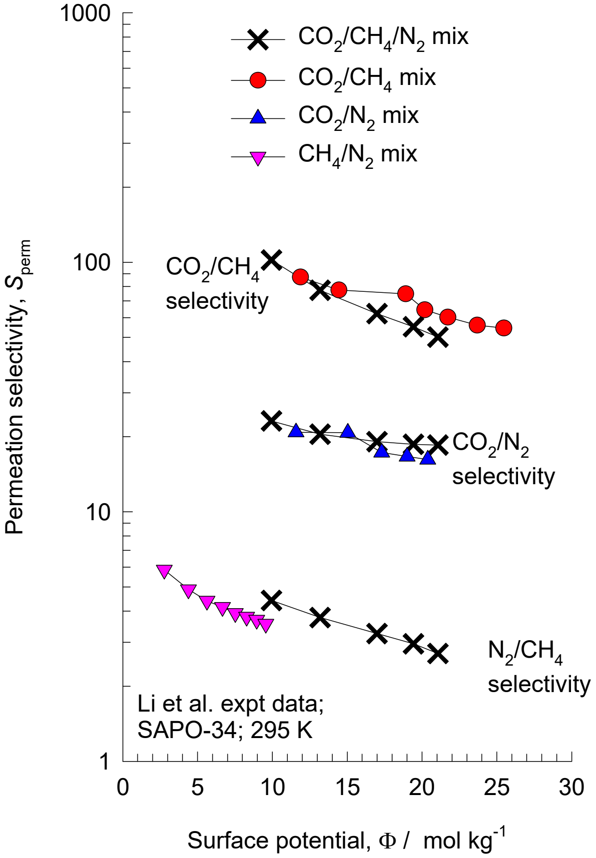

Figure S63. Re-analysis of the experimental data of Li et al.[71-73] for the selectivities of the CO_2/CH_4, CO_2/N_2, and N_2/CH_4 pairs in binary and ternary mixture permeation across SAPO-34 membrane at 295 K; the data are plotted as function of the surface potential Φ at the upstream face of the membrane.

10 Adsorption, Diffusion, Permeation in MFI zeolite

MFI zeolite (also called silicalite-1) has a topology consisting of a set of intersecting straight channels, and zig-zag (or sinusoidal) channels of 5.4 Å × 5.5 Å and 5.4 Å × 5.6 Å size. The pore landscapes and structural details are provided in Figure S64, and Figure S65. The crystal framework density $\rho = 1796$ kg m^{-3}. The accessible pore volume $V_P = 0.165$ cm^3 g^{-1}.

10.1 Adsorption of mixtures of light gaseous molecules in MFI zeolite

The applicability of Raoult's law analog, eq (S4), mandates that all of the adsorption sites within the microporous material are equally accessible to each of the guest molecules, implying a homogeneous distribution of guest adsorbates within the pore landscape, with no preferential locations of any guest species.[39, 40] This requirement of homogeneous distribution of guest molecules within MFI zeolite is fulfilled for light gaseous molecules such as N_2, H_2, CO_2, CH_4, C_2H_6, and C_3H_8. Figure S66a shows computational snapshots for the adsorption of CO_2, and CH_4 within the intersecting channel topology of MFI zeolite. It is noticeable that neither guest species shows any preferential location and there is no visual indication of segregated adsorption. The only charged species is CO_2; the coulombic interactions with the negatively charged oxygen atoms in the zeolite framework are not strong enough to cause segregation between CO_2, and CH_4. We should therefore expect the mixture adsorption characteristics to be adequately well described by the IAST. Figure S66b shows CBMC simulations for the unary isotherms of light gaseous molecules in MFI zeolite at 300 K. The light gaseous guests can locate anywhere along the straight channels and zig-zag channels, and there are no perceptible isotherm inflections. The loadings, plotted on the y-axis are expressed in units of molecules per unit cell, Θ. To obtain the loading q, with units of mol kg^{-1}, the conversion factor is $1 \text{ molecule uc}^{-1} = 0.173366 \text{ mol kg}^{-1}$. These unary isotherms were each fitted with the dual-site Langmuir-Freundlich model, eq (S8); the fit parameters for each guest molecule (with sites A, and B) are tabulated for each guest in Table S17. The IAST calculations for the adsorption selectivity, S_{ads}, for binary CO_2/CH_4, CO_2/H_2, CO_2/N_2, CH_4/N_2, C_3H_8/CH_4 mixtures are compared with the corresponding S_{ads} values determined from CBMC simulations in Figure S67a,b. In Figure S67a the S_{ads} values are plotted as function of the surface potential, Φ. In Figure S67b the S_{ads} values are plotted as function of the pore occupancy, θ, determined from eq (S28). For all five mixtures the IAST estimations are in good agreement with the CBMC simulations. For CO_2/CH_4 and CO_2/N_2 mixtures, the S_{ads} increases as pore saturation conditions are approached, i.e. $\Phi > 10$ mol kg^{-1}; $\theta > 0.5$ because of entropy effects that favor the guest CO_2 with the higher saturation capacity (cf. Figure S66b); the explanation of entropy effects are provided in the published literature.[74, 75] For CO_2/H_2 mixtures, entropy effects favor the smaller H_2 guest, and consequently the CO_2/H_2 selectivity decreases with increasing surface potential Φ. For C_3H_8/CH_4 mixtures, the S_{ads} decreases as pore saturation conditions are approached, i.e. $\Phi > 10$ mol kg^{-1}; $\theta > 0.5$ because entropy effects favor the smaller guest CH_4. The use of the mixed-gas Langmuir model, eq (S24), with equal saturation capacities is unable to cater for entropy effects as evidenced for CO_2/CH_4, CO_2/N_2, and C_3H_8/CH_4 mixtures.

For CH_4/N_2 mixtures, the S_{ads} is practically independent of occupancy because the saturation capacities of CH_4, and N_2 are nearly the same, as evidenced in Figure S66b.

A further important point to note is that for the adsorption selectivity as defined in eq (S13) for component 1 with respect to component 2, also holds for the same guest components in the presence of other guest species, 3, 4, 5, ..etc. Equation (S6) implies that if the comparisons are made at the same surface potential Φ, the value of S_{ads} for component 1 with respect to component 2, remains the same irrespective of the presence of additional guest components in the same host.

In Figure S68, CBMC simulation data for (a) CO_2/CH_4, (b) CO_2/N_2, (c) CH_4/N_2, (d) CO_2/H_2, (e) CH_4/H_2, (f) $C_2H_6//CH_4$, and (g) C_3H_8/CH_4 adsorption selectivities, S_{ads}, determined from binary mixture are compared with the values of the corresponding binary pairs in 5/15/80 $CO_2/CH_4/N_2$, 20/30/50 $CO_2/CH_4/N_2$ and quaternary 1/1/1/1 $CO_2/CH_4/N_2/H_2$ mixtures. Each of the pair selectivities shows a unique dependence on Φ, as prescribed by eq (S13). Put another way, the presence of component 3 and/or component 4 in the ternary mixture has no influence of the adsorption selectivity for the 1-2 pair other than via the sorption pressures and surface potential.

10.2 Diffusion and permeation selectivities of binary pairs

MD simulations of the self-diffusivities $D_{i,self}$ for equimolar $q_1 = q_2; \quad x_1 = 1 - x_2 = 0.5$ binary CO_2/CH_4, CO_2/N_2, CO_2/H_2, CH_4/N_2, CH_4/H_2, CH_4/C_2H_6, CH_4/C_3H_8, and C_2H_6/C_3H_8 mixtures and equimolar $\left(q_1 = q_2 = q_3\right)$ ternary $CO_2/CH_4/N_2$, $CO_2/CH_4/H_2$, $CO_2/N_2/H_2$, and $CH_4/C_2H_6/C_3H_8$ mixtures in MFI zeolite were also performed. For binary CO_2/CH_4, and CO_2/H_2 mixtures, additional MD campaigns were conducted in which the total mixture loading was maintained constant at the value $\left(\Theta_1 + \Theta_2\right) = 10$ molecules uc^{-1}, and the proportions of the two components were varied in the mixtures.

Figure S69a shows MD simulations of the CO_2/CH_4 diffusion selectivities, S_{diff}, determined from both equimolar binary $\left(q_1 = q_2\right)$ mixtures and equimolar $\left(q_1 = q_2 = q_3\right)$ ternary ($CO_2/CH_4/N_2$, and $CO_2/CH_4/H_2$) mixtures in MFI zeolite at 300 K, plotted as function of the surface potential Φ. Also plotted are MD data for binary mixtures in which the total molar loading $\Theta_t = \Theta_2 + \Theta_2 = 10$ molecules uc^{-1} with varying mole fractions $x_1 = \Theta_1 / \left(\Theta_2 + \Theta_2\right)$. All three data sets follow a unique dependence on the surface potential Φ. In view of the fact that IAST also shows that the adsorption selectivity S_{ads} is also uniquely dependent on Φ, we should expect the permeation selectivity $S_{perm} = \frac{D_{1,self} q_1 / f_1}{D_{2,self} q_2 / f_2} = S_{ads} \times S_{diff}$ to be also uniquely dependent on Φ. This is confirmed by the data presented in Figure S69b for the CO_2/CH_4 permeation selectivities, S_{perm}.

Figure S70, Figure S71, Figure S72, Figure S73, Figure S74, Figure S75, and Figure S76 present analogous sets of data on S_{diff} and S_{perm} for CO_2/N_2, CO_2/H_2, CH_4/N_2, CH_4/H_2, CH_4/C_2H_6, CH_4/C_3H_8, and C_2H_6/C_3H_8 binary pairs. In all cases the S_{diff} and S_{perm} for binary and ternary mixtures are uniquely dependent on Φ.

10.3 Component self-diffusivities and permeabilities

Figure S77 presents MD simulation data on the self-diffusivities, $D_{i,self}$, of (a) CO_2, (b) CH_4, (c) N_2, (d) C_2H_6, and (e) H_2 in equimolar $q_1 = q_2; \quad x_1 = 1 - x_2 = 0.5$ binary CO_2/CH_4, CO_2/N_2, CO_2/H_2, CH_4/N_2, CH_4/H_2, CH_4/C_2H_6, CH_4/C_3H_8, and C_2H_6/C_3H_8 mixtures and equimolar $(q_1 = q_2 = q_3)$ ternary $CO_2/CH_4/N_2$, $CO_2/CH_4/H_2$, $CO_2/N_2/H_2$, and $CH_4/C_2H_6/C_3H_8$ mixtures, plotted as a function of the surface potential Φ. The data demonstrate that the component self-diffusivities in binary and ternary mixtures are nearly the same, independent of the partner(s) in the mixtures. Also plotted are the corresponding values of the unary self-diffusivities. Except for H_2, the self-diffusivities in the binary and ternary mixtures are also nearly the same as the unary self-diffusivities. The unary self-diffusivity for H_2, is larger in value for those in mixtures. The lowering of the H_2 self-diffusivity in mixtures is attributable to correlation effects, that slows-down the more mobile H_2.

Figure S78 presents data on the permeabilities, Π_i, of (a) CO_2, (b) CH_4, (c) N_2, (d) C_2H_6, and (e) H_2 in equimolar $q_1 = q_2; \quad x_1 = 1 - x_2 = 0.5$ binary CO_2/CH_4, CO_2/N_2, CO_2/H_2, CH_4/N_2, CH_4/H_2, CH_4/C_2H_6, CH_4/C_3H_8, and C_2H_6/C_3H_8 mixtures and equimolar $(q_1 = q_2 = q_3)$ ternary $CO_2/CH_4/N_2$, $CO_2/CH_4/H_2$, $CO_2/N_2/H_2$, and $CH_4/C_2H_6/C_3H_8$ mixtures, plotted as a function of the surface potential Φ. The data demonstrate that the component permeabilities in binary and ternary mixtures are nearly the same, independent of the partner(s) in the mixtures. Except for H_2, the permeabilities in the binary and ternary mixtures are also nearly the same as the unary permeabilities. The unary permeability for H_2, appears to larger in value for those in mixtures. The lowering of the H_2 permeabilities in mixtures is attributable to correlation effects, that slows-down the more mobile H_2.

10.4 List of Tables for Adsorption, Diffusion, Permeation in MFI zeolite

Table S17. Dual-site Langmuir-Freundlich parameters for guest molecules in MFI at 300 K. To convert from molecules uc^{-1} to mol kg^{-1}, multiply by 0.173367.

	Site A			Site B		
	$\Theta_{A,sat}$ molecules uc^{-1}	b_A $\mathrm{Pa}^{-\nu A}$	ν_A dimensionless	$\Theta_{B,sat}$ molecules uc^{-1}	b_B $\mathrm{Pa}^{-\nu B}$	ν_B dimensionless
H_2	30	3.57E-08	1	42	1.39E-09	1
N_2	16	6.37E-07	1	16	3.82E-07	0.7
CO_2	19	6.12E-06	1	11	1.73E-08	1
CH_4	7	5.00E-09	1	16	3.10E-06	1
C_2H_6	3.3	4.08E-07	1	13	7.74E-05	1
C_3H_8	1.4	3.35E-04	0.67	10.7	6.34E-04	1.06

10.5 List of Figures for Adsorption, Diffusion, Permeation in MFI zeolite

MFI **pore landscape**

	MFI
a /Å	20.022
b /Å	19.899
c /Å	13.383
Cell volume / Å^3	5332.025
conversion factor for [molec/uc] to [mol per kg Framework]	0.1734
conversion factor for [molec/uc] to [kmol/m^3]	1.0477
ρ [kg/m3]	1796.386
MW unit cell [g/mol(framework)]	5768.141
ϕ, fractional pore volume	0.297
open space / Å^3/uc	1584.9
Pore volume / cm^3/g	0.165
Surface area /m^2/g	487.0
DeLaunay diameter /Å	5.16

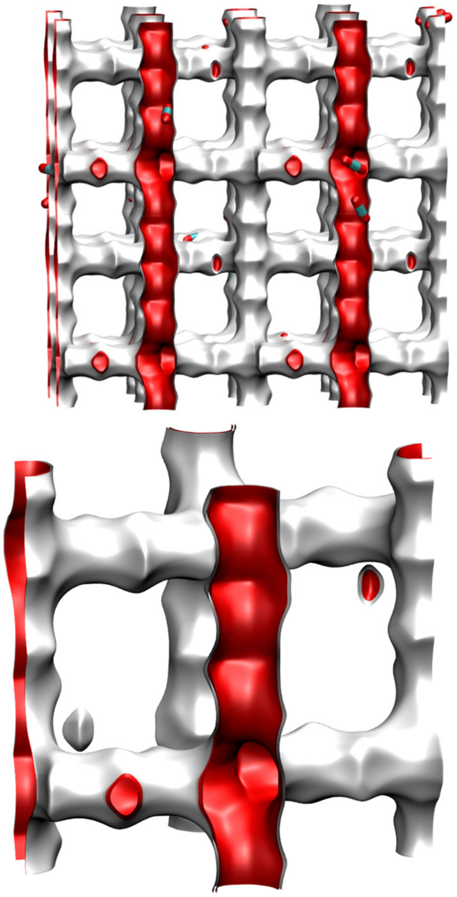

Figure S64. Pore landscape and structural data for MFI zeolite.

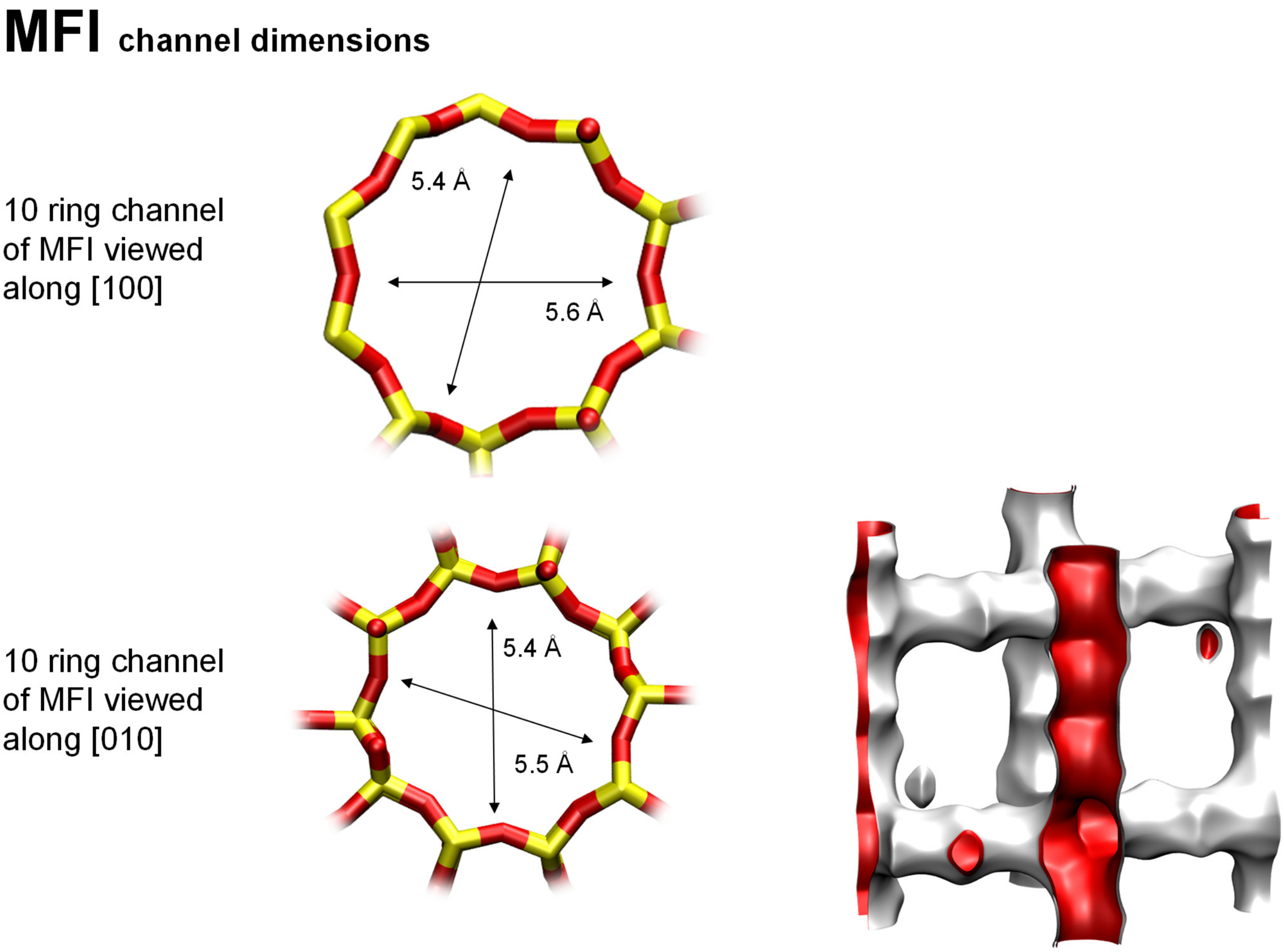

Figure S65. Pore landscape and structural data for MFI zeolite.

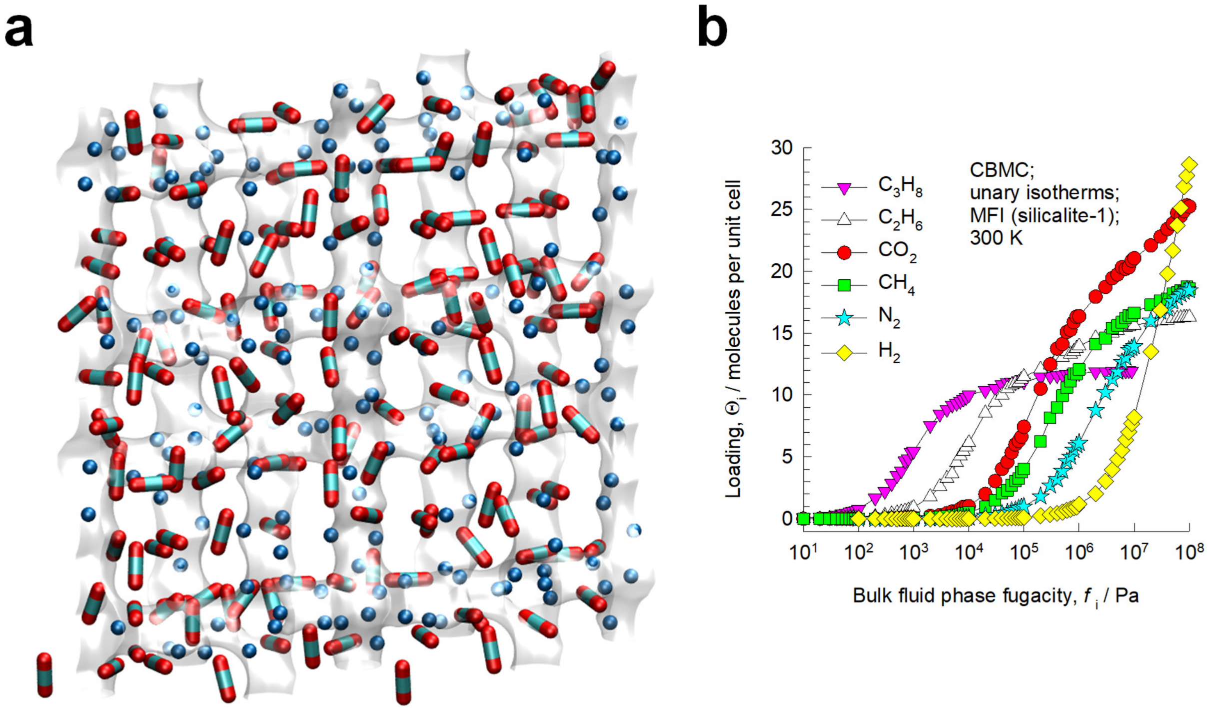

Figure S66. (a) Computational snapshots showing the distribution of. CO_2 and CH_4 for binary mixture adsorption. (b) CBMC simulations of unary isotherms for light gaseous molecules H_2, N_2, CO_2, CH_4, C_2H_6, and C_3H_8 in MFI zeolite at 300 K.

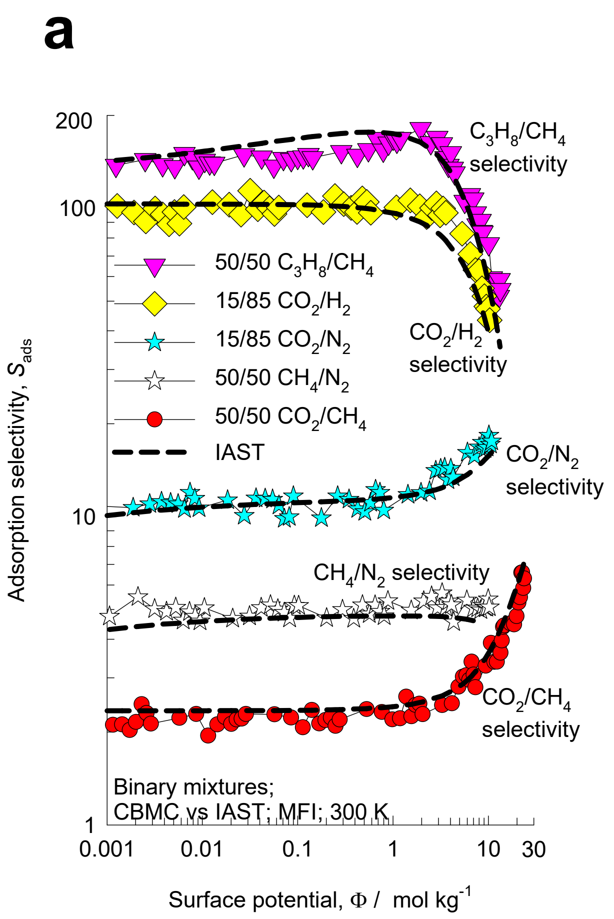

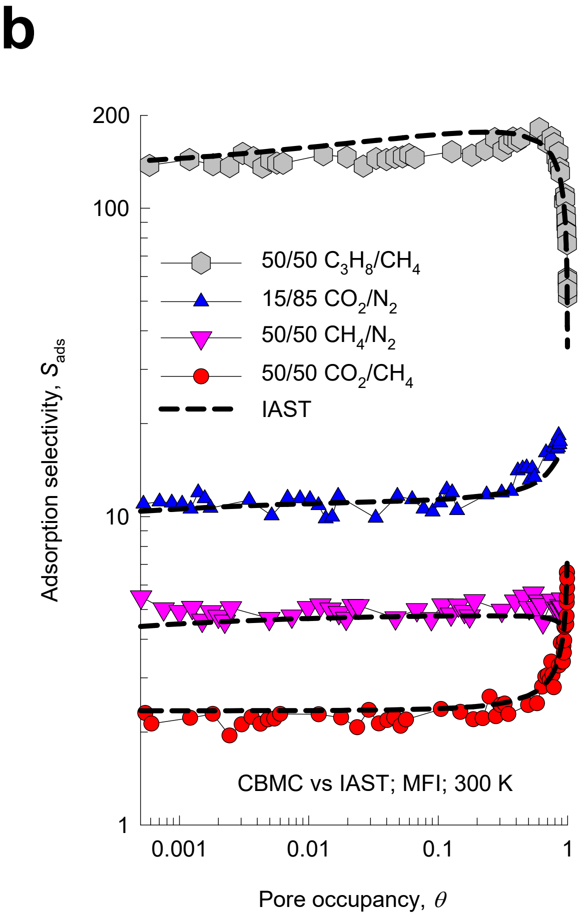

Figure S67. (a, b) CBMC simulations (indicated by symbols) of the adsorption selectivity, S_{ads} , for four different binary CO_2/CH_4, CO_2/H_2, CO_2/N_2, CH_4/N_2, C_3H_8/CH_4 mixtures in MFI zeolite at 300 K are compared with the IAST calculations (indicated by dashed lines) for corresponding S_{ads} values using the Dual-site Langmuir-Freundlich fits of unary isotherms. In (a) the S_{ads} values are plotted as function of the surface potential, Φ. In (b) the S_{ads} values are plotted as function of the pore occupancy, θ, determined from eq (S28).

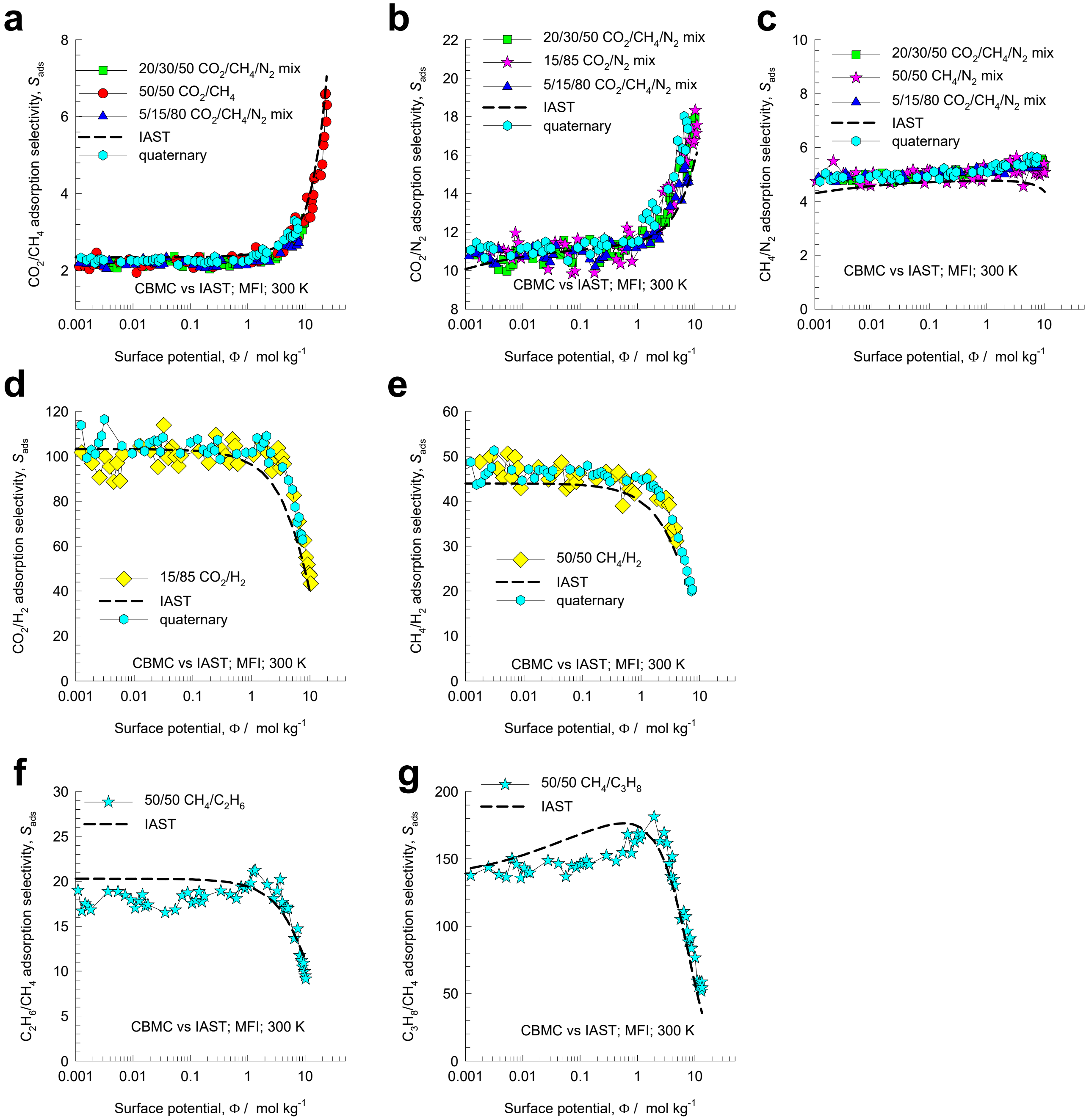

Figure S68. CBMC simulations of (a) CO_2/CH_4, (b) CO_2/N_2, (c) CH_4/N_2, (d) CO_2/H_2, (e) CH_4/H_2, (f) $C_2H_6//CH_4$, and (g) C_3H_8/CH_4 adsorption selectivities, S_{ads} , determined from binary, ternary, and quaternary mixture adsorption in MFI zeolite at 300 K, plotted as function of the surface potential, Φ .

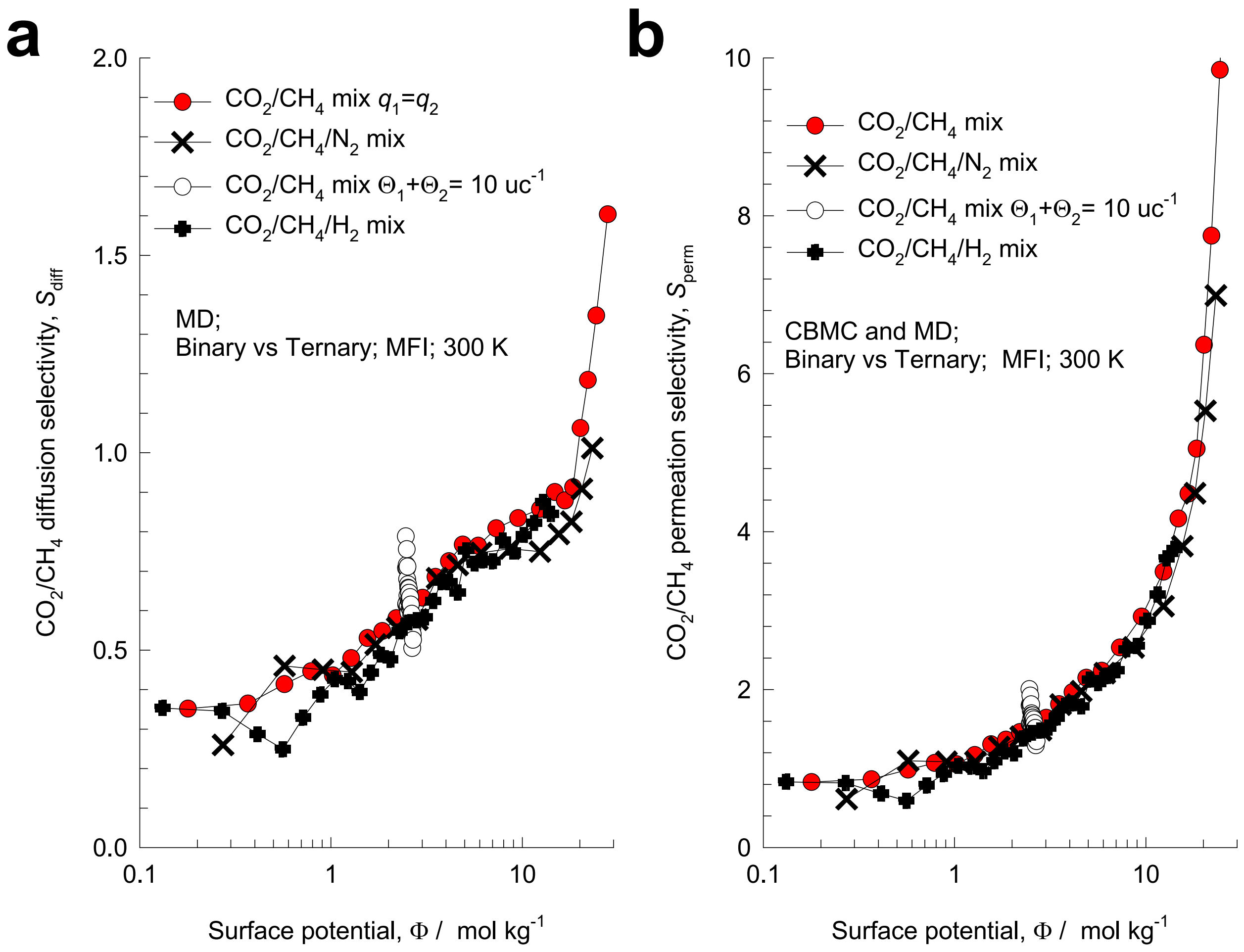

Figure S69. (a) MD simulations of the CO_2/CH_4 diffusion selectivities, S_{diff}, determined from both equimolar $(q_1 = q_2)$ binary mixtures and equimolar $(q_1 = q_2 = q_3)$ ternary ($CO_2/CH_4/N_2$, and $CO_2/CH_4/H_2$) mixtures in MFI zeolite at 300 K, plotted as function of the surface potential Φ. (b) Plot of the CO_2/CH_4 permeation selectivity S_{perm} as function of the surface potential Φ, determined from binary and ternary ($CO_2/CH_4/N_2$, and $CO_2/CH_4/H_2$) MD campaigns.

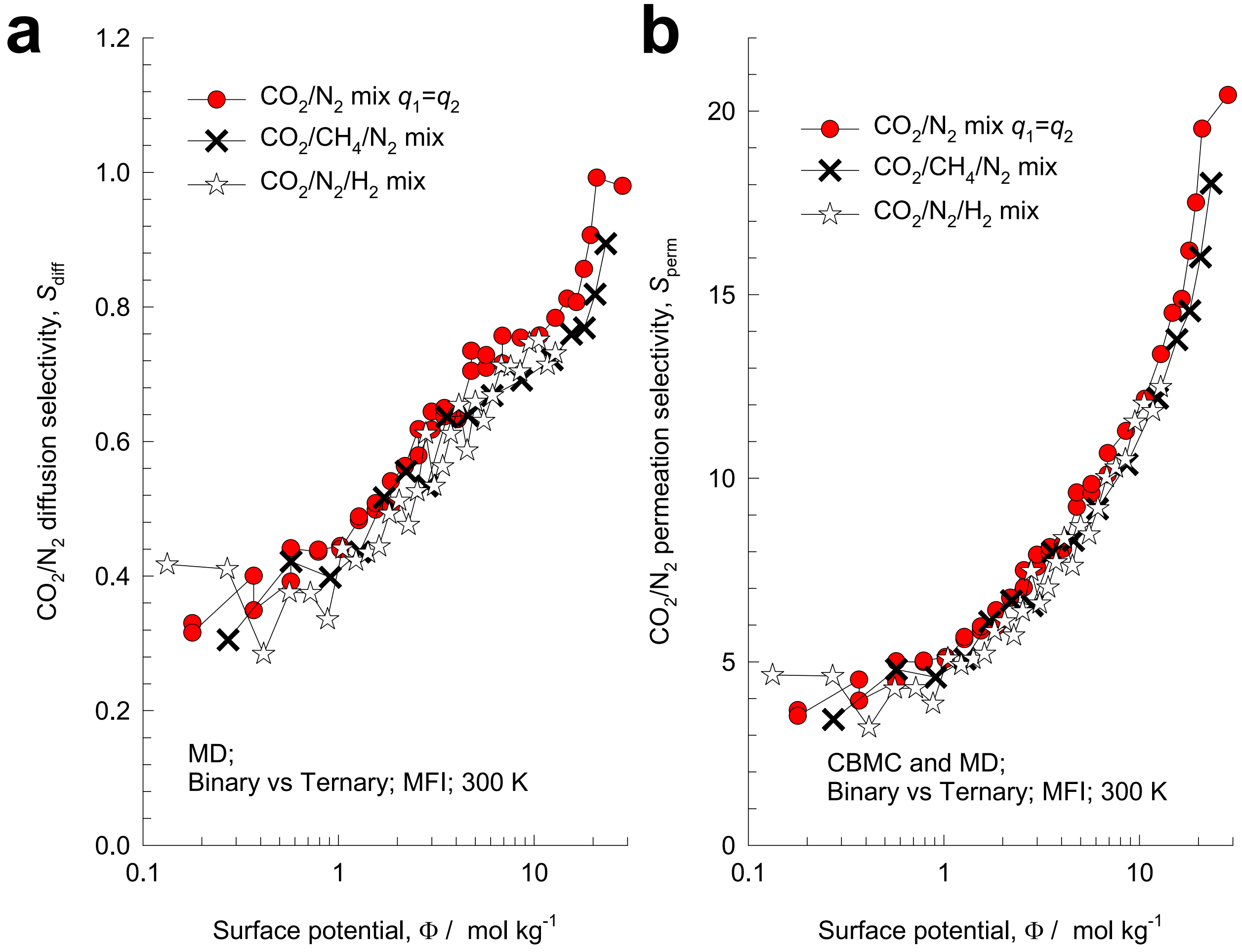

Figure S70. (a) MD simulations of the CO_2/N_2 diffusion selectivities, S_{diff}, determined from both equimolar $(q_1 = q_2)$ binary and equimolar $(q_1 = q_2 = q_3)$ ternary ($CO_2/CH_4/N_2$, and $CO_2/N_2/H_2$) mixtures in MFI zeolite at 300 K, plotted as function of the surface potential Φ. (b) Plot of the CO_2/N_2 permeation selectivity S_{perm} as function of the surface potential Φ, determined from binary and ternary ($CO_2/CH_4/N_2$, and $CO_2/N_2/H_2$) mixtures MD campaigns.

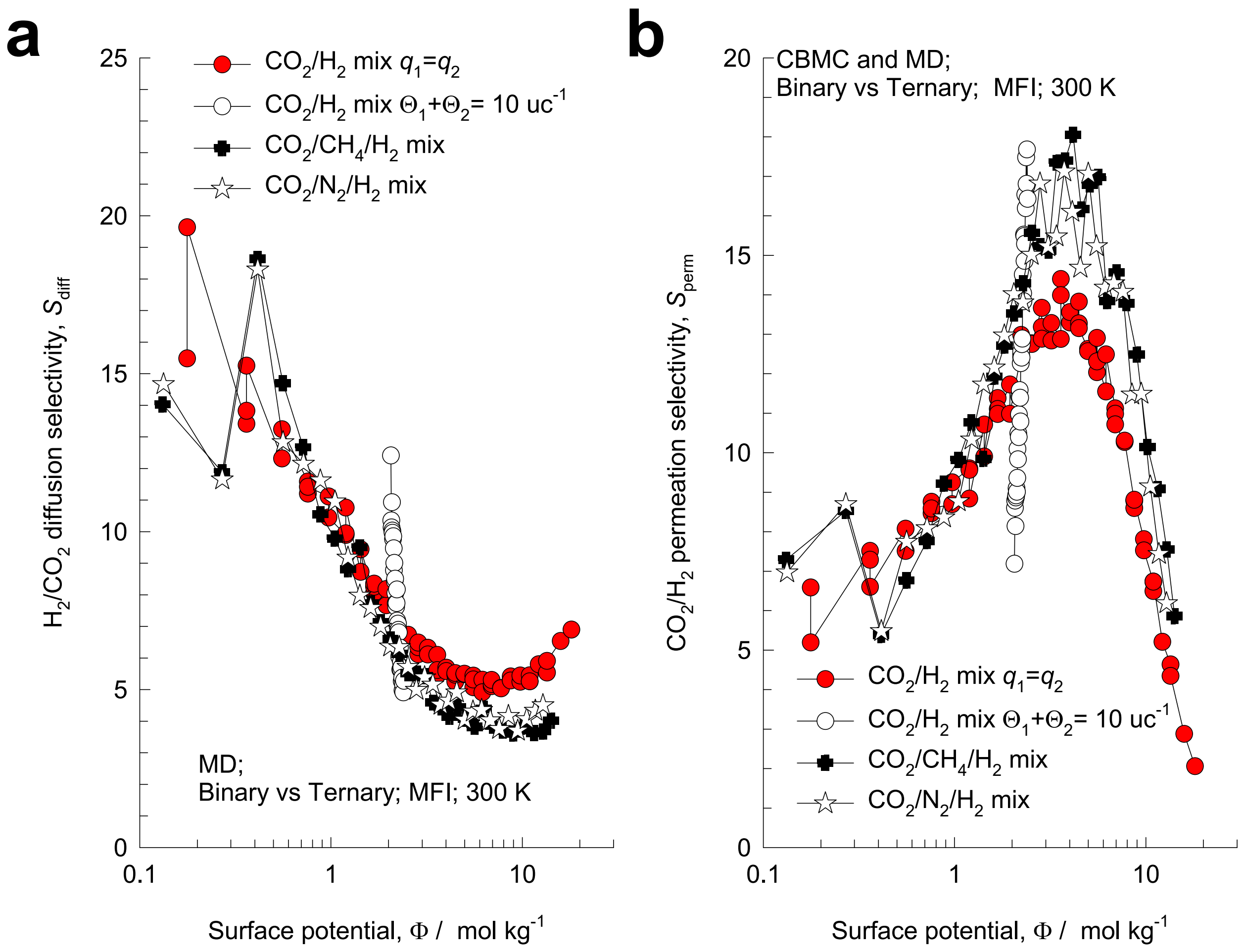

Figure S71. (a) MD simulations of the H_2/CO_2 diffusion selectivities, S_{diff}, determined from both equimolar $(q_1 = q_2)$ binary and equimolar $(q_1 = q_2 = q_3)$ ternary ($CO_2/N_2/H_2$, and $CO_2/CH_4/H_2$) mixtures in MFI zeolite at 300 K, plotted as function of the surface potential Φ. (b) Plot of the CO_2/H_2 permeation selectivity S_{perm} as function of the surface potential Φ, determined from binary and ternary ($CO_2/N_2/H_2$, and $CO_2/CH_4/H_2$) MD campaigns.

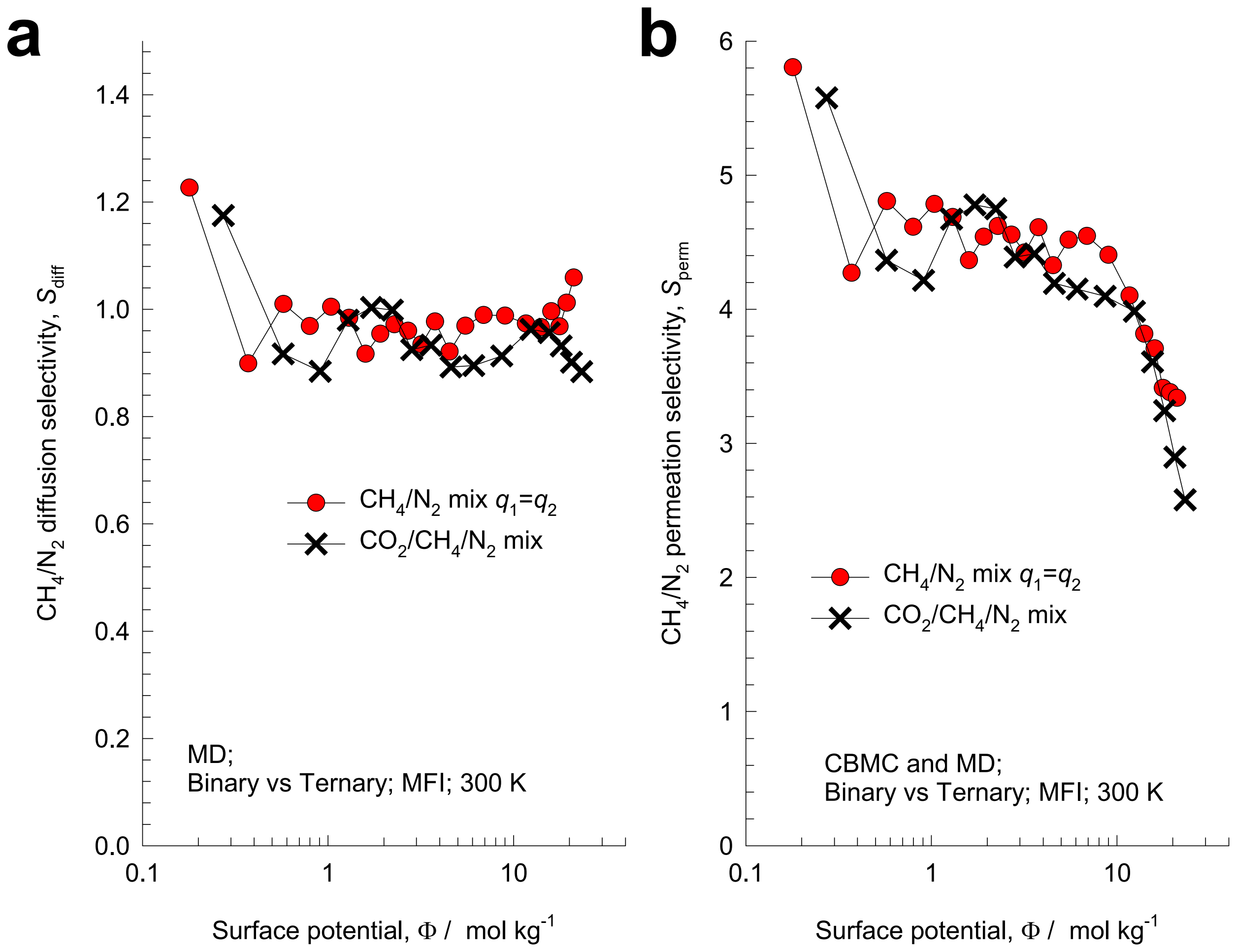

Figure S72. (a) MD simulations of the CH_4/N_2 diffusion selectivities, S_{diff}, determined from both equimolar $(q_1 = q_2)$ binary and equimolar $(q_1 = q_2 = q_3)$ ternary ($CO_2/CH_4/N_2$) mixtures in MFI zeolite at 300 K, plotted as function of the surface potential Φ. (b) Plot of the CH_4/N_2 permeation selectivity S_{perm} as function of the surface potential Φ, determined from binary and ternary ($CO_2/CH_4/N_2$) MD campaigns.

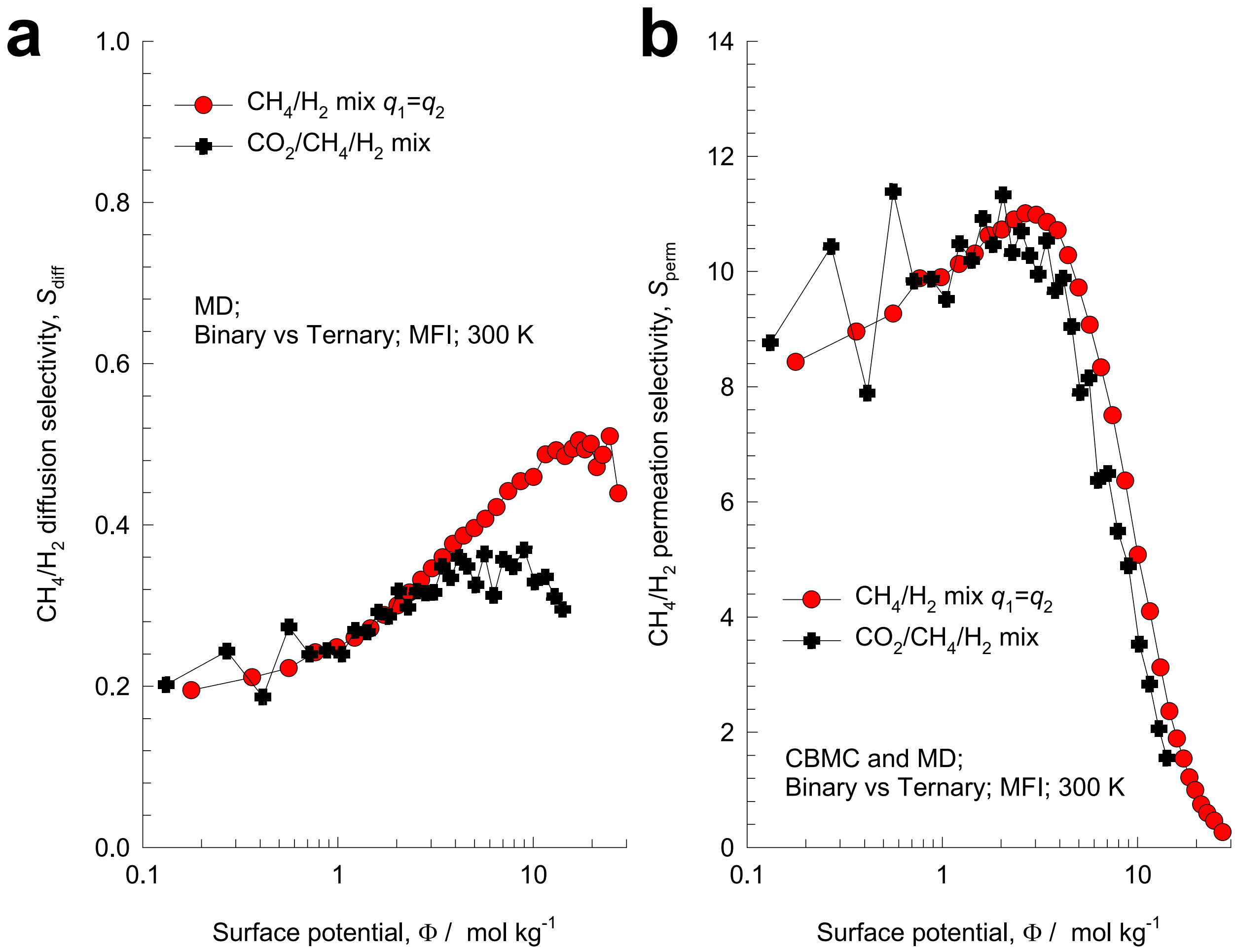

Figure S73. (a) MD simulations of the CH4/H2 diffusion selectivities, S_{diff}, determined from both equimolar $\left(q_1 = q_2\right)$ binary and equimolar $\left(q_1 = q_2 = q_3\right)$ ternary (CO2/CH4/H2) mixtures in MFI zeolite at 300 K, plotted as function of the surface potential Φ. (b) Plot of the CH4/H2 permeation selectivity S_{perm} as function of the surface potential Φ, determined from binary and ternary (CO2/CH4/H2) MD campaigns.

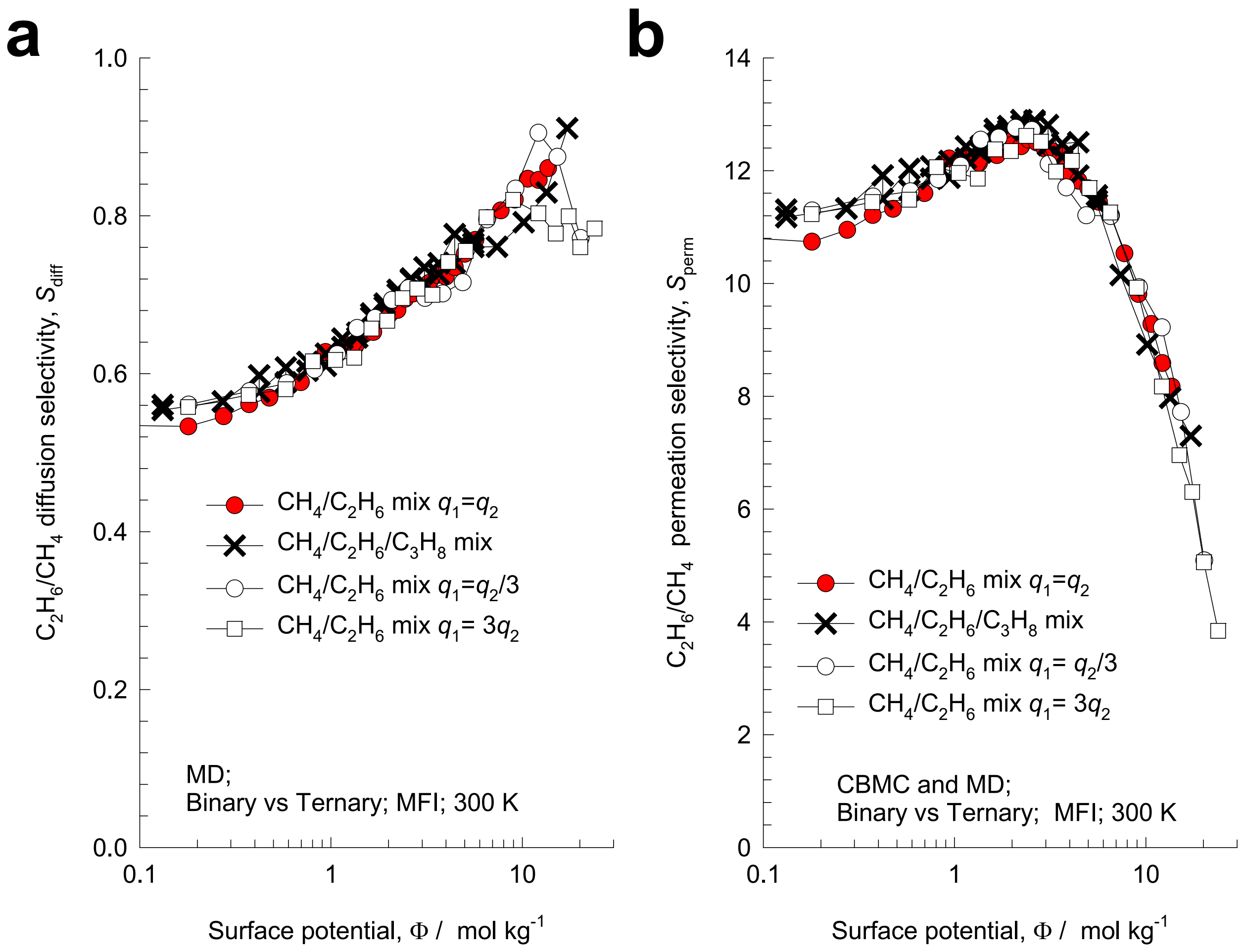

Figure S74. (a) MD simulations of the C_2H_6/CH_4 diffusion selectivities, S_{diff}, determined from both equimolar $(q_1 = q_2)$ binary and equimolar $(q_1 = q_2 = q_3)$ ternary ($CH_4/C_2H_6/C_3H_8$) mixtures in MFI zeolite at 300 K, plotted as function of the surface potential Φ. (b) Plot of the C_2H_6/CH_4 permeation selectivity S_{perm} as function of the surface potential Φ, determined from binary and ternary ($CH_4/C_2H_6/C_3H_8$) MD campaigns.

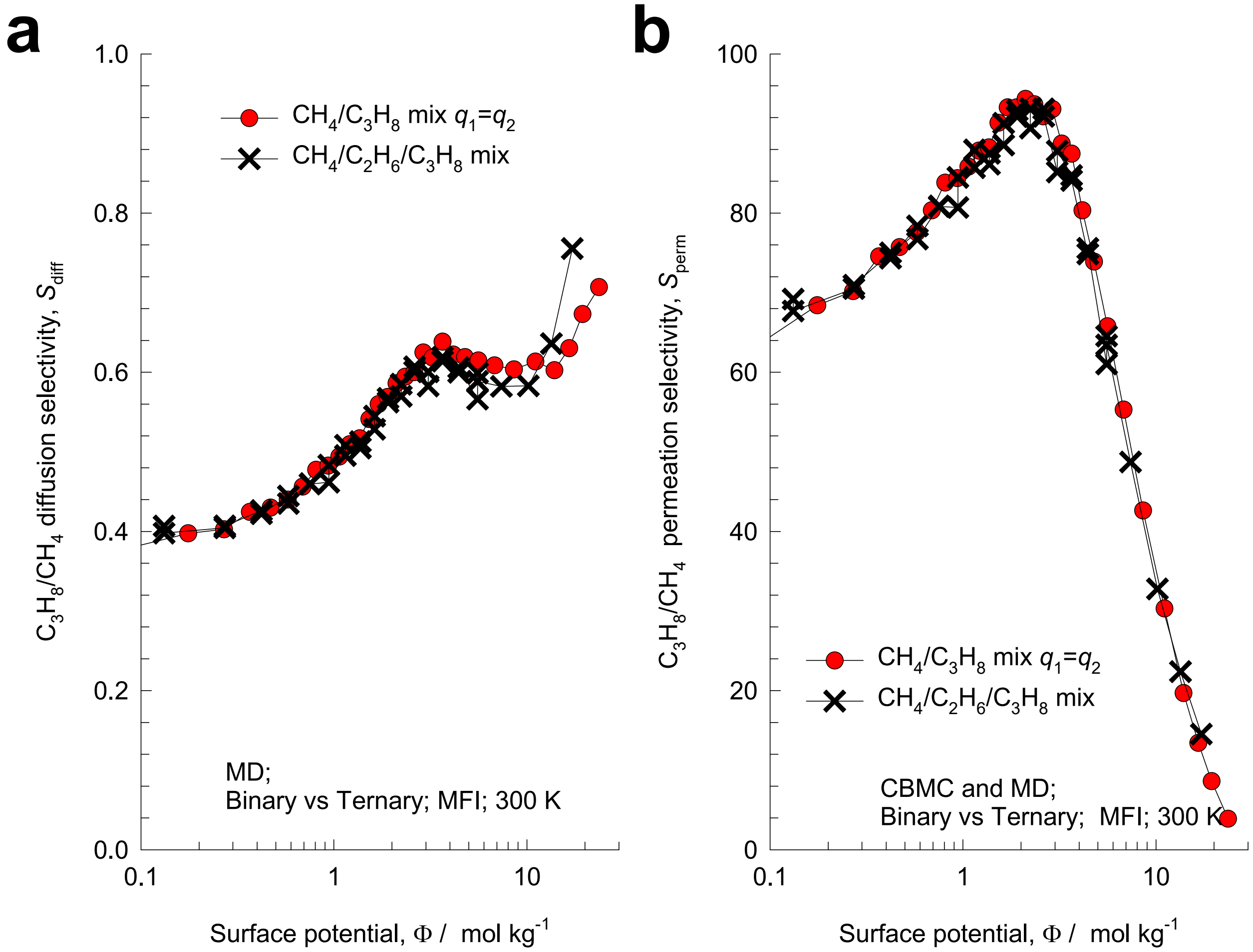

Figure S75. (a) MD simulations of the C_3H_8/CH_4 diffusion selectivities, S_{diff}, determined from both equimolar $(q_1 = q_2)$ binary and equimolar $(q_1 = q_2 = q_3)$ ternary ($CH_4/C_2H_6/C_3H_8$) mixtures in MFI zeolite at 300 K, plotted as function of the surface potential Φ. (b) Plot of the C_3H_8/CH_4 permeation selectivity S_{perm} as function of the surface potential Φ, determined from binary and ternary ($CH_4/C_2H_6/C_3H_8$) MD campaigns.

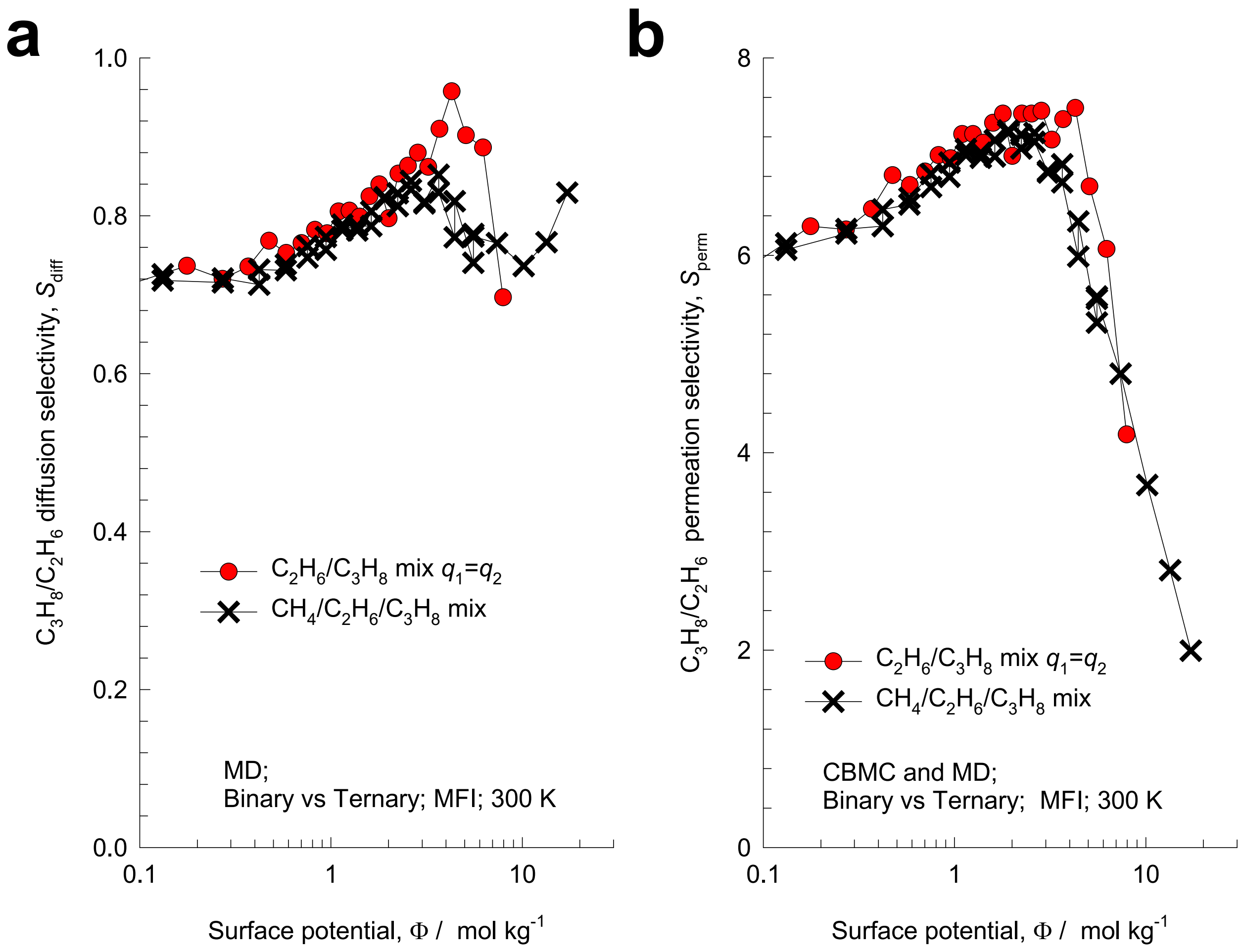

Figure S76. (a) MD simulations of the C_3H_8/C_2H_6 diffusion selectivities, S_{diff}, determined from both equimolar $(q_1 = q_2)$ binary and equimolar $(q_1 = q_2 = q_3)$ ternary ($CH_4/C_2H_6/C_3H_8$) mixtures in MFI zeolite at 300 K, plotted as function of the surface potential Φ. (b) Plot of the C_3H_8/C_2H_6 permeation selectivity S_{perm} as function of the surface potential Φ, determined from binary and ternary ($CH_4/C_2H_6/C_3H_8$) MD campaigns.

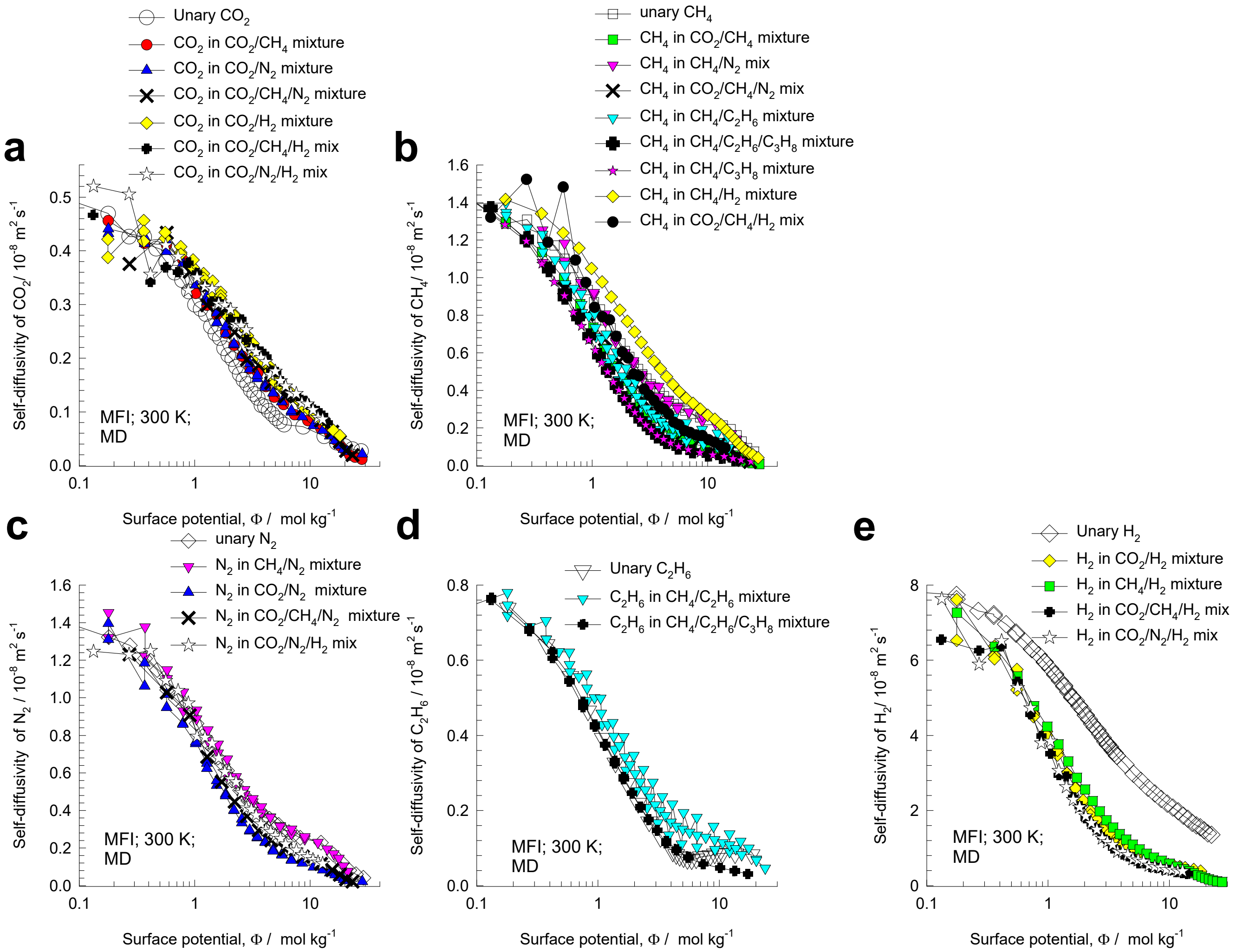

Figure S77. MD simulation data on the self-diffusivities, $D_{i,self}$, of (a) CO_2, (b) CH_4, (c) N_2, (d) C_2H_6, and (e) H_2 in equimolar $q_1 = q_2;\quad x_1 = 1 - x_2 = 0.5$ binary CO_2/CH_4, CO_2/N_2, CO_2/H_2, CH_4/N_2, CH_4/H_2, CH_4/C_2H_6, CH_4/C_3H_8, and C_2H_6/C_3H_8 mixtures and equimolar $(q_1 = q_2 = q_3)$ ternary $CO_2/CH_4/N_2$, $CO_2/CH_4/H_2$, $CO_2/N_2/H_2$, and $CH_4/C_2H_6/C_3H_8$ mixtures in MFI zeolite at 300 K, plotted as a function of the surface potential Φ. Also plotted are the corresponding values of the unary self-diffusivities.

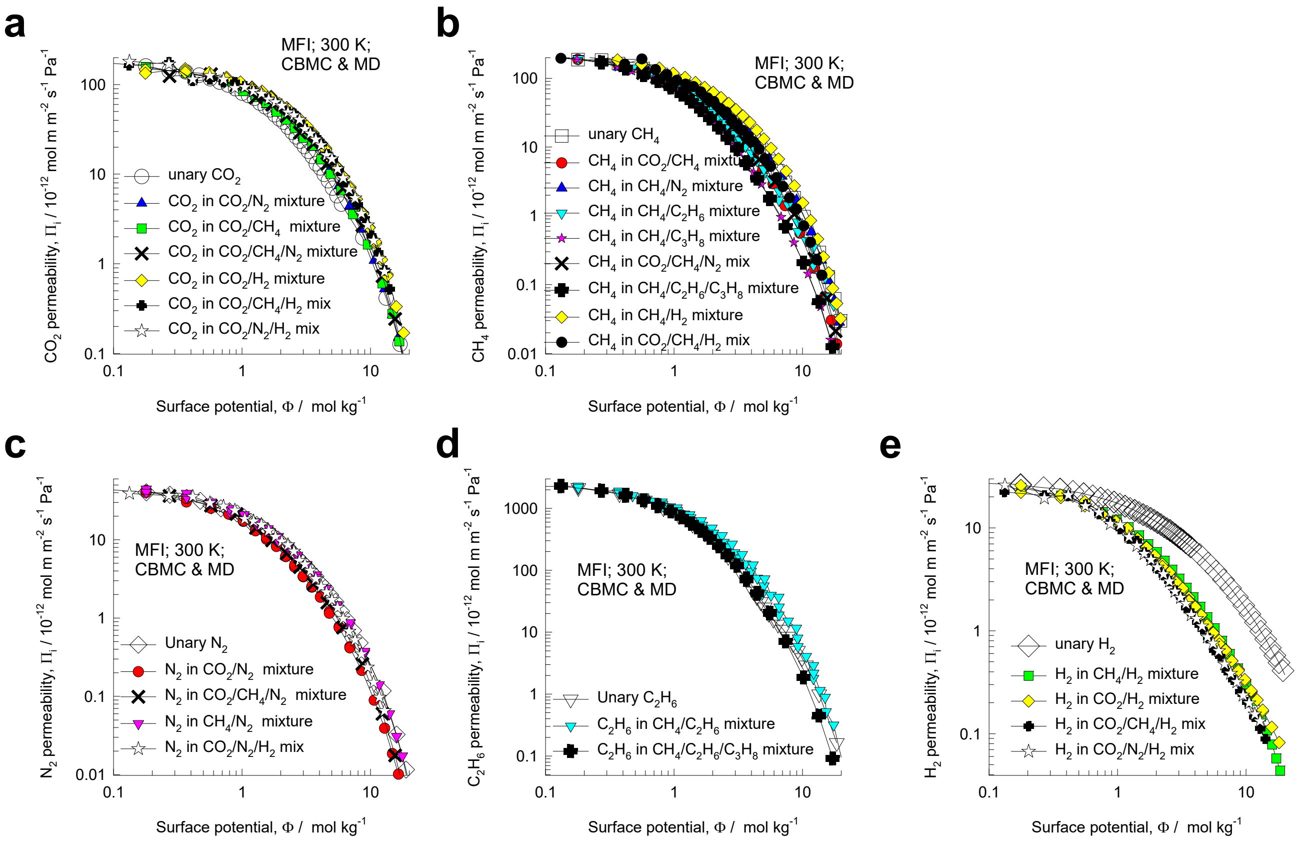

Figure S78. CBMC/MD simulations of the permeabilities, Π_i, of of (a) CO_2, (b) CH_4, (c) N_2, (d) C_2H_6, and (e) H_2 in equimolar $q_1 = q_2$; $x_1 = 1 - x_2 = 0.5$ binary CO_2/CH_4, CO_2/N_2, CO_2/H_2, CH_4/N_2, CH_4/H_2, CH_4/C_2H_6, CH_4/C_3H_8, and C_2H_6/C_3H_8 mixtures and equimolar $\left(q_1 = q_2 = q_3\right)$ ternary $CO_2/CH_4/N_2$, $CO_2/CH_4/H_2$, $CO_2/N_2/H_2$, and $CH_4/C_2H_6/C_3H_8$ mixtures in MFI zeolite at 300 K, plotted as a function of the surface potential Φ. Also plotted are the corresponding values of the unary permeabilities.

11 Adsorption, Diffusion, Permeation in FAU zeolite

Figure S79 presents the structural details of FAU (all-silica) zeolite. It has cages of 786 Å^3 volume, separated by 7.4 Å 12-ring windows. Figure S80 show the structural details of cation-exchanged NaX (= 86 Na$^+$/uc = 13X) zeolite. Per unit cell of NaX zeolite we have 106 Si, 86 Al, 86 Na$^+$ with Si/Al=1.23. This material is also commonly referred to by its trade name: 13X zeolite.

CBMC simulations of the unary isotherms in all-silica FAU were fitted with the dual-site Langmuir-Freundlich model, eq (S8); the fit parameters for each guest molecule (with sites A, and B) are tabulated for each guest in Table S18.

11.1 Adsorption of mixtures in all-silica FAU zeolite

In Figure S81, CBMC simulation data for (a) CO_2/CH_4, (b) CO_2/N_2, (c) CH_4/N_2, (d) CO_2/H_2, and (e) CH_4/H_2 adsorption selectivities, S_{ads} , determined from binary mixture are compared with the values of the corresponding binary pairs in 20/40/40 $CO_2/CH_4/N_2$ and quaternary 1/1/1/1 $CO_2/CH_4/N_2/H_2$ mixtures. The IAST estimations (dashed lines) are in good agreement with the CBMC simulated values of S_{ads}. Each of the pair selectivities shows a unique dependence on Φ, as prescribed by eq (S13). Put another way, the presence of component 3 and/or component 4 in the ternary mixture has no influence of the adsorption selectivity for the 1-2 pair other than via the sorption pressures and surface potential.

11.2 Diffusion and permeation selectivities of binary pairs

MD simulations of the self-diffusivities $D_{i,self}$ for equimolar $q_1 = q_2; \quad x_1 = 1 - x_2 = 0.5$ binary CO_2/CH_4, CO_2/N_2, CO_2/H_2, CH_4/N_2, CH_4/H_2, CH_4/C_2H_6, and CH_4/C_3H_8 mixtures and equimolar $\left(q_1 = q_2 = q_3\right)$ ternary $CO_2/CH_4/N_2$, $CO_2/CH_4/H_2$, $CO_2/N_2/H_2$, and $CH_4/C_2H_6/C_3H_8$ mixtures in all-silica FAU zeolite were also performed. For ternary $CH_4/C_2H_6/C_3H_8$ mixtures, additional MD campaigns were conducted in which the total mixture loading was maintained constant at the value $\left(\Theta_1 + \Theta_2 + \Theta_3\right) = 48$ molecules uc$^-$

^{1}, the loading of propane was held constant at the value of $\Theta_3 = 12$ molecules uc^{-1}, and the proportions of the methane and ethane components were varied in the mixtures, holding the total loading $\left(\Theta_1 + \Theta_2\right) = 36$ molecules uc^{-1}.

Figure S82a shows MD simulations of the CO$_2$/CH$_4$ diffusion selectivities, S_{diff}, determined from both equimolar binary $\left(q_1 = q_2\right)$ mixtures and equimolar $\left(q_1 = q_2 = q_3\right)$ ternary (CO$_2$/CH$_4$/N$_2$, and CO$_2$/CH$_4$/H$_2$) mixtures in all-silica FAU zeolite at 300 K, plotted as function of the surface potential Φ. Also plotted are MD data for binary mixtures in which the total molar loading $\Theta_t = \Theta_2 + \Theta_2 = 10$ molecules uc^{-1}, with varying mole fractions $x_1 = \Theta_1 / \left(\Theta_2 + \Theta_2\right)$. All three MD data sets follow a unique dependence on the surface potential Φ. In view of the fact that IAST also shows that the adsorption selectivity S_{ads} is also uniquely dependent on Φ, we should expect the permeation selectivity $S_{perm} = \dfrac{D_{1,self} q_1 / f_1}{D_{2,self} q_2 / f_2} = S_{ads} \times S_{diff}$ to be also uniquely dependent on Φ. This is confirmed by the data presented in Figure S69b for the CO$_2$/CH$_4$ permeation selectivities, S_{perm}.

Figure S83, Figure S84, Figure S85, Figure S86, Figure S87, and Figure S88 present analogous sets of data on S_{diff} and S_{perm} for CO$_2$/N$_2$, CO$_2$/H$_2$, CH$_4$/N$_2$, and CH$_4$/H$_2$, CH$_4$/C$_2$H$_6$, and CH$_4$/C$_3$H$_8$ pairs. In all cases the S_{diff} and S_{perm} for binary and ternary mixtures is uniquely dependent on Φ.

11.3 Component self-diffusivities and permeabilities

Figure S89 presents MD simulation data on the self-diffusivities, $D_{i,self}$, of (a) CO$_2$, (b) CH$_4$, (c) N$_2$, (d) C$_2$H$_6$, and (e) N$_2$ in equimolar $q_1 = q_2;\ \ x_1 = 1 - x_2 = 0.5$ binary CO$_2$/CH$_4$, CO$_2$/N$_2$, CO$_2$/H$_2$, CH$_4$/N$_2$, CH$_4$/H$_2$, CH$_4$/C$_2$H$_6$, and CH$_4$/C$_3$H$_8$ mixtures and equimolar $\left(q_1 = q_2 = q_3\right)$ ternary CO$_2$/CH$_4$/N$_2$, CO$_2$/CH$_4$/H$_2$, CO$_2$/N$_2$/H$_2$, and CH$_4$/C$_2$H$_6$/C$_3$H$_8$ mixtures, plotted as a function of the surface potential Φ. The data demonstrate that the component self-diffusivities in binary and ternary mixtures are nearly the same, independent of the partner(s) in the mixtures. Also plotted are the corresponding values of the unary self-diffusivities. Except for H_2, the self-diffusivities in the binary and ternary mixtures are also nearly the same as the unary self-diffusivities. The unary self-diffusivity for H_2, is larger in value for those in mixtures. The lowering of the H_2 self-diffusivity in mixtures is attributable to correlation effects, that slows-down the more mobile H_2.

Figure S90 presents data on the permeabilities, Π_i, of a) CO_2, (b) CH_4, (c) N_2, (d) C_2H_6, and (e) H_2 in equimolar $q_1 = q_2$; $x_1 = 1 - x_2 = 0.5$ binary CO_2/CH_4, CO_2/N_2, CO_2/H_2, CH_4/N_2, CH_4/H_2, CH_4/C_2H_6, CH_4/C_3H_8, and C_2H_6/C_3H_8 mixtures and equimolar $(q_1 = q_2 = q_3)$ ternary $CO_2/CH_4/N_2$, $CO_2/CH_4/H_2$, $CO_2/N_2/H_2$, and $CH_4/C_2H_6/C_3H_8$ mixtures, plotted as a function of the surface potential Φ. The data demonstrate that the component permeabilities in binary and ternary mixtures are nearly the same, independent of the partner(s) in the mixtures. Except for H_2, the permeabilities in the binary and ternary mixtures are also nearly the same as the unary permeabilities. The unary permeability for H_2, appears to larger in value for those in mixtures. The lowering of the H_2 permeabilities in mixtures is attributable to correlation effects, that slows-down the more mobile H_2.

11.4 Mixture adsorption in cation-exchanged NaX (=13X) zeolite

Figure S91a shows CBMC simulation data of the adsorption selectivity, S_{ads}, for $CO_2(1)/CH_4(2)$ mixtures in NaX zeolite at 300 K, determined from five different campaigns:

(i) the bulk gas phase mole fractions are maintained at y_1 =0.05, and the total mixture fugacity $f_t = f_1 + f_2$ is varied up to f_t = 10 MPa at which pore saturation conditions are approached,

(ii) the bulk gas phase mole fractions are maintained at $y_1 = 0.10$, and the total mixture fugacity $f_t = f_1 + f_2$ is varied up to f_t = 10 MPa at which pore saturation conditions are approached,

(iii) the bulk gas phase mole fractions are maintained at y_1 =0.20, and the total mixture fugacity $f_t = f_1 + f_2$ is varied up to f_t = 10 MPa at which pore saturation conditions are approached,

(iv) the bulk gas phase mole fractions are maintained at $y_1 = 0.50$, and the total mixture fugacity $f_t = f_1 + f_2$ is varied up to $f_t = 10$ MPa at which pore saturation conditions are approached,

(v) the total bulk gas mixture fugacity is held constant, $f_t = f_1 + f_2 = 10^5$ Pa, and the mole fraction of the bulk gas mixture of CO_2(1), y_1, is varied from 0 to 1

For all five CBMC data sets, the CBMC simulated values of the adsorption selectivity, S_{ads}, follows a near-unique dependence on the surface potential Φ, see Figure S91a. CBMC simulations were also performed for 20/40/40 $CO_2/CH_4/N_2$ and 5/25/70 $CO_2/CH_4/N_2$ mixtures in NaX zeolite at 300 K, in which the bulk gas phase mole fractions are maintained constant and the total mixture fugacity $f_t = f_1 + f_2 + f_3$ is varied up to $f_t = 10$ MPa. The values of the CO_2/CH_4 adsorption selectivity in the ternary mixture are also plotted in Figure S91a. The ternary CBMC data follows the same unique dependence on Φ. Put another way, the presence of component 3 in the ternary mixture has no influence of the adsorption selectivity for the 1-2 pair.

The IAST calculations (indicated by dashed lines in Figure S91a) of the adsorption selectivity show large deviations from the CBMC simulated data due to congregation of the CO_2 molecules around the Na^+ cations; detailed explanations are provided in our earlier works. [28, 39, 40, 63, 67] With the introduction of activity coefficients, the expression for the adsorption selectivity for the CO_2(1)/CH_4(2) pair in binary and ternary mixtures is

$$S_{ads,12} = \frac{q_1/q_2}{f_1/f_2} = \frac{x_1/f_1}{x_2/f_2} = \frac{P_2^0\gamma_2}{P_1^0\gamma_1} \tag{S85}$$

Using the CBMC data for binary and ternary mixture adsorption, the activity coefficients of CO_2(1) and CH_4(2) were determined for both binary and ternary mixtures. Figure S91b plots the ratio of the activity coefficient of CO_2(1) to that of CH_4(2), $\frac{\gamma_1}{\gamma_2}$, as a function of Φ. We note that $\frac{\gamma_1}{\gamma_2}$ for both binary and ternary mixtures are of comparable magnitudes when plotted as a function of Φ. For this reason, the

CO_2/CH_4 adsorption selectivity shows a unique dependence on Φ, despite the significant deviations from IAST estimates.

Figure S92a,b plot data obtained from CBMC simulations of the CO_2/N_2 and CH_4/N_2 adsorption selectivities in binary and ternary $CO_2/CH_4/N_2$ in NaX zeolite at 300 K. The CO_2/N_2 and CH_4/N_2 adsorption selectivities for binary and ternary mixtures display unique dependence on Φ, despite the fact that the IAST estimates are not in perfect agreement with CBMC data.

Figure S93ab plot data obtained from CBMC simulations of the CO_2/C_3H_8 and C_3H_8/CH_4 adsorption selectivities in binary mixtures and ternary $CO_2/CH_4/C_3H_8$ mixtures in NaX zeolite at 300 K. The CO_2/C_3H_8 and C_3H_8/CH_4 adsorption selectivities for binary and ternary mixtures display unique dependence on Φ, in line with the IAST precepts.

Costa et al.[76] and Calleja et al.[77] report experimental data for adsorption of CO_2/C_2H_4, CO_2/C_3H_8, C_2H_4/C_3H_8, and $CO_2/C_2H_4/C_3H_8$ mixtures in NaX zeolite at 293 K. The unary isotherm fits are specified in Table S21. Figure S94a,b,c compare the adsorption selectivities of the three pairs: CO_2/C_2H_4, CO_2/C_3H_8, C_2H_4/C_3H_8 in binary and ternary mixtures. Though there is considerable scatter in the experimental data, it is noteworthy that the selectivities in binary mixtures are of comparable magnitude to those in the ternary mixture, provided the data sets are compared at the same value of the surface potential Φ. The IAST estimates (indicated by continuous solid lines) are in reasonable agreement with experimental data. Thermodynamic non-idealities are of importance, especially for CO_2/C_3H_8 mixtures.[39, 67, 78]

Siperstein and Myers[37] report experimental data for adsorption of CO_2/C_2H_4, C_2H_4/C_2H_6, and $CO_2/C_2H_4/C_2H_6$ mixtures in NaX zeolite at 293 K. A re-analysis of the data, as reported in Tables C1, C5 and C7 of their paper is presented in Figure S95. Figure S95 compares the adsorption selectivities of the two pairs: CO_2/C_2H_4, and C_2H_4/C_2H_6 in binary and ternary mixtures. Though there is considerable scatter in the experimental data, it is noteworthy that the selectivities in binary mixtures are of comparable magnitude to those in the ternary mixture, provided the data sets are compared at the same value of the surface potential Φ. The IAST estimates (indicated by continuous solid lines) are in fair agreement with experimental data.

11.5 List of Tables for Adsorption, Diffusion, Permeation in FAU zeolite

Table S18. Dual-site Langmuir-Freundlich parameters for pure components CO_2, CH_4, N_2, C_2H_6, and C_3H_8 at 300K in all-silica FAU. The fit parameters are based on the CBMC simulations of pure component isotherms presented in earlier works.[1, 79, 80]

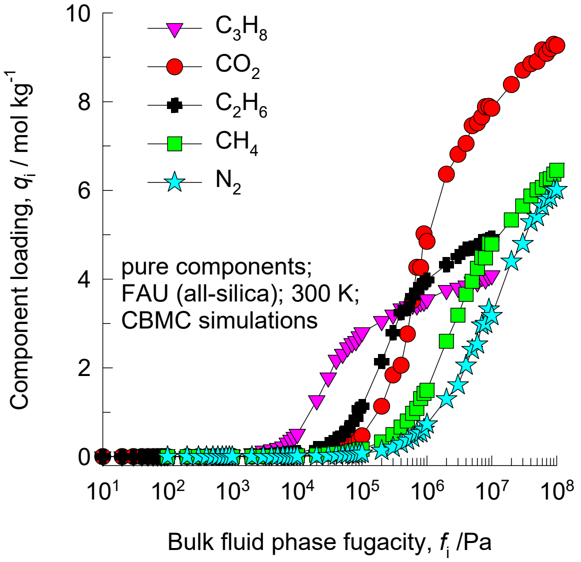

	Site A			Site B		
	$q_{A,sat}$ mol kg^{-1}	b_A $Pa^{-\nu_A}$	ν_A dimensionless	$q_{B,sat}$ mol kg^{-1}	b_B $Pa^{-\nu_B}$	ν_B dimensionless
CO_2	2.4	2.52×10^{-14}	2.4	6.7	6.74×10^{-7}	1
CH_4	4	7×10^{-9}	0.86	6.5	2.75×10^{-7}	1
N_2	5.2	1.55×10^{-9}	1	5.8	1.32×10^{-7}	1
C_2H_6	5.201	2.872E-06	1	5.201	1.000E-09	1
C_3H_8	3.467	1.338E-05	0.6	3.467	1.718E-06	1.27

Table S19. Dual-site Langmuir-Freundlich parameters for pure components CO_2, CH_4, and C_3H_8 at 300 K in NaX zeolite containing 86 Na^+/uc with Si/Al=1.23. The fit parameters are based on the CBMC simulations of pure component isotherms.

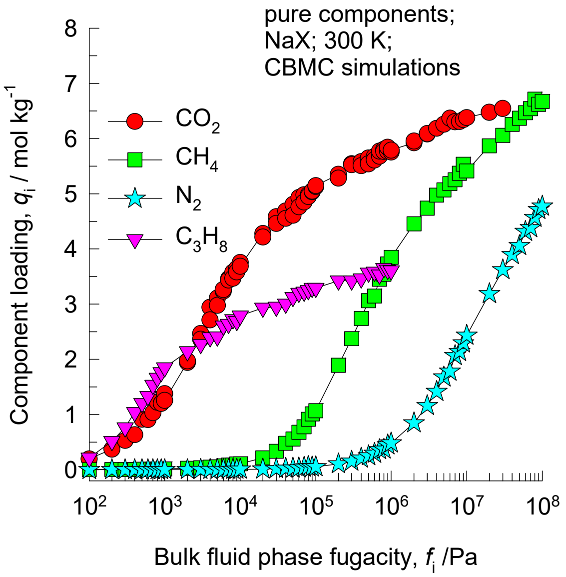

	Site A			Site B		
	$q_{A,sat}$ mol kg^{-1}	b_A $Pa^{-\nu_A}$	ν_A dimensionless	$q_{B,sat}$ mol kg^{-1}	b_B $Pa^{-\nu_B}$	ν_B dimensionless
CO_2	2.1	2.300E-04	0.67	4.4	4.136E-04	1
CH_4	5.8	2.07E-06	1			
N_2	9.8	2.136E-09	0.96	4.2	1.224E-07	1
C_3H_8	2.2	1.194E-04	1.46	1.6	1.15E-03	0.66

Table S20. Dual-site Langmuir parameters for pure components CO_2, C_3H_8, C_2H_4, and C_2H_6 at 293 K in NaX zeolite.[37] The fit parameters were determined by fitting the unary isotherm data presented in Figure 1 of Siperstein and Myers.[37]

	Site A		Site B	
	$q_{A,sat}$ mol kg^{-1}	b_A Pa^{-1}	$q_{B,sat}$ mol kg^{-1}	b_B Pa^{-1}
CO_2	1.7	1.080E-02	4.2	1.326E-04
C_3H_8	3.3	1.034E-03		
C_2H_4	2	2.348E-03	2.1	1.616E-04
C_2H_6	4.5	4.693E-05		

Table S21. Dual-site Langmuir parameters for pure components CO_2, C_2H_4, C_3H_6, and C_3H_8 at 293 K in 13X (= NaX) zeolite. The fit parameters were determined by fitting the unary isotherm data presented in Table I of Costa et al.[76]

	Site A		Site B	
	$q_{A,sat}$ mol kg^{-1}	b_A Pa^{-1}	$q_{B,sat}$ mol kg^{-1}	b_B Pa^{-1}
CO_2	2	6.07×10^{-4}	2.5	3.47×10^{-5}
C_2H_4	1.35	2.25×10^{-4}	1.4	2.57×10^{-4}
C_3H_6	0.95	5.72×10^{-4}	1.5	5.98×10^{-2}
C_3H_8	2.2	7.04×10^{-4}		

11.6 List of Figures for Adsorption, Diffusion, Permeation in FAU zeolite

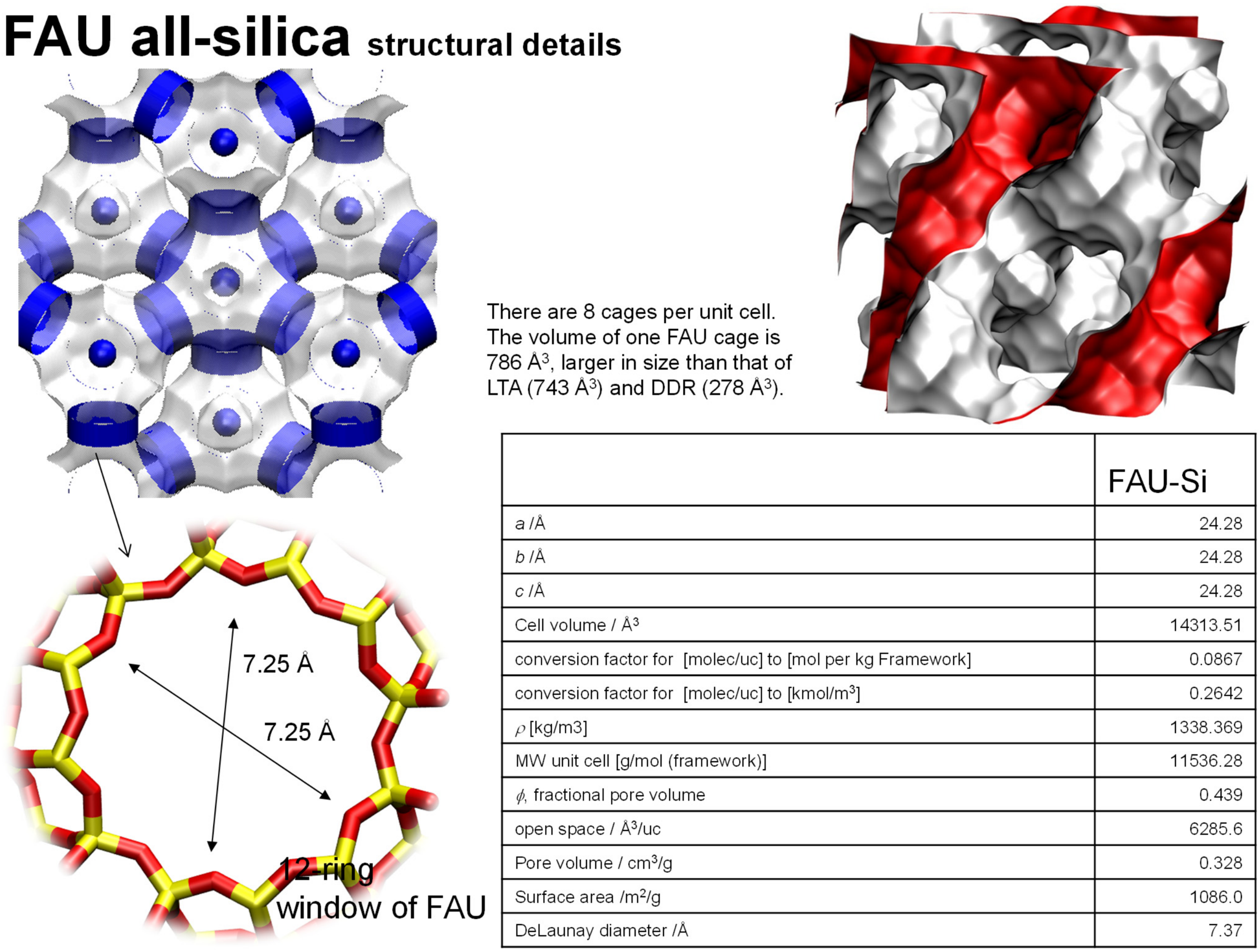

FAU all-silica structural details

There are 8 cages per unit cell. The volume of one FAU cage is 786 Å^3, larger in size than that of LTA (743 Å^3) and DDR (278 Å^3).

	FAU-Si
a /Å	24.28
b /Å	24.28
c /Å	24.28
Cell volume / Å^3	14313.51
conversion factor for [molec/uc] to [mol per kg Framework]	0.0867
conversion factor for [molec/uc] to [kmol/m^3]	0.2642
ρ [kg/m3]	1338.369
MW unit cell [g/mol (framework)]	11536.28
ϕ, fractional pore volume	0.439
open space / Å^3/uc	6285.6
Pore volume / cm^3/g	0.328
Surface area /m^2/g	1086.0
DeLaunay diameter /Å	7.37

Figure S79. Pore landscape for all-silica FAU zeolite.

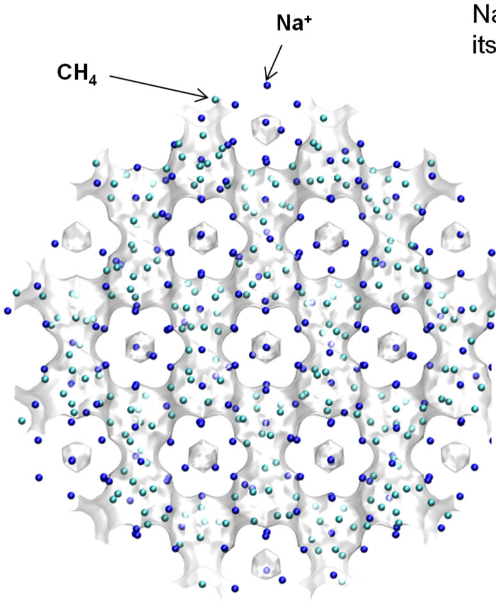

NaX is commonly referred to by its trade name 13X zeolite

	NaX 86 Na/uc
a /Å	25.028
b /Å	25.028
c /Å	25.028
Cell volume / Å^3	15677.56
conversion factor for [molec/uc] to [mol per kg Framework]	0.0745
conversion factor for [molec/uc] to [kmol/m^3]	0.2658
ρ [kg/m3] (with cations)	1421.277
MW unit cell [g/mol(framework+cations)]	13418.42
ϕ, fractional pore volume	0.399
open space / Å^3/uc	6248.0
Pore volume / cm^3/g	0.280
Surface area /m^2/g	
DeLaunay diameter /Å	7.37

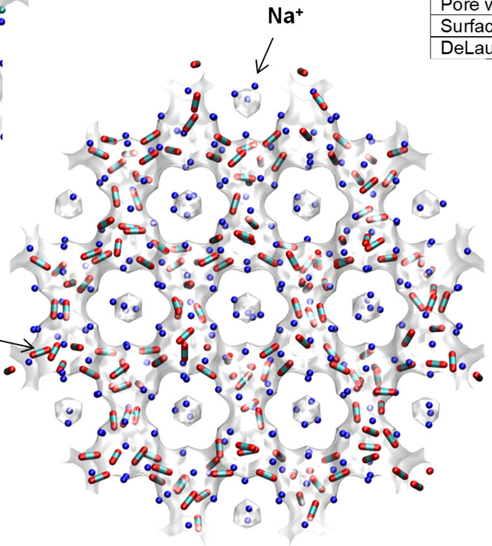

Figure S80. Structural details for NaX zeolite (106 Si, 86 Al, 86 Na$^+$, Si/Al=1.23)

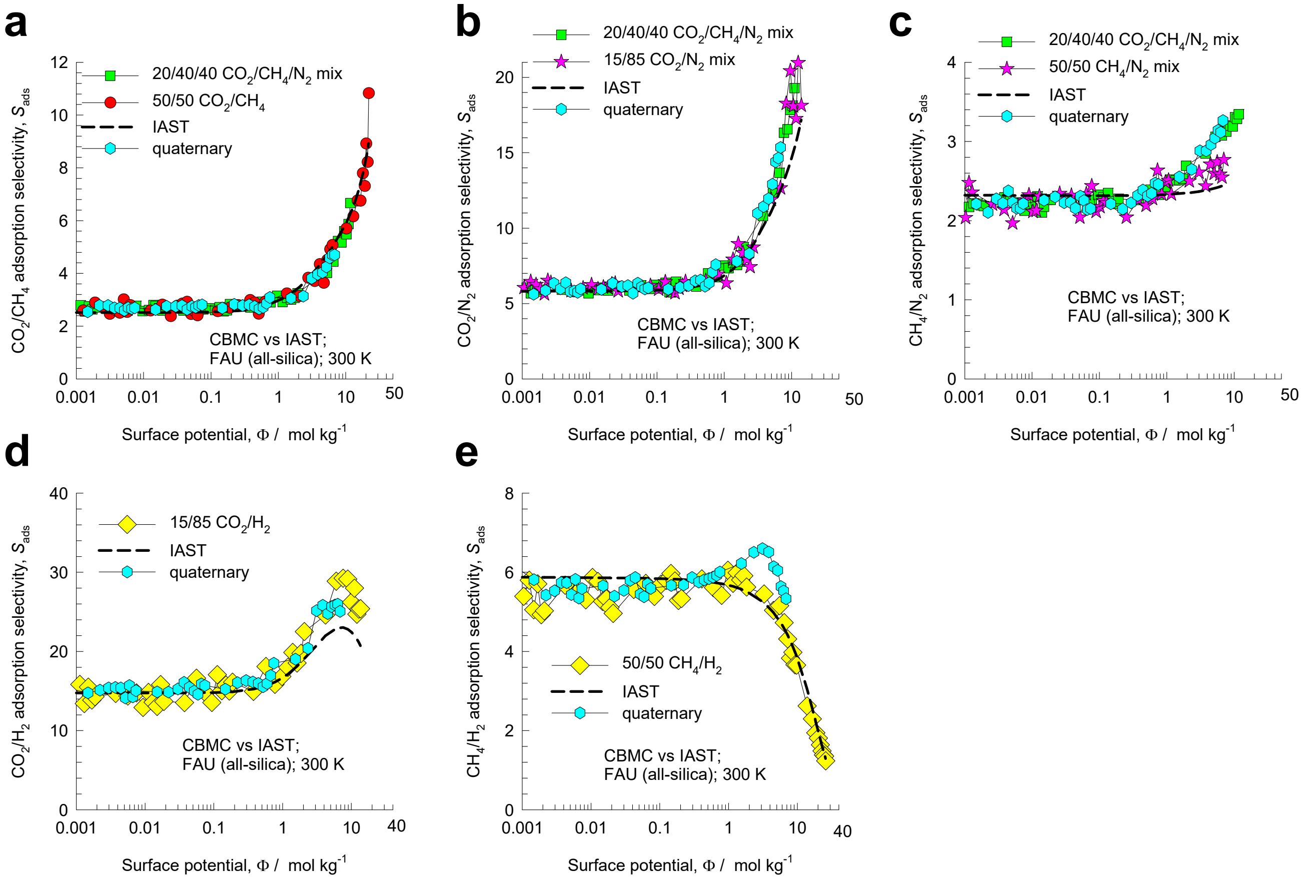

Figure S81. CBMC simulations of (a) CO_2/CH_4, (b) CO_2/N_2, (c) CH_4/N_2, (d) CO_2/H_2, and (e) CH_4/H_2, adsorption selectivities, S_{ads} , determined from binary, ternary, and quaternary mixture adsorption in all-silica FAU zeolite at 300 K, plotted as function of the surface potential, Φ .

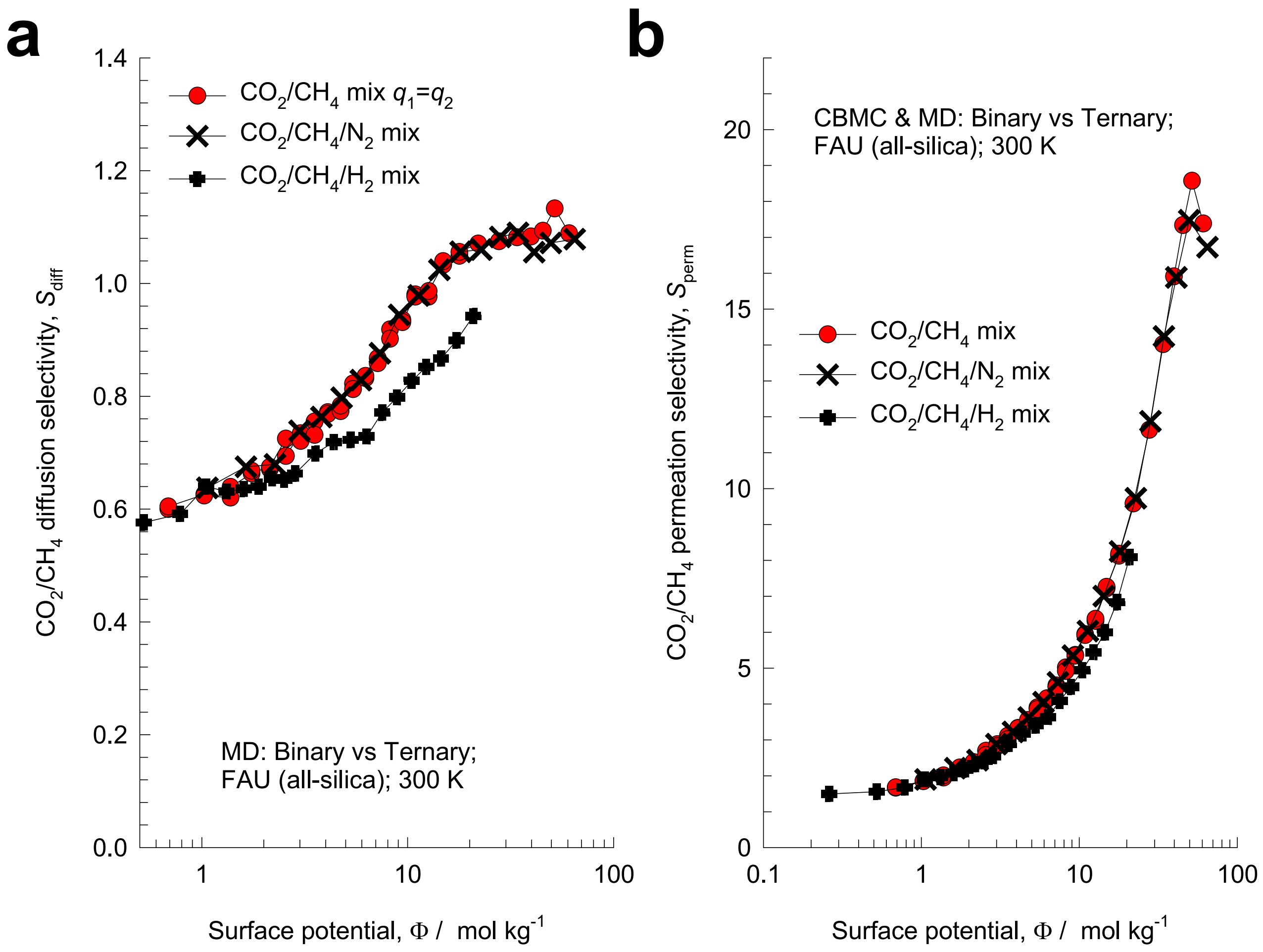

Figure S82. (a) MD simulations of the CO_2/CH_4 diffusion selectivities, S_{diff}, determined from both equimolar $(q_1 = q_2)$ binary mixtures and equimolar $(q_1 = q_2 = q_3)$ ternary ($CO_2/CH_4/N_2$, and $CO_2/CH_4/H_2$) mixtures in all-silica FAU zeolite at 300 K, plotted as function of the surface potential Φ. (b) Plot of the CO_2/CH_4 permeation selectivity S_{perm} as function of the surface potential Φ, determined from binary and ternary ($CO_2/CH_4/N_2$, and $CO_2/CH_4/H_2$) MD campaigns.

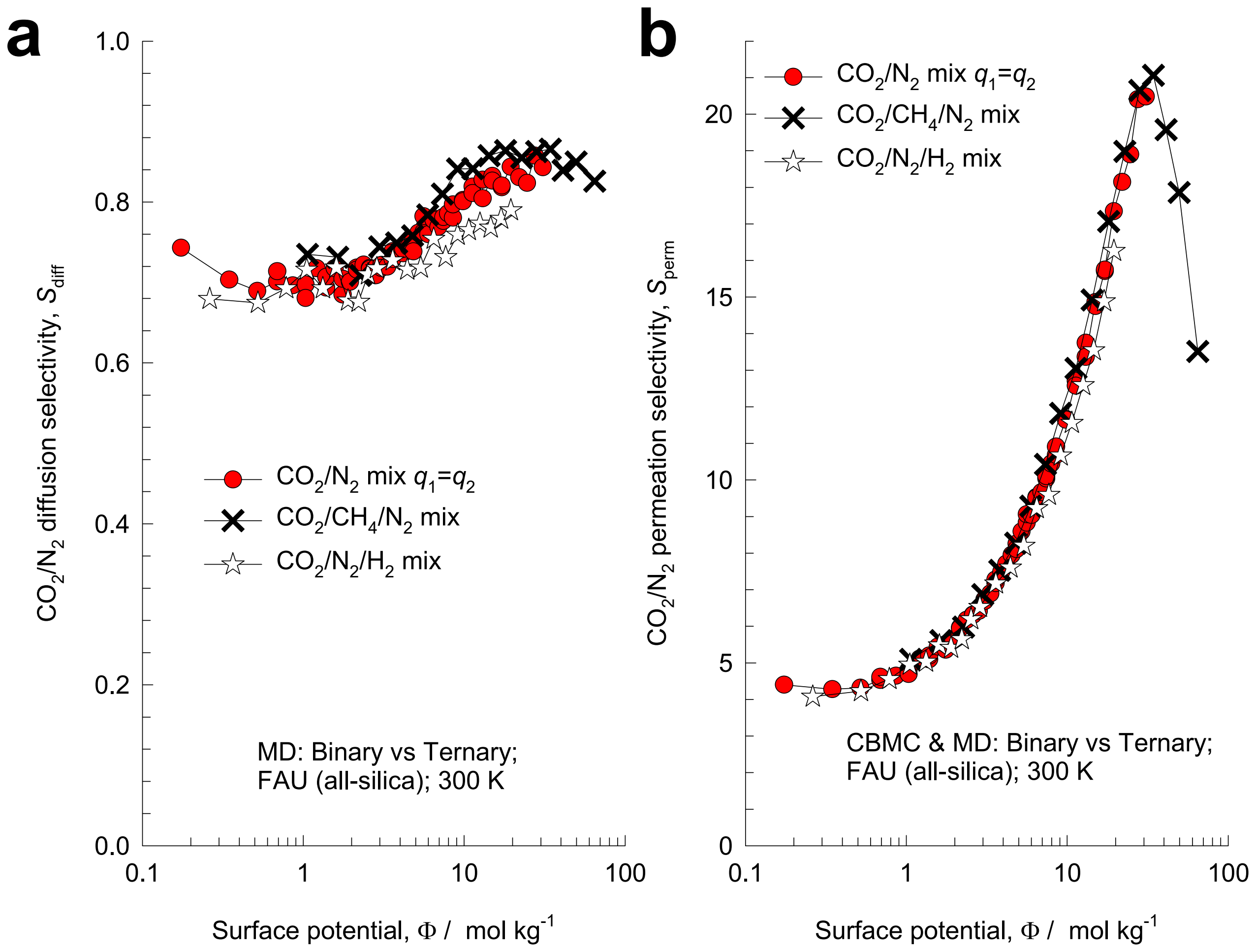

Figure S83. (a) MD simulations of the CO2/N2 diffusion selectivities, S_{diff}, determined from both equimolar $\left(q_1 = q_2\right)$ binary and equimolar $\left(q_1 = q_2 = q_3\right)$ ternary (CO2/CH4/N2, and CO2/N2/H2) mixtures in all-silica FAU zeolite at 300 K, plotted as function of the surface potential Φ. (b) Plot of the CO2/N2 permeation selectivity S_{perm} as function of the surface potential Φ, determined from binary and ternary (CO2/CH4/N2, and CO2/N2/H2) mixtures MD campaigns.

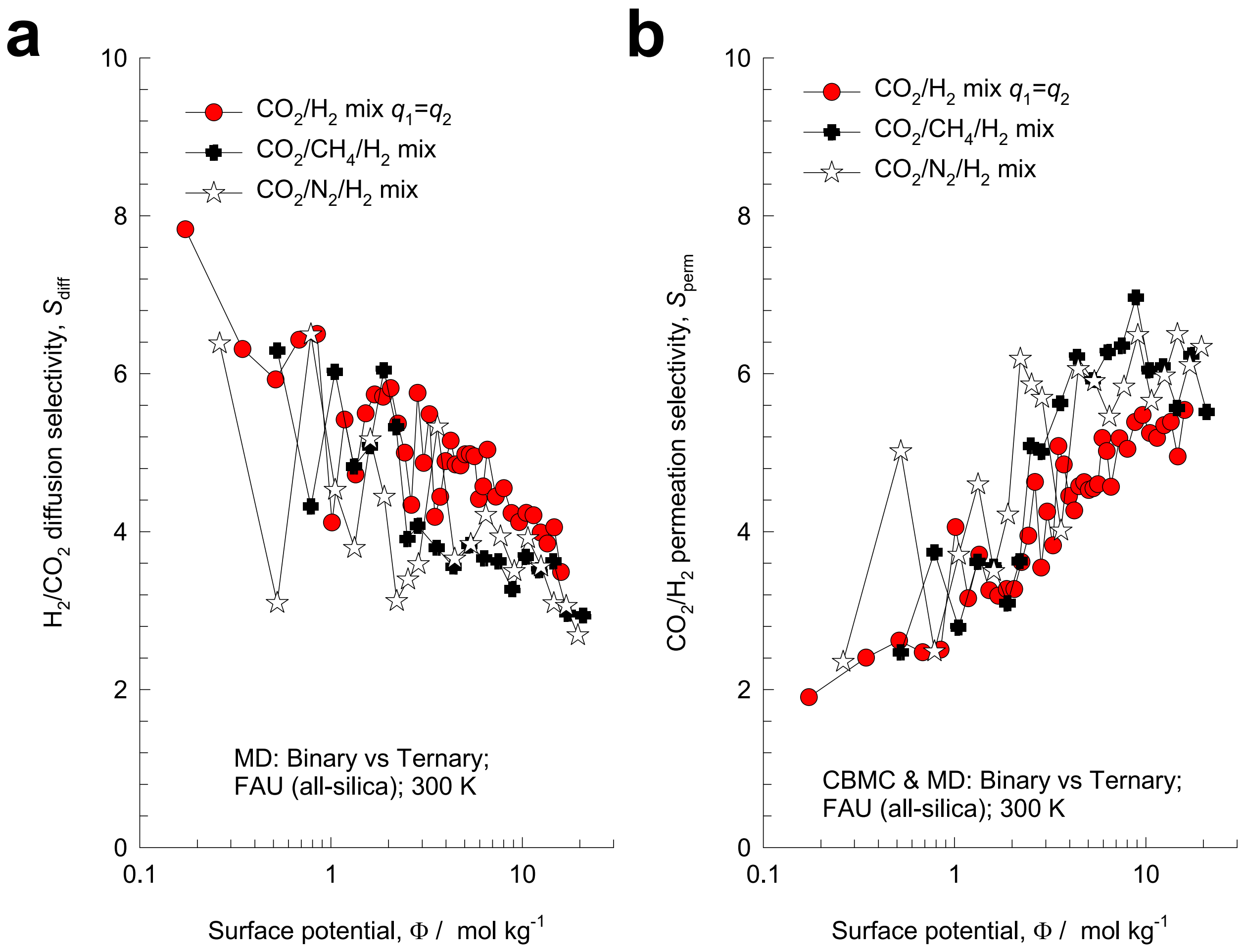

Figure S84. (a) MD simulations of the H_2/CO_2 diffusion selectivities, S_{diff}, determined from both equimolar $\left(q_1 = q_2\right)$ binary and equimolar $\left(q_1 = q_2 = q_3\right)$ ternary ($CO_2/N_2/H_2$, and $CO_2/CH_4/H_2$) mixtures in all-silica FAU zeolite at 300 K, plotted as function of the surface potential Φ. (b) Plot of the CO_2/H_2 permeation selectivity S_{perm} as function of the surface potential Φ, determined from binary and ternary ($CO_2/N_2/H_2$, and $CO_2/CH_4/H_2$) MD campaigns.

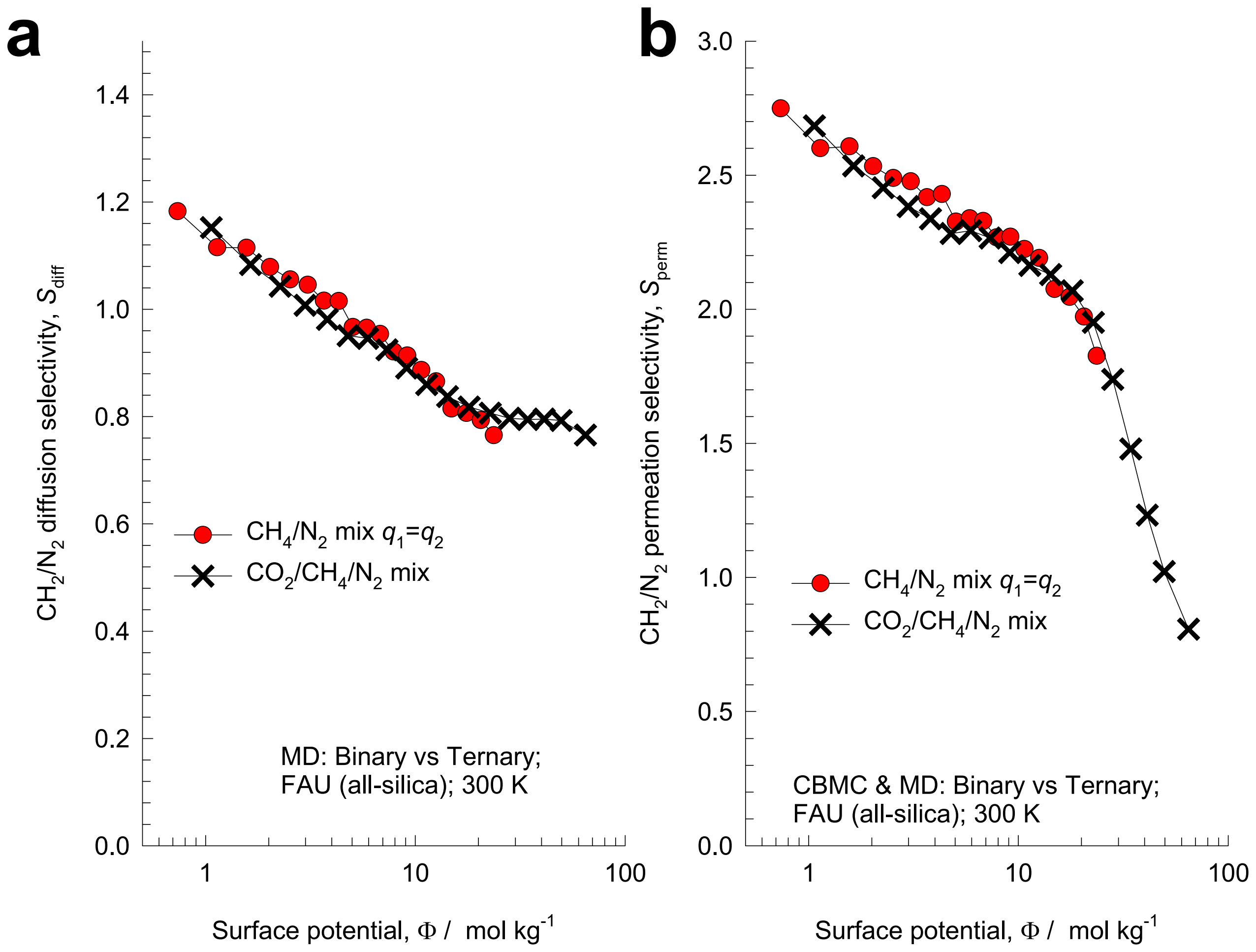

Figure S85. (a) MD simulations of the CH4/N2 diffusion selectivities, S_{diff}, determined from both equimolar $\left(q_1 = q_2\right)$ binary and equimolar $\left(q_1 = q_2 = q_3\right)$ ternary (CO2/CH4/N2) mixtures in all-silica FAU zeolite at 300 K, plotted as function of the surface potential Φ. (b) Plot of the CH4/N2 permeation selectivity S_{perm} as function of the surface potential Φ, determined from binary and ternary (CO2/CH4/N2) MD campaigns.

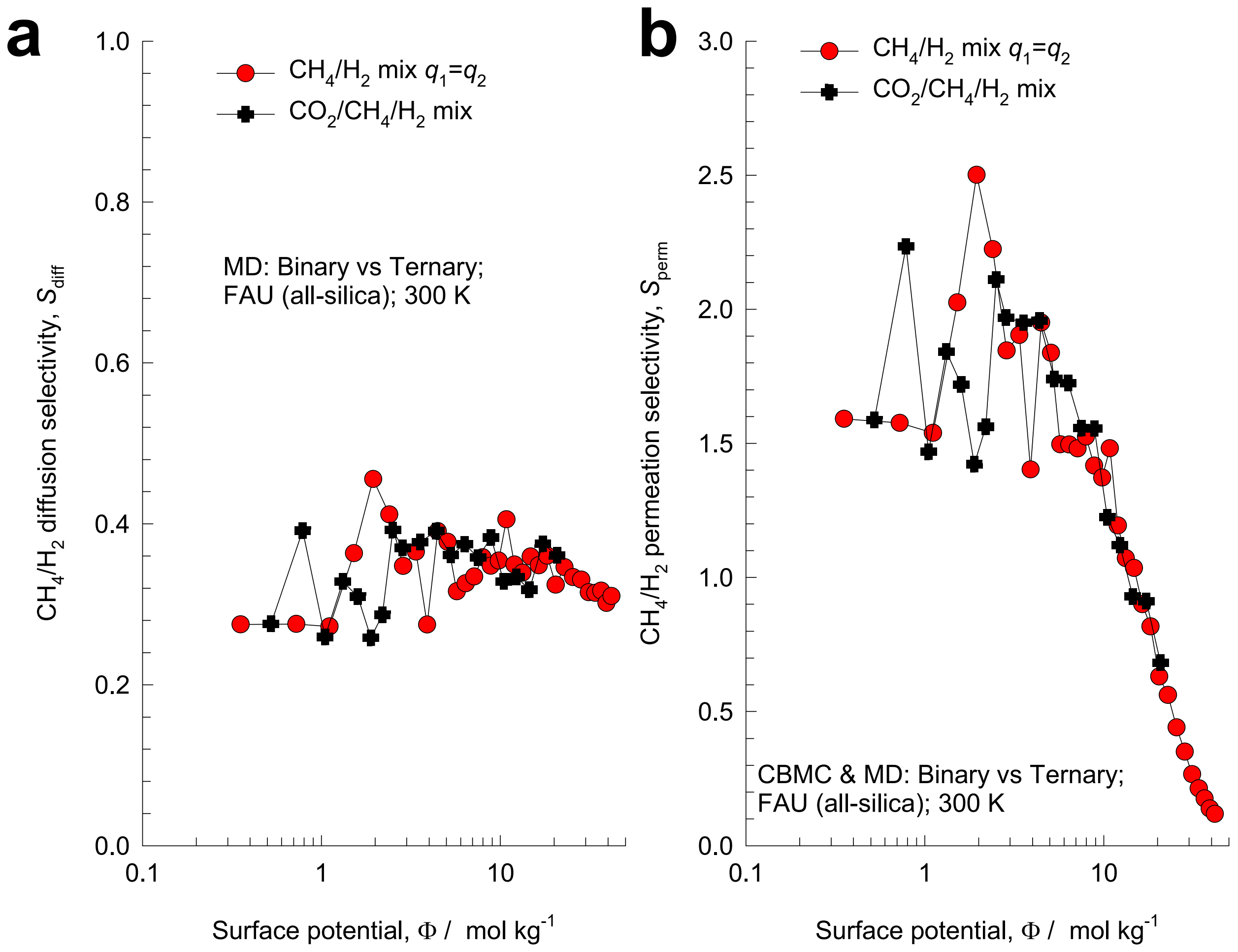

Figure S86. (a) MD simulations of the CH_4/H_2 diffusion selectivities, S_{diff}, determined from both equimolar $(q_1 = q_2)$ binary and equimolar $(q_1 = q_2 = q_3)$ ternary ($CO_2/CH_4/H_2$) mixtures in all-silica FAU zeolite at 300 K, plotted as function of the surface potential Φ. (b) Plot of the CH_4/H_2 permeation selectivity S_{perm} as function of the surface potential Φ, determined from binary and ternary ($CO_2/CH_4/H_2$) MD campaigns.

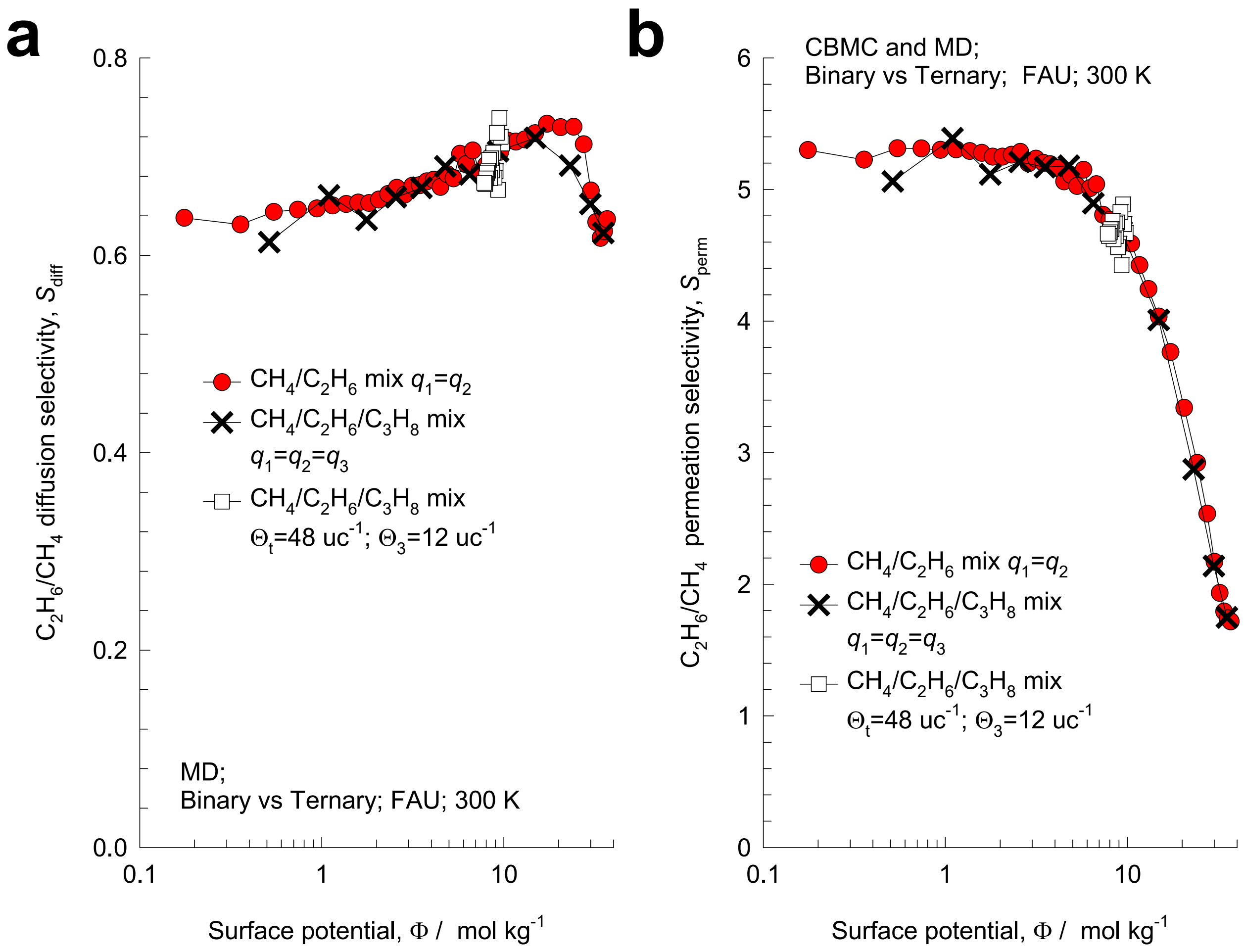

Figure S87. (a) MD simulations of the C_2H_6/CH_4 diffusion selectivities, S_{diff}, determined from both equimolar $(q_1 = q_2)$ binary and equimolar $(q_1 = q_2 = q_3)$ ternary ($CH_4/C_2H_6/C_3H_8$) mixtures in all-silica FAU zeolite at 300 K, plotted as function of the surface potential Φ. (b) Plot of the C_2H_6/CH_4 permeation selectivity S_{perm} as function of the surface potential Φ, determined from binary and ternary ($CH_4/C_2H_6/C_3H_8$) MD campaigns.

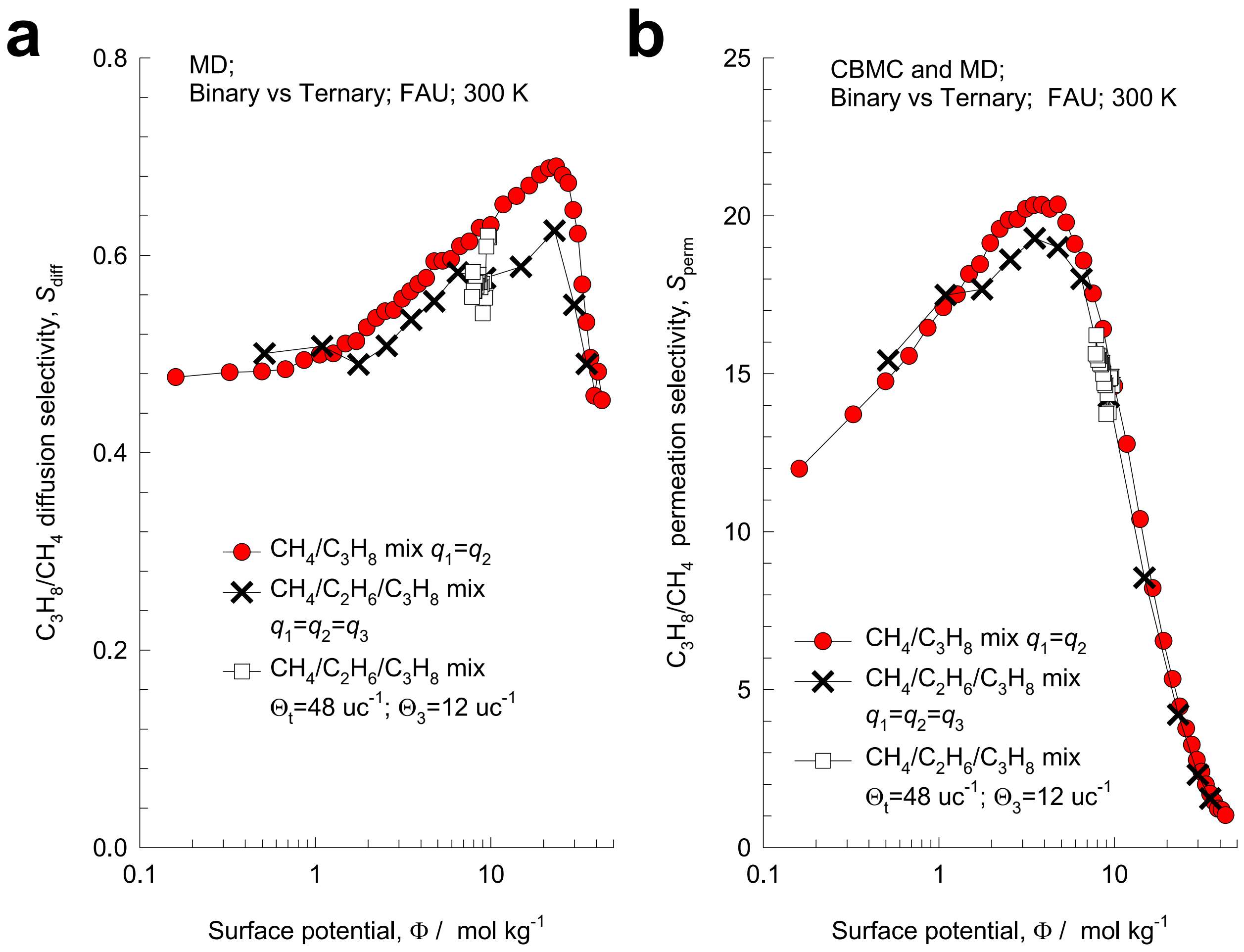

Figure S88. (a) MD simulations of the C_3H_8/CH_4 diffusion selectivities, S_{diff}, determined from both equimolar $\left(q_1 = q_2\right)$ binary and equimolar $\left(q_1 = q_2 = q_3\right)$ ternary ($CH_4/C_2H_6/C_3H_8$) mixtures in all-silica FAU zeolite at 300 K, plotted as function of the surface potential Φ. (b) Plot of the C_3H_8/CH_4 permeation selectivity S_{perm} as function of the surface potential Φ, determined from binary and ternary ($CH_4/C_2H_6/C_3H_8$) MD campaigns.

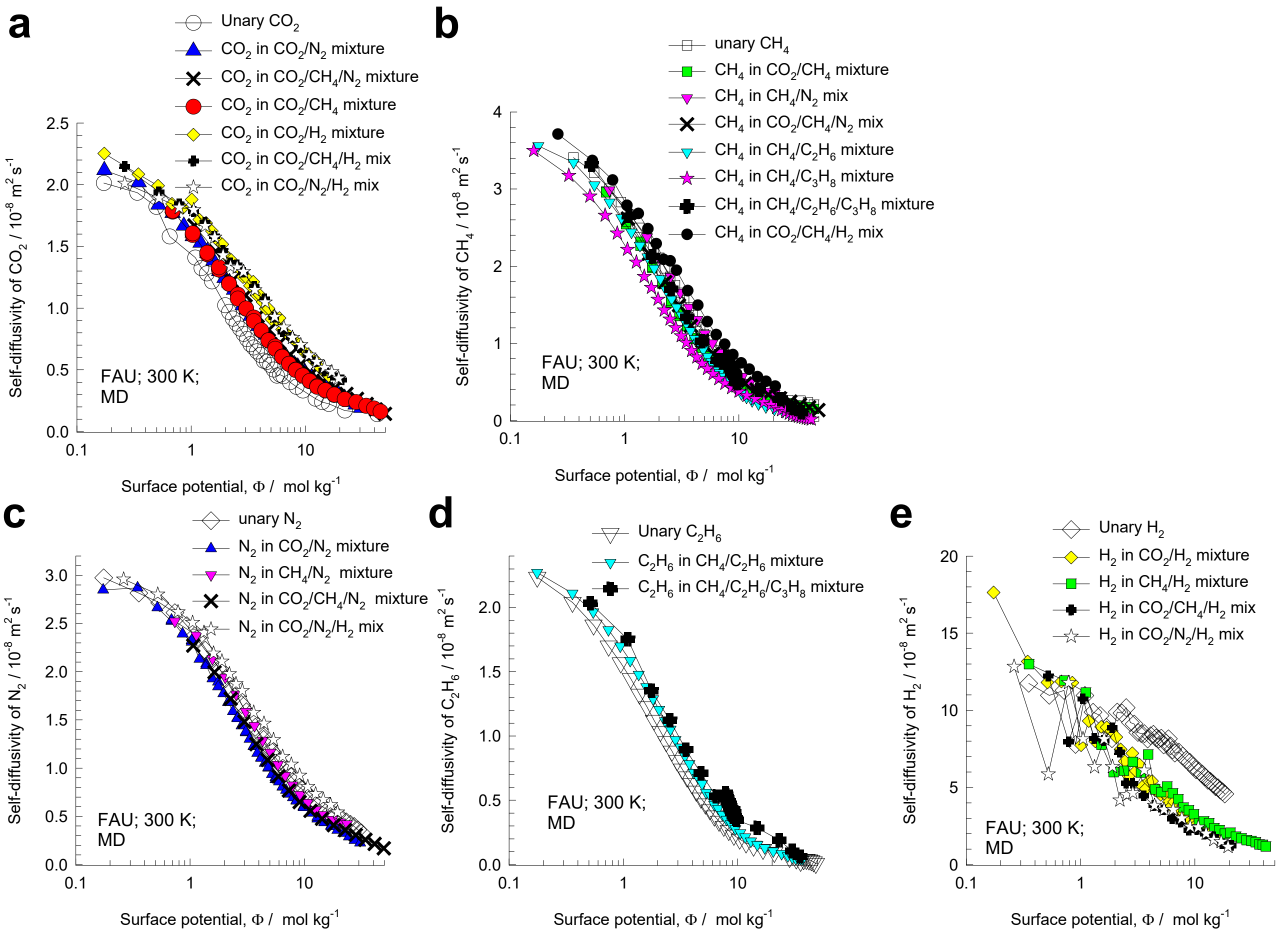

Figure S89. MD simulation data on the self-diffusivities, $D_{i,self}$, of (a) CO_2, (b) CH_4, (c) N_2, (d) C_2H_6, and (e) H_2 in equimolar $q_1 = q_2$; $x_1 = 1 - x_2 = 0.5$ binary CO_2/CH_4, CO_2/N_2, CO_2/H_2, CH_4/N_2, CH_4/H_2, CH_4/C_2H_6, CH_4/C_3H_8, and C_2H_6/C_3H_8 mixtures and equimolar $(q_1 = q_2 = q_3)$ ternary $CO_2/CH_4/N_2$, $CO_2/CH_4/H_2$, $CO_2/N_2/H_2$, and $CH_4/C_2H_6/C_3H_8$ mixtures in FAU zeolite at 300 K, plotted as a function of the surface potential Φ. Also plotted are the corresponding values of the unary self-diffusivities.

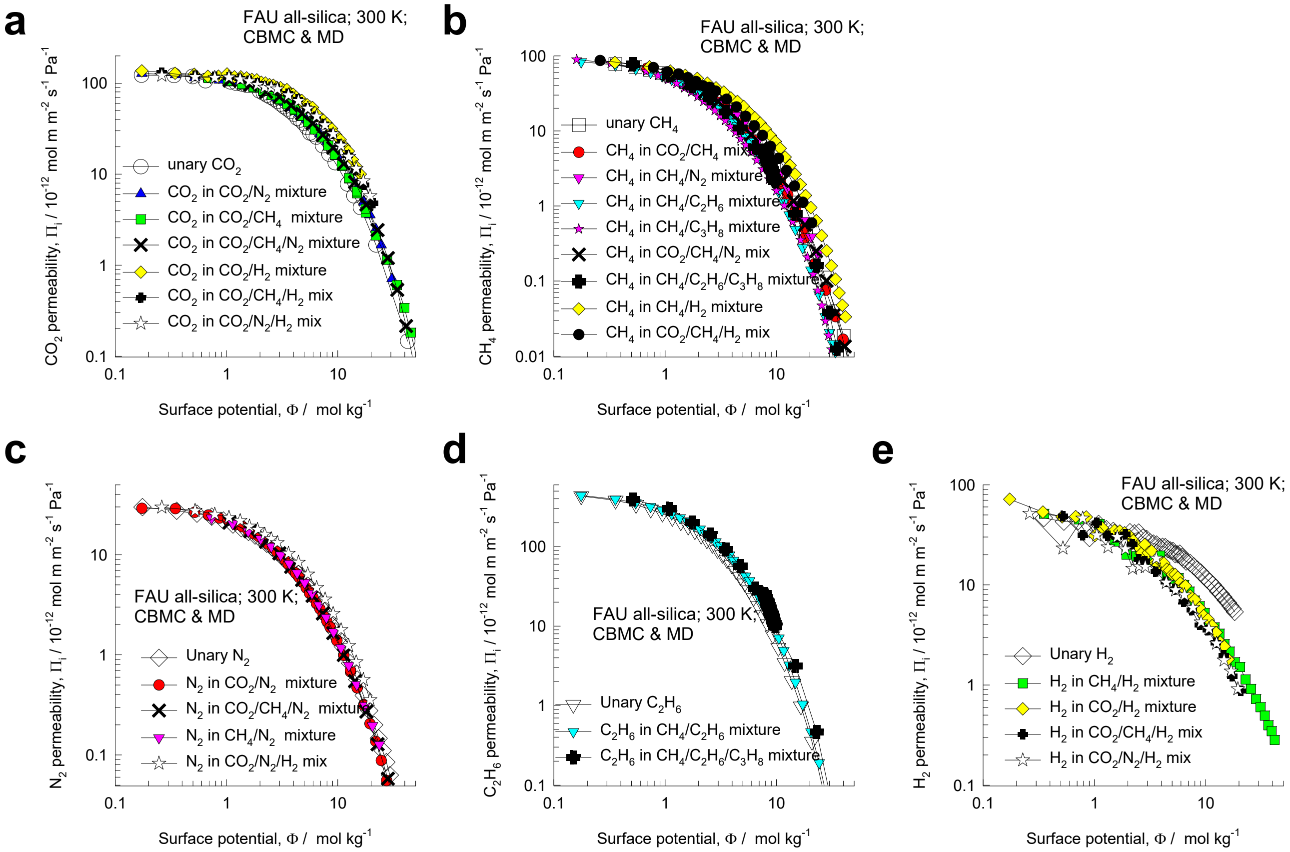

Figure S90. CBMC/MD simulations of the permeabilities, Π_i, of of (a) CO_2, (b) CH_4, (c) N_2, (d) C_2H_6, and (e) H_2 in equimolar $q_1 = q_2$; $x_1 = 1 - x_2 = 0.5$ binary CO_2/CH_4, CO_2/N_2, CO_2/H_2, CH_4/N_2, CH_4/H_2, CH_4/C_2H_6, CH_4/C_3H_8, and C_2H_6/C_3H_8 mixtures and equimolar $\left(q_1 = q_2 = q_3\right)$ ternary $CO_2/CH_4/N_2$, $CO_2/CH_4/H_2$, $CO_2/N_2/H_2$, and $CH_4/C_2H_6/C_3H_8$ mixtures in FAU zeolite at 300 K, plotted as a function of the surface potential Φ. Also plotted are the corresponding values of the unary permeabilities.

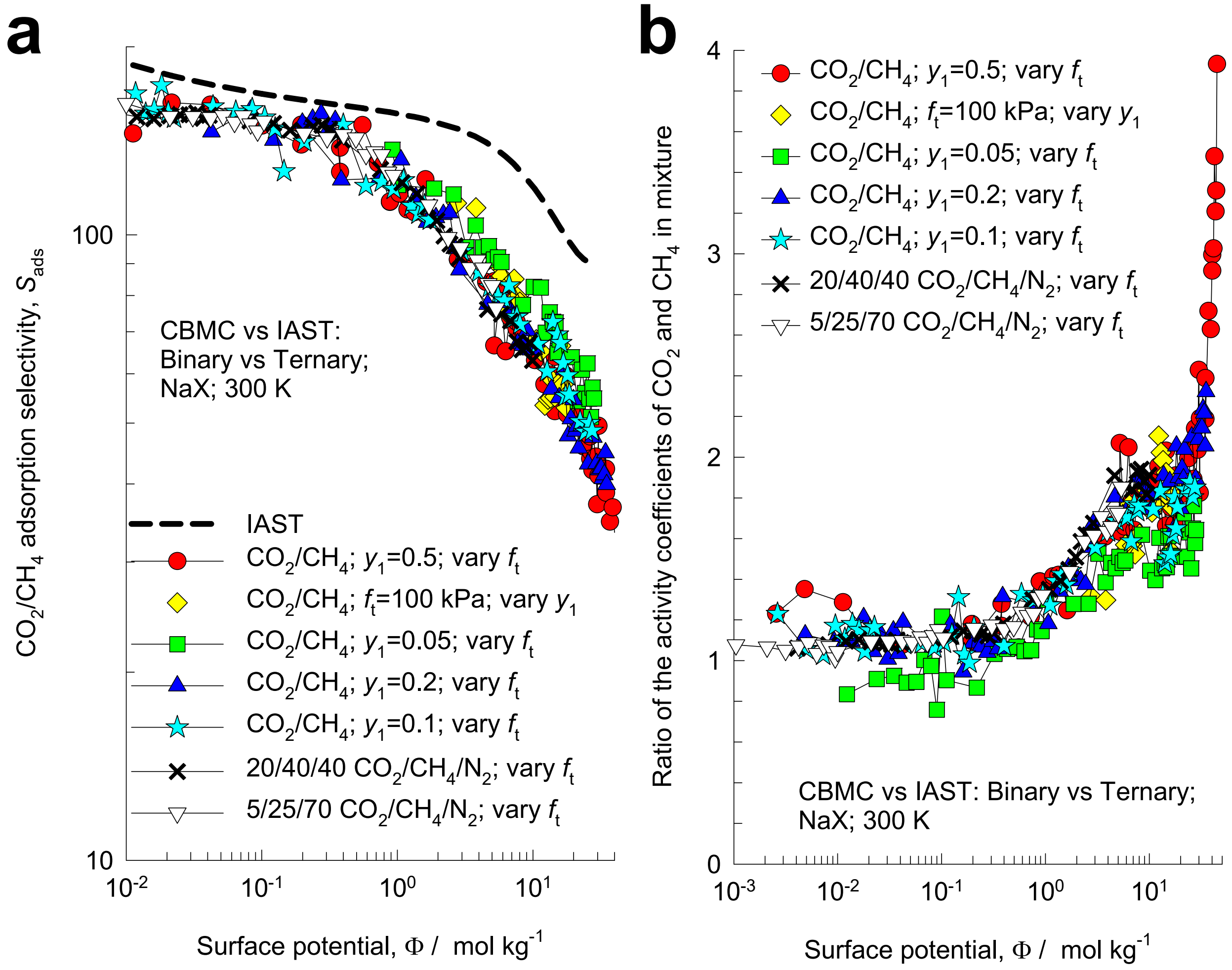

Figure S91. (a) CBMC simulations of the CO2/CH4 adsorption selectivity, S_{ads}, for binary and ternary mixture adsorption in NaX zeolite at 300 K. The adsorption selectivities are plotted as function of the surface potential Φ. The dashed lines are the IAST calculations; the unary isotherm fit parameters are provided in Table S19. (b) CBMC simulations of the ratio of activity coefficients of CO2, and CH4 plotted as function of the surface potential Φ.

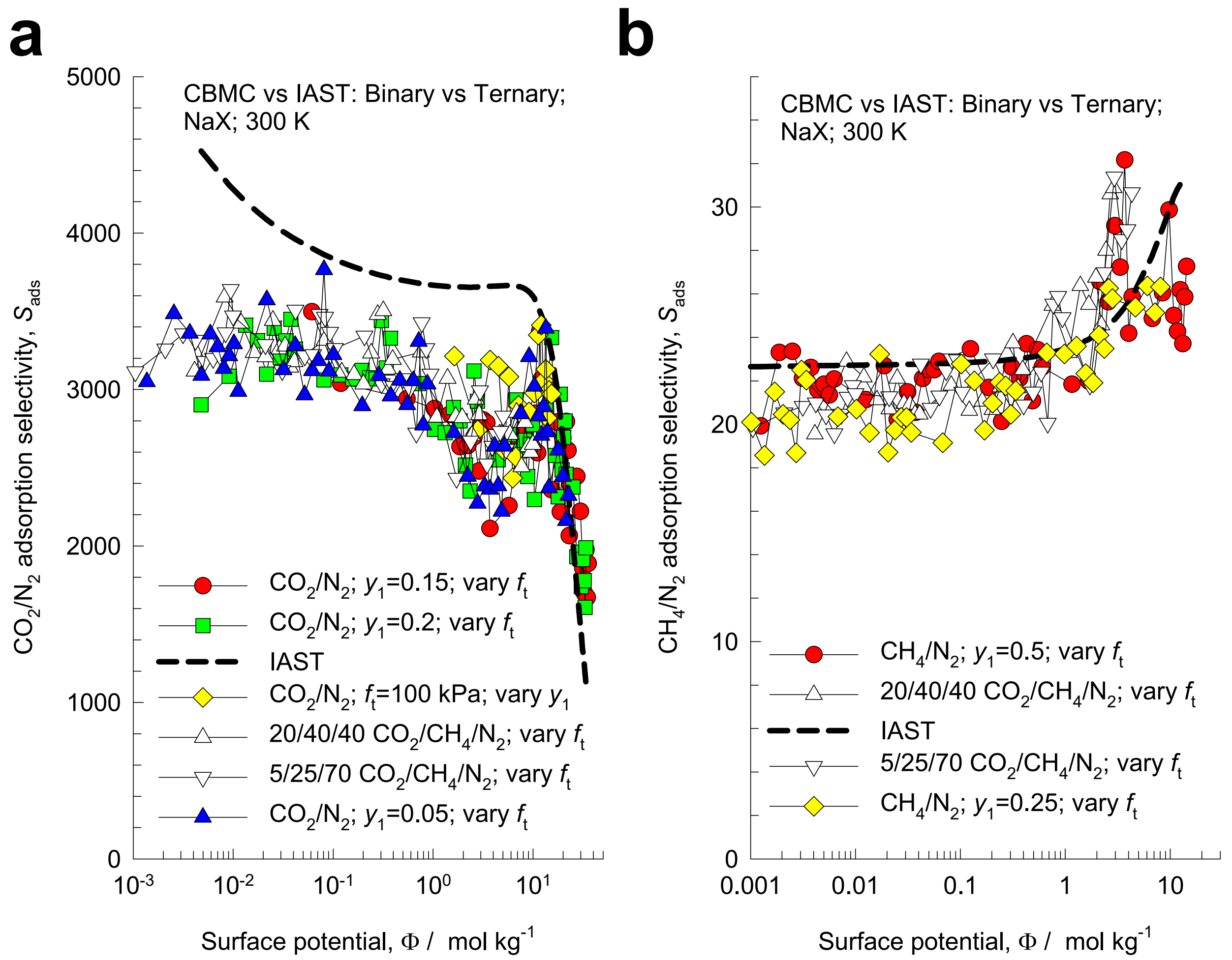

Figure S92. (a) CBMC simulations of the CO_2/N_2 adsorption selectivity, S_{ads}, for binary and ternary mixture adsorption in NaX zeolite at 300 K. (b) CBMC simulations of the CH_4/N_2 adsorption selectivities in binary and ternary mixtures in NaX zeolite at 300 K. The selectivities are plotted as function of the surface potential Φ. The dashed lines are the IAST calculations; the unary isotherm fit parameters are provided in Table S19.

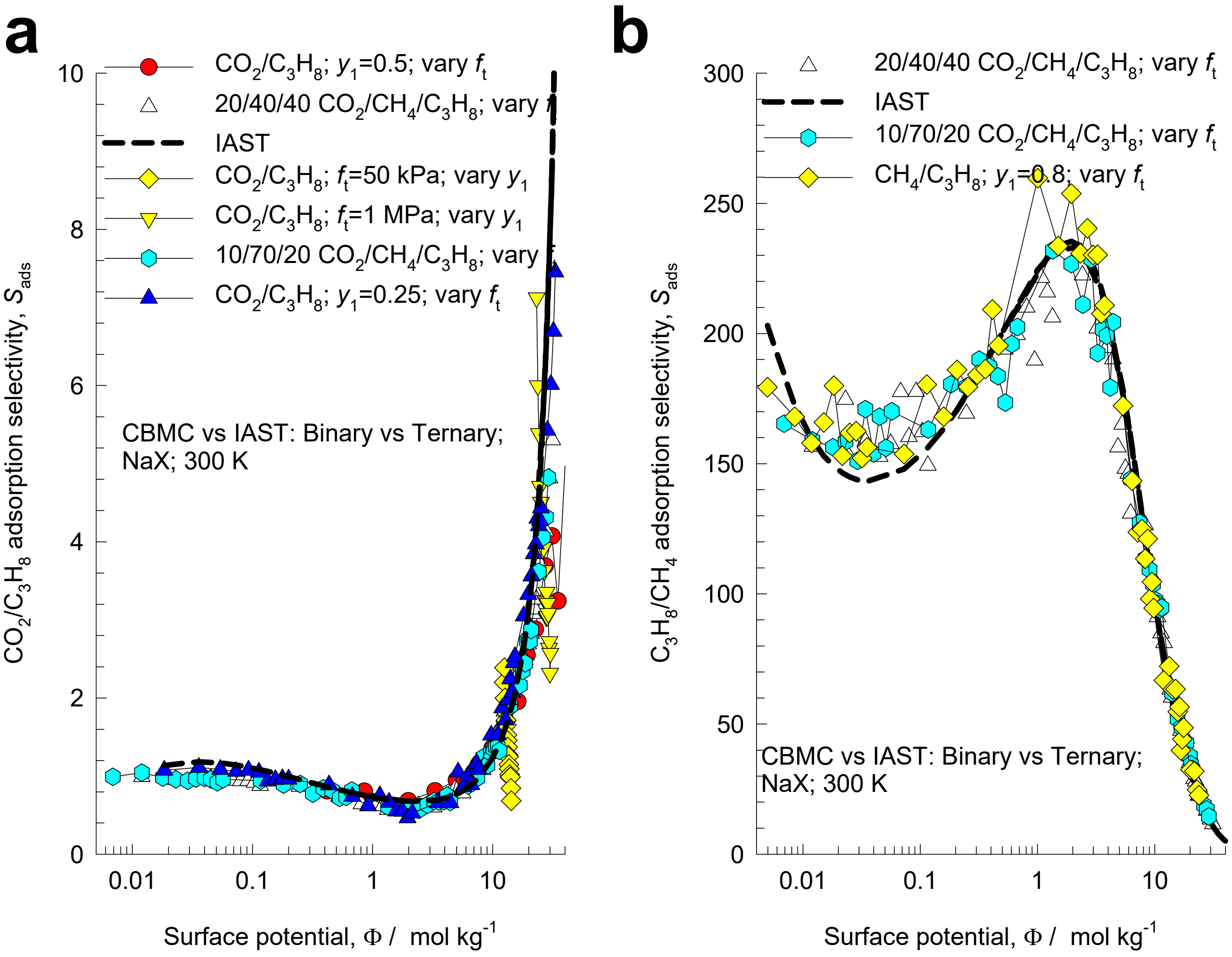

Figure S93. (a) CBMC simulations of the CO_2/C_3H_8 adsorption selectivity, S_{ads}, for binary and ternary mixture adsorption in NaX zeolite at 300 K. (b) CBMC simulations of the C_3H_8/CH_4 adsorption selectivities in binary and ternary mixtures in NaX zeolite at 300 K. The selectivities are plotted as function of the surface potential Φ. The dashed lines are the IAST calculations; the unary isotherm fit parameters are provided in Table S19.

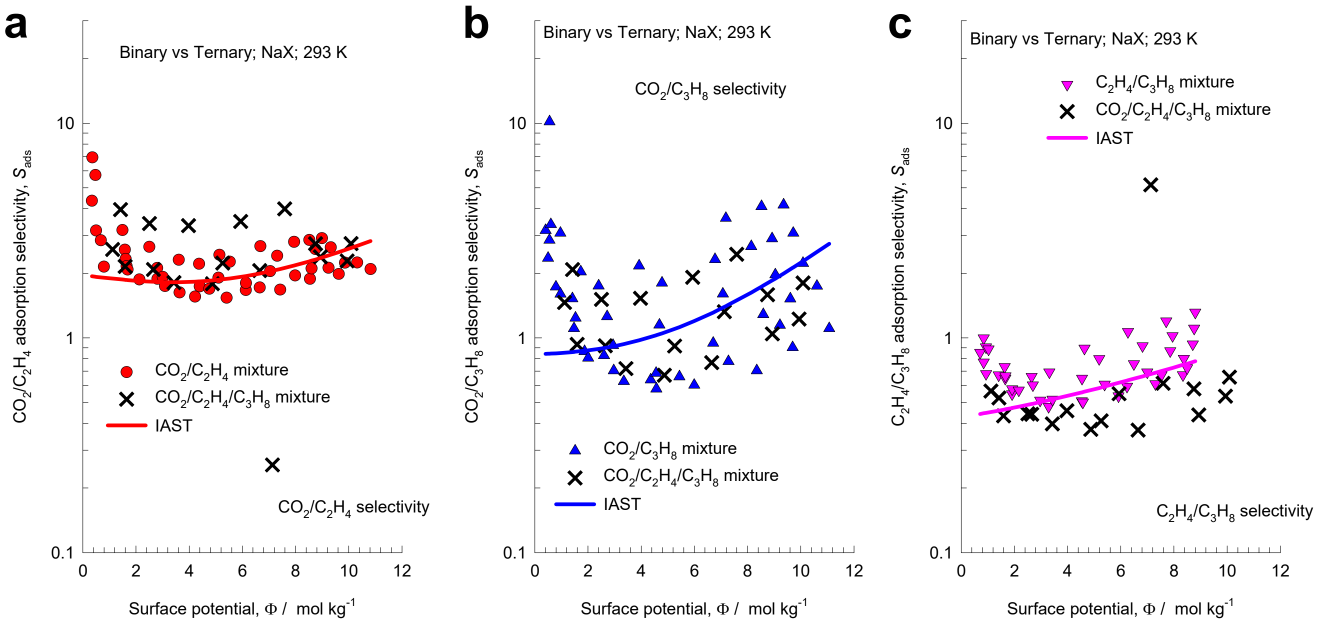

Figure S94. (a, b, c) Re-analysis of the experimental data of Costa et al.[76] and Calleja et al.[77] for adsorption of CO$_2$/C$_2$H$_4$, CO$_2$/C$_3$H$_8$, C$_2$H$_4$/C$_3$H$_8$, and CO$_2$/C$_2$H$_4$/C$_3$H$_8$ mixtures in NaX (=13X) zeolite at 293 K. (a) CO$_2$/C$_2$H$_4$ adsorption selectivities in binary (symbols) and ternary mixtures (crosses). (b) CO$_2$/C$_3$H$_8$ adsorption selectivities in binary (symbols) and ternary mixtures (crosses). (c) C$_2$H$_4$/C$_3$H$_8$ adsorption selectivities in binary (symbols) and ternary mixtures (crosses). Also shown are IAST estimations (continuous solid lines) of S_{ads}. The unary isotherm fits are specified in Table S21.

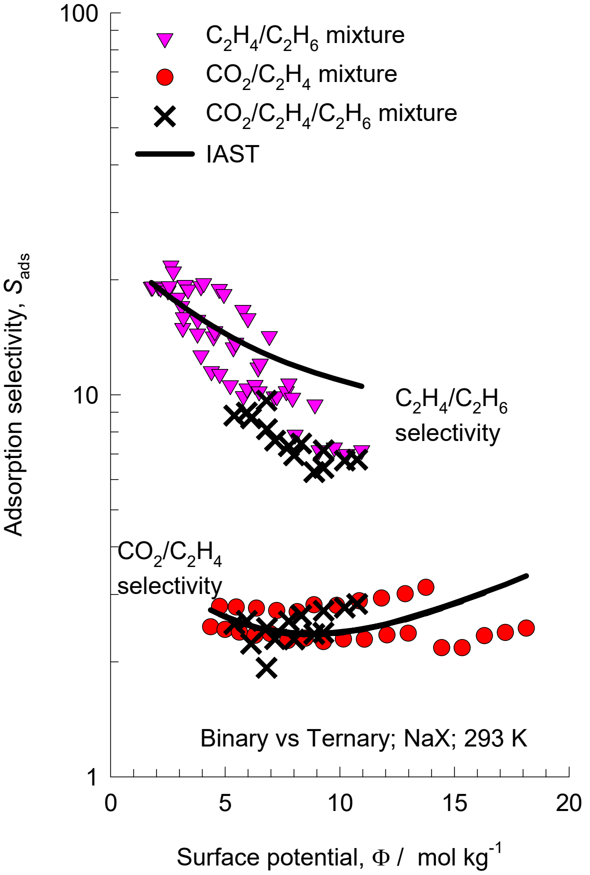

Figure S95. Re-analysis of the experimental data of Siperstein and Myers[37] for adsorption of CO_2/C_2H_4, C_2H_4/C_2H_6, and $CO_2/C_2H_4/C_2H_6$ mixtures in NaX zeolite at 293 K. Also shown are IAST estimations (continuous solid lines) of S_{ads}. The unary isotherm fits are specified in Table S20.

12 Adsorption of mixtures of hydrocarbons

The separation of hexane isomers, n-hexane (nC6), 2-methylpentane (2MP), 3-methylpentane (3MP), 2,2 dimethylbutane (22DMB), and 2,3 dimethylbutane (23DMB) is required for production of high-octane gasoline. The values of the Research Octane Number (RON) increases with the degree of branching.[81] The di-branched isomers (22DMB, 23DMB) have significantly higher RON values than that of the linear isomer (nC6), and mono-branched isomers (2MP, 3MP). The RON values are: nC6 = 30, 2MP = 74.5, 3MP = 75.5, 22DMB = 94, 23DMB = 105. Therefore, di-branched isomers are preferred products for incorporation into the high-octane gasoline pool.[48, 82, 83]

Our earlier works,[1, 48, 81, 84, 85] had presented CBMC data for the adsorption of unary, ternary and 5-component mixtures of hexane isomers in a wide variety of zeolites, and MOFs. Here we analyze the adsorption of equimolar ternary $\left(f_1 = f_2 = f_3\right)$ nC6/2MP/22DMB, equimolar ternary $\left(f_1 = f_2 = f_3\right)$ nC6/3MP/22DMB, and equimolar quinary $\left(f_1 = f_2 = f_3 = f_4 = f_5\right)$ nC6/2MP/3MP/22DMB/23DMB mixtures at 433 K in Mg_2(dobdc) (with hexagonal 11 Å channels). Computational snapshots of the conformation of hexane isomers within the channels of Mg_2(dobdc) are shown in Figure S98.

Figure S99 presents CBMC simulations for adsorption of (a, b) equimolar $\left(f_1 = f_2 = f_3\right)$ ternary nC6/2MP/22DMB, equimolar $\left(f_1 = f_2 = f_3\right)$ ternary nC6/3MP/22DMB, and (c) equimolar $\left(f_1 = f_2 = f_3 = f_4 = f_5\right)$ quinary nC6/2MP/3MP/22DMB/23DMB mixtures at 433 K in Mg_2(dobdc). The component loadings are plotted as function of the surface potential Φ. On the basis of the CBMC simulation data, Figure S100a,b,c plots the calculations of the (a) nC6/2MP, (b) nC6/3MP and (c) nC6/22DMB adsorption selectivities in Mg_2(dobdc) as function of the surface potential Φ, calculated for both ternary mixtures and quinary mixtures. We note that the adsorption selectivities show a unique dependence on the surface potential Φ for both ternary and quinary mixtures.

With the introduction of activity coefficients, the expression for the adsorption selectivity for the *i-j* pair in *n*-component mixtures is

$$S_{ads,ij} = \frac{q_i/q_j}{f_i/f_j} = \frac{x_i/f_i}{x_j/f_j} = \frac{P_j^0\gamma_j}{P_i^0\gamma_i} \tag{S86}$$

The ratios of the activity coefficients $\frac{\gamma_{nC6}}{\gamma_{2MP}}$, $\frac{\gamma_{nC6}}{\gamma_{3MP}}$, and $\frac{\gamma_{nC6}}{\gamma_{22DMB}}$, determined from CBMC simulation data are plotted in Figure S100d,e,f. It is noteworthy that $\frac{\gamma_{nC6}}{\gamma_{2MP}}$, $\frac{\gamma_{nC6}}{\gamma_{3MP}}$, and $\frac{\gamma_{nC6}}{\gamma_{22DMB}}$ show a unique dependence on the surface potential Φ for both ternary and quinary mixtures.

The pore landscapes and structural details of Co(BDP) are presented in Figure S101, and Figure S102. Computational snapshots of the conformation of hexane isomers within the 10 Å square channels of Co(BDP) are shown in Figure S103. Figure S104 presents CBMC simulations for adsorption of (a) $(f_1 = f_2 = f_3)$ ternary nC6/3MP/22DMB, and (b) equimolar $(f_1 = f_2 = f_3 = f_4 = f_5)$ quinary nC6/2MP/3MP/22DMB/23DMB mixtures at 433 K in Co(BDP) (with square 10 Å channels). The component loadings are plotted as function of the surface potential Φ.

On the basis of the CBMC simulation data, Figure S105a,b plots the calculations of the (a) nC6/3MP, and (b) nC6/22DMB adsorption selectivities in Co(BDP) as function of the surface potential Φ, calculated for both ternary mixtures and quinary mixtures. We note that the adsorption selectivities show a unique dependence on the surface potential Φ for both ternary and quinary mixtures. The ratios of the activity coefficients $\frac{\gamma_{nC6}}{\gamma_{3MP}}$, and $\frac{\gamma_{nC6}}{\gamma_{22DMB}}$, determined from CBMC simulation data are plotted in Figure S105c,d. It is noteworthy that $\frac{\gamma_{nC6}}{\gamma_{3MP}}$, and $\frac{\gamma_{nC6}}{\gamma_{22DMB}}$ show a unique dependence on the surface potential Φ for both ternary and quinary mixtures.

The pore landscapes and structural details of MFI are presented in Figure S64, and Figure S65. Computational snapshots of the conformation of hexane isomers within the intersecting channels of MFI are shown in Figure S106. The unary isotherm fits are specified in Table S24. Figure S107 presents

CBMC simulations for adsorption of (a) $\left(f_1 = f_2 = f_3\right)$ ternary nC5/2MP/neo-Pentane, (b) $\left(f_1 = f_2 = f_3\right)$ ternary nC6/3MP/22DMB, (c) equimolar $\left(f_1 = f_2 = f_3 = f_4 = f_5\right)$ quinary nC6/2MP/3MP/22DMB/23DMB, and (d) equimolar 8-component nC5/2MB/neo-P/nC6/2MP/3MP/22DMB/23DMB mixtures at 433 K in MFI zeolite. (with intersecting channels). The component loadings are plotted as function of the surface potential Φ.

On the basis of the CBMC simulation data, Figure S108a,b plots the calculations of the (a) nC6/3MP, and (b) nC6/22DMB adsorption selectivities in MFI as function of the surface potential Φ, calculated for both ternary mixtures and quinary mixtures. We note that the adsorption selectivities show a unique dependence on the surface potential Φ for ternary, quinary, and 8-component mixtures. The ratios of the activity coefficients $\frac{\gamma_{nC6}}{\gamma_{3MP}}$, and $\frac{\gamma_{nC6}}{\gamma_{22DMB}}$, determined from CBMC simulation data are plotted in Figure S108c,d. It is noteworthy that $\frac{\gamma_{nC6}}{\gamma_{3MP}}$, and $\frac{\gamma_{nC6}}{\gamma_{22DMB}}$ show a unique dependence on the surface potential Φ for ternary, quinary, and 8-component mixtures.

Figure S109a,b plots the calculations of the (a) nC5/2MB, and (b) nC5/neo-P adsorption selectivities in MFI as function of the surface potential Φ, calculated for both ternary mixtures and 8-component mixtures. We note that the adsorption selectivities show a unique dependence on the surface potential Φ for ternary, and 8-component mixtures. The ratios of the activity coefficients $\frac{\gamma_{nC5}}{\gamma_{2MB}}$, and $\frac{\gamma_{nC5}}{\gamma_{neo-P}}$, determined from CBMC simulation data are plotted in Figure S109c,d. It is noteworthy that for $\frac{\gamma_{nC5}}{\gamma_{2MB}}$, and $\frac{\gamma_{nC5}}{\gamma_{neo-P}}$, show a unique dependence on the surface potential Φ for ternary, and 8-component mixtures.

Adsorption of mixtures of hydrocarbons

Figure S110a,b provides a comparison of (a) benzene/ethene and (b) ethylbenzene/ethene adsorption selectivities in MFI at 653 K. In the plots the adsorption selecitivities were determined from CBMC simulations for adsorption of equimolar ethene/benzene, ethene/ethylbenzene, and ethene/benzene/ethylbenzene, mixtures. We note that the adsorption selectivities show a unique dependence on the surface potential Φ for binary and ternary mixtures. The ratios of the activity coefficients for $\frac{\gamma_{ethene}}{\gamma_{benzene}}$, and $\frac{\gamma_{ethene}}{\gamma_{ethylbenzene}}$, determined from CBMC simulation data are plotted in Figure S110c,d. It is noteworthy that $\frac{\gamma_{ethene}}{\gamma_{benzene}}$, and $\frac{\gamma_{ethene}}{\gamma_{ethylbenzene}}$, show a unique dependence on the surface potential Φ for ternary, and 8-component mixtures.

12.1 List of Tables for Adsorption of mixtures of hydrocarbons

Table S22. Dual-site Langmuir-Freundlich parameters for pure component hexane isomers at 433 K in $Mg_2(dobdc)$. The fits are based on CBMC simulation data of Krishna and van Baten.[1]

	Site A			Site B		
	$q_{i,A,sat}$ mol kg^{-1}	$b_{i,A}$ $\mathrm{Pa}^{-\nu_i}$	$\nu_{i,A}$ dimensionless	$q_{i,B,sat}$ mol kg^{-1}	$b_{i,B}$ $\mathrm{Pa}^{-\nu_i}$	$\nu_{i,B}$ dimensionless
nC6	3.3	4.396E-07	2.2	1.25	1.081E-03	0.7
2MP	3.25	2.350E-07	2.27	1.35	6.855E-04	0.76
3MP	2.25	5.478E-11	3.55	2.1	4.813E-04	1
22DMB	2.9	6.410E-06	1.5	1.45	2.514E-04	0.76
23DMB	2.8	1.401E-08	2.65	1.55	5.595E-04	0.9

Table S23. Dual-site Langmuir-Freundlich parameters for pure component hexane isomers at 433 K in Co(BDP). The fits are based on CBMC simulation data of Krishna and van Baten.[1]

	Site A			Site B		
	$q_{\mathrm{i,A,sat}}$ mol kg^{-1}	$b_{\mathrm{i,A}}$ $\mathrm{Pa}^{-\nu_i}$	$\nu_{\mathrm{i,A}}$ dimensionless	$q_{\mathrm{i,B,sat}}$ mol kg^{-1}	$b_{\mathrm{i,B}}$ $\mathrm{Pa}^{-\nu_i}$	$\nu_{\mathrm{i,B}}$ dimensionless
nC6	1.47	2.813E-04	0.77	4	2.286E-07	2
2MP	1.66	2.508E-04	0.75	3.95	6.834E-07	1.8
3MP	1.8	2.002E-04	0.76	3.9	1.151E-06	1.7
22DMB	2.06	5.431E-05	0.8	3.45	1.800E-05	1.2
23DMB	4.08	1.016E-04	1	1.1	1.055E-09	2.65

Table S24. Dual-site Langmuir-Freundlich parameters for pure component pentane and hexane isomers at 433 K in MFI zeolite. The fits are based on CBMC simulation data of Krishna and van Baten.[1, 86]

$\Theta = \Theta_{A,sat} \frac{b_A f^{\nu_A}}{1+b_A f^{\nu_A}} + \Theta_{B,sat} \frac{b_B f^{\nu_B}}{1+b_B f^{\nu_B}}$	Site A			Site B		
	$\Theta_{A,sat}$ molecules uc^{-1}	b_A $Pa^{-\nu_A}$	ν_A dimensionless	$\Theta_{B,sat}$ molecules uc^{-1}	b_B $Pa^{-\nu_B}$	ν_B dimensionless
nC5	4	6.26×10^{-6}	1.12	4	1.94×10^{-4}	1
2MB	4	1.69×10^{-4}	1	2	4.93×10^{-7}	1
Neo-pentane	4	1.24×10^{-4}	1			
nC6	3.2	2.21×10^{-8}	1.6	4.3	7.42×10^{-4}	1
2MP	4	7.85×10^{-4}	1.03			
3MP	4	4.22×10^{-4}	1.02	1	9.88×10^{-7}	1
22DMB	4	2.55×10^{-4}	1.02			
23DMB	4	4.59×10^{-4}	1.02			

Table S25. Dual-site Langmuir-Freundlich parameters for hydrocarbons in MFI at 653 K; the data are fitted to CBMC simulation data from earlier publications.[87-89]

	Site A			Site B		
	$q_{i,A,sat}$ mol kg^{-1}	$b_{i,A}$ Pa^{-1}	$\nu_{i,A}$ dimensionless	$q_{i,B,sat}$ mol kg^{-1}	$b_{i,B}$ Pa^{-1}	$\nu_{i,B}$ dimensionless
C_2H_4	0.83	2.682E-09	1	2	8.939E-08	1
Benzene	1	1.479E-09	1	0.75	1.716E-06	1
EthylBenzene	0.36	2.526E-06	1	0.36	2.526E-06	1

12.2 List of Figures for Adsorption of mixtures of hydrocarbons

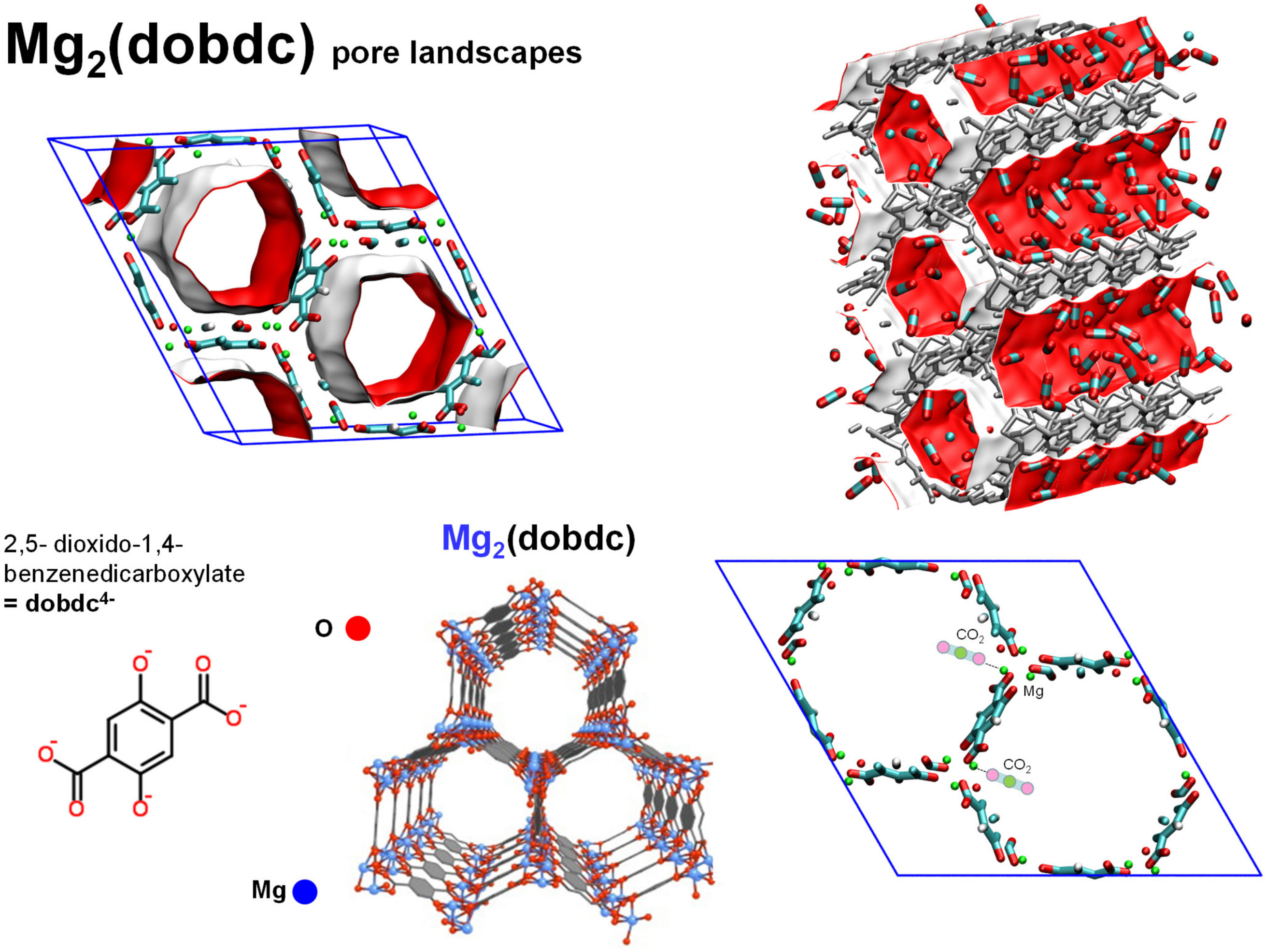

Figure S96. Pore landscape of Mg$_2$(dobdc).

Mg_2(dobdc) pore dimensions

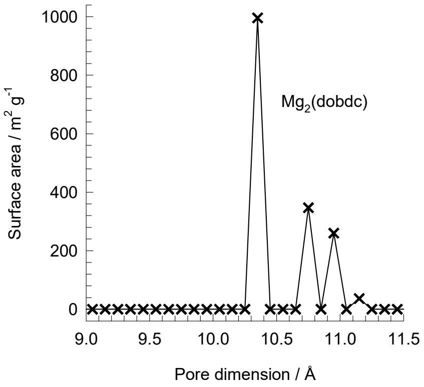

This plot of surface area versus pore dimension is determined using a combination of the DeLaunay triangulation method for pore dimension determination, and the procedure of Düren for determination of the surface area.

	MgMOF-74
a /Å	25.8621
b /Å	25.8621
c /Å	6.91427
Cell volume / Å^3	4005.019
conversion factor for [molec/uc] to [mol per kg Framework]	0.4580
conversion factor for [molec/uc] to [kmol/m^3]	0.5856
ρ [kg/m3]	905.367
MW unit cell [g/mol(framework)]	2183.601
ϕ, fractional pore volume	0.708
open space / Å^3/uc	2835.6
Pore volume / cm^3/g	0.782
Surface area /m^2/g	1640.0
DeLaunay diameter /Å	10.66

Figure S97. Structural details for Mg_2(dobdc).

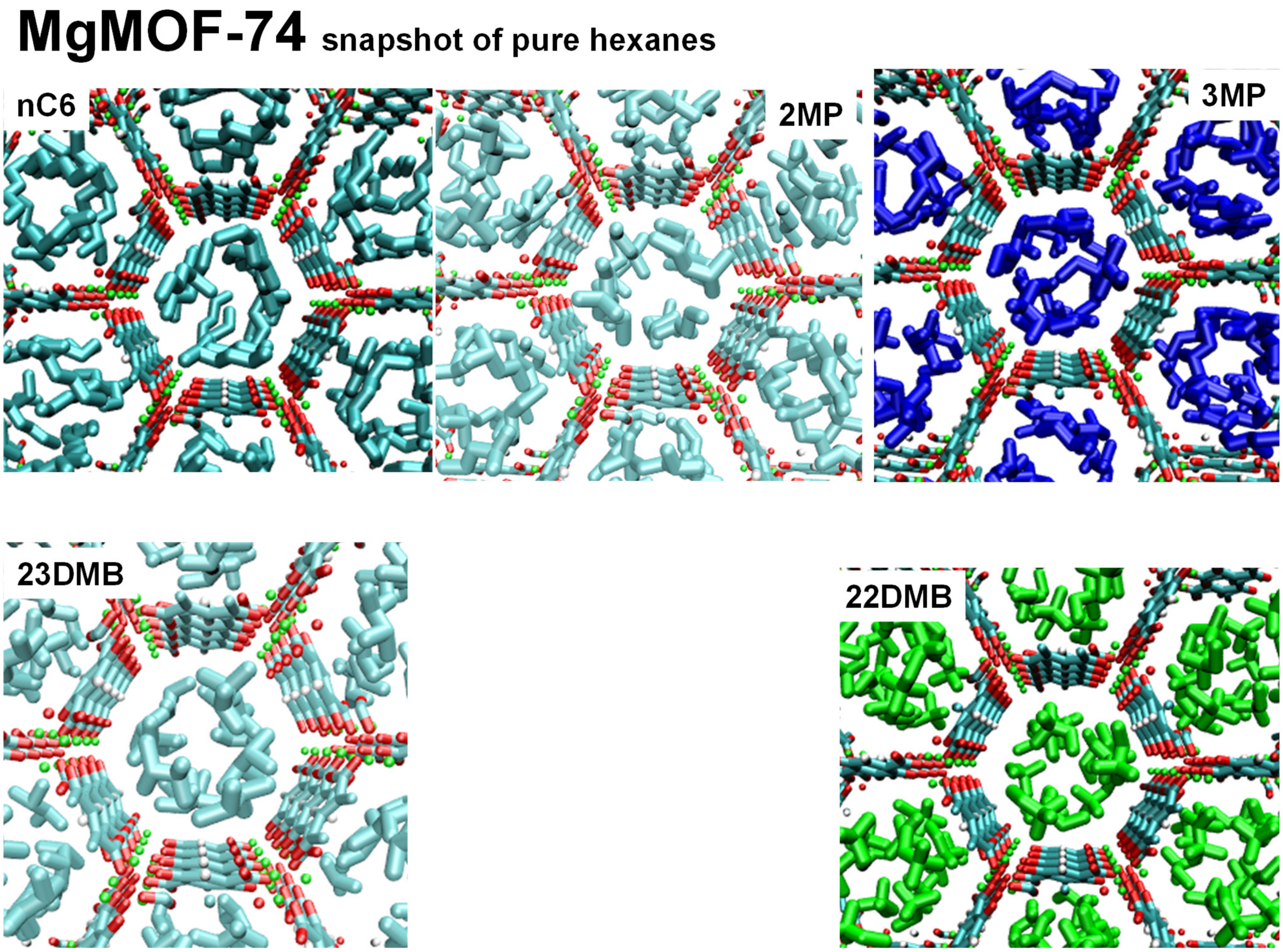

Figure S98. Computational snapshots of the conformation of hexane isomers within the 1D channels of Mg_2(dobdc).

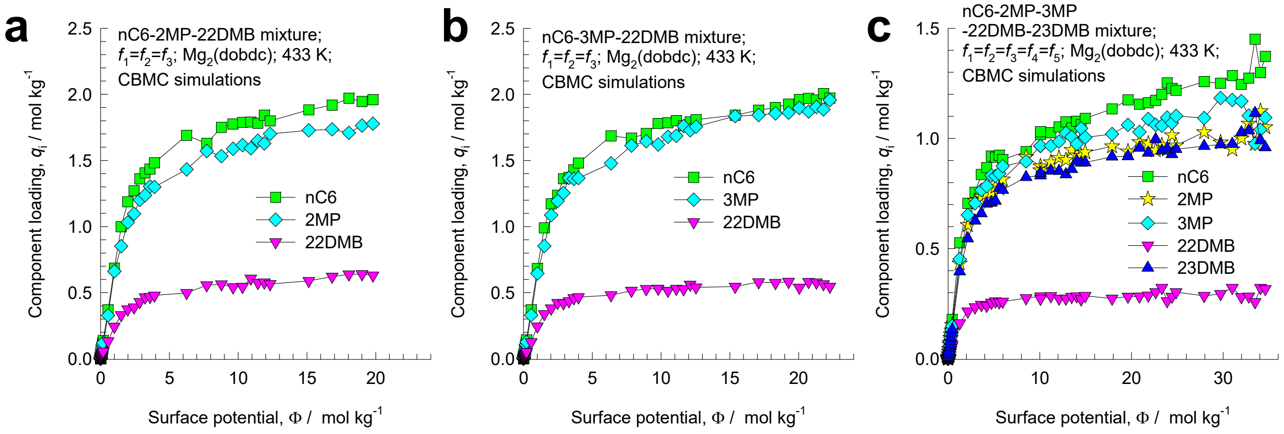

Figure S99. CBMC simulations for adsorption of (a, b) equimolar $\left(f_1 = f_2 = f_3\right)$ ternary nC6/2MP/22DMB, $\left(f_1 = f_2 = f_3\right)$ ternary nC6/3MP/22DMB, and (c) equimolar $\left(f_1 = f_2 = f_3 = f_4 = f_5\right)$ quinary nC6/2MP/3MP/22DMB/23DMB mixtures at 433 K in Mg_2(dobdc) (with hexagonal 11 Å channels).

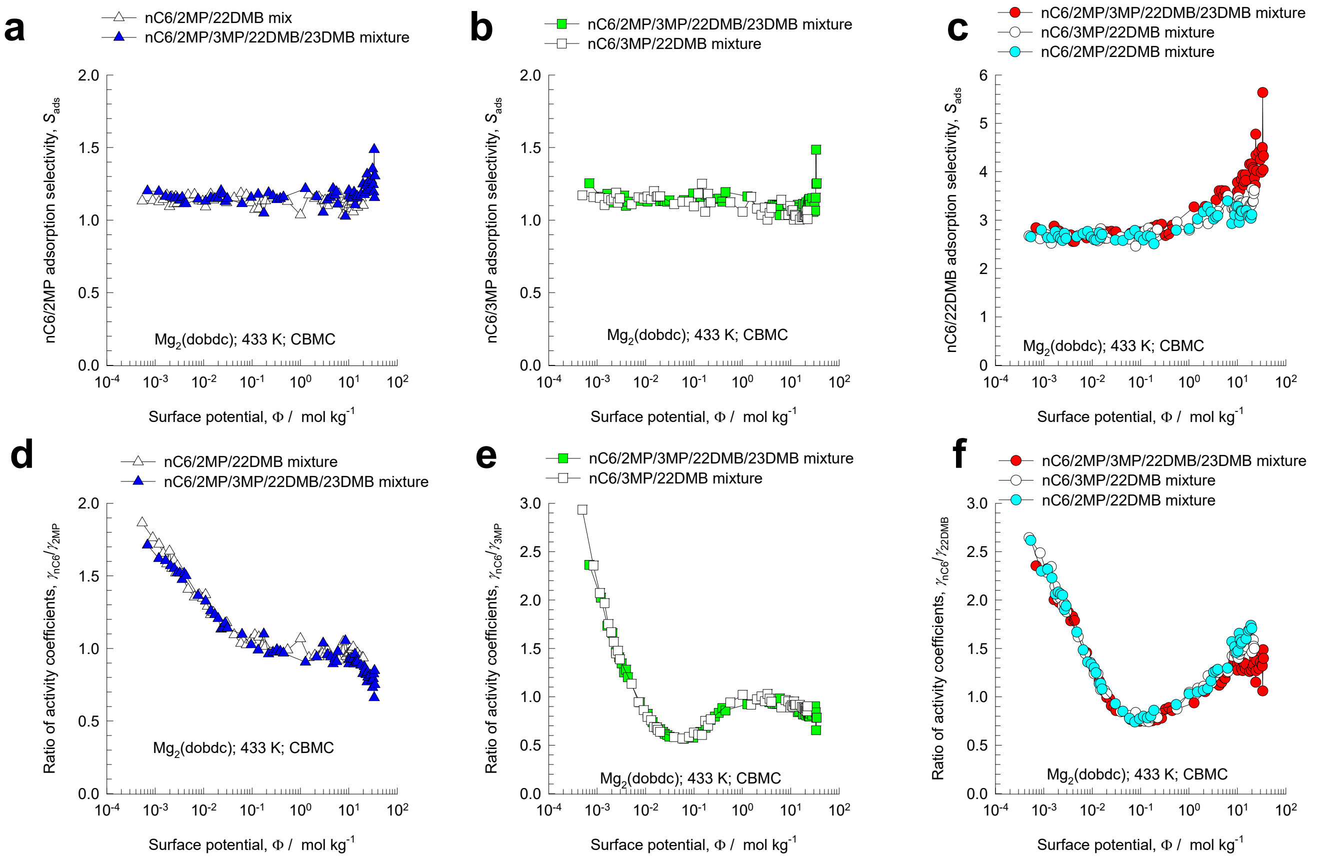

Figure S100. Comparison of (a) nC6/2MP, (b) nC6/3MP and (c) nC6/22DMB adsorption selectivities in Mg$_2$(dobdc). In the plots the adsorption selecitivities were determined from CBMC simulations for adsorption of equimolar $\left(f_1=f_2=f_3\right)$ ternary nC6/2MP/22DMB, $\left(f_1=f_2=f_3\right)$ ternary nC6/3MP/22DMB, and equimolar $\left(f_1=f_2=f_3=f_4=f_5\right)$ quinary nC6/2MP/3MP/22DMB/23DMB mixtures at 433 K. The *x*-axis represents the surface potential, Φ, determined using the IAST for either 3-component or 5-component mixtures as appropriate. (d, e, f) Plots of the ratios of activity coefficients vs Φ.

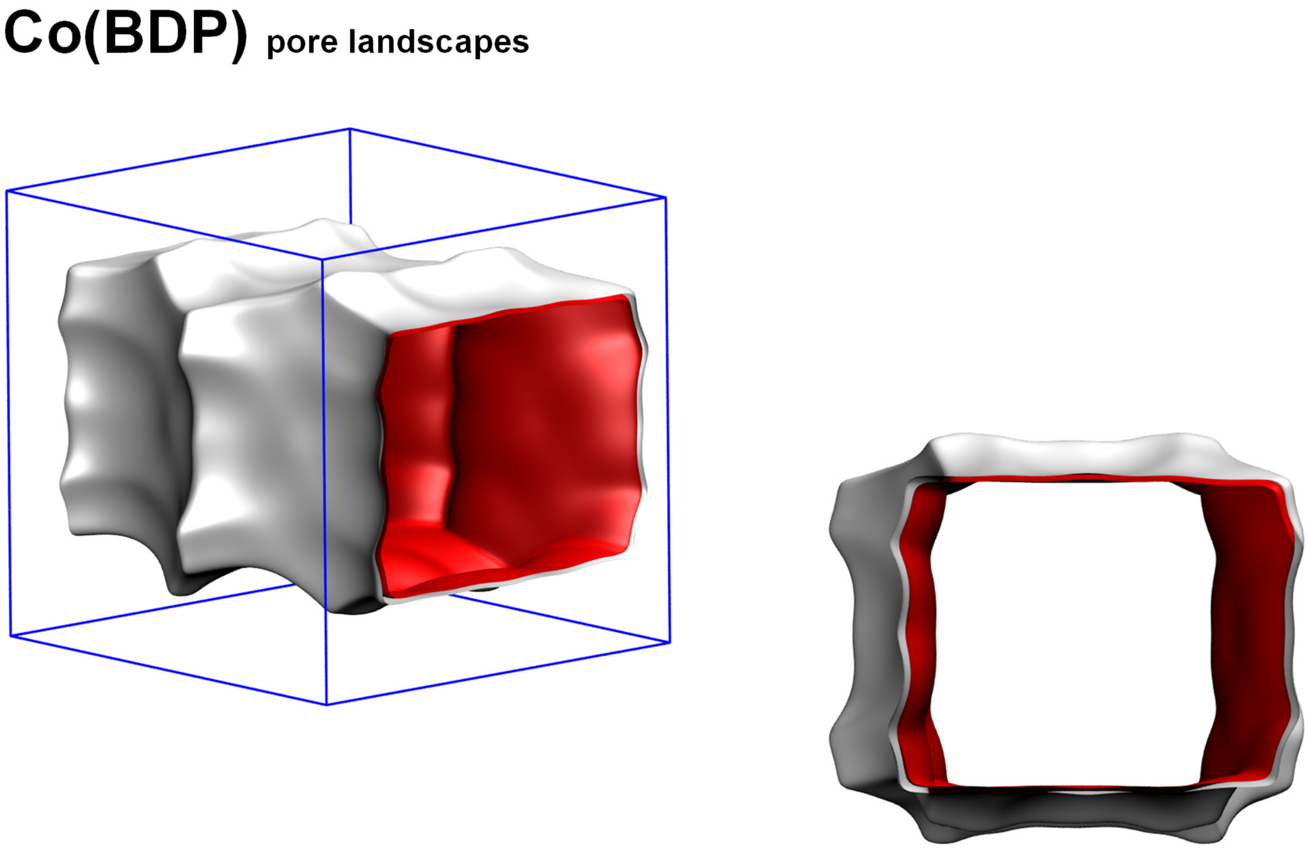

Figure S101. Pore landscape of Co(BDP)

Co(BDP) pore landscapes

	CoBDP
a /Å	13.2529
b /Å	13.253
c /Å	13.995
Cell volume / Å^3	2458.091
conversion factor for [molec/uc] to [mol per kg Framework]	0.9362
conversion factor for [molec/uc] to [kmol/m^3]	1.0102
ρ [kg/m3] (with cations)	721.5517
MW unit cell [g/mol(framework+cations)]	1068.094
ϕ, fractional pore volume	0.669
open space / Å^3/uc	1643.9
Pore volume / cm^3/g	0.927
Surface area /m^2/g	2148.8
DeLaunay diameter /Å	9.97

To convert from molecules per unit cell to mol kg^{-1}, multiply by 0.9362.
The pore volume is 0.927 cm^3/g.

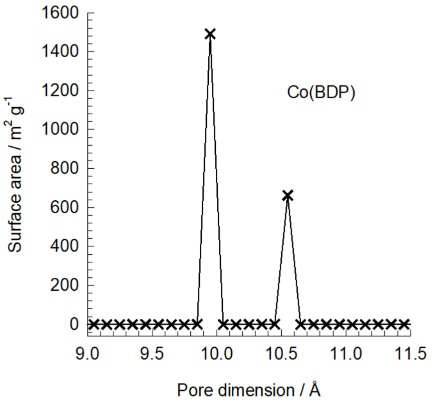

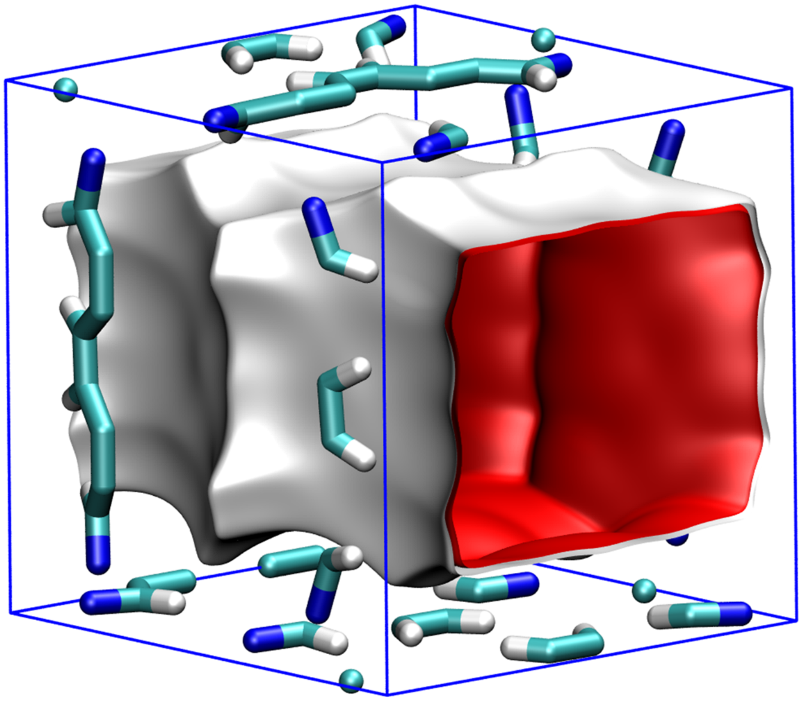

Figure S102. Structural details for Co(BDP).

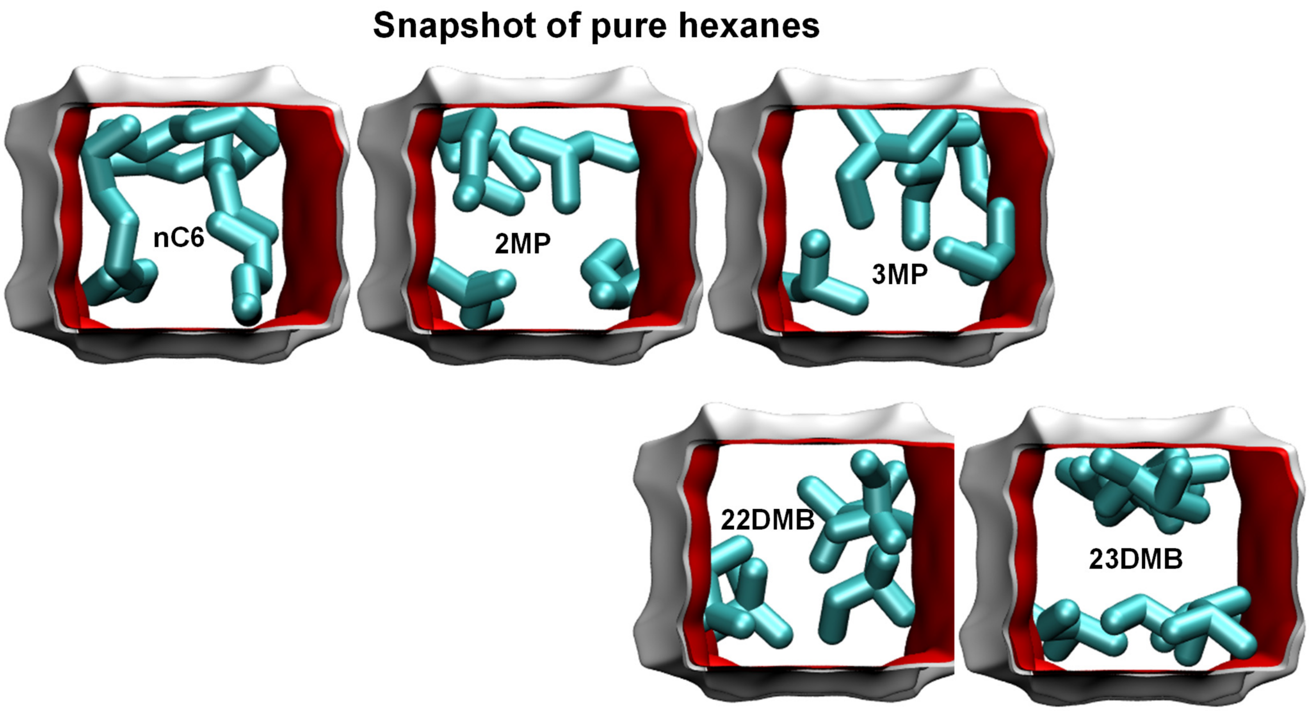

Figure S103. Computational snapshots of the conformation of hexane isomers within the 1D channels of Co(BDP).

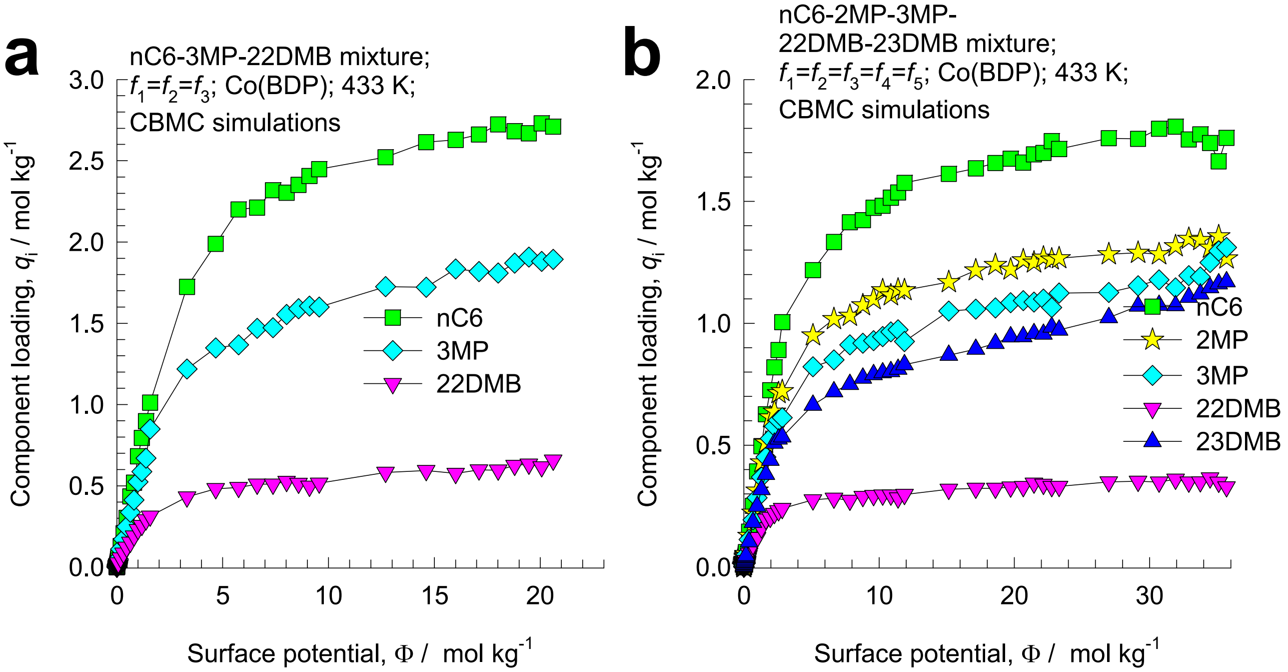

Figure S104. CBMC simulations for adsorption of (a) $(f_1 = f_2 = f_3)$ ternary nC6/3MP/22DMB, and (b) equimolar $(f_1 = f_2 = f_3 = f_4 = f_5)$ quinary nC6/2MP/3MP/22DMB/23DMB mixtures at 433 K in Co(BDP) (with square 10 Å channels).

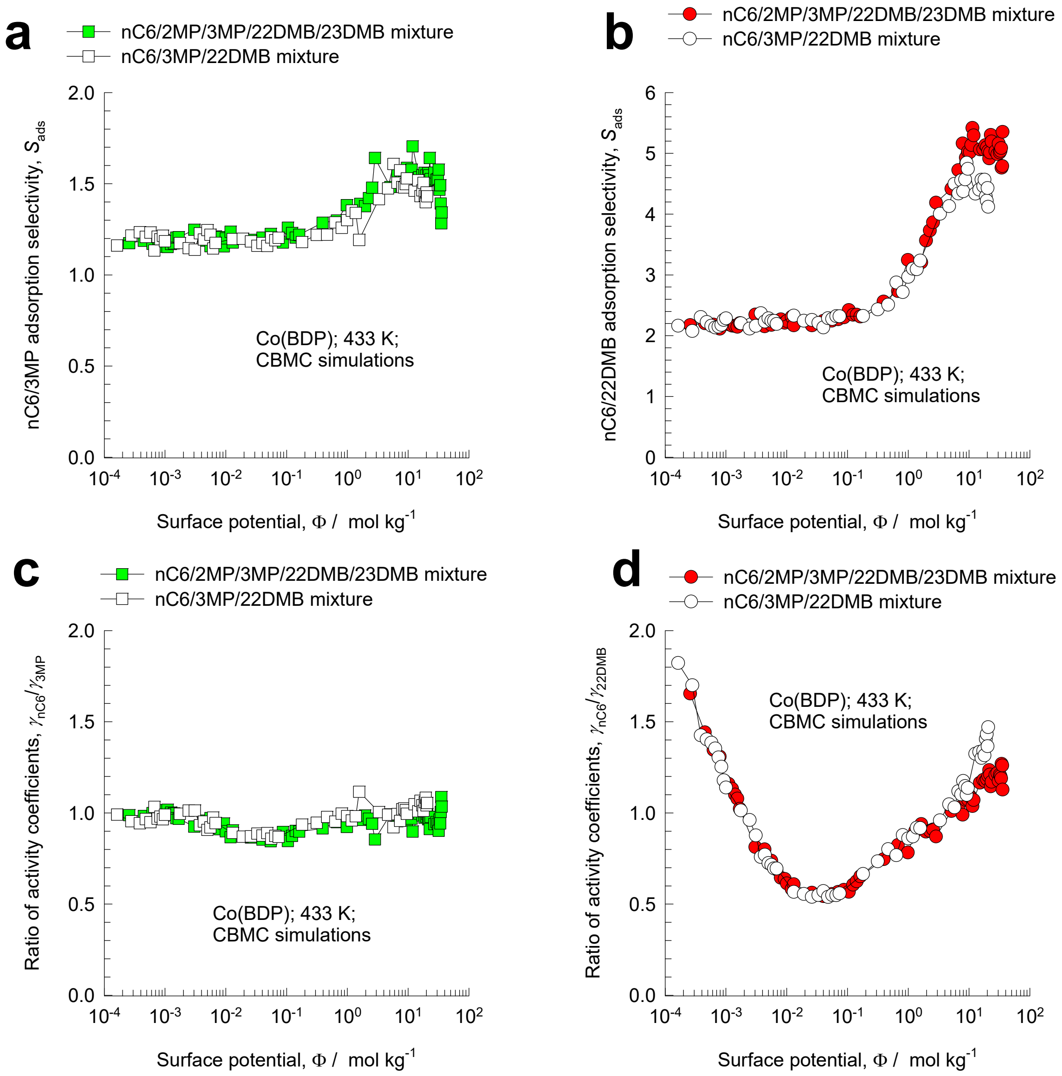

Figure S105. Comparison of (a) nC6/3MP and (b) nC6/22DMB adsorption selectivities in Co(BDP). In the plots the adsorption selecitivities were determined from CBMC simulations for adsorption of $(f_1 = f_2 = f_3)$ ternary nC6/3MP/22DMB, and equimolar $(f_1 = f_2 = f_3 = f_4 = f_5)$ quinary nC6/2MP/3MP/22DMB/23DMB mixtures at 433 K. The *x*-axis represents the surface potential, Φ, determined using the IAST for either 3-component or 5-component mixtures as appropriate. (c, d) Plots of the ratios of activity coefficients vs Φ. The *x*-axis represents the surface potential, Φ.

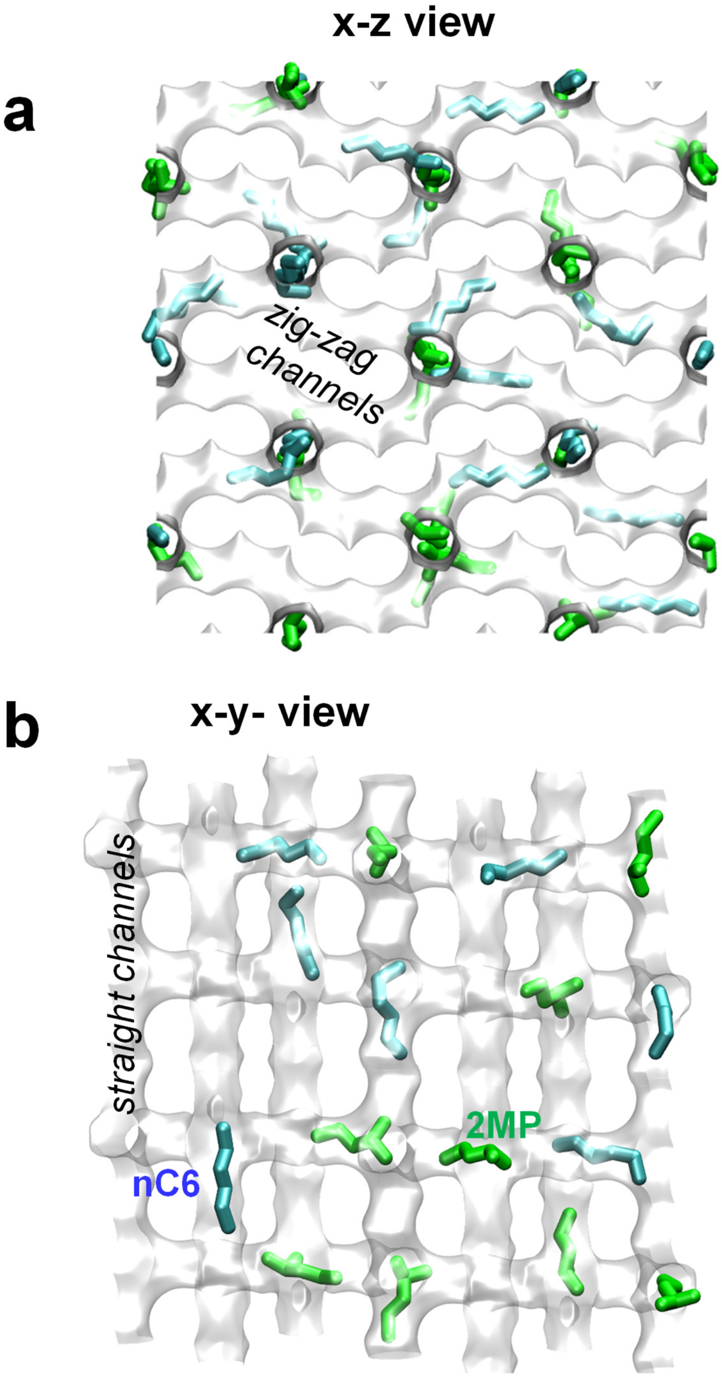

Figure S106. (a, b) Computational snapshots showing the location of guest molecules for nC6(1)/2MP(2) mixture adsorption in MFI zeolite at 300 K.

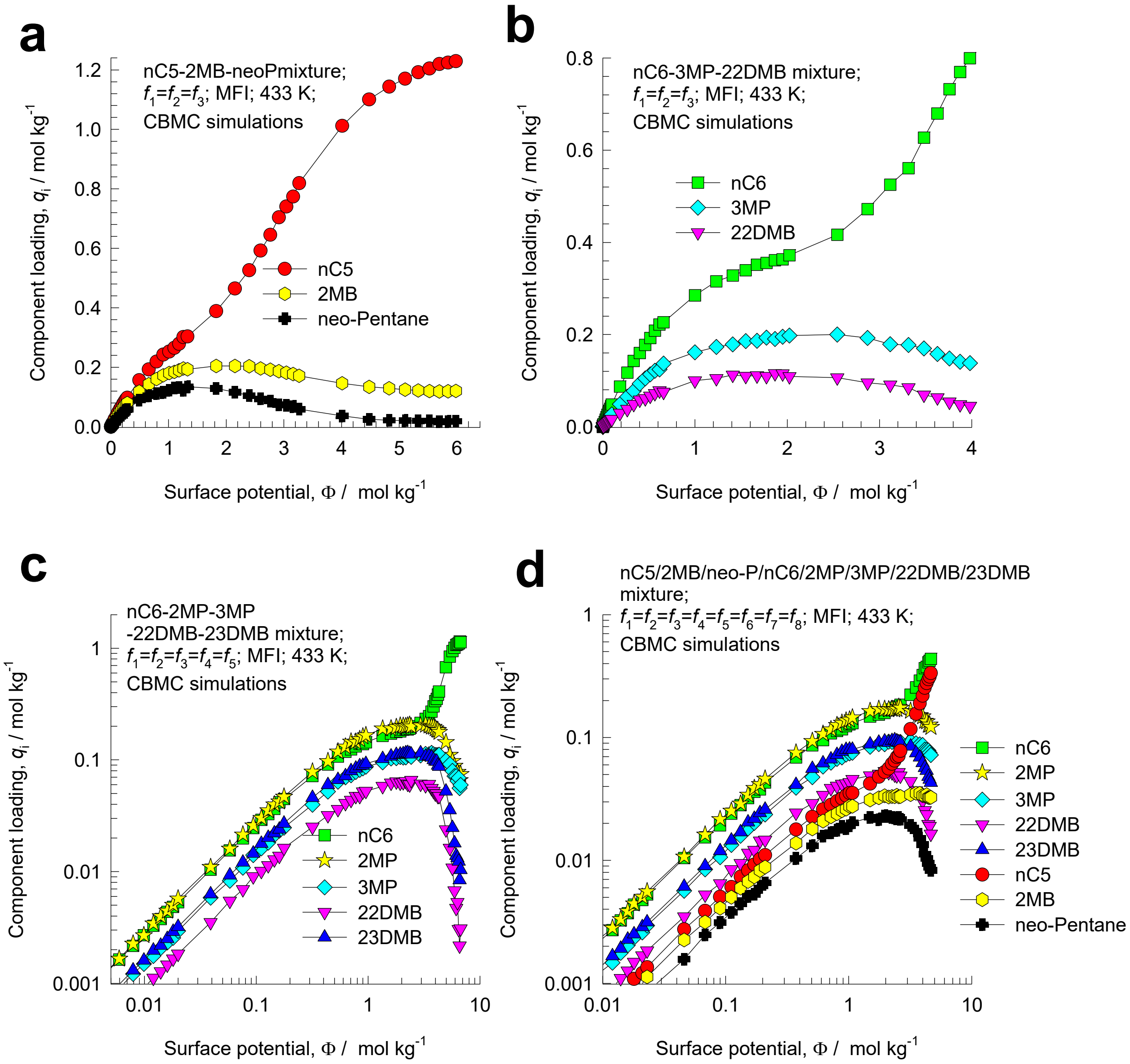

Figure S107. CBMC simulations for adsorption of (a) $\left(f_1 = f_2 = f_3\right)$ ternary nC5/2MP/neo-Pentane, (b) $\left(f_1 = f_2 = f_3\right)$ ternary nC6/3MP/22DMB, (c) equimolar $\left(f_1 = f_2 = f_3 = f_4 = f_5\right)$ quinary nC6/2MP.3MP/22DMB/23DMB, and (d) equimolar 8-component nC5/2MB/neo-P/nC6/2MP/3MP/22DMB/23DMB mixtures at 433 K in MFI zeolite.

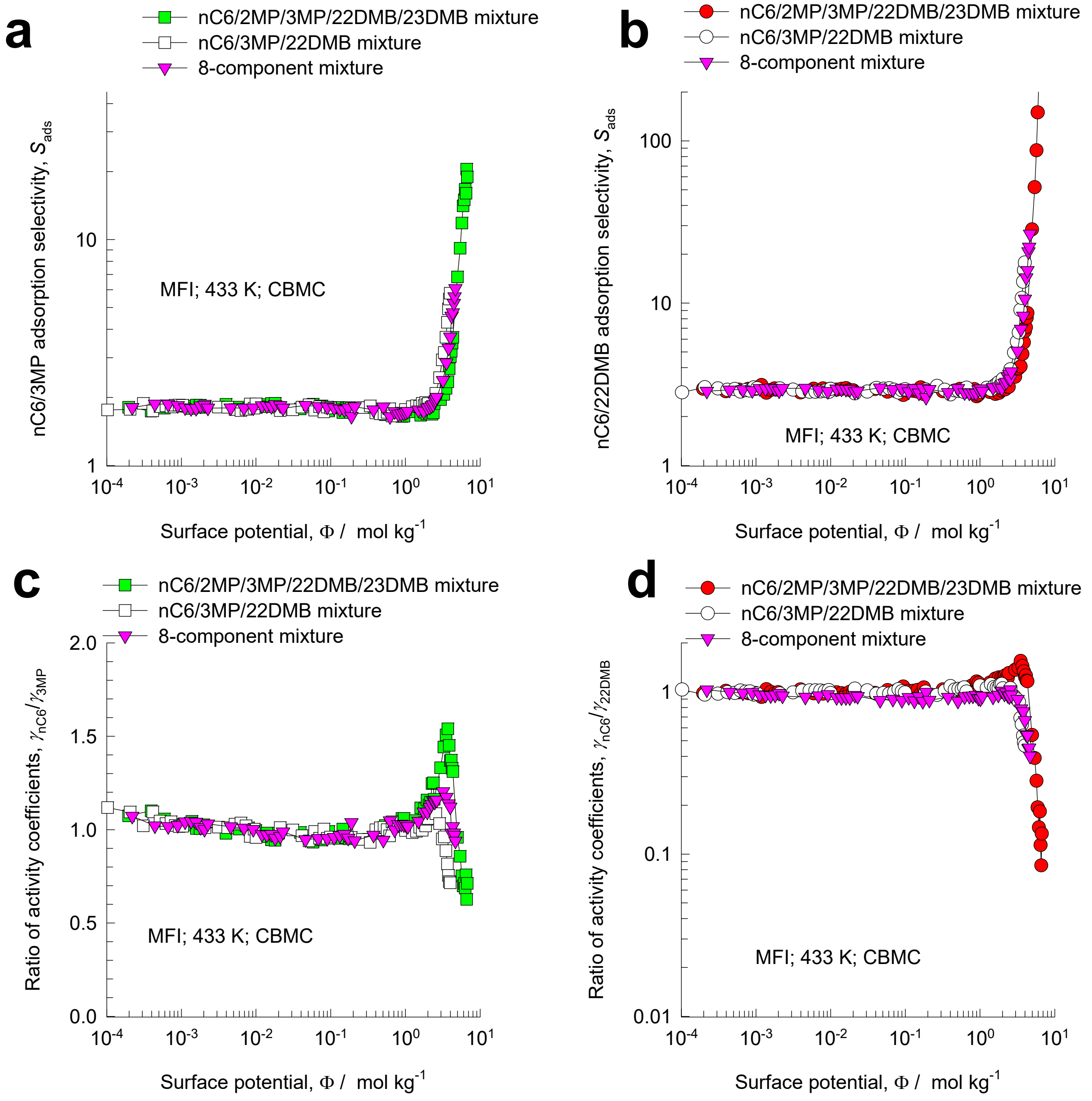

Figure S108. Comparison of (a) nC6/3MP and (b) nC6/22DMB adsorption selectivities in MFI zeolite. In the plots the adsorption selecitivities were determined from CBMC simulations for adsorption of ternary nC6/3MP/22DMB, equimolar quinary nC6/2MP/3MP/22DMB/23DMB, and equimolar 8-component mixtures at 433 K. The *x*-axis represents the surface potential, Φ, determined using the IAST for 3-component, 5-component, and 8-component mixtures as appropriate. (c, d) Plots of the ratios of activity coefficients vs Φ. The *x*-axis represents the surface potential, Φ.

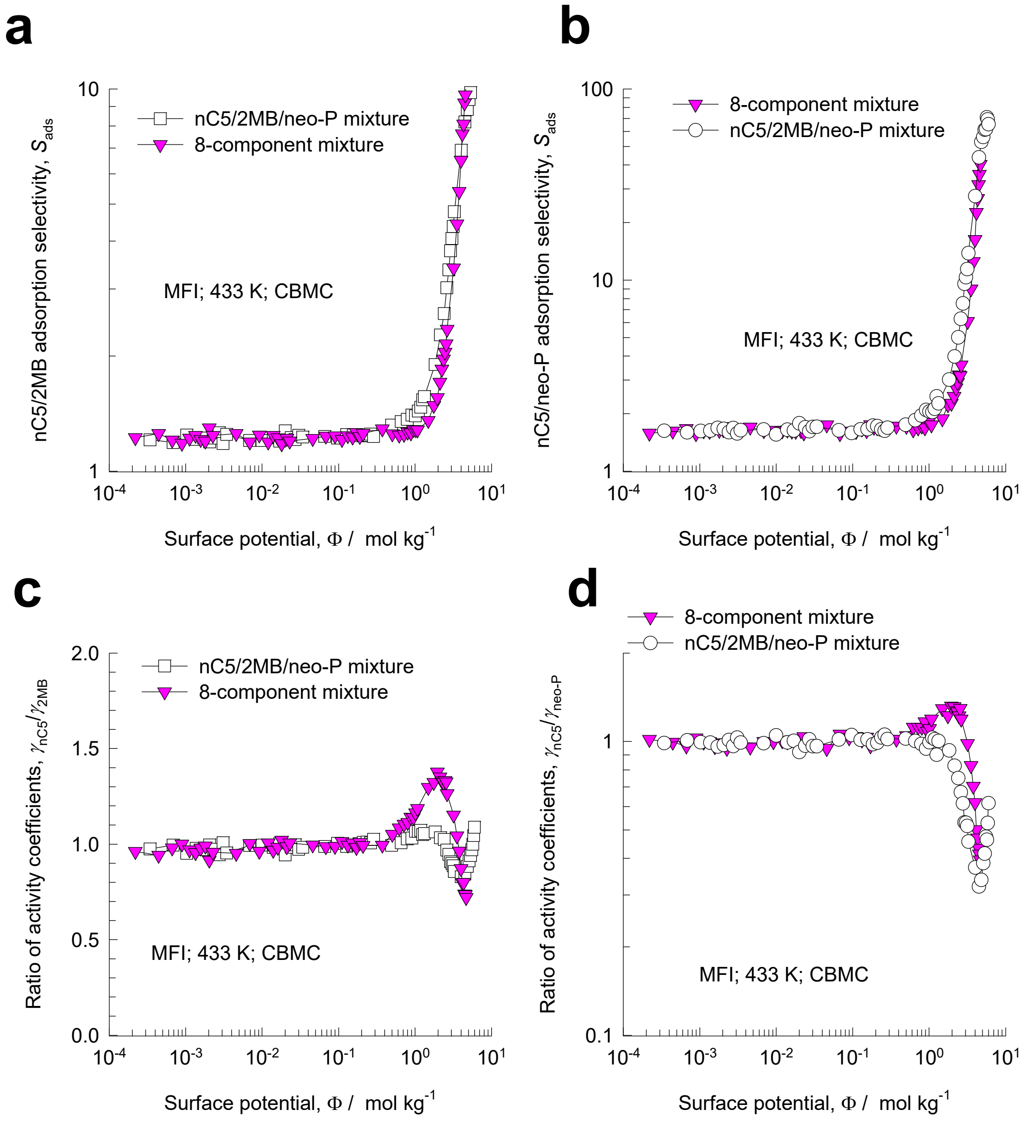

Figure S109. Comparison of (a) nC5/2MB and (b) nC5/neo-P adsorption selectivities in MFI zeolite. In the plots the adsorption selecitivities were determined from CBMC simulations for adsorption of ternary nC6/3MP/22DMB, equimolar quinary nC6/2MP/3MP/22DMB/23DMB, and equimolar 8-component mixtures at 433 K. The *x*-axis represents the surface potential, Φ, determined using the IAST for 3-component, 5-component, and 8-component mixtures as appropriate. (c, d) Plots of the ratios of activity coefficients vs Φ. The *x*-axis represents the surface potential, Φ.

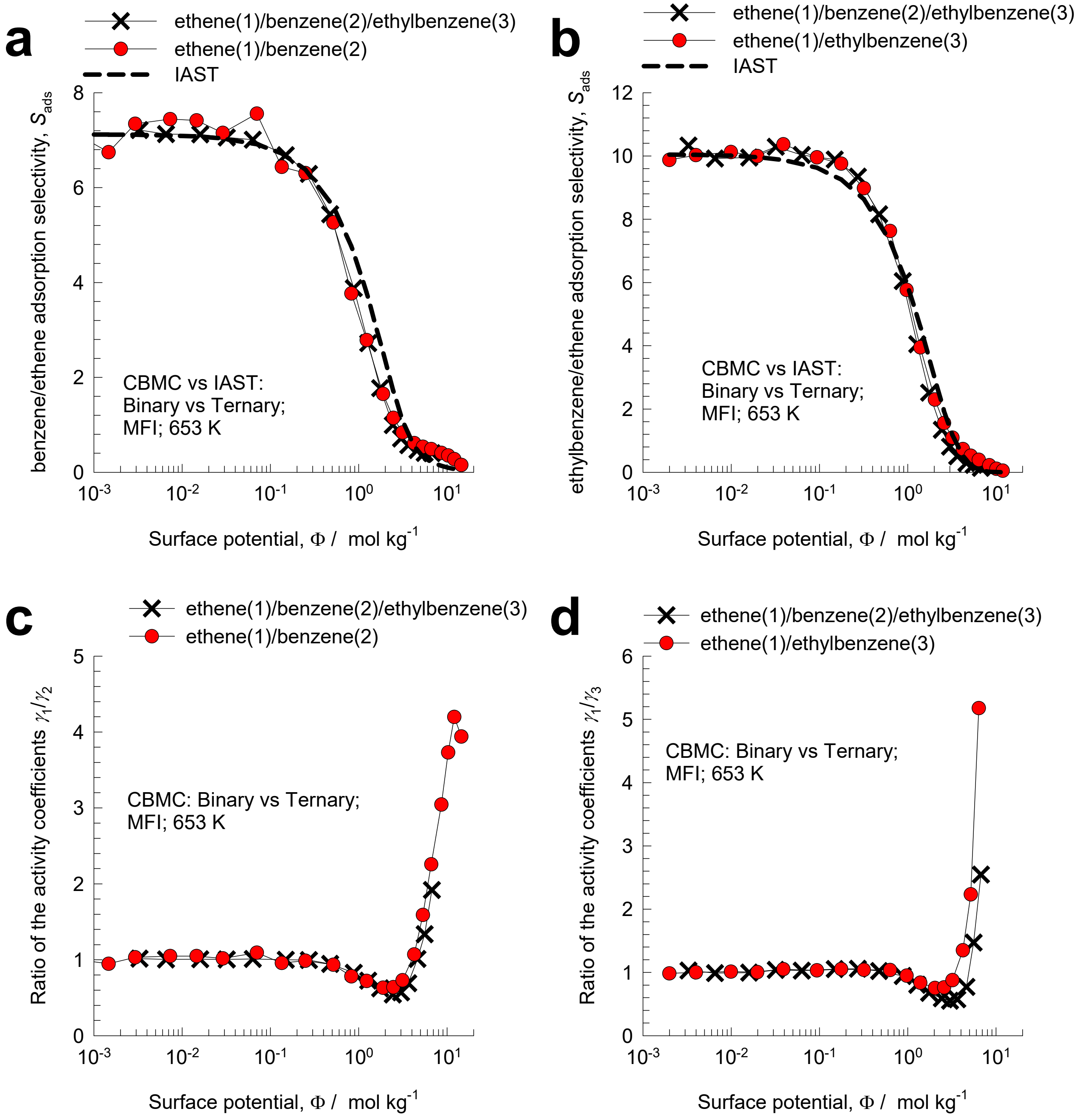

Figure S110. Comparison of (a) benzene/ethene and (b) ethylbenzene/ethene adsorption selectivities in MFI at 653 K. In the plots the adsorption selecitivities were determined from CBMC simulations for adsorption of equimolar ethene/benzene, ethene/ethylbenzene, and ethene/benzene/ethylbenzene, mixtures. (c, d) Plots of the ratios of activity coefficients vs Φ. The *x*-axes represent the surface potential, Φ.

13 Adsorption of water/methanol/ethanol mixtures

Two types of mixture adsorption campaigns were conducted in CHA, DDR, and MFI zeolites.

(a) Adsorption of binary water(1)/methanol(2), water(1)/ethanol(3), and methanol(2)/ethanol(3) mixtures. The bulk fluid phase composition held constant at $y_1 = y_2 = 0.5$, and the bulk fluid phase fugacity $f_t = f_1 + f_2$ was varied over a wide range from the Henry regime of adsorption, $f_t \to 0; \quad \Phi \to 0$, to pore saturation conditions, typically $\Phi > 50$.

(b) Ternary water(1)/methanol(2)/ethanol(3) mixture adsorption. The bulk fluid phase composition held constant at $y_1 = y_2 = y_3 = 1/3$, and the bulk fluid phase fugacity $f_t = f_1 + f_2 + f_3$ was varied over a wide range from the Henry regime of adsorption, $f_t \to 0; \quad \Phi \to 0$, to pore saturation conditions, typically $\Phi > 50$.

The objective of these simulations is to determine whether the adsorption selectivity for any binary pair of components in binary and ternary mixture adsorption campaigns is uniquely related to the surface potential, Φ. The unary isotherm fits using CBMC data on unary isotherms are provided in Table S26, Table S27, and Table S28.

(a, b, c) CBMC simulations of the water(1)/methanol(2), water(1)/ethanol(3), and methanol(2)/ethanol(3) adsorption selectivities, S_{ads}, for binary and ternary mixture adsorption in CHA zeolite at 300 K. The selectivities are plotted as function of the surface potential Φ. The dashed lines are the IAST calculations. (d, e, f) CBMC simulations of the ratio of activity coefficients of $\frac{\gamma_1}{\gamma_2}$, $\frac{\gamma_1}{\gamma_3}$, and $\frac{\gamma_2}{\gamma_3}$ for the three binary water(1)/methanol(2), water(1)/ethanol(3), and methanol(2)/ethanol(3) pairs plotted as function of the surface potential Φ.

Adsorption of water/methanol/ethanol mixtures

Figure S111, Figure S112, and Figure S113 summarize the CBMC data for CHA, DDR, and MFI zeolites, respectively.

Figure S111a,b,c, Figure S112a,b,c, and Figure S113a,b,c present CBMC simulation data on the adsorption selectivties of the three binary pairs water(1)/methanol(2), water(1)/ethanol(3), and methanol(2)/ethanol(3) in the three zeolites. Due to strong thermodynamic non-idealities resulting from molecular clustering, induced by hydrogen bonding, the IAST calculations for the selectivity are not in good agreement, generally speaking with CBMC data for adsorption selectivitities, determined from binary and ternary mixture adsorption.

Despite the quantitative failure of the IAST, the selectivity values for the three binary pairs show a more-or-less unique dependence on the surface potential Φ. The reason for this can be traced to the ratios of the activity coefficients $\frac{\gamma_1}{\gamma_2}$, $\frac{\gamma_1}{\gamma_3}$, and $\frac{\gamma_2}{\gamma_3}$ for the three binary water(1)/methanol(2), water(1)/ethanol(3), and methanol(2)/ethanol(3) pairs. The three ratios shown a unique dependence on the surface potential Φ; see Figure S111d,e,f, Figure S112d,e,f, and Figure S113d,e,f.

13.1 List of Tables for Adsorption of water/methanol/ethanol mixtures

Table S26. Dual-site Langmuir-Freundlich parameters for water, methanol, and ethanol in CHA at 300 K. The fit parameters are based on the CBMC simulations of pure component isotherms presented in earlier works.[27, 28, 90]

	Site A			Site B		
	$q_{A,sat}$ mol kg^{-1}	b_A Pa$^{-\nu A}$	ν_A dimensionless	$q_{A,sat}$ mol kg^{-1}	b_A Pa$^{-\nu A}$	ν_B
water	16.8	3.031E-54	15.6	4.6	2.218E-05	1
methanol	3.7	4.281E-11	3.37	3.7	4.545E-04	1
ethanol	2.5	8.578E-06	1.07	2.9	3.505E-03	1.1

Adsorption of water/methanol/ethanol mixtures

Table S27. Dual-site Langmuir-Freundlich parameters for pure component water, methanol, and ethanol at 300 K in all-silica DDR zeolite. The fit parameters are based on the CBMC simulations of pure component isotherms presented in earlier works. [27, 28, 90]

	Site A			Site B		
	$q_{A,sat}$ mol kg^{-1}	b_A Pa$^{-\nu A}$	ν_A	$q_{A,sat}$ mol kg^{-1}	b_A Pa$^{-\nu A}$	ν_B
water	6.45	2.776E-17	4.3	2.4	1.300E-05	1.06
methanol	1.7	1.186E-04	1.3	1.7	6.055E-04	0.78
ethanol	1.6	9.962E-03	0.88	1.2	9.160E-05	0.66

Table S28. Dual-site Langmuir-Freundlich parameters for adsorption of water, methanol, and ethanol at 300 K in all-silica MFI zeolite. The fit parameters are based on CBMC simulations of Krishna and van Baten.[23, 27, 28, 90]

Adsorbate	Site A			Site B		
	$q_{A,sat}$ mol kg^{-1}	b_A $\mathrm{Pa}^{-\nu_A}$	ν_A	$q_{B,sat}$ mol kg^{-1}	b_B $\mathrm{Pa}^{-\nu_B}$	ν_B
water	6.7	6.37×10^{-24}	6.2	3.6	1.09×10^{-5}	1.04
methanol	2.4	1×10^{-4}	1.64	1.4	1.92×10^{-3}	0.7
ethanol	0.7	1.083×10^{-18}	13.6	2.03	1.774×10^{-2}	1

13.2 List of Figures for Adsorption of water/methanol/ethanol mixtures

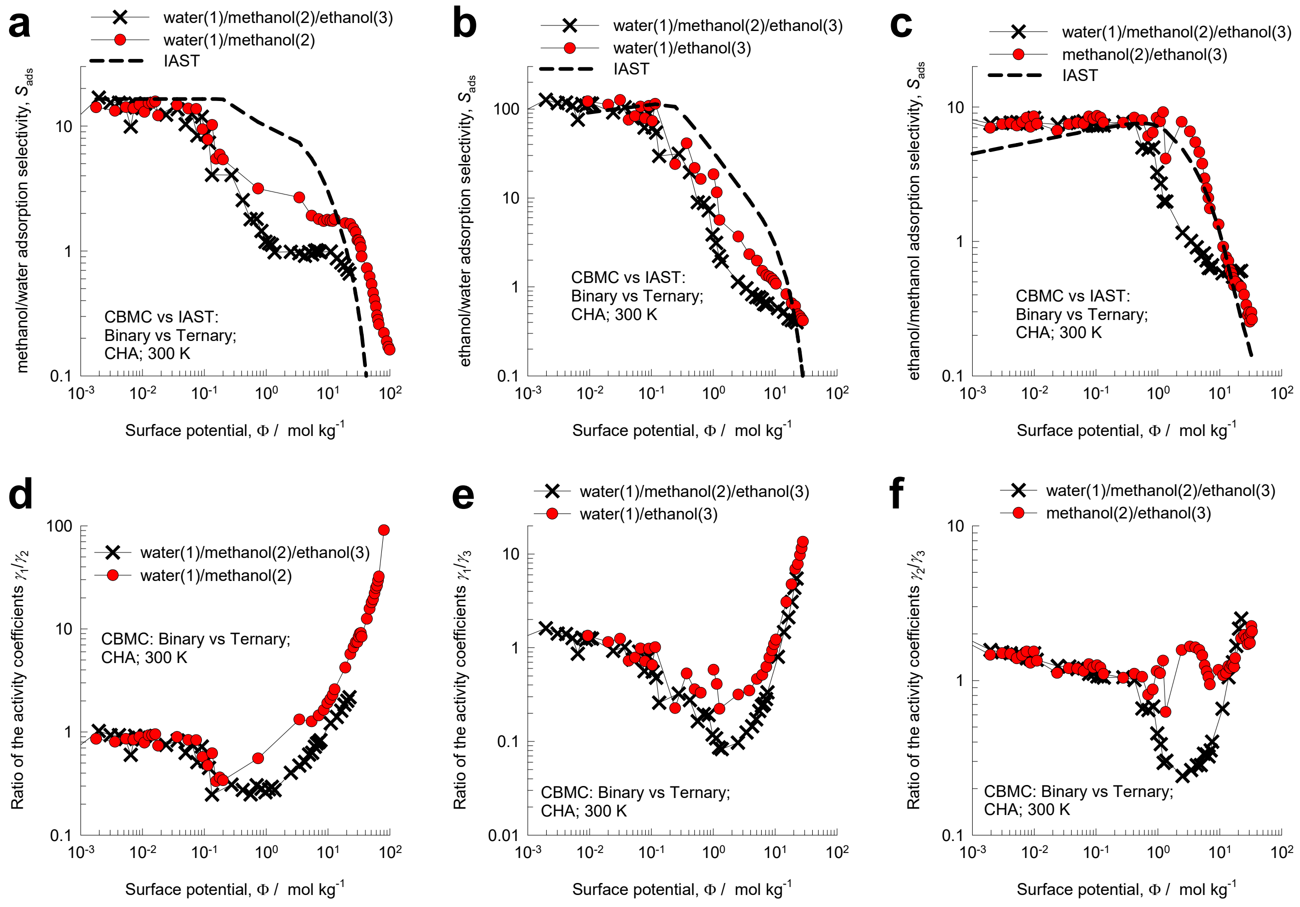

Figure S111. (a, b, c) CBMC simulations of the water(1)/methanol(2), water(1)/ethanol(3), and methanol(2)/ethanol(3) adsorption selectivities, S_{ads}, for binary and ternary mixture adsorption in CHA zeolite at 300 K. The selectivities are plotted as function of the surface potential Φ. The dashed lines are the IAST calculations. (d, e, f) CBMC simulations of the ratio of activity coefficients of $\frac{\gamma_1}{\gamma_2}$, $\frac{\gamma_1}{\gamma_3}$, and $\frac{\gamma_2}{\gamma_3}$ for the three binary water(1)/methanol(2), water(1)/ethanol(3), and methanol(2)/ethanol(3) pairs plotted as function of the surface potential.

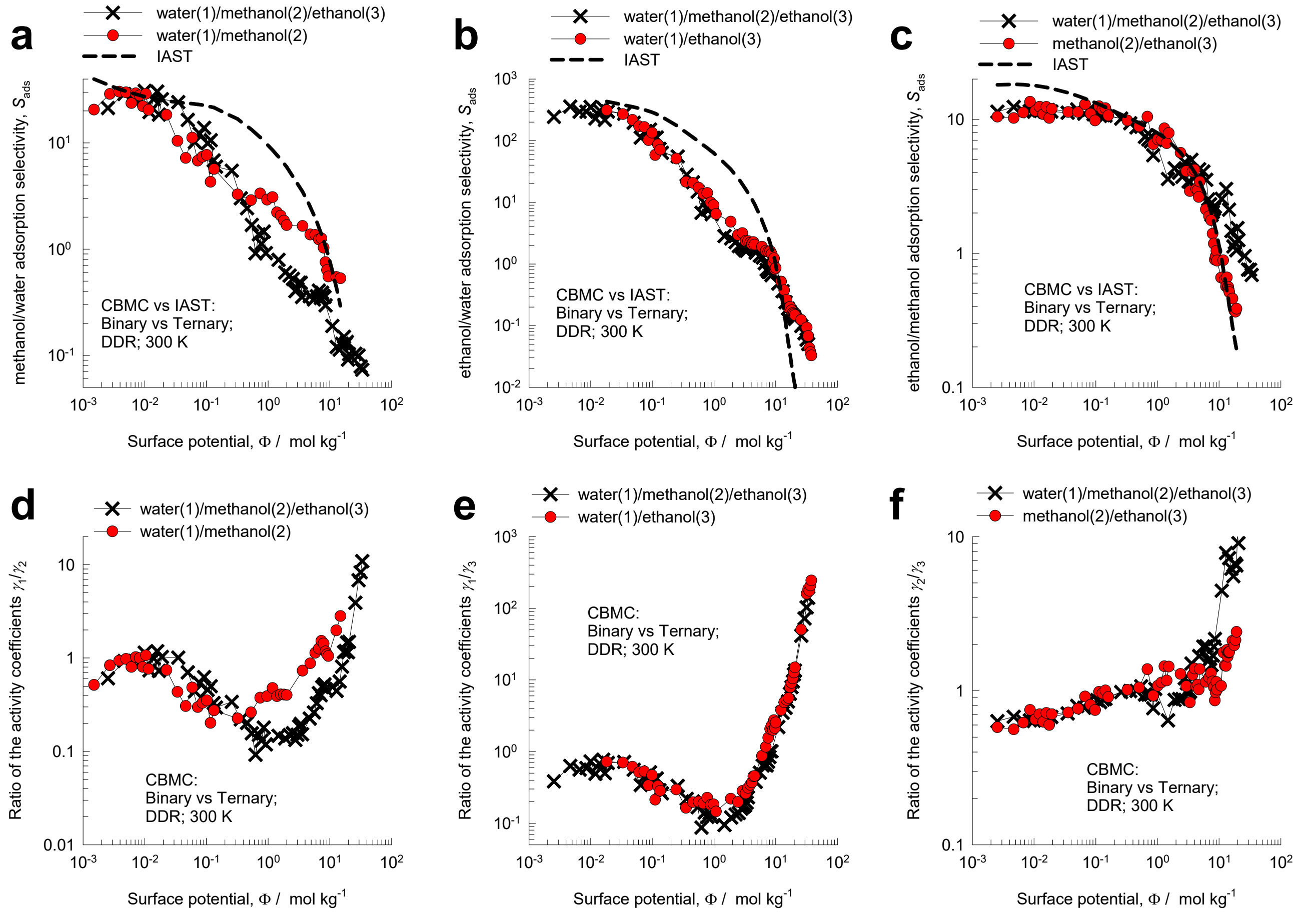

Figure S112. (a, b, c) CBMC simulations of the water(1)/methanol(2), water(1)/ethanol(3), and methanol(2)/ethanol(3) adsorption selectivities, S_{ads}, for binary and ternary mixture adsorption in DDR zeolite at 300 K. The selectivities are plotted as function of the surface potential Φ. The dashed lines are the IAST calculations. (d, e, f) CBMC simulations of the ratio of activity coefficients of $\frac{\gamma_1}{\gamma_2}$, $\frac{\gamma_1}{\gamma_3}$, and $\frac{\gamma_2}{\gamma_3}$ for the three binary water(1)/methanol(2), water(1)/ethanol(3), and methanol(2)/ethanol(3) pairs plotted as function of the surface potential.

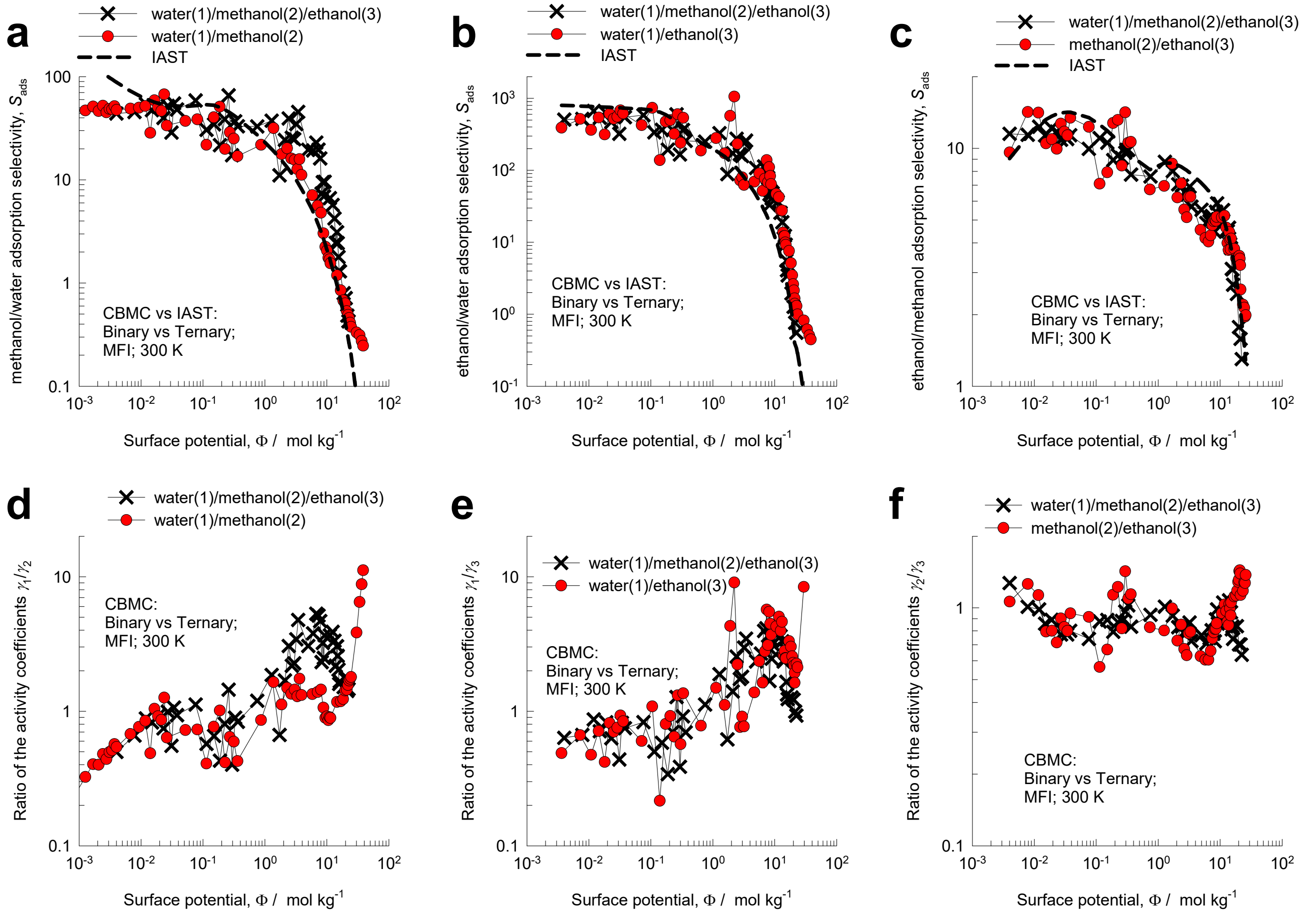

Figure S113. (a, b, c) CBMC simulations of the water(1)/methanol(2), water(1)/ethanol(3), and methanol(2)/ethanol(3) adsorption selectivities, S_{ads}, for binary and ternary mixture adsorption in MFI zeolite at 300 K. The selectivities are plotted as function of the surface potential Φ. The dashed lines are the IAST calculations. (d, e, f) CBMC simulations of the ratio of activity coefficients of $\frac{\gamma_1}{\gamma_2}$, $\frac{\gamma_1}{\gamma_3}$, and $\frac{\gamma_2}{\gamma_3}$ for the three binary water(1)/methanol(2), water(1)/ethanol(3), and methanol(2)/ethanol(3) pairs plotted as function of the surface potential.

14 Nomenclature

Latin alphabet

A	surface area per kg of framework, m^2 kg^{-1}
b_A	dual-Langmuir-Freundlich constant for species i at adsorption site A, $Pa^{-\nu A}$
b_B	dual-Langmuir-Freundlich constant for species i at adsorption site B, $Pa^{-\nu B}$
$[B]$	inverted Maxwell-Stefan diffusivity matrix, m^{-2} s
$Đ_i$	Maxwell-Stefan diffusivity for molecule-wall interaction, m^2 s^{-1}
$Đ_i(0)$	Maxwell-Stefan diffusivity at zero-loading, m^2 s^{-1}
$Đ_{ij}$	Maxwell-Stefan exchange coefficient, m^2 s^{-1}
$D_{i,self}$	self-diffusivity of species i, m^2 s^{-1}
f_i	partial fugacity of species i, Pa
f_t	total fugacity of bulk fluid mixture, Pa
$[I]$	Identity matrix with elements δ_{ij}, dimensionless
n	number of species in the mixture, dimensionless
N_i	molar flux of species i with respect to framework, mol m^{-2} s^{-1}
p_i	partial pressure of species i in mixture, Pa
p_t	total system pressure, Pa
P_i^0	sorption pressure, Pa
q_i	component molar loading of species i, mol kg^{-1}
$q_{i,sat}$	molar loading of species i at saturation, mol kg^{-1}
q_t	total molar loading in mixture, mol kg^{-1}

Nomenclature

$\mathbf{r}_{l,i}(t)$	position vector for molecule *l* of species *i* at any time *t*, m
R	gas constant, 8.314 J mol^{-1} K^{-1}
S_{ads}	adsorption selectivity, dimensionless
S_{diff}	diffusion selectivity, dimensionless
S_{perm}	permeation selectivity, dimensionless
T	absolute temperature, K
u_i	velocity of motion of adsorbate species *i* with respect to the framework material, m s^{-1}
V_p	accessible pore volume, m^3 kg^{-1}
x_i	mole fraction of species *i* in adsorbed phase, dimensionless
y_i	mole fraction of species *i* in bulk gas phase, dimensionless
z	distance coordinate, m

Greek alphabet

δ	thickness of membrane, m
δ_{ij}	Kronecker delta, dimensionless
γ_i	activity coefficient of component *i* in adsorbed phase, dimensionless
$[\Lambda]$	matrix of Maxwell-Stefan diffusivities, m^2 s^{-1}
μ_i	molar chemical potential of component *i*, J mol^{-1}
π	spreading pressure, N m^{-1}
θ	fractional occupancy, dimensionless
Θ_i	loading of species *i*, molecules per unit cell
$\Theta_{i,sat}$	saturation loading of species *i*, molecules per unit cell
Θ_t	total mixture loading, molecules per unit cell
ν	exponent in Langmuir-Freundlich isotherm, dimensionless
Π_i	membrane permeability of species *i*, mol m m^{-2} s^{-1} Pa^{-1}

Nomenclature

ρ	framework density, kg m^{-3}
Φ	surface potential, mol kg^{-1}

Subscripts

1	referring to component 1
2	referring to component 2
i	referring to component *i*
t	referring to total mixture
sat	referring to saturation conditions
δ	referring to conditions at downstream face of membrane

15 References

(1) Krishna, R.; van Baten, J. M. In silico screening of metal-organic frameworks in separation applications. *Phys. Chem. Chem. Phys.* **2011**, *13*, 10593-10616. https://doi.org/10.1039/C1CP20282K.

(2) Krishna, R.; van Baten, J. M. In Silico Screening of Zeolite Membranes for CO_2 Capture. *J. Membr. Sci.* **2010**, *360*, 323-333.

(3) Krishna, R.; van Baten, J. M. Describing Mixture Diffusion in Microporous Materials under Conditions of Pore Saturation. *J. Phys. Chem. C* **2010**, *114*, 11557-11563.

(4) Krishna, R.; van Baten, J. M. Diffusion of alkane mixtures in zeolites. Validating the Maxwell-Stefan formulation using MD simulations. *J. Phys. Chem. B* **2005**, *109*, 6386-6396.

(5) Krishna, R.; van Baten, J. M. Insights into diffusion of gases in zeolites gained from molecular dynamics simulations. *Microporous Mesoporous Mater.* **2008**, *109*, 91-108.

(6) Krishna, R. Describing the Diffusion of Guest Molecules inside Porous Structures. *J. Phys. Chem. C* **2009**, *113*, 19756-19781. https://doi.org/10.1021/jp906879d.

(7) Krishna, R. Diffusion in Porous Crystalline Materials. *Chem. Soc. Rev.* **2012**, *41*, 3099-3118. https://doi.org/10.1039/C2CS15284C.

(8) Ryckaert, J. P.; Bellemans, A. Molecular dynamics of liquid alkanes. *Faraday Discuss. Chem. Soc.* **1978**, *66*, 95-106.

(9) Dubbeldam, D.; Calero, S.; Vlugt, T. J. H.; Krishna, R.; Maesen, T. L. M.; Smit, B. United Atom Forcefield for Alkanes in Nanoporous Materials. *J. Phys. Chem. B* **2004**, *108*, 12301-12313.

(10) Kumar, A. V. A.; Jobic, H.; Bhatia, S. K. Quantum effects on adsorption and diffusion of hydrogen and deuterium in microporous materials *J. Phys. Chem. B* **2006**, *110*, 16666-16671.

(11) Makrodimitris, K.; Papadopoulos, G. K.; Theodorou, D. N. Prediction of permeation properties of CO_2 and N_2 through silicalite via molecular simulations. *J. Phys. Chem. B* **2001**, *105*, 777-788.

(12) García-Pérez, E.; Parra, J. B.; Ania, C. O.; García-Sánchez, A.; Van Baten, J. M.; Krishna, R.; Dubbeldam, D.; Calero, S. A computational study of CO_2, N_2 and CH_4 adsorption in zeolites. *Adsorption* **2007**, *13*, 469-476.

(13) Rappé, A. K.; Casewit, C. J.; Colwel, K. S.; Goddard, W. A.; Skiff, W. M. UFF, A Full Periodic Table Force Field for Molecular Mechanics and Molecular Dynamics Simulations. *J. Am. Chem. Soc.* **1992**, *114*, 10024-10035.

(14) Mayo, S. L.; Olafson, B. D.; Goddard, W. A. DREIDING: A Generic Force Field for Molecular Simulations. *J. Phys. Chem.* **1990**, *94*, 8897-8909.

(15) Britt, D.; Furukawa, H.; Wang, B.; Glover, T. G.; Yaghi, O. M. Highly efficient separation of carbon dioxide by a metal-organic framework replete with open metal sites. *Proc. Natl. Acad. Sci. U.S.A.* **2009**, *106*, 20637-20640.

(16) Rosi, N. L.; Kim, J.; Eddaoudi, M.; Chen, B.; O'Keeffe, M.; Yaghi, O. M. Rod Packings and Metal-Organic Frameworks Constructed from Rod-Shaped Secondary Building Units. *J. Am. Chem. Soc.* **2005**, *127*, 1504-1518.

(17) Dietzel, P. D. C.; Panella, B.; Hirscher, M.; Blom, R.; Fjellvåg, H. Hydrogen adsorption in a nickel based coordination polymer with open metal sites in the cylindrical cavities of the desolvated framework. *Chem. Commun.* **2006**, 959-961.

(18) Dietzel, P. D. C.; Besikiotis, V.; Blom, R. Application of metal–organic frameworks with coordinatively unsaturated metal sites in storage and separation of methane and carbon dioxide. *J. Mater. Chem.* **2009**, *19*, 7362-7370.

(19) Caskey, S. R.; Wong-Foy, A. G.; Matzger, A. J. Dramatic Tuning of Carbon Dioxide Uptake via Metal Substitution in a Coordination Polymer with Cylindrical Pores. *J. Am. Chem. Soc.* **2008**, *130*, 10870-10871.

(20) Yazaydın, A. Ö.; Snurr, R. Q.; Park, T. H.; Koh, K.; Liu, J.; LeVan, M. D.; Benin, A. I.; Jakubczak, P.; Lanuza, M.; Galloway, D. B.; Low, J. J.; Willis, R. R. Screening of Metal-Organic Frameworks for Carbon Dioxide Capture from Flue Gas using a Combined Experimental and Modeling Approach. *J. Am. Chem. Soc.* **2009**, *131*, 18198-18199.

(21) Choi, H. J.; Dincă, M.; Long, J. R. Broadly Hysteretic H_2 Adsorption in the Microporous Metal-Organic Framework Co(1,4-benzenedipyrazolate). *J. Am. Chem. Soc.* **2008**, *130*, 7848-7850.

(22) Salles, F.; Maurin, G.; Serre, C.; Llewellyn, P. L.; Knöfel, C.; Choi, H. J.; Filinchuk, Y.; Oliviero, L.; Vimont, A.; Long, J. R.; Férey, G. Multistep N_2 Breathing in the Metal-Organic Framework Co(1,4-benzenedipyrazolate). *J. Am. Chem. Soc.* **2010**, *132*, 13782-13788.

(23) Krishna, R.; van Baten, J. M. Hydrogen Bonding Effects in Adsorption of Water-alcohol Mixtures in Zeolites and the Consequences for the Characteristics of the Maxwell-Stefan Diffusivities. *Langmuir* **2010**, *26*, 10854-10867. https://doi.org/10.1021/la100737c.

(24) Krishna, R.; van Baten, J. M. Mutual slowing-down effects in mixture diffusion in zeolites. *J. Phys. Chem. C* **2010**, *114*, 13154-13156. https://doi.org/10.1021/jp105240c.

(25) Krishna, R.; van Baten, J. M. Highlighting Pitfalls in the Maxwell-Stefan Modeling of Water-Alcohol Mixture Permeation across Pervaporation Membranes. *J. Membr. Sci.* **2010**, *360*, 476-482.

(26) Kuhn, J.; Castillo-Sanchez, J. M.; Gascon, J.; Calero, S.; Dubbeldam, D.; Vlugt, T. J. H.; Kapteijn, F.; Gross, J. Adsorption and Diffusion of Water, Methanol, and Ethanol in All-Silica DD3R: Experiments and Simulation. *J. Phys. Chem. C* **2009**, *113*, 14290-14301.

(27) Krishna, R.; Van Baten, J. M. Water/Alcohol Mixture Adsorption in Hydrophobic Materials: Enhanced Water Ingress caused by Hydrogen Bonding. *ACS Omega* **2020**, *5*, 28393-28402. https://doi.org/10.1021/acsomega.0c04491.

(28) Krishna, R.; Van Baten, J. M. How Reliable is the Ideal Adsorbed Solution Theory for Estimation of Mixture Separation Selectivities in Microporous Crystalline Adsorbents? *ACS Omega* **2021**, *6*, 15499–15513. https://doi.org/10.1021/acsomega.1c02136.

(29) Rick, S. W. A Reoptimization of the Five-site Water Potential (TIP5P) for use with Ewald Sums. *J. Chem. Phys.* **2004**, *120*, 6085-6093.

(30) Chen, B.; Potoff, J. J.; Siepmann, J. I. Monte Carlo Calculations for Alcohols and Their Mixtures with Alkanes. Transferable Potentials for Phase Equilibria. 5. United-Atom Description of Primary, Secondary, and Tertiary Alcohols. *J. Phys. Chem. B* **2001**, *105*, 3093-3104.

(31) Kiselev, A. V.; Lopatkin, A. A.; Shul'ga, A. A. Molecular statistical calculation of gas adsorption by silicalite. *Zeolites* **1985**, *5*, 261-267.

(32) Frenkel, D.; Smit, B. *Understanding Molecular Simulations: From Algorithms to Applications*. 2nd Edition, Academic Press: San Diego, 2002.

(33) García-Sánchez, A.; Ania, C. O.; Parra, J. B.; Dubbeldam, D.; Vlugt, T. J. H.; Krishna, R.; Calero, S. Development of a Transferable Force Field for Carbon Dioxide Adsorption in Zeolites. *J. Phys. Chem. C* **2009**, *113*, 8814-8820.

(34) Myers, A. L.; Prausnitz, J. M. Thermodynamics of Mixed Gas Adsorption. *A.I.Ch.E.J.* **1965**, *11*, 121-130.

(35) Ruthven, D. M. *Principles of Adsorption and Adsorption Processes*. John Wiley: New York, 1984.

(36) Talu, O.; Myers, A. L. Rigorous Thermodynamic Treatment of Gas-Adsorption. *A.I.Ch.E.J.* **1988**, *34*, 1887-1893.

(37) Siperstein, F. R.; Myers, A. L. Mixed-Gas Adsorption. *A.I.Ch.E.J.* **2001**, *47*, 1141-1159.

(38) Krishna, R.; Van Baten, J. M. Elucidation of Selectivity Reversals for Binary Mixture Adsorption in Microporous Adsorbents. *ACS Omega* **2020**, *5*, 9031-9040. https://doi.org/10.1021/acsomega.0c01051.

(39) Krishna, R.; Van Baten, J. M. Using Molecular Simulations for Elucidation of Thermodynamic Non-Idealities in Adsorption of CO_2-containing Mixtures in NaX Zeolite. *ACS Omega* **2020**, *5*, 20535-20542. https://doi.org/10.1021/acsomega.0c02730.

(40) Krishna, R.; Van Baten, J. M. Investigating the Non-idealities in Adsorption of CO_2-bearing Mixtures in Cation-exchanged Zeolites. *Sep. Purif. Technol.* **2018**, *206*, 208-217. https://doi.org/10.1016/j.seppur.2018.06.009.

(41) Krishna, R. Occupancy Dependency of Maxwell−Stefan Diffusivities in Ordered Crystalline Microporous Materials. *ACS Omega* **2018**, *3*, 15743-15753. https://doi.org/10.1021/acsomega.8b02465.

(42) Talu, O.; Zwiebel, I. Multicomponent Adsorption Equilibria of Nonideal Mixtures. *A.I.Ch.E.J.* **1986**, *32*, 1263-1276.

(43) Erto, A.; Lancia, A.; Musmarra, D. Real Adsorbed Solution Theory model for competitive multicomponent liquid adsorption onto granular activated carbon. *Microporous Mesoporous Mater.* **2012**, *154*, 45-50. https://doi:10.1016/j.micromeso.2011.10.041.

(44) Smith, W.; Forester, T. R.; Todorov, I. T. The DL_POLY Molecular Simulation Package. http://www.cse.clrc.ac.uk/msi/software/DL_POLY/index.shtml, Warrington, England, March 2006.

(45) SARA Computing & Networking Services. https://subtrac.sara.nl/userdoc/wiki/lisa/description, Amsterdam, 16 January 2008.

(46) Babbitt, J. D. On the Differential Equations of Diffusion. *Canad. J. Res.* **1950**, *28 A*, 449-474.

(47) Babbitt, J. D. A Unified Picture of Diffusion. *Canad. J. Phys.* **1951**, *29*, 427-436.

(48) Krishna, R. The Maxwell-Stefan Description of Mixture Diffusion in Nanoporous Crystalline Materials. *Microporous Mesoporous Mater.* **2014**, *185*, 30-50. https://doi.org/10.1016/j.micromeso.2013.10.026.

(49) Krishna, R. Uphill Diffusion in Multicomponent Mixtures. *Chem. Soc. Rev.* **2015**, *44*, 2812-2836. https://doi.org/10.1039/C4CS00440J.

(50) Skoulidas, A. I.; Sholl, D. S.; Krishna, R. Correlation effects in diffusion of CH_4/CF_4 mixtures in MFI zeolite. A study linking MD simulations with the Maxwell-Stefan formulation. *Langmuir* **2003**, *19*, 7977-7988.

(51) Chempath, S.; Krishna, R.; Snurr, R. Q. Nonequilibrium MD simulations of difusion of binary mixtures containing short n-alkanes in faujasite. *J. Phys. Chem. B* **2004**, *108*, 13481-13491.

(52) Krishna, R.; van Baten, J. M. Onsager coefficients for binary mixture diffusion in nanopores. *Chem. Eng. Sci.* **2008**, *63*, 3120-3140.

(53) Hansen, N.; Keil, F. J. Multiscale modeling of reaction and diffusion in zeolites: from the molecular level to the reactor. *Soft Mater.* **2012**, *10*, 179-201.

(54) Krishna, R.; van Baten, J. M. An Investigation of the Characteristics of Maxwell-Stefan Diffusivities of Binary Mixtures in Silica Nanopores. *Chem. Eng. Sci.* **2009**, *64*, 870-882.

(55) Krishna, R.; van Baten, J. M. Unified Maxwell-Stefan Description of Binary Mixture Diffusion in Micro- and Meso- Porous Materials. *Chem. Eng. Sci.* **2009**, *64*, 3159-3178.

(56) Krishna, R.; van Baten, J. M. Investigating the Influence of Diffusional Coupling on Mixture Permeation across Porous Membranes *J. Membr. Sci.* **2013**, *430*, 113-128.

(57) Krishna, R.; Baur, R. Modelling Issues in Zeolite Based Separation Processes. *Sep. Purif. Technol.* **2003**, *33*, 213-254.

(58) Krishna, R. Thermodynamically Consistent Methodology for Estimation of Diffusivities of Mixtures of Guest Molecules in Microporous Materials. *ACS Omega* **2019**, *4*, 13520-13529. https://doi.org/10.1021/acsomega.9b01873.

(59) van Baten, J. M.; Krishna, R. Entropy effects in adsorption and diffusion of alkane isomers in mordenite: An investigation using CBMC and MD simulations. *Microporous Mesoporous Mater.* **2005**, *84*, 179-191. https://doi.org/10.1016/j.micromeso.2005.05.025.

(60) Krishna, R.; van Baten, J. M. Describing binary mixture diffusion in carbon nanotubes with the Maxwell-Stefan equations. An investigation using molecular dynamics simulations. *Ind. Eng. Chem. Res.* **2006**, *45*, 2084-2093.

(61) Krishna, R.; Van Baten, J. M. Using Molecular Simulations to Unravel the Benefits of Characterizing Mixture Permeation in Microporous Membranes in Terms of the Spreading Pressure. *ACS Omega* **2020**, *5*, 32769−32780. https://dx.doi.org/10.1021/acsomega.0c05269.

(62) Krishna, R.; van Baten, J. M. Influence of segregated adsorption on mixture diffusion in DDR zeolite. *Chem. Phys. Lett.* **2007**, *446*, 344-349.

(63) Krishna, R.; van Baten, J. M. Segregation effects in adsorption of CO_2 containing mixtures and their consequences for separation selectivities in cage-type zeolites. *Sep. Purif. Technol.* **2008**, *61*, 414-423. https://doi.org/10.1016/j.seppur.2007.12.003.

(64) Krishna, R.; van Baten, J. M. A molecular dynamics investigation of the diffusion characteristics of cavity-type zeolites with 8-ring windows. *Microporous Mesoporous Mater.* **2011**, *137*, 83-91. https://doi.org/10.1016/j.micromeso.2010.08.026.

(65) Krishna, R.; van Baten, J. M. Maxwell-Stefan modeling of slowing-down effects in mixed gas permeation across porous membranes. *J. Membr. Sci.* **2011**, *383*, 289-300. https://doi.org/10.1016/j.memsci.2011.08.067.

(66) Krishna, R.; Baur, R. Analytic solution of the Maxwell-Stefan equations for multicomponent permeation across a zeolite membrane. *Chem. Eng. J.* **2004**, *97*, 37-45.

(67) Krishna, R.; van Baten, J. M.; Baur, R. Highlighting the Origins and Consequences of Thermodynamic Nonidealities in Mixture Separations using Zeolites and Metal-Organic Frameworks. *Microporous Mesoporous Mater.* **2018**, *267*, 274-292. http://dx.doi.org/10.1016/j.micromeso.2018.03.013.

(68) van den Bergh, J.; Zhu, W.; Groen, J. C.; Kapteijn, F.; Moulijn, J. A.; Yajima, K.; Nakayama, K.; Tomita, T.; Yoshida, S. Natural Gas Purification with a DDR Zeolite Membrane; Permeation Modelling with Maxwell-Stefan Equations. *Stud. Surf. Sci. Catal.* **2007**, *170*, 1021-1027.

(69) van den Bergh, J.; Zhu, W.; Gascon, J.; Moulijn, J. A.; Kapteijn, F. Separation and Permeation Characteristics of a DD3R Zeolite Membrane. *J. Membr. Sci.* **2008**, *316*, 35-45.

(70) Himeno, S.; Tomita, T.; Suzuki, K.; Nakayama, K.; Yoshida, S. Synthesis and Permeation Properties of a DDR-type zeolite membrane for Separation of CO_2/CH_4 Gaseous Mixtures. *Ind. Eng. Chem. Res.* **2007**, *46*, 6989-6997.

(71) Li, S.; Falconer, J. L.; Noble, R. D.; Krishna, R. Interpreting unary, binary and ternary mixture permeation across a SAPO-34 membrane with loading-dependent Maxwell-Stefan diffusivities. *J. Phys. Chem. C* **2007**, *111*, 5075-5082.

(72) Li, S.; Falconer, J. L.; Noble, R. D.; Krishna, R. Modeling permeation of CO_2/CH_4, CO_2/N_2, and N_2/CH_4 mixtures across SAPO-34 membrane with the Maxwell-Stefan equations. *Ind. Eng. Chem. Res.* **2007**, *46*, 3904-3911.

(73) Krishna, R.; Li, S.; van Baten, J. M.; Falconer, J. L.; Noble, R. D. Investigation of slowing-down and speeding-up effects in binary mixture permeation across SAPO-34 and MFI membranes. *Sep. Purif. Technol.* **2008**, *60*, 230-236.

(74) Krishna, R. Separating Mixtures by Exploiting Molecular Packing Effects in Microporous Materials. *Phys. Chem. Chem. Phys.* **2015**, *17*, 39-59. https://doi.org/10.1039/C4CP03939D.

(75) Krishna, R. Elucidation and Characterization of Entropy Effects in Mixture Separations with Micro-porous Crystalline Adsorbents. *Sep. Purif. Technol.* **2019**, *215*, 227-241. https://doi.org/10.1016/j.seppur.2019.01.014.

(76) Costa, E.; Calleja, G.; Jimenez, A.; Pau, J. Adsorption Equilibrium of Ethylene, Propane, Propylene, Carbon Dioxide, and Their Mixtures in 13X Zeolite. *J. Chem. Eng. Data* **1991**, *36*, 218-224.

(77) Calleja G.; Pau J.; Perez P.; J.A., C. *Binary and Ternary Adsorption Equilibria at High Pressure on Molecular Sieves*. Fundamentals of Adsorption FOA 1996; Edited by L. M.D., 147-154, The Kluwer International Series in Engineering and Computer Science: Boston, Massachusetts, 1996.(https://doi.org/10.1007/978-1-4613-1375-5_17)

(78) Krishna, R.; van Baten, J. M. Using Molecular Dynamics Simulations for Elucidation of Molecular Traffic in Ordered Crystalline Microporous Materials. *Microporous Mesoporous Mater.* **2018**, *258*, 151-169. https://doi.org/10.1016/j.micromeso.2017.09.014.

(79) Krishna, R.; van Baten, J. M. Investigating cluster formation in adsorption of CO_2, CH_4, and Ar in zeolites and metal organic frameworks at sub-critical temperatures. *Langmuir* **2010**, *26*, 3981-3992.

(80) Krishna, R.; van Baten, J. M. Highlighting a variety of unusual characteristics of adsorption and diffusion in microporous materials induced by clustering of guest molecules. *Langmuir* **2010**, *26*, 8450-8463.

(81) Herm, Z. R.; Wiers, B. M.; Van Baten, J. M.; Hudson, M. R.; Zajdel, P.; Brown, C. M.; Maschiocchi, N.; Krishna, R.; Long, J. R. Separation of Hexane Isomers in a Metal-Organic Framework with Triangular Channels *Science* **2013**, *340*, 960-964.

(82) Krishna, R.; van Baten, J. M. Screening of zeolite adsorbents for separation of hexane isomers: A molecular simulation study. *Sep. Purif. Technol.* **2007**, *55*, 246-255.

(83) Dubbeldam, D.; Krishna, R.; Calero, S.; Yazaydın, A. Ö. Computer-Assisted Screening of Ordered Crystalline Nanoporous Adsorbents for Separation of Alkane Isomers. *Angew. Chem. Int. Ed.* **2012**, *51*, 11867-11871.

(84) Krishna, R. Methodologies for Evaluation of Metal-Organic Frameworks in Separation Applications. *RSC Adv.* **2015**, *5*, 52269-52295. https://doi.org/10.1039/C5RA07830J.

(85) Krishna, R. Metrics for Evaluation and Screening of Metal-Organic Frameworks for Applications in Mixture Separations. *ACS Omega* **2020**, *5*, 16987−17004. https://doi.org/10.1021/acsomega.0c02218.

(86) Krishna, R.; van Baten, J. M. Screening Metal-Organic Frameworks for Separation of Pentane Isomers. *Phys. Chem. Chem. Phys.* **2017**, *19*, 8380-8387.

(87) Hansen, N.; Krishna, R.; van Baten, J. M.; Bell, A. T.; Keil, F. J. Analysis of Diffusion Limitation in the Alkylation of Benzene over H-ZSM-5 by Combining Quantum Chemical Calculations, Molecular Simulations, and a Continuum Approach. *J. Phys. Chem. C* **2009**, *113*, 235-246.

(88) Hansen, N.; Krishna, R.; van Baten, J. M.; Bell, A. T.; Keil, F. J. Reactor simulation of benzene ethylation and ethane dehydrogenation catalyzed by ZSM-5: A multiscale approach. *Chem. Eng. Sci.* **2010**, *65*, 2472-2480.

(89) Krishna, R.; Baur, R.; Van Baten, J. M. Highlighting Diffusional Coupling Effects in Zeolite Catalyzed Reactions by Combining the Maxwell-Stefan and Langmuir-Hinshelwood Formulations. *React. Chem. Eng.* **2017**, *2*, 324-336.

(90) Krishna, R.; van Baten, J. M. Entropy-based Separation of Linear Chain Molecules by Exploiting Differences in the Saturation Capacities in Cage-type Zeolites. *Sep. Purif. Technol.* **2011**, *76*, 325-330. https://doi.org/10.1016/j.seppur.2010.10.023.